

Needle's Eye

A Drone to Find the Last Ones
Final Report

AE3200: Design Synthesis Exercise
DSE Group 9



Needle's Eye

A Drone to Find the Last Ones Final Report

Final Report

by

DSE Group 9

Student Name	Student Number
Ryan Bergmans	5211662
Mischa de Gooijer	4836553
Julia Huigen	4867874
Rosa de Jong	5016495
Jonas Meij	5247160
Jelmer Ottens	5307600
Timo van der Paardt	5309824
Liam Saanen	5288576
Alexandra Schelling	5107245
Egemen Sүүлker	5214874

Tutors : A.G. Anisimov & M.J. Ribeiro
Coache J.S. Sonneveld
Project Duration: 4, 2023 - 6, 2023
Faculty: Faculty of Aerospace Engineering, Delft

Style: TU Delft Report Style, with modifications by Daan Zwaneveld
Cover: Background by hot pot AI art generator [1]

Preface

A preface is a place to thank people, and as a group, we would certainly like to express our gratitude to some. Friends, family and roommates who acknowledge the time and effort put into this report. Time in which no other activities could be done, either social, personal or professional. We would also like to thank the people who gave feedback, motivated and stimulated us throughout the project (Andrei Anisimov, Marta Ribeiro and Jente Sonneveld). Even when sceptical sounds arose about whether the project could be finished on time, we kept on pushing to make these people and ourselves proud.

This project spoke to the members of the team because of its social relevance. Combining all our knowledge gained from the bachelor into such a subject motivated us. Writing the Design Synthesis Exercise (DSE) proved to be no small thing and no individual exercise. Every word written contributed to the bigger picture of the research. While the direction of research was steered by the subject, this research is our own. The approach taken by the group differs from the approach taken in larger research programmes because DSE is unique. The distinctiveness of the DSE lies in its ability to allow us to work together as friends, turned colleagues, unrestricted by external influences that do not contribute to the research. This opportunity has granted us the freedom to explore, innovate, and create a report that resonates with our shared aspirations.

Throughout the DSE project, we have been influenced by the invaluable insights provided by external experts. Therefore our gratitude extends to Mathijs Schellaars, Robbert Nijs, and Steven van Campen for their contributions to this research. Their expertise has shaped our perspectives, and we hope our work reflects the standards they have inspired.

We hope this report enlightens, inspires, and sparks new ideas for you as a reader, just as it has for us.

*Ryan Bergmans, Mischa de Gooijer, Julia Huigen, Rosa de Jong, Jonas Meij, Jelmer Ottens,
Timo van der Paardt, Liam Saanen, Alexandra Schelling and Egemen Sүүлker
Delft, June 2023*

Executive Overview

This report aims to detail the design process and final design for a Search and Rescue (SAR) drone that will search for victims under collapsed buildings. Firstly, the objectives and requirements for the drone system are given by the overall mission objectives. Then a detailed description of the design for each subsystem is presented. This is followed by an overview of the combined and integrated system. Subsequently, a performance analysis and a use case example of the system are given to indicate how the drone will perform during a mission. Furthermore, the Reliability, Availability, Maintainability and Safety (RAMS) characteristics are displayed together with an overview of how sustainability has been integrated into the design. The plan for how further development and eventual production will be tackled is proposed. The operational aspect is also discussed. The report finishes with an overall financial evaluation of the product and the main conclusions and recommendations found during the design process. The report is a continuation and overview of the work done and detailed in the *Project Plan*, *Baseline Report* and *Midterm Report* by Bergmans et al. [2–4].

Objectives, Requirements and Functionality

As previously stated, the purpose of the drone is to aid Urban Search And Rescue (USAR) workers in locating victims in collapsed buildings. From this mission statement, the most important objectives for the system are concluded as follows:

- The drone shall be small enough to fit inside a hole of 40x40 [cm]
- The drone has to have an operational time of at least 20 minutes
- The drone needs to be able to navigate through a dusty and dark environment
- The total cost of the drone needs to be below €5,000
- The operational cost of the drone has to be less than €300
- The drone has to be able to continue its mission in case of communication loss
- The drone has to be quickly rechargeable to allow for semi-continuous operation during the mission.

Using the mission objectives and user input, the technical requirements and functionalities the drone should have were set up. A summarised overview of how the mission is structured and the high-level functions the drone is required to have is shown in Figure 1.

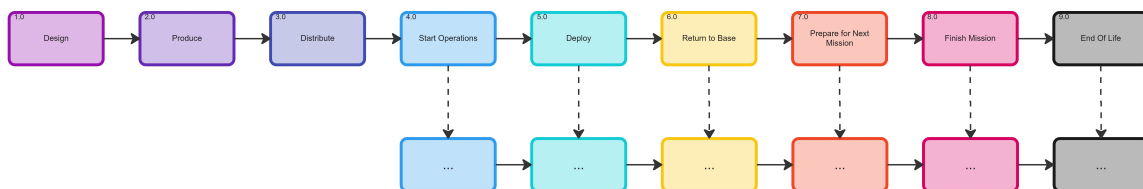


Figure 1: Simplified Functional Flow Diagram

Propulsion and Power

For the propulsion system, a ducted fan design was chosen due to the high disc loading (thrust per area) the drone has because of the size constraint. A duct design optimised for

aerodynamic performance and structural weight by Hu et al.[5] was selected. Subsequently, the propeller was designed using two different models, one for quick qualitative iteration and one for accurate data. The models used for this are a Blade Element Analysis (BEA) model and a Computational Fluid Dynamics (CFD) model, respectively. The BEA model was used to create an initial set of designs for the individual blades of the propeller, after which CFD was used to optimise the overall propeller parameters (i.e. number of blades and rotational speed). The propulsion system designed (shown in Figure 2a) fulfils the requirements posed on it and performs adequately. However, as can be seen from the results of the CFD simulation, see Figure 2b, shows that further optimisation is still possible. In particular, due to the short length of the duct, the exit velocity is angled away from the axis of rotation, resulting in less useful thrust. A duct with a longer diffuser will, in all likelihood, perform better.

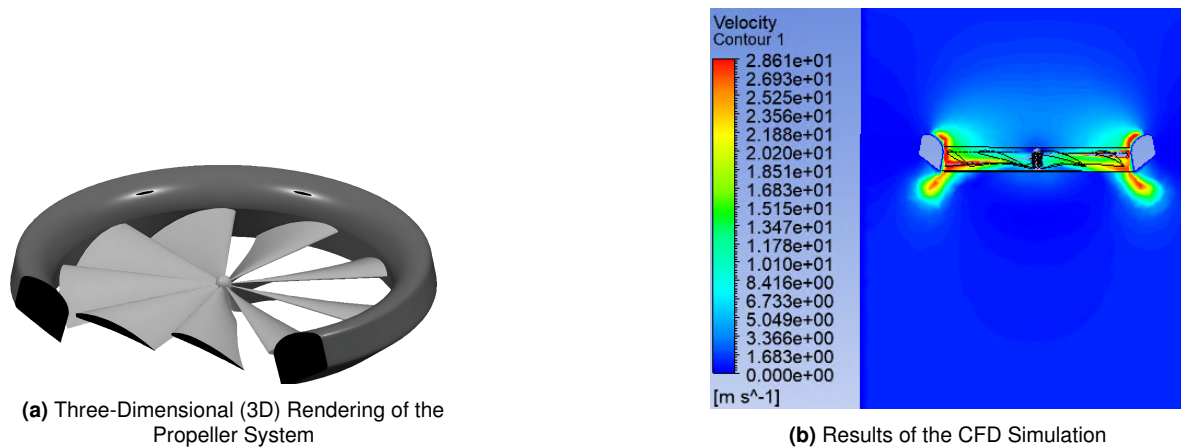


Figure 2: Design and CFD Analysis of the Propulsion System

The power system is divided into three different categories: the source, loads and distributor. The power source for the drone is a Lithium Polymer (LiPo) battery of 3300 *mAh*, selected mainly based on its mass cost and size for the amount of energy stored. The battery is connected to the distributor, called the Power Distribution Board (PDB), which is responsible for distributing the power provided to the various loads in the drone. The PDB regulates the current, voltage and thus power provided to all these systems by using Switching Voltage Regulators.

The main loads in the drone are the motors for the propulsion and track subsystems and the lighting system. These account for almost 90% of the power consumption of the drone. The electrical motors chosen are brushless Direct Current (DC) motors. These motors need a tri-phase oscillating electric signal (not to be confused with an Alternating Current (AC) signal as it never becomes negative) to operate. This signal is generated by the Electronic Speed Controllers (ESCs). The ESCs take the constant DC power from the battery and a throttle signal from the flight controller and create the necessary oscillating signal using solid-state circuitry. All these electrical components, the battery, in particular, generate heat. This heat needs to be managed to prevent performance losses or thermal runaway due to overheating. A passive cooling channel, proposed by Son et al. [6], is chosen for this purpose. The channel is a 3D-printed Aluminium Alloy Tetrahedral Lattice Porous Plate (TLPP), the electrical components can be thermally connected to this plate and deposit their heat into the environment.

Structures and Tracks

To determine the overall design of the structure of the drone, the maximum forces acting on the drone were determined. Forces taken into account are the maximum collision speed, thrust-to-weight ratio and weight of the drone. These loads were analysed analytically and using a Finite Element Model (FEM). These analyses show that the structure holds all loads considered with minimum deflection. Based on a trade-off, Continuous Fibre Reinforced Polymer (CFRP)

has been chosen as the material for both the main structure and the ducts as its structural properties meet the requirements, while also minimising the weight of the drone. The structure will be manufactured using continuous carbon fibre 3D printing as this reduces manufacturing costs and increases flexibility in the design.

The amount of tractive force needed by the tracks of the drone for the movement was determined by creating a model of the pressure distribution of the tracks and using a simulation software called RecurDyn 2023. Using the pressure distribution model this was calculated to be 8.467 N per track with a slip of 5%, allowing the drone to operate with a maximum angle of 29.32° . The simulation software comes up with a value of 33° , which is attributed to a difference in ground properties and track slips. For the material of the tracks, two options were considered: plastics or rubber. Hydrogenated Nitrile Rubber (HNR) was chosen for its ability to dampen vibrations and tear resistance compared to plastic. Using RecurDyn, the performance of the track is analysed in relation to the slope of the track. It was concluded that the maximum angle for this is the most advantageous, this angle is 63° . The track motors were selected based on the requirements of the torque, power usage and constant velocity. Both tracks will be driven by one motor each to minimise the weight of the drone. Based on RecurDyn analysis, the limitations of the tracks could be determined, indicating the terrain the drone would be able to drive.

Sensors and Data Handling

The drone will be equipped with several sensors that will be used for navigation, communication and victim identification. The three sensors types of main importance are an optical camera, Light Detection And Ranging (LiDAR) and a thermal camera. One optical camera provides a live video feed to the operator in case of a stable connection and in this way provides visual feedback for navigation as well as victim identification. In addition, the data obtained by the camera can be processed together with point clouds from LiDAR scanners to map its surroundings. Two LiDAR scanners will map the drone's surroundings, facilitating Simultaneous Localisation And Mapping (SLAM), used by the navigation subsystem. As LiDAR can measure distance, the scanners also aid in collision avoidance. One thermal, or infrared (IR) camera enables the detection of (heat) signatures. It complements the optical camera in providing data for victim identification, as well as simplifying the distinction of persons from other heat-emitting objects.

To improve the design, sensor redundancy is taken into account. To ensure continuous functioning of the drone during the mission, it is necessary to consider the failure of one or multiple sensors. Also, a set of additional features have been added to the sensor configuration of the drone to optimise performance. Firstly, the drone will be equipped with twelve Light Emitting Diodes (LEDs), to provide lighting of at least $6,000\text{ lm}$ to improve visual feedback for navigation and victim identification. Secondly, five IR distance sensors will complement the LiDAR in avoiding collision with the drone and improve distance measurements. Lastly, an Inertial Measurement Unit (IMU) containing a 3-axis gyroscope and a 3-axis accelerometer is embedded into the flight computer. These measure its angular rate and change in acceleration relatively.

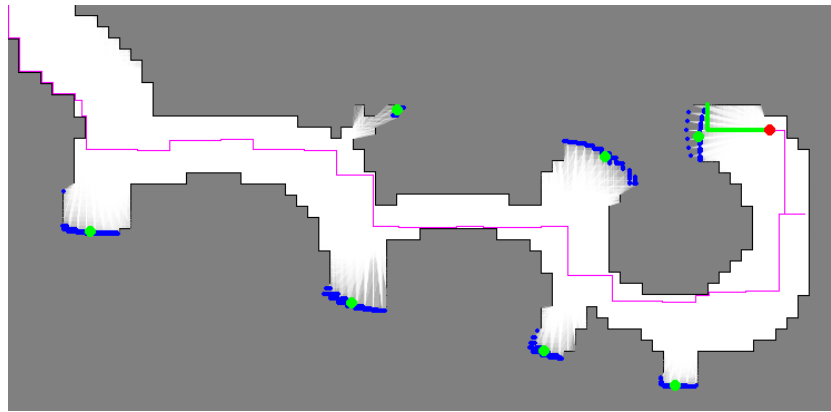


Figure 3: Snapshot of the Simulation Showing the PoI's (blue dots) and Goals (green dots)

Navigation, Stability and Control

Due to the constrained communication system, connection with the ground station is not always possible, creating the need for the drone to navigate autonomously using the sensors chosen. To achieve this, the drone has to be able to generate a map of its surroundings, detect and avoid obstacles and locate itself within the map. The locating part in particular is difficult as the drone has to fly indoors where Global Positioning System and WiFi signals are not readily available. To still be able to locate itself, the drone uses a combination of its Inertial Measurement Unit, optical camera and LiDAR scanner. When the map is created and the drone is located within the map, an algorithm can be used to determine where the drone should move next. Different mapping and path-finding algorithms are compared in a simulated environment to ascertain their performance. A composite algorithm that does both 'full coverage' and 'shortest path', based partially on the A* algorithm, is set up to do this. An example of how the JuLiam algorithm works is graphically shown in Figure 3.

The movement during navigating has to be done in a stable and controllable manner. A model of the drone is set up using the equations of motion. A controller proposed by Mellinger et al. is used to control the drone, this controller can perform applicable manoeuvres like flying through narrow gaps. To fly optimally, both indoors and outdoors, two different sets of gains are considered for the controller. For the outdoor a 'soft' gain set is used with a lower rise time but higher inaccuracies, whereas, for indoor a 'stiff' gain set is selected, having a higher rise time but with lower inaccuracies. In addition, the stability of the drone for different disturbance cases is investigated. The scenarios investigated are collision, wind gust and rotor failure. It is shown that while in stiff control mode, the drone can deal with the wind gusts and collisions encountered during the mission. However, the drone is unable to continue flying in the case of rotor failure. Nonetheless, if the drone is located in an unobstructed area it can still land softly enough to drive back to the operator using the tracks.

Communication

The communication system of the drone will have to provide a data link between the drone and the ground station while the drone operates inside a collapsed building. This means that the signal will have to penetrate reinforced concrete walls. To allow a maximum range for the drone to operate within, it was decided to split the data transmission over two separate frequencies, as visualised in Figure 4. Based on a comparison of available, off-the-shelf options, transmitters, antennas, receivers, and transceivers have been selected to provide a data connection between the drone and the operator, in accordance with their related requirements. To assess the feasibility of this connection, a link budget was created, which

resulted in an excess power margin. However, for this budget only free space loss was taken into account due to project constraints, meaning that this margin will decrease once the link budget will be assessed more thoroughly in a future design phase.

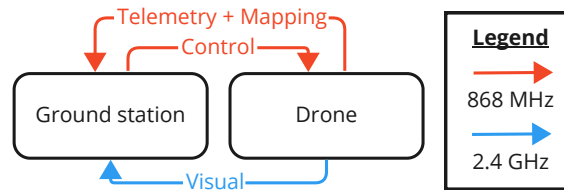


Figure 4: Data Transmission over Two Separate Frequency Links

In addition, the limitations of the communication system have been assessed. From this analysis, it has been established that the 868 *GHz* signal can penetrate three concrete walls of 30.5 *cm* in thickness before a total signal loss. For the 2.4 *GHz* signal, only two of those walls can be penetrated. Additionally, a communication flow diagram has been created to outline the flow of data between the operator and the drone. Finally, it should be noted that the drone will switch to autonomous operation once the ground station no longer receives a video feed with a quality above an established threshold. The ground station will then send a signal via the 868 *MHz* frequency link, changing the drone's controls to autonomous until it once again receives a stable video feed for over ten seconds.

Performance, Risk and Use Case Analysis

An analysis was done on the performance of the drone and its sensitivity to changes in the performance due to e.g. a change in the mission environment. An overview of the effects of the non-nominal performance of these characteristics is shown in Table 1. Furthermore, an analysis was done on the mission profile. As the power consumption of flying the drone and driving the drone differ, this has an impact on the mission time available before the battery is depleted. A graphical overview of this is shown in Figure 5 where everything above the shaded area fulfils the 10 minutes of flight time required.

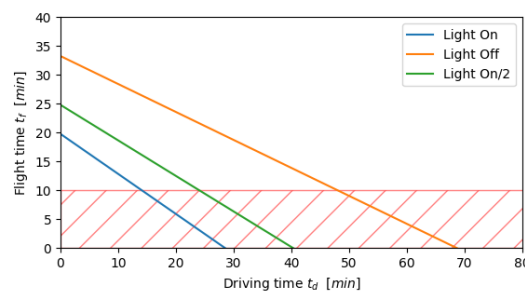


Figure 5: The Flight Time t_f versus Driving Time t_d for a Battery of 3300 *mAh*

Table 1: Effects of Non-Nominal Performance on Subsystems and the Mission

Non-Nominal Parameter	Mission Influence	Mitigation
Thrust T Power P	Flight Speed v_f Mission time, Sensor capabilities, Redundancy	Increase driving time t_d Selectively turn off electrical components
Temperature \mathcal{T}	Power, Sensor Capabilities, Data Processing	Return to base, avoid hot areas.
Operational Velocity v	Mission Distance	Accept

A use case scenario was then set up to show how well the drone performs during a typical mission. This simulation was run with and without the optimisation of the 'JuLiam' navigation algorithm. From the results, it is clear that the drone performs considerably better when using the 'JuLiam' algorithm and that is able to perform the mission within the requirements and constraints set up.

A number of technical systems risks are set up for both the over system and the individual subsystems. A risk mitigation analysis was performed to decrease either the likelihood or impact of the risks considered. This was done while taking the influence of the mitigation strategy on all the risks into account. Two risks remain a big risk to the performance of the system, namely, 'the drone is not able to stabilise after a collision' and 'the drone is not able to fly through all openings' respectively.

RAMS, Sustainability and Operations

The Reliability, Availability, Maintainability and Safety characteristics of the drone are analysed. To improve these characteristics, the reliability and reparability of the components are assessed and a maintenance schedule is set up for the drone. As the drone is designed in a modular way, maintenance can be performed quickly, efficiently and at low cost. This modular swapping of components also substantially increases the sustainability of the drone as less waste is created due to partially broken components. Additional efforts to improve the sustainability of the design have been undertaken, these focus mainly on reducing waste and using renewable energy during production and shipping. In addition, End Of Life (EOL) solutions for all the components in the drone are set up. The options considered are: repair, reuse, recycle and remove. Finally, the operations of drone usage are detailed. A box and controller are selected and the operational costs of the drone are calculated. These costs come from the operator training, which will be available for €2000, or €66.67 per mission.

Development, Production and Financial Evaluation

Further development of the drone is detailed in the Product Design & Development (PD&D) plan. This plan details the steps that still have to be taken to bring the product to the market. A high-level overview of these steps is given in Figure 6. A detailed manufacturing plan is also set up. The tools and machines to be used are specified and the overall timeline of drone manufacturing is presented. Lastly, the financial aspects of the project are evaluated. The expected costs associated with the further development of the drone are broken down. From these, a market and Strengths, Weaknesses, Opportunities and Threats (SWOT) analysis and the costs found for each component, the return on investment is calculated for the drone price of €5,000. This is found to be 2.54% but can be raised significantly through a minimal increase in price, as can be seen in Figure 7.

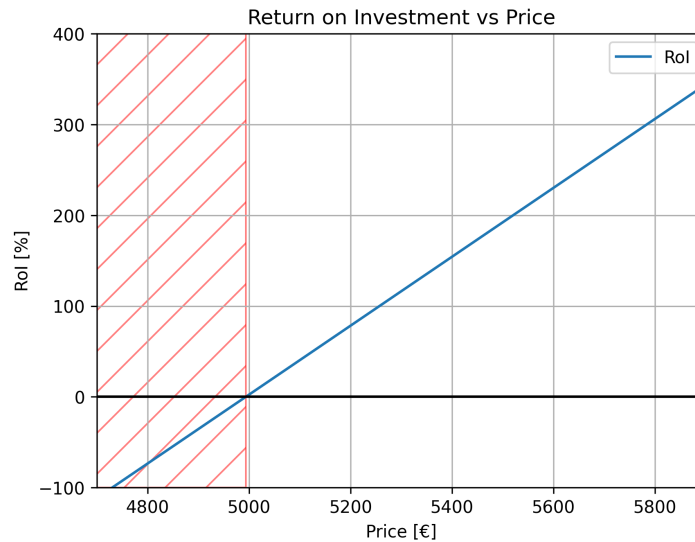


Figure 7: Return of Investment versus Asking Price



Figure 6: High-Level Overview of the Product Design & Development Plan

Final Design Overview

The final design of the drone is shown in chapter 8. As can be seen, it consists of a body with rounded sides, which is connected directly to four ducted fans. Each fan has a blade diameter of 60 *mm*, a GOE 450 airfoil profile, nine blades and is powered by a separate motor. The tracks are connected to the fans via rods that are partially integrated into the ducts. One motor per track provides the necessary torque for the tracks to drive the drone. These motors are located at the backside of the drone to counteract the weight of the sensors on the front side. The optical camera, thermal camera and lights are located on an arc connected to the front part of the tracks to prevent them from obstructing the field of view of the LiDAR sensors, while still being protected by the tracks. On each side of the body, a distance sensor is located to complement the LiDAR measurements of the drone's distance with respect to its surroundings. The only exception is the bottom of the drone, as the tracks provide a minimum clearance from the ground. The body houses the battery, which is separated by the VOXL Flight with a thermal layer to dissipate the heat generated by both components. Figure 9a shows the internal layout of all components included in the body. Figure 9b illustrates this layout from the side perspective. The final dimensions of the drone are 28.2 *cm* x 25.7 *cm* x 10.9 *cm* (l x w x h). This means that the drone fits within requirement SYS-TC-STRC-3 dictating its maximum size.



Figure 8: Final Drone Configuration

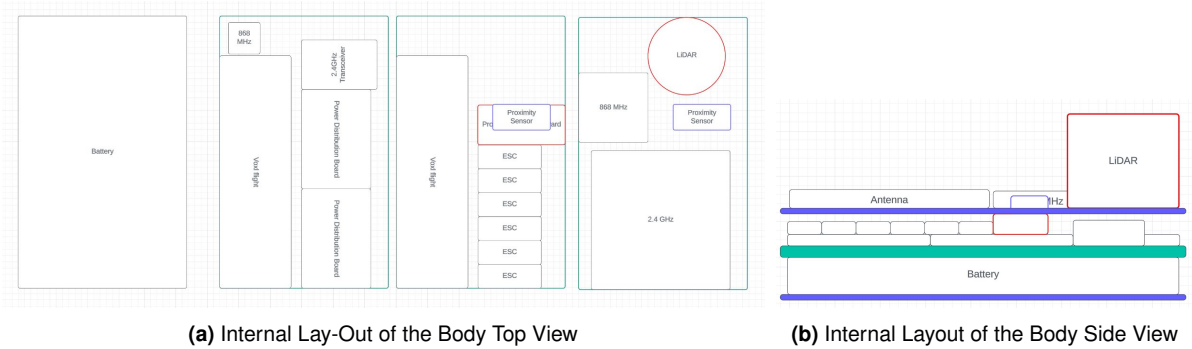


Figure 9: External and Internal Layout of the Drone

The mass, cost and power budget are displayed in Figure 10. In Figure 10a, as expected, the biggest fraction of the mass budget is allocated to the power subsystem due to the weight of the battery. However, the structure fraction is about the same size, as its volume is significantly higher than any other subsystem. In Figure 10b, it was also expected that the sensors would need the biggest portion of the costs, as sensors are relatively expensive compared to the other components of the drone. For Figure 10c the communications will need the most power due to the challenge of communicating through multiple layers of reinforced concrete. Ensuring a connection strong enough to transmit a live video feed, requires relatively much power, illustrated by its share of the budget being about twice as big as the propulsion subsystem.

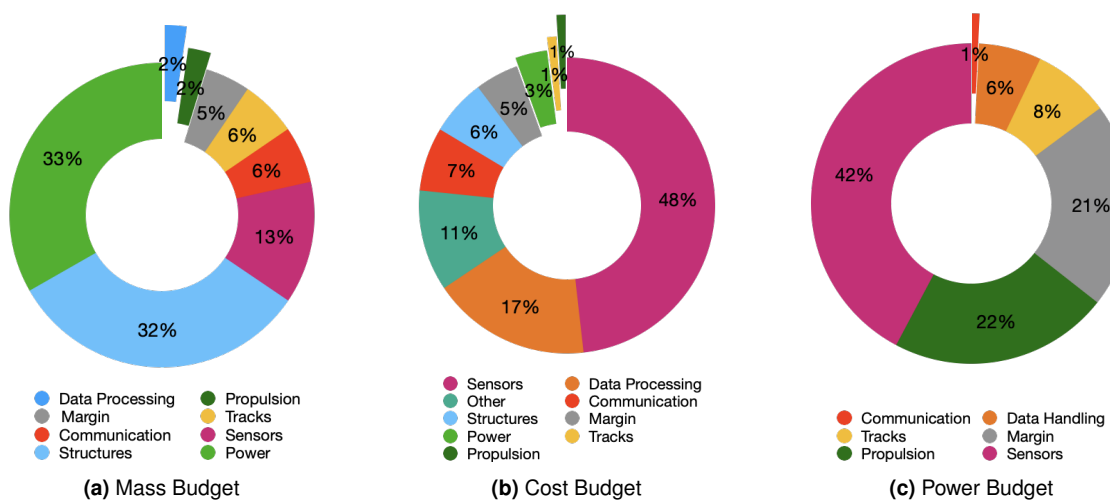


Figure 10: The Different Budgets for the Drone

Table of Contents

Preface	i	4.2.5 Track Motor and Track Wheel	40
Executive Overview	ii	4.2.6 Track Limitations	41
Nomenclature	xii	4.3 Final Structure	41
1 Introduction	1	4.3.1 Final Parameters chosen	42
2 Objectives, Requirements and Drone Functionality	2	4.3.2 Weight of Structure & Costs	42
2.1 Project Objectives	2	4.3.3 FEM Analysis	42
2.2 Technical Requirements	3	4.3.4 Eigenfrequency Frequency Analysis	45
2.3 User Input	5	5 Sensors and Data Handling	46
2.4 Drone Functionality	6	5.1 Sensors Subsystem	46
3 Propulsion and Power	11	5.1.1 Sensor Choice	46
3.1 Propulsion Subsystem	11	5.1.2 Additional Drone Features and Sensors	48
3.1.1 Blade Element Analysis	11	5.1.3 Sensor Allocation	49
3.1.2 Computational Fluid Dynamics	14	5.1.4 Malfunctioning of Sensors	50
3.1.3 Method & Results	16	5.2 Data Handling	51
3.2 Power Subsystem	23	5.2.1 Data Processor and Flight Controller	51
3.2.1 Electrical Components Selection	23	5.2.2 Sensor Data Processing	52
3.2.2 Electric Systems Overview	27	5.2.3 Kalman Filter	56
4 Structures and Tracks	29	5.3 Victim Identification	56
4.1 Structures Subsystem	29	5.3.1 Minimum Resolvable Temperature Difference	56
4.1.1 Force analysis	29	5.3.2 Required Visible Area	58
4.1.2 Material choice	30	5.3.3 Depth of Field	58
4.1.3 Structural Analysis for Flying, Driving and Collision	30	5.3.4 Victim Identification Algorithms	59
4.1.4 Model Verification	33	6 Navigation, Stability and Control	61
4.1.5 Production Method & Costs	34	6.1 Navigation Subsystem	61
4.2 Tracks Subsystem	35	6.1.1 Mapping and Obstacle Detection	61
4.2.1 Traction, Maximum Slope and Track Width	35	6.1.2 Full Coverage Algorithms	63
4.2.2 Material and Profile Selection	37	6.1.3 JuLiam Algorithm	63
4.2.3 Track Route	39		
4.2.4 Track Tension	40		

6.1.4	Positioning/Localisation	66	10 Reliability, Availability, Maintainability and Safety	101
6.1.5	Collision Handling	66	10.1 Reliability Characteristics	101
6.2	Stability and Control Sub-system	67	10.2 Availability Characteristics	102
6.2.1	Quadcopter Model	67	10.3 Maintainability Characteristics	102
6.2.2	Controller Design .	69	10.3.1 Scheduled Maintenance	103
6.2.3	Stability	73	10.3.2 Unscheduled Maintenance	104
6.2.4	Implications and Remarks	75	10.4 Safety Characteristics	104
7	Communication	78	11 Sustainability	105
7.1	Concept	78	12 Development, Production and Operations	107
7.2	Component Selection	78	12.1 Product Design and Development	107
7.2.1	868 MHz	79	12.2 Manufacturing, Assembly and Integration	110
7.2.2	2.4 GHz	79	12.2.1 Manufacturing Timeline	110
7.2.3	Component Overview	80	12.2.2 Tools and Personnel Use	110
7.3	Data Transmission and Link Budget	81	12.3 Project Gantt Chart	113
7.4	Limitations of the Communication System	82	12.4 Operations and Logistics	113
7.5	Communication Flow Diagram	84	12.5 Verification and Validation	115
8	Drone Design	86	13 Financial Evaluation	117
8.1	Configuration	86	13.1 Cost Breakdown	117
8.2	Hardware and Software Overview	87	13.2 Market Analysis	118
8.3	Resource Allocation	88	13.3 Return on Investment	121
8.4	Feasibility Analysis	90	14 Conclusion	123
8.5	Technical Risk Assessment	93	15 Recommendations	126
9	Performance Analysis and Use Case Example	96	A Task Distribution	134
9.1	Performance Analysis	96		
9.2	Sensitivity Analysis	97		
9.3	Use Case Example	99		

Nomenclature

Abbreviations

Abbreviation	Definition		
2D	Two-Dimensional	LiDAR	Light Detection And Ranging
3D	Three-Dimensional	LiPo	Lithium Polymer
A	Analysis	M	Method
AC	Alternating Current	MAI	Manufacturing, Assembly and Integration
BEA	Blade Element Analysis	MRF	Multiple Reference Frame
BEMT	Blade Element Momentum Theory	MRT	Minimum Resolvable Temperature Difference
BFS	Breadth-First Search	MTBF	Mean Time Between Failute
C	Compliance	MTTF	Mean Time To Failure
CAD	Computer-Aided Design	PID	Proportional Integral Derivative Controller
CFD	Computational Fluid Dynamics	PDB	Power Distribution Board
CFRC	Continuous Fibre Reinforced Composites	PD&D	Product Design and Development
CoC	Circle of Confusion	PID	Proportional Integral Derivative
CPU	Central Processing Unit	PoI	Point of Interest
CSI	Camera Serial Interface	RAMS	Reliability, Availability, Maintainability, and Safety
D	Demonstration	RANS	Reynolds-Averaged Navier-Stokes
DC	Direct Current	R/C	Remote Control
DoF	Depth of Field	RoI	Return on Investment
DSE	Design Synthesis Exercise	RPM	Rotations Per Minute
ESC	Electronic Speed Controller	RRT	Rapidly exploring Random Trees
EOL	End Of Life	SAR	Search And Rescue
FBD	Free Body Diagram	S&C	Stability and Control
FBS	Functional Breakdown Structure	SCCPP	Smooth Complete Coverage Path Planning
FEM	Finite Element Method	SLAM	Simultaneously Localise And Map
FFD	Functional Flow Diagram	SST	Shear-Stress Transport
GEKO	Generalised κ - ω	STC	Spanning Tree Covering
GNSS	Global Navigation Satellite System	SWOT	Strengths, Weaknesses, Opportunities and Threats
GPS	Global Positioning System	T	Test
GPU	Graphical Processing Unit	TLPP	Tetrahedral Lattice Porous Plate
HNR	Hydrogenated Nitrile Rubber	UAV	Unmanned Aerial Vehicle
I	Inspection	USAR	Urban Search And Rescue
ICP	Iterative Closest Point		
ID	Identifier		
IMU	Internal Measurement Unit		
IR	infrared		
LED	Light Emitting Diode		

Symbols

Symbol	Definition	Unit			
A	Aperature Number	[-]	L_T	Total Loss	[dB]
A	Area	[m ²]	ϕ_v	Luminous Flux	[lm]
AF	Blade activity factor	-	M	Moment	[Nm]
B	Number of blades	-	m	Mass	[Kg]
E	Elastic modulus	[GPa]	P	Power	[W]
c_l	Lift coefficient	-	P_s	Receiver sensitivity	-
c_d	Lift coefficient	-	P_m	Excess margin	[W]
CoC	Circle of Confusion	[pixels]	P_R	Receiver Power	[dBm]
D	Drag	[N]	P_T	Transmitter Power	[dBm]
D_b	Bit depth	[m]	s	Subject distance	[m]
F	Force	[N]	T	Thrust	[T]
f	Focal length	[mm]	t	Operating Time	[sec]
f	Frame rate	[frame/s]	V	Velocity	[m/s]
G_R	Receiver Antenna Gain	[dBi]	V	Voltage	[V]
G_T	Transmitter Antenna Gain	[dBi]	W	Weight	[N]
H	Hyperfocal distance	[m]	Q	Torque	[Nm]
I	Moment of Inertia	[mm ⁴]	σ	Stress	[Pa]
i	Slip rate	-	ϵ	Strain	[%]
k_t	Motor torque constant	[Nm/A]	τ	Shear stress	[Pa]
k_v	Motor velocity constant	[rad/(Vs)]	ω	Rotational speed	[rad/s]
L	Lift	[N]	ϕ	Flow angle	[rad]
L_f	Free space loss	[W]	ϕ	Angle of shear displacement	[rad]
L_A	Attenuation Loss	[dB]	α	Angle of attack	[rad]
L_O	Other Fading Loss	[dB]	θ	Pitch	[rad]
			θ	Tip over angle	[rad]
			Φ	Figure of merit	-
			η	Efficiency	-
			ρ	Density	[kg/m ³]

Introduction

In February 2023 thousands of people passed away in the aftermath of a tragic earthquake that happened in Turkey and Syria [7]. Most people did not die immediately after the earthquake. This was primarily due to the inability of Search and Rescue (SAR) teams to advance quickly enough. Collapsed buildings were often too difficult or too dangerous to enter for SAR teams. Due to these significant challenges, their ability to perform their duties effectively was hindered. In similar situations like explosions, fires and building collapses drones could be of significant help in locating victims and saving lives.

The purpose of this report is to finalise and present the design of a SAR drone that is able to localise victims while moving within confined environments underneath the debris. The design is realised by combining various in-depth technical analyses of all the subsystems proving the design concept selected in the *Midterm Report* by Bergmans et al. [4]. By exploring these subsystems individually, the aim is to optimise the overall performance of the drone and enhance the efficiency of SAR operations. This report builds on the *Project Plan, Baseline Report* and the *Midterm Report* by Bergmans et al. [2–4].

The intended use case for the drone's design is to provide assistance to SAR teams operating in disaster areas. The drone will be able to access collapsed buildings with openings too small for humans or dogs to enter. Also, the drone needs to be able to map its surroundings while moving within the confined spaces and localise victims within the debris. This limits the size of the drone to 40x40x40 *cm* at maximum to perform its mission. Furthermore, to increase the accessibility of the drone, the cost of the drone will remain limited to 5,000 euros.

First, in chapter 2 overview of the required input for the design of the drone is given with the objectives, requirements and the drone's functionality. After this, in-depth analyses of the different subsystems are demonstrated starting with Power and Propulsion chapter 3. Next, the Structures and Tracks are analysed in chapter 4 and the sensor suite is decided upon in chapter 5 together with an explanation of how all sensors are integrated within a single system. The navigation of the drone is explained in chapter 6 together with the analysis on the stability & control of the drone. The last subsystem, communication, is discussed in chapter 7. After the subsystems, the configuration is completed in the drone design chapter 8. With the design completed, an example of a use case is stated in chapter 9 to show that the requirements of the mission are met. Afterwards, Reliability, Availability, Maintainability and Safety (RAMS) characteristics are listed in chapter 10. Furthermore, the sustainability plan and the development, production and operations are discussed in chapter 11 and chapter 12, respectively. A financial assessment of the drone is done in chapter 13. The report ends with a conclusion and recommendations for further development in chapter 14 chapter 15, respectively.

Objectives, Requirements and Drone Functionality

This chapter provides an overview of the required input for the design of the drone. The project objectives will be described in section 2.1. Additionally, the user requirements are provided in this section. The in-depth subsystem requirements, which are based on these user requirements and objectives, are given in section 2.2. In section 2.3 the input of a possible user of the drone, the Urban Search and Rescue team (USAR) is discussed. Finally, an overview of the functions the drone will be able to perform is discussed in section 2.4.

2.1. Project Objectives

The aim is to design a drone that can assist Urban Search And Rescue (USAR) teams in finding victims inside collapsed buildings. The design of the drone is established based on the user requirements and project objectives, which are presented in Table 2.1 and Table 2.2, respectively [4]. These user requirements and objectives were defined based on the USAR-use case. All user requirements are labelled with their own identifier (ID). This allows for easy referencing to the user requirement without having to repeat the entire requirement. The mission need statement is also based on these objectives and is given below.

Mission Need Statement: The *Needle's Eye* system will find victims of structural collapses in environments too small or dangerous for humans.

Table 2.1: User Requirements

ID	Requirement/Objective
U-REQ-1	The drone shall not come within 20 centimetres of a victim inside a building
U-REQ-2	The drone shall not come closer than 0.5 meters from a witness during landing
U-REQ-3	The drone shall be able to operate in a dusty and dark environment
U-REQ-4	The drone with casing shall be less than 10 kilograms for operators to carry
U-REQ-6	The total cost of the drone for the end user shall not exceed 5,000 euros
U-REQ-7	The operational cost of the drone shall not exceed 300 euros
U-REQ-8	The drone shall be operable with training time below 1 week
U-REQ-9	The drone shall be able to detect people in need during operation
U-REQ-10	The drone shall be quickly deployable within 10 minutes
U-REQ-11	The drone shall continue its mission in case of a communication loss
U-REQ-12	The drone shall be repairable within the operational budget of 300 euros per mission
U-REQ-13	The drone shall be able to fit through holes with a maximum diameter of 40 centimetres
U-REQ-14	The drone shall be able to provide audio and/or visual feedback to the operator within an unobstructed range of 150 meters
U-REQ-15	The drone shall be rechargeable
U-REQ-16	The recharging time of the drone shall allow for continuous operation during mission
U-REQ-17	The drone shall be able to switch from flying to moving on the ground
U-REQ-18	The drone shall have a collision avoidance system
U-REQ-19	The drone shall have a flight time of at least 10 minutes
U-REQ-20	The drone shall have an operational time of 20 minutes

Table 2.2: Additional Project Objectives

ID	Requirement/Objective
OBJ-2	The drone shall be collision tolerant
OBJ-3	The drone shall comply with European drone regulations

2.2. Technical Requirements

Based on the user requirements and objectives, technical requirements are defined. In Table 2.3 and Table 2.4, the requirements for technically being able to perform the mission and the requirements for performing the mission within constraints are presented [4]. These requirements are used in the designing phase of the drone's subsystems.

Table 2.3: Subsystem Requirements for performing Mission Technically

Identifier	Requirement
Propulsion (SYS-TC-PROP)	
SYS-TC-PROP-1	The propulsion subsystem shall provide 30 <i>N</i> of thrust
SYS-TC-PROP-2	The propulsion subsystem shall consume 115 <i>W</i> on average while operating
SYS-TC-PROP-3	The propulsion subsystem shall provide a thrust-to-weight ratio of 2:1
SYS-TC-PROP-4	The propulsion subsystem shall have a maximum weight of 130 <i>g</i>
Power (SYS-TC-PWR)	
SYS-TC-PWR-1	The power subsystem shall provide drone power storage
SYS-TC-PWR-1-1	The battery shall store 4,500 <i>mAh</i>
SYS-TC-PWR-1-2	The battery shall provide 190 <i>W</i> of average power
SYS-TC-PWR-2	The batteries shall be rechargeable
SYS-TC-PWR-2-1	The battery shall be rechargeable in 60 minutes
SYS-TC-PWR-2-2	The battery shall be swappable
SYS-TC-PWR-3	The power subsystem shall have a maximum weight of 400 <i>g</i>
Communication (SYS-TC-COM)	
SYS-TC-COM-1	Visual data shall be able to be transmitted by the communication subsystem to the base station when the 5.8 <i>GHz</i> antenna has a stable connection
SYS-TC-COM-1-1	Transmitted visual data shall be video data
SYS-TC-COM-1-1-2	Transmitted video data shall have a minimum quality of 1280 x 720 pixels
SYS-TC-COM-1-1-3	Transmitted video data shall have a minimum frame rate of at least 24 <i>fps</i>
SYS-TC-COM-1-2	Transmitted visual data shall be picture data
SYS-TC-COM-1-2-1	Transmitted picture data shall have a minimum quality of 3840 x 2160 pixels
SYS-TC-COM-2	Audio data shall be able to be transmitted by the communication subsystem to the base station when the 5.8 <i>GHz</i> antenna has a stable connection
SYS-TC-COM-2-2	Transmitted audio data shall have a minimum quality of 128 <i>kbits/s</i>
SYS-TC-COM-3	The communication subsystem shall be able to transmit telemetry data to the base station as long as a stable connection with the telemetry antenna exists
SYS-TC-COM-3-4	The data transmission shall be encrypted
SYS-TC-COM-3-5	A controller shall allow real-time monitoring of the drone's system performance parameters when a stable connection exists between the base station and the drones telemetry antenna
SYS-TC-COM-5	The communication subsystem shall have a maximum weight of 80 <i>g</i>
SYS-TC-COM-6	The communication subsystem shall consume 15 <i>W</i> on average
Deployment (SYS-TC-DEP)	
SYS-TC-DEP-1	The drone shall be able to take off and land
SYS-TC-DEP-1-1	The drone shall be able to take off from and land on terrain with a gradient of 15 %
SYS-TC-DEP-1-2	The drone shall be able to land with a maximum force of 20 <i>N</i>
SYS-TC-DEP-1-3	The drone shall be able to analyse the landing terrain
SYS-TC-DEP-2	The drone shall be able to take off and land from the operator's hand
SYS-TC-DEP-2-1	The drone shall have supports on the bottom for the operator to grab
SYS-TC-DEP-2-2	The collision avoidance system shall allow grabbing the drone from below
Navigation (SYS-TC-NAV)	
SYS-TC-NAV-1	The drone shall have automated flight
SYS-TC-NAV-1-1	The drone shall be able to continue all operations except transmission when the connection is lost

SYS-TC-NAV-1-2	The drone shall be able to return to the operator when the battery percentage is equal to the required battery level to return to the operator plus an extra 10 %
SYS-TC-NAV-1-3	The drone shall be able to retrace its exact flight path
SYS-TC-NAV-1-4	The autopilot shall be able to react to changes in values of environmental data gathered by the sensors on the drone
SYS-TC-NAV-2	The operator shall be informed of the drone's position when connected
SYS-TC-NAV-2-1	The drone's location shall be accurate to less than 1 <i>m</i>
SYS-TC-NAV-2-2	The drone shall be able to determine its orientation with an accuracy of 1 <i>deg</i>
Operation (SYS-TC-OP)	
SYS-TC-OP-2	The drone shall be able to operate in environments of minimum light intensity of 0 <i>lm</i>
SYS-TC-OP-2-1	The drone shall have a light system of at least 6,000 <i>lm</i>
SYS-TC-OP-3	The navigation subsystem shall have a static obstacle collision avoidance subsystem
SYS-TC-OP-3-2	The static obstacle collision avoidance subsystem shall be able to avoid bodily contact
SYS-TC-OP-3-3	The static obstacle collision avoidance shall allow a 10 <i>cm</i> clearance to obstructions
SYS-TC-OP-3-4	The static obstacle collision avoidance shall allow a clearance of 20 <i>cm</i> to humans
SYS-TC-OP-4	The drone shall be operable for 20 minutes
SYS-TC-OP-4-1	The drone shall have a flight time of at least 10 minutes
SYS-TC-OP-4-2	The drone shall have an operational time of at least 20 minutes
SYS-TC-OP-5	The drone shall be operable when exposed to temperatures between 273.15 - 323.15 <i>K</i>
Safety (SYS-TC-SFTY)	
SYS-TC-SFTY-1	The safety system shall protect people from the propulsion subsystem
SYS-TC-SFTY-2	In case of detected damage, the drone shall attempt to land on the ground
Sensors (SYS-TC-SNSR)	
SYS-TC-SNSR-1	The drone shall have visual sensory capabilities
SYS-TC-SNSR-1-1	The drone shall be able to make a digital map of its surroundings
SYS-TC-SNSR-1-2	The camera system shall be able to take a picture of the victim
SYS-TC-SNSR-1-3	The camera system shall be able to take a video feed of the victim
SYS-TC-SNSR-4	The sensor subsystem shall have a maximum weight of 170 <i>g</i>
SYS-TC-SNSR-5	The sensors subsystem shall consume 80 <i>W</i> on average
Manoeuverability (SYS-TC-MNVR)	
SYS-TC-MNVR-1	The drone shall be able to fly longitudinally
SYS-TC-MNVR-1-1	The drone shall be able to fly forward with 1 <i>m/s</i>
SYS-TC-MNVR-1-2	The drone shall be able to fly backwards with 1 <i>m/s</i>
SYS-TC-MNVR-2	The drone shall be able to fly laterally
SYS-TC-MNVR-2-1	The drone shall fly up with a velocity of 1 <i>m/s</i>
SYS-TC-MNVR-2-2	The drone shall fly down with a velocity of 1 <i>m/s</i>
SYS-TC-MNVR-3	The drone shall have rotational movement
SYS-TC-MNVR-3-1	The drone shall have a minimum pitch rate of 0.15 <i>rad/s</i>
SYS-TC-MNVR-3-2	The drone shall have a minimum roll rate of 0.15 <i>rad/s</i>
SYS-TC-MNVR-3-3	The drone shall have a minimum yaw rate of 0.75 <i>rad/s</i>
SYS-TC-MNVR-4	The drone shall be stable
SYS-TC-MNVR-4-1	The drone shall withstand wind gusts of 2 <i>m/s</i>
SYS-TC-MNVR-4-2	The drone shall be able to maintain stable flight with a pitch rate of at least 0.1 <i>rad</i>
SYS-TC-MNVR-4-3	The drone shall be able to maintain stable flight with a roll rate of at least 0.1 <i>rad</i>
Structures (SYS-TC-STRC)	
SYS-TC-STRC-1	The drone shall have a maximum weight of 1,560 <i>g</i> in total
SYS-TC-STRC-2-2	The drone shall be able to sustain 1000 loading cycles
SYS-TC-STRC-3	The drone shall be within the dimensions of 400 <i>mm</i> x 400 <i>mm</i> x 400 <i>mm</i>
SYS-TC-STRC-4	The drone shall sustain a head-on collision of 1 <i>m/s</i>
SYS-TC-STRC-5	The drone shall be dust-proof and water-resistant with an IP rating of IP34
SYS-TC-STRC-6	The frame of the drone shall have a maximum weight of 220 <i>g</i> in total
Data Processing (SYS-TC-DAT)	
SYS-TC-DAT-1	The data processing subsystem shall have computational power of 1.5 <i>Tflops</i>
SYS-TC-DAT-2	The DP&S subsystem shall be able to remove distortions
SYS-TC-DAT-3	The DP&S subsystem shall be able to detect victims from data gathered by the sensors
SYS-TC-DAT-4	The DP&S subsystem shall consume 15 <i>W</i> on average
SYS-TC-DAT-5	The DP&S subsystem shall provide data storage of 128 <i>Gb</i>
SYS-TC-DAT-5-1	The DP&S subsystem shall provide storage of audio data for the operating time
SYS-TC-DAT-5-2	The DP&S subsystem shall provide storage of visual data for the operating time

SYS-TC-DAT-5-3	The DP&S subsystem shall provide storage of mission path data for twice the operating time
Tracks (SYS-TC-TRA)	
SYS-TC-TRA-1	The tracks subsystem shall provide the drone with the ability to drive
SYS-TC-TRA-1-1	The drone shall be able to drive with the speed of 1 <i>m/s</i>
SYS-TC-TRA-1-2	The drone shall be able to traverse slopes with a gradient of 15 %
SYS-TC-TRA-1-3	The drone shall be able to drive over obstacles of 10 <i>cm</i>
SYS-TC-TRA-2	The tracks subsystem shall consume 95 <i>W</i> on average while operating
SYS-TC-TRA-3	The tracks subsystem shall have a maximum weight of 100 <i>g</i>
Thermal Management (SYS-TC-TM)	
SYS-TC-TM-1	The thermal management system shall provide cooling to the drone's subsystems
SYS-TC-TM-1-1	The thermal management system shall keep the operating temperature of the drone between 288.15 - 308.15 <i>K</i> during operation

Table 2.4: Subsystem Requirements for performing within Constraints

Identifier	Requirement
Keep within budget (SYS-CO-1)	
SYS-CO-1-1	The drone shall not cost more than 5000 euros
SYS-CO-1-1-1	The propulsion subsystem shall not cost more than 300 euros
SYS-CO-1-1-2	The power subsystem shall not cost more than 300 euros
SYS-CO-1-1-3	The communication subsystem shall not cost more than 500 euros
SYS-CO-1-1-4	The sensors subsystem shall not cost more than 2,150 euros
SYS-CO-1-1-5	The structures subsystem shall not cost more than 600 euros
SYS-CO-1-1-6	The data processing subsystem shall not cost more than 700 euros
SYS-CO-1-1-6	The tracks subsystem shall not cost more than 100 euros
SYS-CO-1-2	The drone shall not cost more than 300 euros per operation
Keep within schedule (SYS-CO-2)	
SYS-CO-2-1	The drone shall be operable with required training of 1 week
SYS-CO-2-2-1	The drone shall be developed within 44 working days
SYS-CO-2-2-2	The drone shall be completed by 10 full-time team members
Adhere to legal constraints and regulations (SYS-CO-3)	
SYS-CO-3-2	The drone shall be operated by a licenced pilot
SYS-CO-3-3	The drone shall be certified by EASA
Make efficient use of resources (SYS-CO-4)	
SYS-CO-4-4-1	The drone parts shall be recyclable or reusable
SYS-CO-4-4-2	The drone production shall use green energy
SYS-CO-4-4-3	The drone development shall use green energy
SYS-CO-4-4-4	The recycling of the drone parts shall use green energy

2.3. User Input

To further gain knowledge of the needs and opportunities of possible customers in the market, a meeting was set up with M. Schellaars from the USAR team in the Netherlands. From this meeting, a number of points of interest were acquired, that will be discussed in this section.

A possible problem with using drones for SAR missions internationally, which was pointed out, is the laws and regulations in the countries of deployment. The regulations around drones vary a lot from country to country, and having a piece of equipment that might not be legal in every place of operation is a big hinder to the adoption of the product. Additionally, getting batteries or fuel cells through customs might prove to be difficult.

The most viable use case is mapping collapsed structures and determining an as exact possible location of the victim. This allows the SAR team to find and rescue the victim quicker and more efficiently and prevents "sawing through 3 meters of concrete" when a quicker route is available, according to M. Schellaars. Additionally, a detailed Three-Dimensional (3D) map of the collapsed structure could help the structural engineer in the team assess if the building is safe to enter.

The drone would only become useful if it is 40x40x40 *cm* or smaller. If the drone is larger, it will only fit through holes that dogs can also crawl through. This would reduce the use case of the drone, as it should have added value to the use of SAR dogs. Additional useful functionality of the drone would be to act as a relay between the operator and victim to allow them to communicate with each other. By being able to talk to the victim, the victim can be reassured, potential medical needs identified and the viability of rescue assessed. Detection of the environmental conditions (e.g. CO₂ levels, gas leaks and chemical hazards) would be helpful. However, they have their own handheld sensors/sniffers, so it does not provide totally new capabilities to the SAR team. Therefore, the inclusion of these sensors in the drone design is not of great importance. Having medical equipment on the drone is not very useful. If a victim has an injury that needs quick medical attention that cannot be given without a medical kit, they will most likely have perished already before the team arrives at the site.

In general, rescue teams are almost always right on top of the collapsed building with the collapsible area of a building being defined as 1.5 times the height of the building. This area is usually the working area of the team. It also dictates the size of the working area of the drone. Assuming a maximum height of 100 *m* for the building height gives a collapsible area of 150x150 *m*, and thus a minimum operating range for the drone to be 150 *m* [8].

With the inputs from the customer, the team had a better view of which areas to focus on. It was decided to keep in mind the use case presented by M. Schellaars with every decision made on the design. This way, the drone can be designed for optimal functionality. Based on the customer's input, the drone design will prioritise compact size, the ability to map collapsed structures accurately, and identify victims.

2.4. Drone Functionality

The functional analysis provides an overview of the functions the drone will be able to perform. These functions are based on the objectives, user requirements and inputs given during the user meeting. This section will provide an overview of all the functions of the drone. This will first be done with the Functional Flow Diagram (FFD). Afterwards, the Functional Breakdown Structure (FBS) is shown to provide an overview of the functions from a different perspective. They are discussed in section 2.4 and section 2.4, respectively.

Functional Flow Diagram

The FFD shows the drone's functionalities in chronological order. From left to right the different capabilities, from the drone's perspective, are presented. The FFD can be seen in Diagram 1 [9]. The flow starts on the first level (at the top). Here, nine functionality elements are shown in their respective blocks. This is the highest level functionality flow of the drone in its current state of the design process. There are three subsequent levels of detail. Each level is more detailed than the previous one. As such, level four is the most detailed. In the bottom left of the diagram, a legend is given.

First, the colour scheme used is explained. Also, the different kinds of elements that are used in the figure are listed. An additional explanation is given below each element when the name itself does not provide sufficient information. Each element has a unique identifier, shown in the top left of the block.

To clarify the structuring of the elements relative to each other, different colours are given to different phases in the FFD. For example, the 'Start Operations' phase, between blocks 4.0 and 5.0, is coloured light blue. Even when examining blocks in the third level, it is clear that they are located within this phase. The blocks that start a new phase have been given a thick outer line in their respective colour.

The diagram features 'Portal' elements. There are two kinds, an entry and an exit. To improve legibility, portals are included to prevent continuous arrows between blocks from crossing. A portal takes the colour of the 'phase' where its entry is located, therefore, the exit of a portal may be red, even though it is located in the blue 'phase' (the A portal).

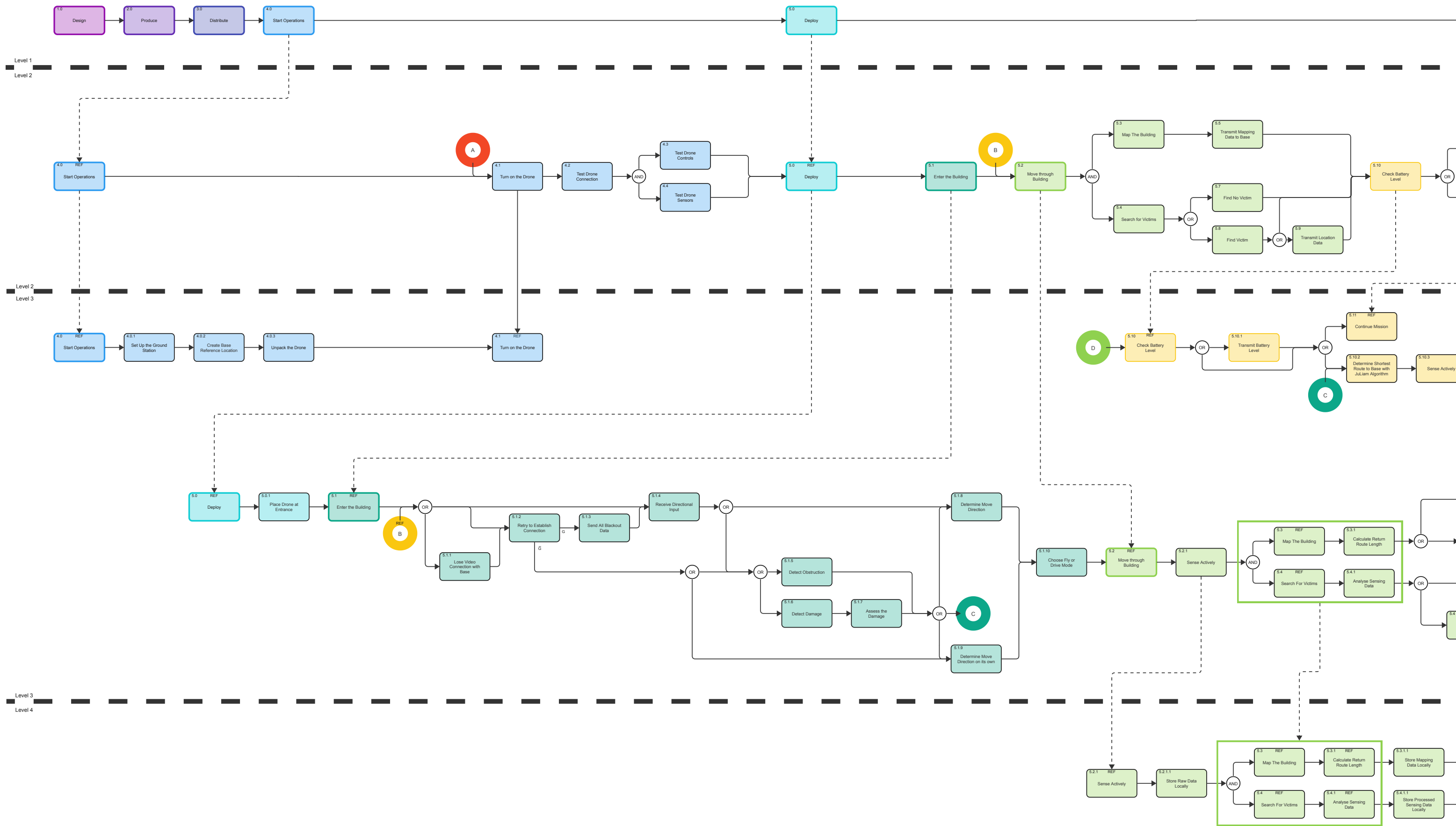
Just like with the portals, it is sometimes illogical to include a certain dashed arrow (these connect a reference function to its parent in the level above it). Either as it would cross other lines, or just because the diagram would become too cluttered. For this case, the 'Higher- and Lower-Level Connections' exist. They function in a manner similar to portals. However, as both the entrance and exit are located in the same phase, they are not coloured.

Functional Breakdown Structure

Below the FFD, the FBS is presented in Diagram 2. The FBS shows all the functions the drone will be able to perform. It is presented in the form of a hierarchical AND tree [9]. It does this through the use of eight 'grandparent' elements. These are the green blocks, that are broken down into yellow blocks, which are the 'parent' elements. This breaking up of functionality elements continues with the grey ('child') and purple ('grandchild') elements of said functionalities. Square blocks are elements that can also be found in the FFD. However, round blocks are new and are not found in the FFD. Once again, each element has a unique identifier presented in the top left of the block. The elements that can also be found in the FFD will have the same identifiers. Elements that can not be found in the FFD will have an identifier including a letter starting with 'a'.

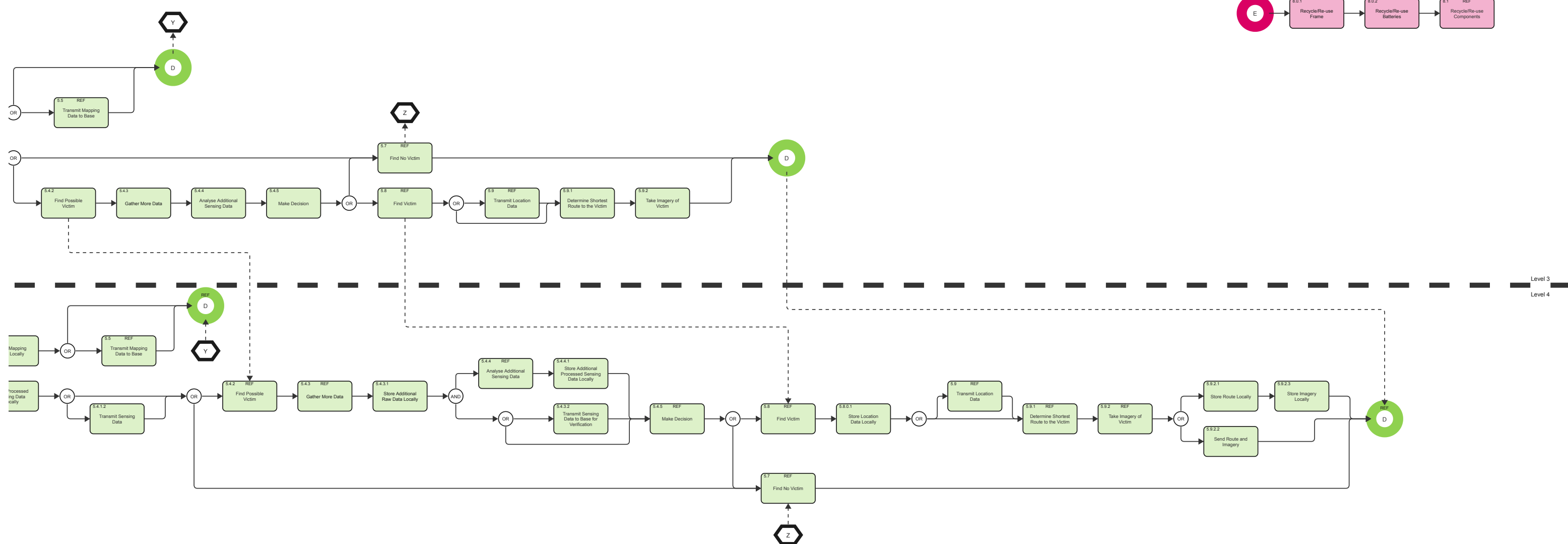
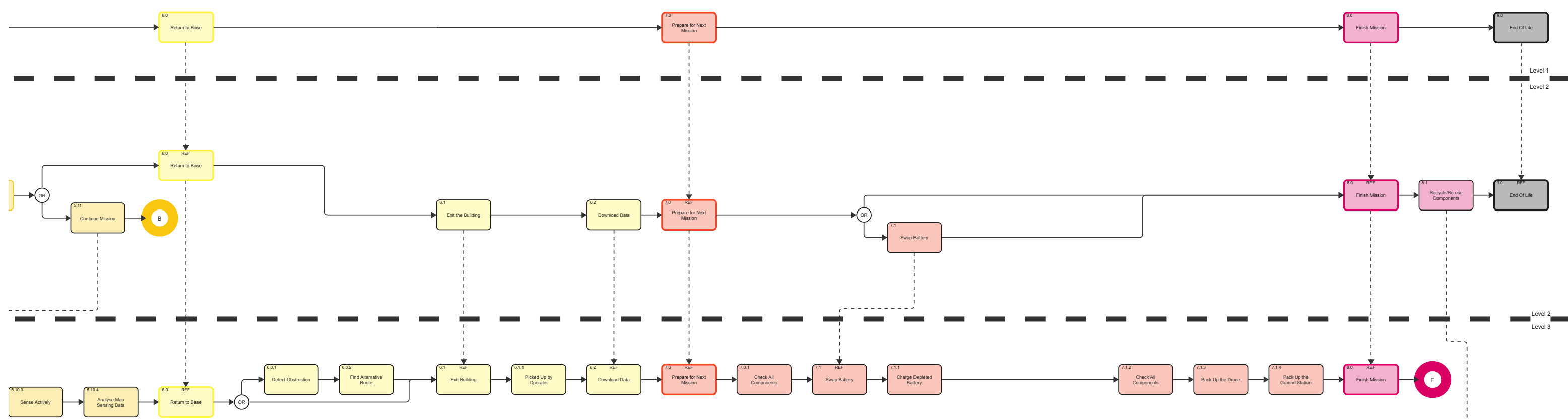
'Needle's Eye': Functional Flow Diagram

Diagram 1

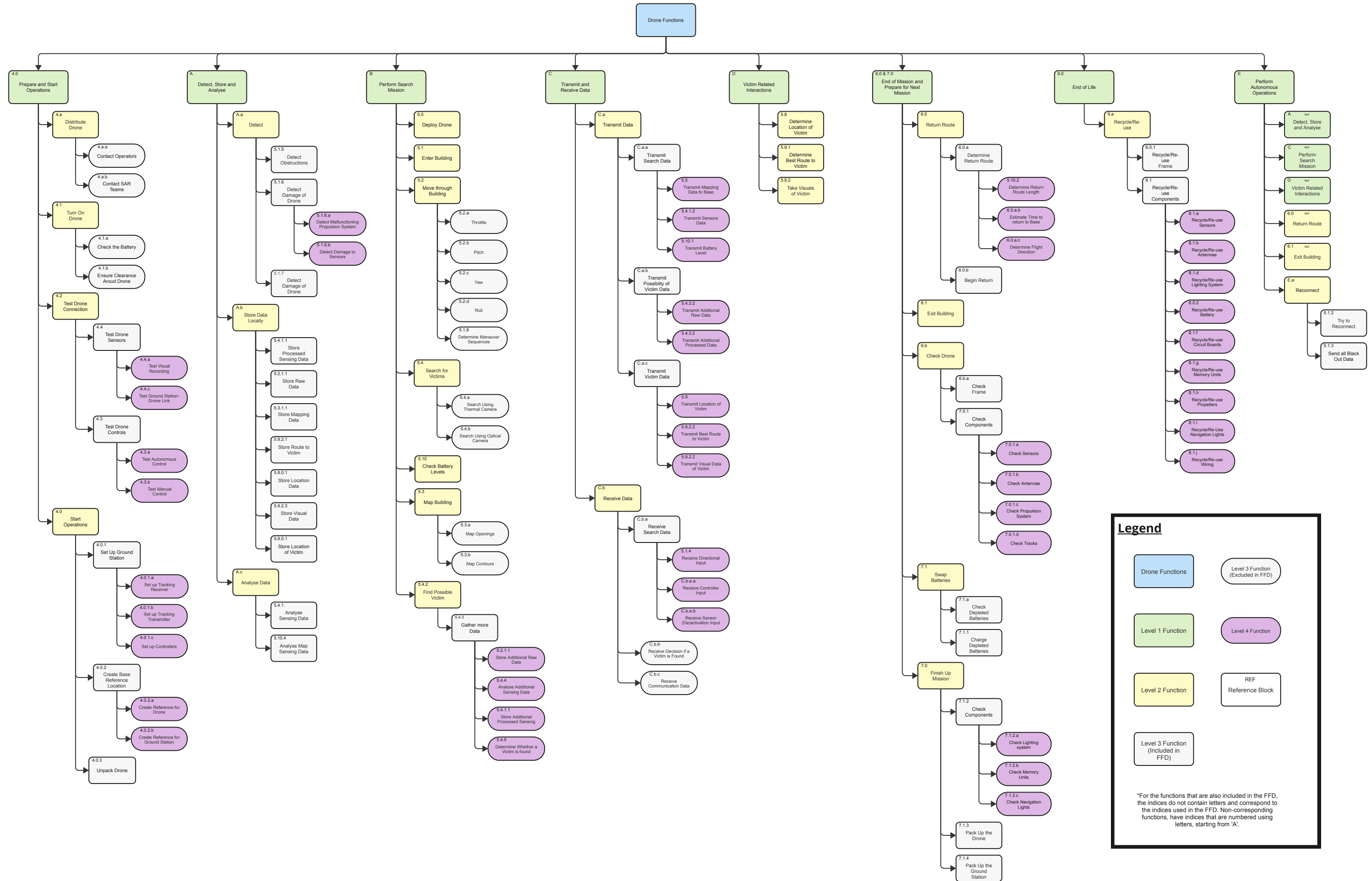


Legend

- Element of Functionality
- REF Reference Block
- G Go No-Go
- A Portal Entry
- A Portal Exit
- F Higher Level Connection
- F Lower Level Connection
- Level Separator
- Block Grouping, for Cross Level Connection



'Needle's Eye': Functional Breakdown Structure Diagram 2



Legend

- Drone Functions (Level 1 Function)
- Level 2 Function
- Level 3 Function (Included in FFD)
- Level 3 Function (Excluded in FFD)
- Level 4 Function
- REF Reference Block

*For the functions that are also included in the FFD, the indices do not contain letters and correspond to the indices used in the FFD. Non-corresponding functions, have indices that are numbered using letters, starting from 'A'.

Propulsion and Power

In this chapter, the power and the propulsion subsystems are discussed and their respective design methodologies are presented. For the propulsion subsystem, the two analysis methods used are discussed in subsection 3.1.1 and subsection 3.1.2. Subsequently, in subsection 3.1.3, the design method and its results are covered. For the power subsystem, the various electrical components needed are considered and selected by performing a trade-off on components available in the industry, see subsection 3.2.1. Finally, an analysis is done on the electrical systems as a whole and its performance during the mission subsection 3.2.2.

3.1. Propulsion Subsystem

For the determination of the propulsion system parameters, a number of models were set up and tied together in order to perform the necessary analysis. Firstly, Blade Element Analysis (BEA) was used as a qualitative model to create and perform trade-offs on different blade designs. The theory behind, and layout of, the BEA model used is explained in subsection 3.1.1. From the blade designs created and optimised using BEA, 3D propeller designs were created. These are then varied for a number of parameters (see Figure 3.6) and compared on their thrust and efficiency. This is done using a Computational Fluid Dynamics (CFD) model, The CFD model used is explained in subsection 3.1.2. The overall design method used and the results obtained are then discussed in subsection 3.1.3.

3.1.1. Blade Element Analysis

Blade Element Analysis is a relatively straightforward method to calculate the performance of a propeller. The method is based on slicing a propeller into small sections (see Figure 3.1) and calculating the lift L and drag D for each section based on the airfoil properties and the calculated airflow with respect to that section. The thrust T and torque Q are then computed by integrating the axial and normal components of the lift and drag. Blade Element Momentum Theory (BEMT) is an often-used subset of BEA. This model uses inflow factors a and a' in order to account for induced flow into the propeller. These factors are then iteratively solved using momentum theory. However, this method does not allow for the explicit solving of parameters and thus also not for the backward solving of the propeller system. Therefore a simplified model is used which assumes that the inflow factors a and a' are equal to zero, which they are usually close to [10]. By making this assumption the model can be solved backwards for some parameters like the pitch of the airfoil needed in order to obtain a certain angle of attack α . In this report, the simplified model is called the BEA model to differentiate it from the BEMT model, although BEMT can be seen as a subset of BEA. The simplified model is verified using the pyBEMT model, an already existing BEMT model. The thrust and torque values obtained from the two models for the created optimised blades are compared. Six blade designs are compared, and these are optimised for different airfoils¹, this is shown in Figure 3.4.

¹Choosing a different airfoil changes the $\left(\frac{c_l}{c_d}\right)_{max}$ and thus the optimal geometry.

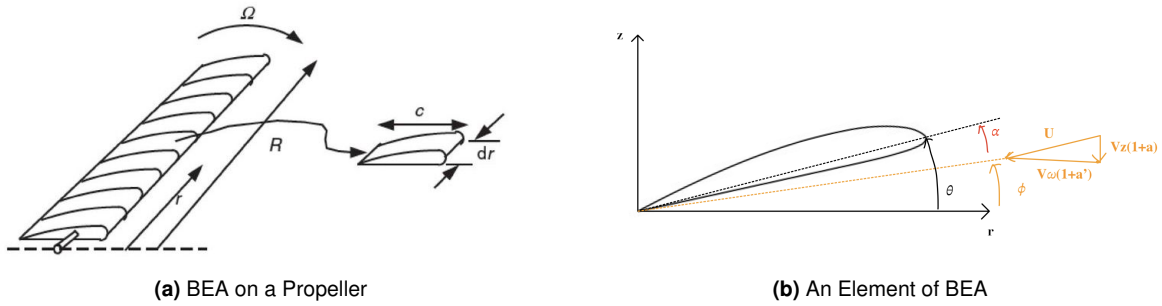


Figure 3.1: Blade Element Analysis

The first step in BEA is discretising the blade into elements, after which the incoming velocity U on the element that is being considered is determined. The airflow can be divided into the axial direction V_z and the rotational direction V_ω , see Figure 3.1b. As the inflow factors are assumed to be zero, these velocities can be readily obtained using Equation 3.1. They can then be combined in Equation 3.2 to obtain the incoming velocity. Here ω is the rotational speed of the propeller, r the distance from the propeller centre to the centre of the element being analysed. V_∞ is the velocity of the air coming into the propeller, as the propeller is sized for hovering this is set to 1 m/s . The local flow angle ϕ can then be obtained explicitly by the simplified relation shown in Equation 3.3.

$$\begin{aligned} V_z &= V_\infty (1 + a(\phi)) = V_\infty \\ V_\omega &= \omega r (1 + a'(\phi)) = \omega r \end{aligned} \quad (3.1)$$

$$U = \sqrt{V_z^2 + V_\omega^2} \quad (3.2)$$

$$\phi = \arctan\left(\frac{V_z}{V_\omega}\right) \quad (3.3)$$

The model is set up according to Figure 3.2. Airfoil data is taken from the *Airfoiltools* library [11], specifically the airfoil data at an angle of attack α where $\left(\frac{c_l}{c_d}\right)$ is at a maximum is taken. This is done as this is the most efficient point for the airfoil and thus the point for which the propeller is designed. The data used is displayed in Table 3.1. For every element the pitch θ required for the element to be at this α is then calculated² using Equation 3.4. Phi can be straightforwardly determined using the geometric relation $\phi = \theta - \alpha$, see Figure 3.1b.

$$\theta = \alpha + \arctan\left(\frac{V_z}{\omega r}\right) \quad (3.4)$$

Subsequently, the cord length (width of the blade) is constructed for every element by choosing a blade profile. This profile is a function that determines the change in cord length over the length of the blade. Multiple blade profiles were considered, this will be discussed in subsection 3.1.3. The lift and drag for each element, L_i and D_i , respectively, can then be calculated using Equation 3.5. From this the thrust T and torque Q can be determined using Equation 3.6.

²This changes over the length of the blade as the radial velocity V_ω is higher at the tip than at the root because the blade is spinning at a constant rotational speed.

$$L_i = \frac{1}{2} \rho c_i U_i^2 c_l \Delta r$$

$$D_i = \frac{1}{2} \rho c_i U_i^2 c_d \Delta r$$
(3.5)

$$T = \sum^R L_i \cos(\phi) - D_i \sin(\phi)$$

$$Q = \sum^R r_i (L_i \cos(\phi) - D_i \sin(\phi))$$
(3.6)

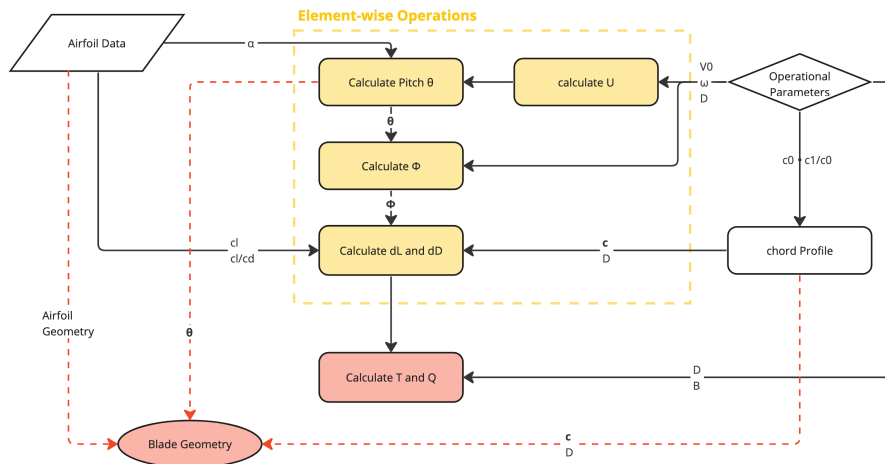


Figure 3.2: The BEA Model that has been Developed

The simplified blade element analysis model was then verified using the full Blade Element Momentum Theory. This is done by exporting the generated blades for different airfoils and analysing them using pyBEMT. The Thrust T and Torque Q values are then compared to the values generated by the simplified model. The results of this analysis are displayed in Figure 3.4. Here, the percentile difference of the T and Q values from the BEA model are compared to the values obtained from the BEMT model. This is shown for the different blades, which are optimised for different airfoils. The NRELS airfoil performs significantly worse compared to the other airfoils, this is probably due to the highly irregular c_l - α curve the airfoil has at this Re , see Figure 3.3. As the pyBEMT model iterates over different ϕ and thus α values, the results from the model can be sensitive to this irregular curve. For the better-performing blades, the deviation is below 10%, with the notable exception of the torque for the NACA 4412 and the thrust of the NACA 63812 blades. As was the case for the NRELS airfoil the c_l - α curves of these airfoils exhibit non-regular behaviour. For the NACA 63812 this is mainly at $\alpha = 3^\circ$ and $\alpha = 9^\circ$, while for the NACA 4412 this only occurs at $\alpha = 9^\circ$. While the BEA and BEMT models do not produce exactly the same values due to the simplifications made, this is not a significant concern as the model is only used to generate a blade geometry. The calculation of the resulting thrust is only done by the CFD analysis. For the subsequent analysis, the Clark-y, GOE 408, GOE 450 and NACA 4412 airfoils are chosen to compare, as

Table 3.1: Xfoil Airfoil Data Prediction at $\left(\frac{c_l}{c_d}\right)_{max}$ and $Re = 50,000$

Airfoil	c_l	c_l/c_d	α
CLARKY	1.05	29.62	9.25
NACA 4412	0.9857	33.45	9.75
GOE 408	0.9176	29.72	8.25
GOE 450	1.3248	39.64	8.75
NACA 63815	0.9176	29.72	8.25
NRELS 814	0.6601	4.43	14.25

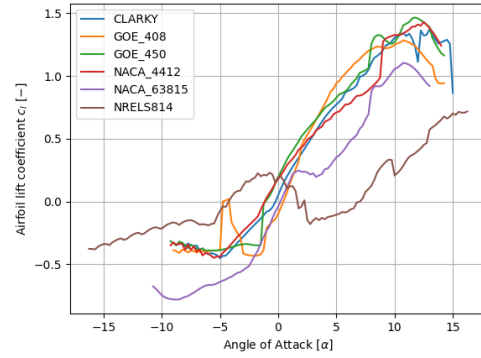


Figure 3.3: The c_l - α Curve for the NREL S814 Airfoil at $Re = 50,000$, generated using xfoil

these conform the best to the BEMT model, with the exception of the torque for the NACA 4412 airfoil. Reliable thrust data is chosen to be more important than reliable torque data as obtaining the correct thrust is more important for this application than the correct efficiency.

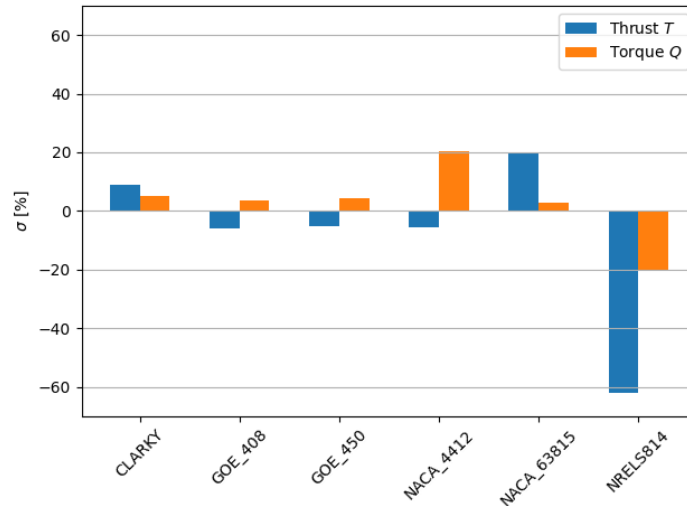


Figure 3.4: Comparison between the Simplified BEA Model and pyBEMT

3.1.2. Computational Fluid Dynamics

From the propeller designs generated using the BEA model, analysis was done using CFD. This CFD analysis is performed in the Ansys software, this software is able to create a mesh of the imported propeller designs and analyse them using a broad range of viscous and turbulence models. The specific models used are discussed later in this section.

In this case, a rotating propeller is analysed in a free stream flow. In CFD there are two methods used to analyse a system like this, mainly, the Multiple Reference Frame (MRF) method and the sliding mesh method. As the name already states, the MRF method uses multiple frames, namely a stationary (representing the free stream) and a dynamic frame (representing the movement-induced flow). The dynamic domain, fitting only the moving object, is created inside the static domain (shown in Figure 3.5). Now, the dynamic frame is rotated compared to the static frame and the object is kept stationary, creating a circular flow around the object. So two separate meshes are created, one for the static and one for the dynamic domain. These

meshes are then analysed separately each time step and the flow parameters in contact regions are then linked. In contrast, the sliding mesh approach consists of only one mesh that is solved completely for each time step. The mesh is then updated and at the start of each time step a part of the mesh is rotated. This sliding of the mesh may create an offset between the different parts of the mesh and interpolation may be needed to solve the flow equations. To keep the interpolation error low, small time steps and fine meshes are needed, increasing the computational time. Additionally, because the mesh needs to be re-generated for every time step, increasing the computational time further. The sliding mesh approach is better at capturing unsteady flow phenomena, as it obtains a single transient solution. However, as the propeller is analysed at steady state operations (constant rotational speed), this advantage is not utilised. Considering the penalties on computational time, MRF is a more applicable method.

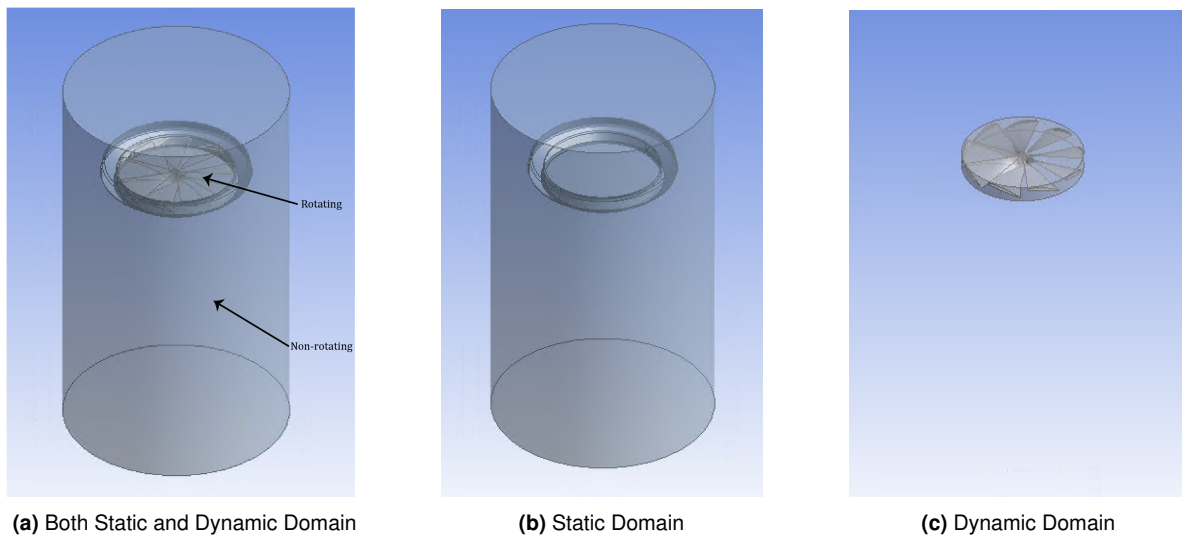


Figure 3.5: Static and Dynamic Domains shown Together and Apart

As stated before various different viscous models are available to perform a CFD simulation in the software of Ansys. Commonly used models in CFD simulations are the Spalart-Allmaras, the $\kappa-\epsilon$ and the $\kappa-\omega$ model. The $\kappa-\epsilon$ is omitted directly as this model produces non-physical turbulence viscosities when used in a MRF set-up [12]. Although the Spalart-Allmaras model is a safe option as it is a relatively simple one-equation model, the $\kappa-\omega$ model is used more often in analysing the flow through a ducted fan. According to research done this model has a higher accuracy in predicting separation and is better calibrated for free shear flows³. Therefore the latter model is used.

The $\kappa-\omega$ model is a so-called two-equation model, using the Reynolds-Averaged Navier-Stokes (RANS) equations. Within this model three different forms are present: the standard option, the generalised $\kappa-\omega$ (abbreviated to GEKO) option and the Shear-Stress Transport (SST) option. All these forms have a slightly different method for calculating turbulent viscosity and model constants. The GEKO option is recommended, as this model allows the user to change free parameters to optimise the accuracy of the model without negatively impacting the basic model calibration [13].

Nevertheless, no analysis is perfect and it is possible that inaccuracies are present in this model. Firstly, physical modelling errors are present due to uncertainties and the deliberate

³A free shear flow is an inhomogeneous flow with velocity gradients that develop in the absence of boundaries.

simplifications made. Additionally, discretisation errors such as spatial discretisation errors, due to a finite grid resolution, and temporal discretisation errors, due to finite step size, are acknowledged. By making the resolution and step size as small as possible, the errors are reduced. The partial differential equations that are approximated by algebraic equations give discretisation errors too, which can be reduced by using higher-order equations. This method is an iterative process and thus iterative convergence errors occur, depending on the stopping criteria. Lastly, round-off errors due to the finite precision of the computer arithmetic are acknowledged. Two unacknowledged errors are computer programming errors, such as bugs in coding and logical mistakes, and usage errors, such as wrong parameter values, models or boundary conditions.

3.1.3. Method & Results

With both analysis models set up, the method that is used to design the propeller can be set up. An overview of the design methodology used is shown in Figure 3.6. First of all, the size of the propeller is determined using the equation for static thrust and constants obtained from literature (step 1). Additionally, an optimised parametric design for the duct was also obtained from literature (step 2). Subsequently, using the BEA method set up in subsection 3.1.1, the propeller pitch geometry was optimised for the different blade profiles and airfoils (step 3). This geometry and the constraints from the duct were used to optimise the ratio between the root and tip chord (step 4). A blade profile was then chosen using the tip and root chord chosen (step 5). This is all done for the set of four airfoils chosen in subsection 3.1.1, thus four 3D blades are obtained using the BEA method. A comparison between the different airfoils and their respective blades was then made using the CFD set-up in subsection 3.1.2 (step 6). Subsequently, a blade was chosen and the number of blades and rotational speed was iterated over to obtain the thrust required (step 7 and 8).

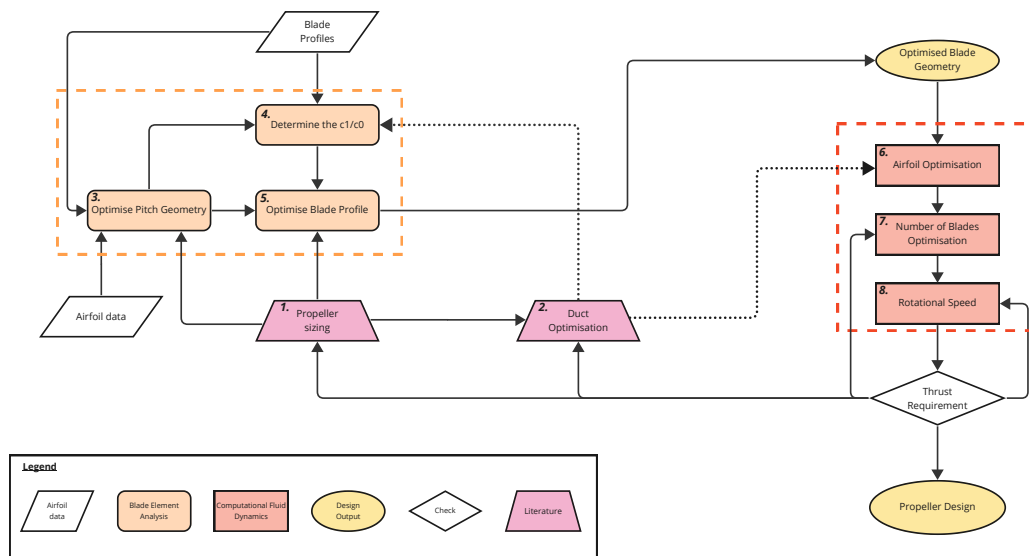


Figure 3.6: The Method used to design the Propulsion System

The propeller is sized using the equation for static thrust (see Equation 3.7), as described by Sforza [14]. Using the values for blade solidity σ and activity factor AF also obtained from the work by Sforza, see Table 3.2. A graph plotting the power against the propeller diameter and the provided thrust was constructed, see Figure 3.7. A blade size of 60 mm was selected from this graph, as this is around the point where increasing the propeller size provides minor

benefits for the power required. This gives a power required of around 20 W for the thrust levels of 60 N.

Table 3.2: Preliminary Sizing of the Propulsion Subsystem

Parameter	Value
Blade Activity Factor AF	100
Number of blades B	3
Figure-of-Merit Φ	0.7
Motor efficiency η_m	0.85
Thrust-to-Weight T/W	4
Thrust T	60 [N]
Power P_{req}	20 [W]
Blade diameter d	60 [mm]

$$F_s = 124 \left(\Phi P_{s,a} d \sqrt{1.28 \cdot 10^{-3} \frac{B}{\pi} AF} \right)^{\frac{2}{3}} \quad (3.7)$$

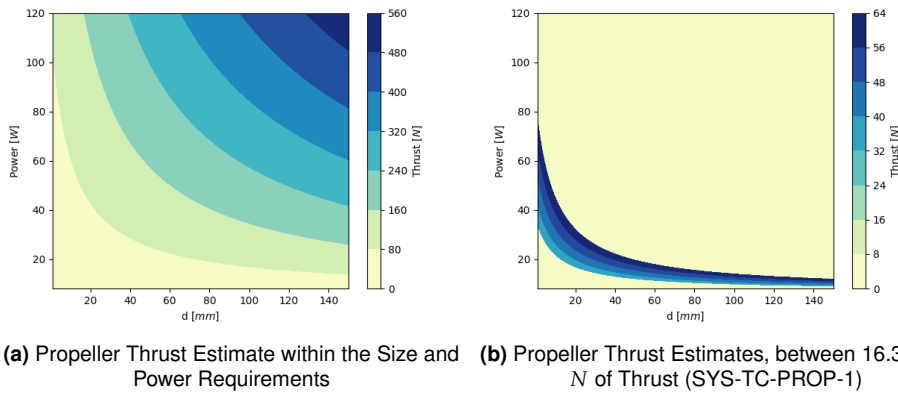


Figure 3.7: Preliminary Propeller Thrust Estimates

The duct around the propeller was based upon work done by Hu et al. [5]. It was shown that for a propeller within the disk loading ($\frac{T}{A}$) range set up, the duct design shown in Figure 3.8a had an optimal aerodynamic efficiency compared to its weight. This parameterised duct design was taken and the propeller diameter of 60mm with a clearance of 1mm was used. This clearance was taken due to manufacturing tolerances and elongation of the material due to the centrifugal force⁴ the propeller experiences, further research into this value needs to be done to be certain that the blade does not collide with the duct during operation. Airfoil data for the airfoils being considered (see subsection 3.1.1) was taken from the *Airfoiltools* library [10], see Table 3.1. The profile of a propeller blade is defined as the way the chord length (or width) of the blade changes over the length of the blade. To simplify the optimisation of the blade profile, it was chosen to keep the leading edge of the propeller straight, but vary the chord length such that the trailing edge has a certain profile. The blade profiles that were considered are shown in Figure 3.8b.

⁴The expansion due to a change in temperature is far less important in this case, as the temperature differences are very small and carbon fibre composites do not have a high expansion ratio.

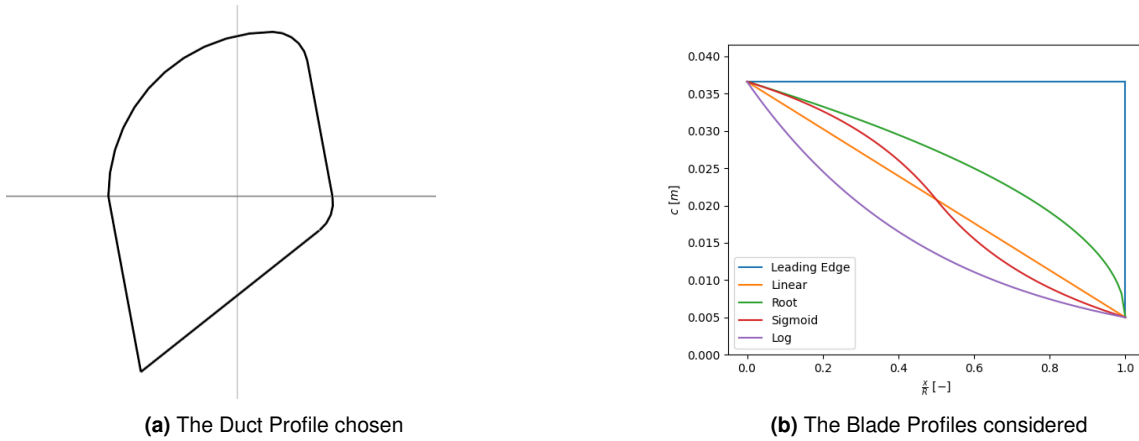


Figure 3.8: The Duct and Blade Profiles

Subsequently, an analysis of the influence of the ratio of tip chord c_0 and root chord c_1 on the thrust to torque ratio $\frac{T}{Q}$ was done, for a constant ω and V_0 this gives an indication of the efficiency of the propeller, see Equation 3.11. The chord ratio analysis is done for all blade profiles considered, the resulting graphs are displayed in Figure 3.9a, these are constructed by iterating over a range of possible combinations for c_1 and c_0 at a rotational speed ω of 5,000 Rotations Per Minute (RPM) and an inlet velocity V_0 of 1. It can clearly be seen from this that the highest $\frac{c_1}{c_0}$ generates the most thrust for a certain blade size. This conforms to the theory as the tip experiences a higher velocity ($V_\omega = \omega r$) and thus generates more thrust for the same chord length.

Next to the thrust generated, the stresses induced by the propeller forces are important. The most important stress is the bending stresses at the root of the blade, here the bending moment is the largest as all the forces are summed to this point, see Equation 3.8. The other forces are discarded for simplicity, taking the maximum Von Mises stress in the root of the blade for every c_0 - c_1 combination gives Figure 3.9b. As can be seen, for a higher $\frac{c_1}{c_0}$ ratio, the higher the stresses. However, the influence of increasing the root chord is higher than the influence of reducing the tip chord. Thus for the desired tip chord, a root chord of $0.1c_1$ is chosen.

$$\sigma_F = \frac{M_F}{A} = \frac{1}{A} \int_R F dr \quad (3.8)$$

$$\sigma_v = \max \left(\frac{\sigma_x + \sigma_y}{2} \pm \sqrt{\left(\frac{\sigma_x - \sigma_y}{2} \right)^2 + \tau_{xy}^2} \right) \quad (3.9)$$

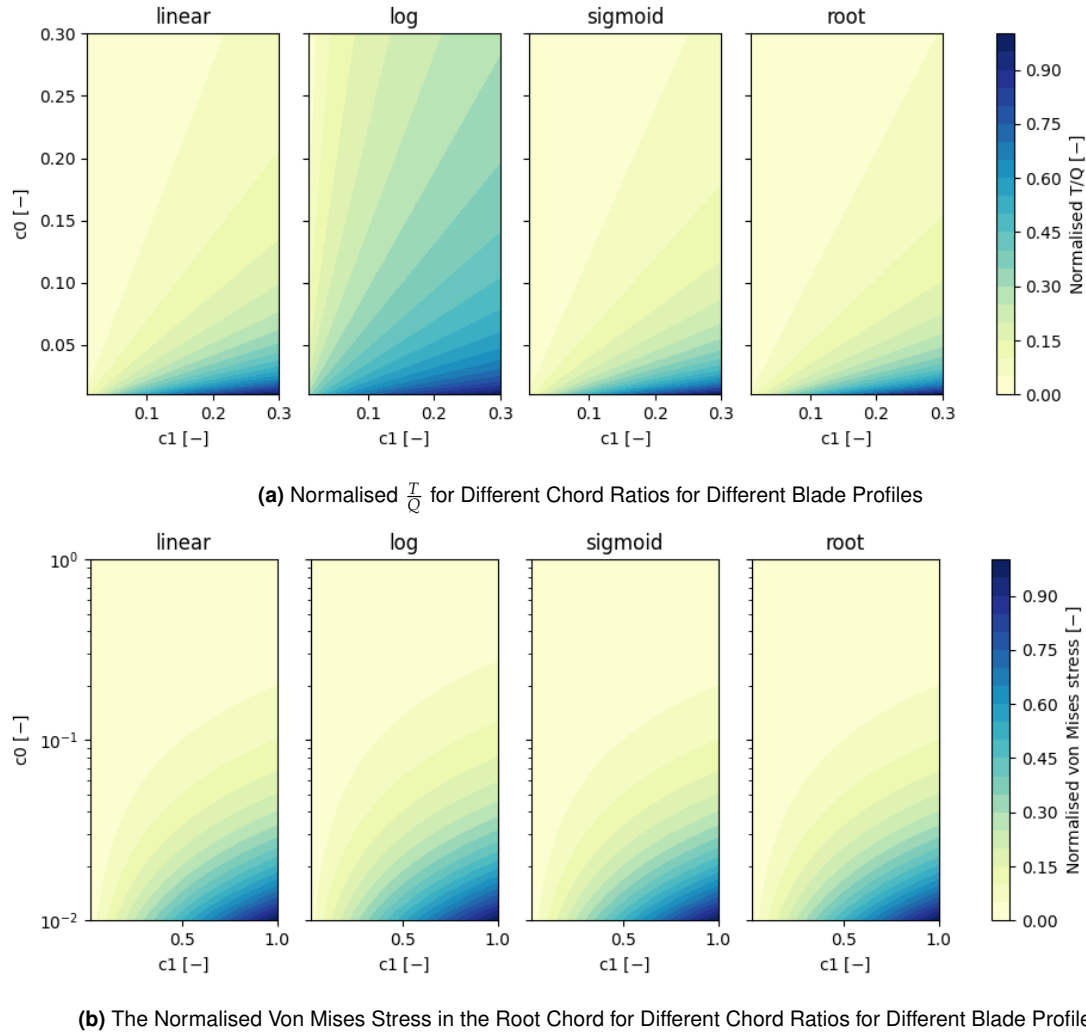


Figure 3.9: The Normalised $\frac{T}{Q}$ and Root Chord Stress for Different Chord Ratios for Different Blade Profiles at $\omega = 5,000$ RPM and $V_0 = 0.5$ m/s

Additionally, the tip chord of the propeller should fit within the diffuser length L_d of the chosen duct, see Figure 3.8a. Adding some margin means that the propeller height at the tip cannot be more than 90% of the duct height. Therefore constraining the tip chord following Equation 3.10. Here θ_1 is the pitch of the propeller at the tip of the propeller.

$$c_1 = \frac{0.9L_d}{\sin(\theta_1)} \rightarrow c_0 = \frac{0.09L_d}{\sin(\theta_1)} \quad (3.10)$$

Next, a blade profile is chosen by optimising for the $\frac{T}{Q\omega}$ parameter. This parameter is derived from the propeller efficiency from Equation 3.11. As V_0 is kept constant, this variable is discarded when ranking the blade profiles. The airfoil that the blade is optimised for is varied together with the rotational speed to make sure the chosen blade profile is optimal under a varied range of design conditions. The results from this analysis are displayed in Figure 3.10. As can be seen, the *log* blade profile consistently has a higher $\frac{T}{Q\omega}$ than its competitors at the same rotational speed, thus this blade profile is chosen.

$$\eta_{prop} = \frac{P_a}{P_{shaft}} = \frac{TV_0}{Q\omega} \quad (3.11)$$

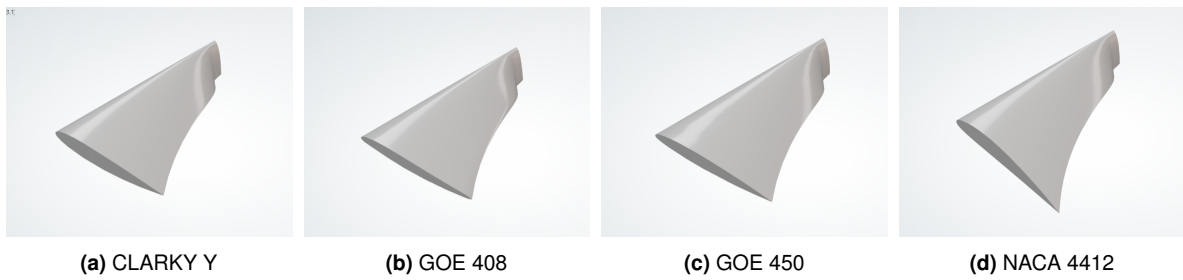


Figure 3.11: Optimised Blades for Different Airfoils

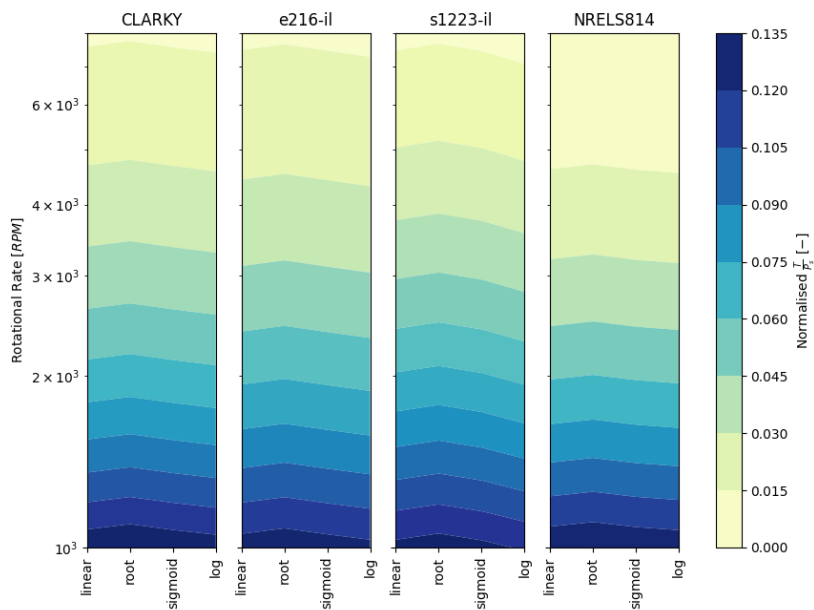


Figure 3.10: RPM vs Prop vs Airfoil

With the blade profile and $\frac{c_1}{c_0}$ determined, the blades can be created. The blades are exported to CATIA to generate a 3D rendering for every airfoil, these are displayed in Figure 3.11. As can be expected for blades optimised for the same parameters, they are similar in shape. These 3D models were then combined with the 3D model of the duct to create the basis for the CFD simulations, see Figure 3.12. The performance of these blades, in a 3-bladed configuration, spinning at 11,000 RPM, is investigated using CFD. From preliminary results, it was found that obtaining the required value for the thrust was the most constraining parameter. Thus the subsequent trade-off done using CFD took this as the parameter to optimise. The results from this analysis are shown in Figure 3.13a. As can be seen, the GEO 450 performs the best for the chosen metric in every situation, thus this airfoil and blade type is chosen.

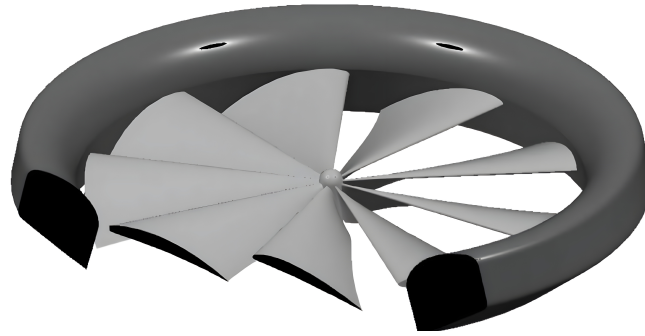
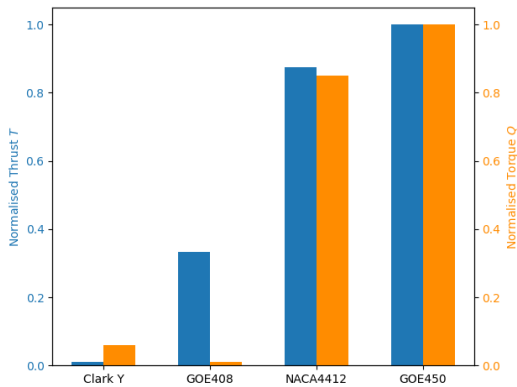
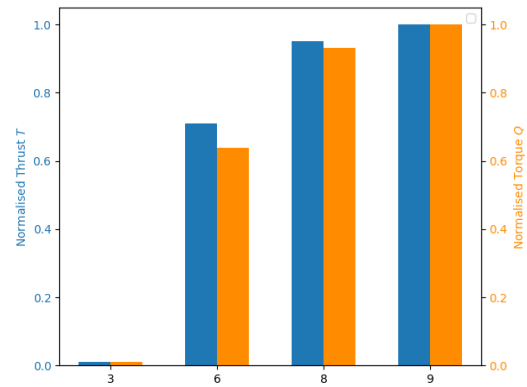


Figure 3.12: 3D Rendering of the Propeller System

Using the GEO 450 blades, the influence of the amount of blades on the thrust and torque was analysed. From Figure 3.13b it can be seen that the configuration consisting of nine blades obtains the highest thrust value. The numerical results of the CFD analysis for this propeller design are displayed in Table 3.3. Additionally, in Table 3.4 the velocity around the duct and propeller with nine blades is shown, extracted from the CFD simulation. From this figure it can be seen that the propeller design is sub-optimal as a significant part of the flow is directed to the sides instead of in downwards direction. Further optimisation of the duct would be a recommendation for further design.



(a) Performance of Different Airfoils in the CFD Simulation, $B = 3, \omega = 11,000RPM$



(b) Performance of Different Amounts of Blades from the CFD Simulation for the GEO 450, $\omega = 11,000RPM$

Figure 3.13: Performance Results from the CFD simulation

Table 3.3: Data Obtained from the CFD Model for the GOE 450 Blade, $B = 9, \omega = 5,500 RPM$

Parameter	Value	Unit
T_{des}	7.8	[N]
ω_{des}	5,500	[RPM]
Q_{des}	0.17	[Nm]
P_{des}	97.9	[W]
v_e	27.0	[m/s]
T_{nom}	5.9	[N]
ω_{nom}	4,200	[RPM]
Q_{nom}	0.13	[Nm]
P_{nom}	70.2	[W]

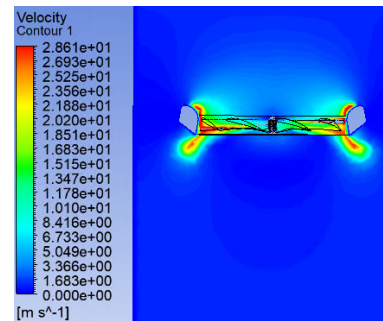


Table 3.4: CFD Results Velocity around Duct and Propeller for the GOE 450 Blade, $B = 9, \omega = 5,500 RPM$

When flying at the nominal mission speed a thrust of 5.9 (see section 6.2) is required, this is at 73% throttle. Sizing to this and including the average motor efficiency [15] of 85% and a margin of 3% to account for additional manoeuvres, an average power consumption of 70 W is determined.

Propeller Motors

From the designed propulsion system, the motors needed to drive the propellers can be chosen. These motors need to be small, lightweight and cheap. Additionally, the RPM at which the motor can spin, the voltage it needs to attain a certain rotational speed (KV-value) and the current it can take are important parameters. These are therefore also the trade-off criteria used. The criteria are weighted and a quantitative trade-off was performed, this is shown in Table 3.5 and Figure 3.14a. The sensitivity analysis of the trade-off is discussed in section 3.2.

Table 3.5: Propeller Motor Trade-Off

Criteria	Rated RPM 20.0%	KV 10.0%	Rated Current 20.0%	Size 30.0%	Mass 10.0%	Cost 10.0%	Aggregate $\sigma_w = 0.07$
Options	$\sigma = 3.42$	$\sigma = 3.11$	$\sigma = 3.19$	$\sigma = 3.25$	$\sigma = 2.87$	$\sigma = 3.14$	
DB28S01, Nanotec	1.27 $\omega = 0.01$	1.14 $\omega = 0.01$	1.0 $\omega = 0.02$	3.4 $\omega = 0.01$	4.39 $\omega = 0.03$	1.0 $\omega = 0.0$	2.13 $\omega = 0.0$
DBL36S0240 A, Nanotec	1.0 $\omega = 0.01$	1.0 $\omega = 0.01$	1.08 $\omega = 0.01$	1.0 $\omega = 0.0$	1.0 $\omega = 0.0$	6.28 $\omega = 0.05$	1.54 $\omega = 0.0$
B1020N	3.92 $\omega = 0.04$	3.11 $\omega = 0.03$	3.19 $\omega = 0.06$	8.8 $\omega = 0.24$	5.63 $\omega = 0.06$	9.18 $\omega = 0.21$	5.86 $\omega = 0.0$
Happymodel SE0802	8.7 $\omega = 0.34$	10.0 $\omega = 0.73$	2.25 $\omega = 0.03$	8.65 $\omega = 0.22$	10.0 $\omega = 0.54$	9.34 $\omega = 0.22$	7.72 $\omega = 0.11$
Racerstar BR1103B	10.0 $\omega = 0.55$	5.05 $\omega = 0.09$	10.0 $\omega = 0.87$	7.72 $\omega = 0.15$	8.4 $\omega = 0.28$	9.22 $\omega = 0.21$	8.58 $\omega = 0.89$
PCS4 Mi- cro motor	4.41 $\omega = 0.06$	5.94 $\omega = 0.14$	1.08 $\omega = 0.01$	10.0 $\omega = 0.38$	6.35 $\omega = 0.09$	10.0 $\omega = 0.3$	6.33 $\omega = 0.0$

From the trade-off table, the Racerstar BR1103B wins with a win rate of 89%. This winrate shows that the result is relatively insensitive to changes in the weights. The Racerstar performs well in every category except for the KV value of the motor.

Limitations

The blade element model uses airfoil data, namely the c_l and c_d values for differing α , and calculates the lift and drag assuming an infinite wing. This results in the negligence of tip losses of the propeller. However, as the propeller uses a ducted fan design, these tip losses are minimised [16]. Additionally, the blade-blade interactions⁵ are not accounted for in the BEA model, as it sees every element analysed as a stand-alone element. This interaction is only modelled in the CFD analysis, this can lead to a sub-optimal design for the blades.

Not all possible geometries are considered using the design method setup. In further research, the design space can be expanded to look for a more optimised design. Due to the blade-duct geometry, the blade tip area is slightly reduced, because this area is at the tip it might have an impact that is significant. Blades are optimised for thrust and energy efficiency, not for mass and structural efficiency, the mass might be significantly higher than expected. The twist is completely determined by the design angle of attack α , which is at $\left(\frac{c_l}{c_d}\right)_{max}$, while this

⁵The propellers move partially in the wake of the propeller before it, this changes the flow over the propeller blade and thus the resulting performance of the propellers.

might be the most efficient angle for this airfoil, in a 3D environment this might not be the optimal design. It should be noted that keeping a straight leading edge might not necessarily be the optimal design for the structural aspect of the blade design a straight leading edge with these particular profiles induces a higher twisting torque on the blade. Further research on the trade-off between structural weight and aerodynamic performance needs to be done.

3.2. Power Subsystem

The power subsystem consists of three main parts: the loads (e.g. the flight board, motors/- Electronic Speed Controllers (ESC) and the antenna), the source (battery) and the distributor and the Power Distribution Board (PDB). The components for these main parts and how they connect to each other are discussed in this section.

3.2.1. Electrical Components Selection

In this subsection, the electrical components needed for the power systems are selected from off-the-shelf components. A quantitative trade-off on these components was performed based on the relevant criteria for the specific components. The values for the specific criteria are normalised on a 1-10 scale and a sensitivity analysis was performed. This is done because the exact values for the criteria and the weight can have a significant impact on the trade-off result. Thus it is important to check how sensitive the trade-off is to a change in a specific grade and the weights assigned.

To analyse the sensitivity of the grades for specific criteria, first the average of the grades is calculated. Then it is assumed that the assigned grades are normally distributed around the average. This means that the standard deviation of the assigned grades can be calculated. This is shown in the same box as the criteria at the bottom with $\sigma = \dots$. For all the assigned grades for that criteria, it is assumed that they are normally distributed around the value they are assigned with a standard deviation equal to the standard deviation for the entire criteria. Using this normal distribution of the value of the grade a random value is picked. This is done for all the assigned values. Then all the values are compared and the option with the highest grade wins. This is repeated 10000 times and for each option, it is determined what fraction of the time they win. These fractions are written down with $\omega = \dots$ in the same box as the value the option was assigned for the criteria. This win rate shows how confidently it can be said that an option is preferred. If the win rate is a lot higher than the others it can confidently be said that it is superior to the other options. Whereas, if the win rates of multiple options are close together, a small difference in grades obtained can mean that a different option than the one with the highest grade is superior.

The analysis for the weights is done similarly to the analysis for the grade sensitivity. From the sampling of the weights, the win rate ω of the aggregate scores is computed for each option. A high win rate will give confidence in the result obtained, as it indicates that the result will not change significantly for a small change in grading or weights. Note that the standard deviation of the weights w is displayed in the box of the aggregate score. Based on the aggregate score components are picked, the win rate is then used to give an indication of how confidently the winner can be picked.

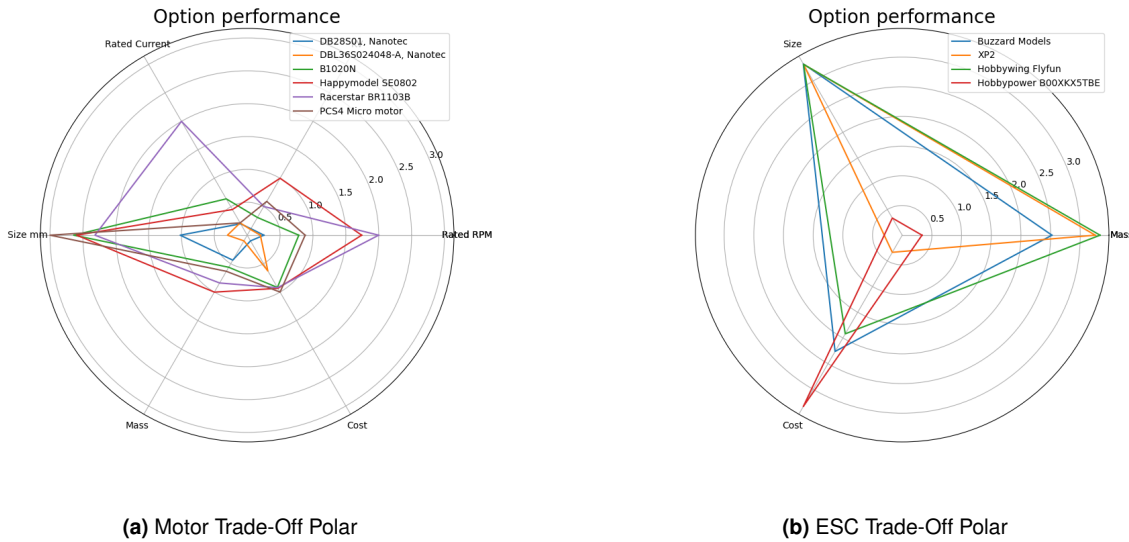


Figure 3.14: Propulsion Motors and ESC Trade-Off Polars

Electronic Speed Controller

The ESC take a throttle input from the flight controller using Pulse-Width-Modulation to generate a triphase semi-Alternating Current (AC) signal from the Direct Current (DC) power supplied to give to the motor. The voltage V , phases ϕ and frequency f of the signal sent to the motor determine the speed at which the motor turns. The microcontroller included in the ESC also keeps track of the motor’s position in order to ensure smooth acceleration and give feedback to the flight controller. The ESC needs to be able to run the motors, as these take a maximum operating current of $6A$. All the ESCs considered are sized for this current. Additionally, the mass, cost and size of the ESCs are important. These are weighted equally and a number of ESCs that are available on the market are traded-off, see Table 3.6 and Figure 3.14b. From the trade-off performed, it can be seen that the Hobbywing Flyfun is the winner, winning mainly in the mass category.

Table 3.6: Electronic Speed Controller Trade-Off

Criteria	Mass 33.33%	Size 33.33%	Cost 33.33%	Aggregate $\sigma_w = 0.0$
Options	$\sigma = 3.64$	$\sigma = 3.89$	$\sigma = 3.23$	
Buzzard Models	7.57 $\omega = 0.18$	10.0 $\omega = 0.34$	6.79 $\omega = 0.2$	8.12 $\omega = 0.0$
XP2	9.76 $\omega = 0.39$	9.97 $\omega = 0.32$	1.0 $\omega = 0.01$	6.91 $\omega = 0.0$
Hobbywing Flyfun	10.0 $\omega = 0.43$	9.97 $\omega = 0.33$	5.76 $\omega = 0.13$	8.58 $\omega = 1.0$
Hobypower B00XKX5TBE	1.0 $\omega = 0.0$	1.0 $\omega = 0.0$	10.0 $\omega = 0.67$	4.0 $\omega = 0.0$

Power Distribution Board

The PDB takes power from the battery and regulates the voltage and current (and thus power) output to the various electrical components. The main power-taking components are the electric motors via the ESCs and the lights. The board needs at least six ESC connections of at least $6A$ and a connection to the lights of $4.05A$. The considered boards all support this, thus they are judged on size mass and cost equally. The results are shown in Table 3.7 and

Figure 3.15a. As can be seen from the trade-off, the Matek PDB-XT60 performs the best in every category, only being contested by the HexSoon for the size criteria.

Table 3.7: Power Distribution Board Trade-Off

Criteria	Size 33.33%	Mass 33.33%	Cost 33.33%	Aggregate $\sigma_w = 0.0$
Options	$\sigma = 4.11$	$\sigma = 3.67$	$\sigma = 3.85$	
Matek PDB-XT60	10.0 $\omega = 0.53$	10.0 $\omega = 0.79$	10.0 $\omega = 0.86$	10.0 $\omega = 1.0$
HexSoon PIX-HAWK	9.39 $\omega = 0.46$	5.5 $\omega = 0.19$	1.0 $\omega = 0.04$	5.3 $\omega = 0.0$
Alien Copter	1.0 $\omega = 0.02$	1.0 $\omega = 0.02$	3.05 $\omega = 0.1$	1.68 $\omega = 0.0$



Figure 3.15: PDB and Battery Trade-Off Polars

Battery

The battery is sized for ten minutes of flight t_f and ten minutes driving t_d , the battery energy can then be calculated using Equation 3.12, where P_0 is the average base power consumption of the drone not considering the propulsion.

$$E_{bat} = P_0 (t_f + t_d) + P_f t_f + P_d t_d \tag{3.12}$$

A battery voltage of 14.8 V was selected as this is a standard value in the industry and works for the components selected. The most important parameters of the battery are the size and mass as they account for a large percentage of the overall drone mass budget and size constraint. All batteries considered achieve the required energy needed, but some provide more, this will increase the flight time which is also desirable. Additionally, the cost of the battery also needs to be considered. As done previously, different options available in the industry were considered and a trade-off was performed, see Table 3.8 and Figure 3.15b.

Table 3.8: Battery Trade-Off

Criteria	Excess energy 20.0%	Mass 30.0%	Cost 20.0%	Size 30.0%	Aggregate $\sigma_w = 0.05$
Options	$\sigma = 3.08$	$\sigma = 3.39$	$\sigma = 2.95$	$\sigma = 3.29$	
Tattu R-Line 1550mAh	10.0 $\omega = 0.86$	1.0 $\omega = 0.0$	5.47 $\omega = 0.07$	1.0 $\omega = 0.0$	3.69 $\omega = 0.0$
Tattu R-Line 1300mAh	2.74 $\omega = 0.03$	5.7 $\omega = 0.06$	7.47 $\omega = 0.21$	6.03 $\omega = 0.07$	5.56 $\omega = 0.0$
Tattu R-Line 1550mAh Version 4	1.0 $\omega = 0.01$	9.65 $\omega = 0.32$	6.4 $\omega = 0.12$	7.68 $\omega = 0.16$	6.68 $\omega = 0.0$
Gens ace Soaring 3300mAh	3.32 $\omega = 0.05$	10.0 $\omega = 0.38$	10.0 $\omega = 0.59$	10.0 $\omega = 0.4$	8.66 $\omega = 1.0$
E-flite 3300mAh	3.32 $\omega = 0.05$	8.95 $\omega = 0.24$	1.0 $\omega = 0.0$	9.8 $\omega = 0.37$	6.49 $\omega = 0.0$

The battery chosen is the Gens Ace Soaring battery as it wins on everything except for the excess energy it can store. While it does not win in this category, it should be noted that it is still above the required capacity and the second-best in this category. The sensitivity analysis also gives a win rate of 100%, giving a high confidence in the result. The characteristics of the battery are displayed in Table 3.9. The battery consists of four rectangular Lithium Polymer (LiPo) cells that are connected in series and wrapped in plastic to keep them together, for the integration in the drone the geometric layout of the cells is changed. The four cells are stacked in a plate configuration instead of a bar configuration.

Table 3.9: Electrical Components Overview

Component	Mass [g]	Size [mm]	Cost [€]	I_{peak} [A]	Additional Parameters
Propulsion Motors (4x)	3.7	13.6x15h	9.80	6.2	$KV = 10,000 \text{ RPM/V}$ $E = 3300 \text{ mAh}$
ESC (6x)	5.4	32x12x4.5	12.81	8	
PDB (1x)	11	50x35x4	6.92	123.3	
Battery (1x)	328	137x85x13	54.87	99	

Thermal management

All the electronic components generate heat during operation due to losses. This heat has to be managed for the drone to be able to operate effectively. The biggest heat producer is the battery, which can overheat due to high-temperature conditions. This reduces battery capacity, battery life, and performance. It also creates a risk of thermal runaway, which can lead to the battery catching fire [6]. Multiple options for the thermal management system, both passive and active, were discussed and compared based on the criteria displayed in Table 3.10 and Figure 3.16a. From the trade-off, passive airflow cooling is selected as the best option for the use case.

Table 3.10: Trade-Off Table for Thermal Management

Criteria	Cost 20.0%	Mass 20.0%	Power consumption 20.0%	Heat flow rate 30.0%	Durability 10.0%	Aggregate $\sigma_w = 0.06$
Options	$\sigma = 1.33$	$\sigma = 3.25$	$\sigma = 2.53$	$\sigma = 1.33$	$\sigma = 2.79$	
Thermoelectric	8.0 $\omega = 0.11$	10.0 $\omega = 0.46$	4.0 $\omega = 0.01$	8.0 $\omega = 0.24$	8.0 $\omega = 0.15$	7.6 $\omega = 0.03$
Forced Liquid	6.0 $\omega = 0.0$	2.0 $\omega = 0.01$	6.0 $\omega = 0.04$	9.0 $\omega = 0.6$	3.0 $\omega = 0.0$	5.8 $\omega = 0.0$
Forced Air	7.0 $\omega = 0.03$	4.0 $\omega = 0.03$	5.0 $\omega = 0.02$	7.0 $\omega = 0.08$	5.0 $\omega = 0.02$	5.8 $\omega = 0.0$
Heat Sink	8.0 $\omega = 0.1$	5.0 $\omega = 0.05$	10.0 $\omega = 0.47$	7.0 $\omega = 0.08$	10.0 $\omega = 0.42$	7.7 $\omega = 0.01$
Passive Air-flow Cooling	10.0 $\omega = 0.75$	10.0 $\omega = 0.45$	10.0 $\omega = 0.46$	5.0 $\omega = 0.0$	10.0 $\omega = 0.4$	8.5 $\omega = 0.96$

For optimum passive cooling of the internal electrical components, both the airflow and surface area connected to the components need to be maximised. Son et al. [6] have shown that by using a 3D printed Aluminium Alloy Tetrahedral Lattice Porous Plate (TLPP) to mount the electrical components, the heat dissipation to the environment can be maximised. A depiction of a generalised TLPP is shown in Figure 3.16b. Additionally, the electrical components can be attached to the TLPP using thermal paste to improve conductivity further. A large advantage of this approach over direct cooling of the components is that the electronic circuits are still isolated from the outside. This decreases the risk of component failure due to dust or water. The exact heat dissipation needed is a point of further research and the cable management has to be taken into account when the cooling channel is integrated into the wider design.

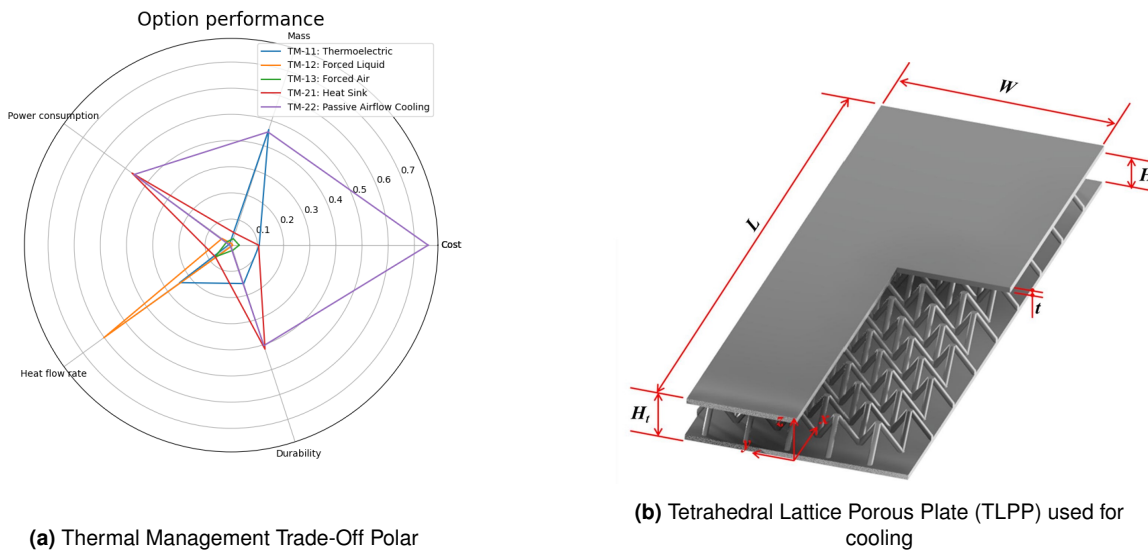


Figure 3.16: Thermal Management Trade-Off Polar and Proposal

3.2.2. Electric Systems Overview

All the electrical components and components connected to the electrical system are gathered in this section. An overview of how these components are connected is shown in the electrical block diagram in Figure 3.17. Together with this diagram, a table showing all the components and the power budget is displayed in Table 3.11. This power budget is established to make sure the drone meets the requirements of operational and flying time. The maximum average

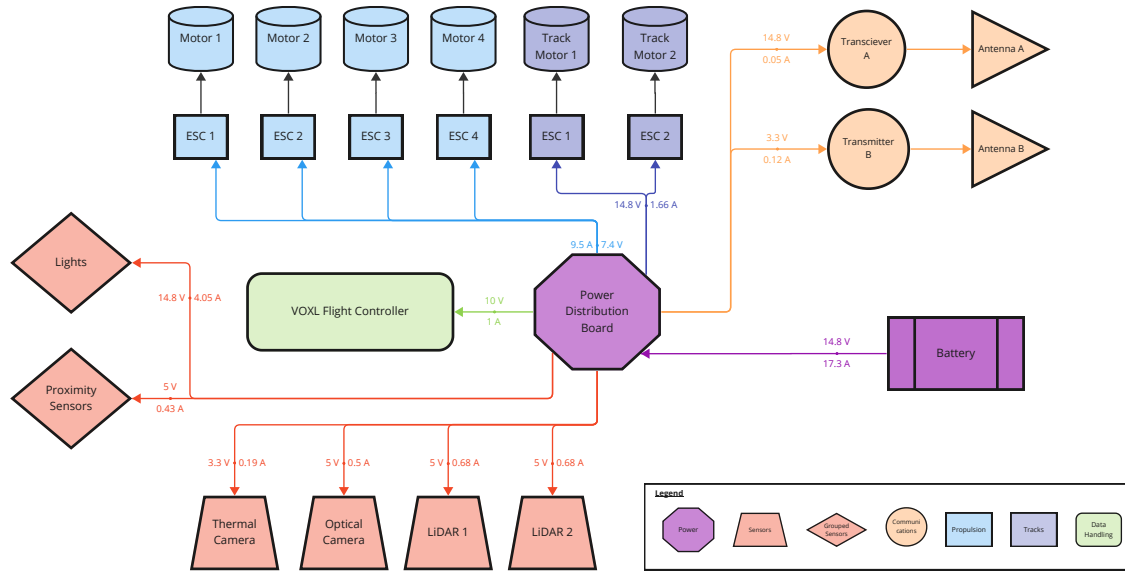


Figure 3.17: Electrical Block Diagram

power is calculated in order to estimate the operational and flying time. Next to the power consumption, the table also shows the other important electrical characteristics of the various electrical components. From the table it can be seen that the lighting system accounts for 40.5% of the total power budget, while this is a striking percentage, this mostly due to the high amount of lumen the lights need to produce. This is further discussed in chapter 9. Next to the lighting, propulsion and tracks subsystems, the only significant power consumption comes from the VOXL Flight board. The rest of the components together only account for 5.4% of the power budget. Note that all the components added up to more than 100% of the budget, this is due to the fact that the Tracks and Propulsion subsystem do not operate simultaneously.

Table 3.11: Power Budget

Component	Power [%]	Power[W]	Voltage V [V]	Current I [A]
Propulsion				
Motors	47.4	70.2	7.4	9.5
Communication				
Drone Transceiver A	0.3	0.396	3.3	0.120
Drone Transmitter B	0.5	0.8	14.8	0.05
Sensors				
Optical Camera	1.7	2.5	5	0.5
Thermal Camera	0.4	0.6	3.3	0.19
2 LiDAR	2.3	3.4	5	1.36
6 Proximity Sensors	0.2	0.36	5	0.432
12 Lighting Systems	40.5	60	14.8	4.05
Data Processing				
VOXL Flight	6.7	10	10	1
Tracks				
Motors	16.6	24.6	14.8	1.66
Total	100%	148.256	14.8	17.3
Margin	1.4%	150		

Structures and Tracks

In this chapter, the structures and tracks subsystem will be detailed. These subsystems are of vital importance as they provide structural rigidity and protection for all mission-critical components. Additionally, since these subsystems are generally a big component of the weight, therefore, it is important to reduce this. Finally, in this chapter, a total structure verification using Finite Element methods (FEM) is performed in order to verify all constituents' parts work together as proposed.

4.1. Structures Subsystem

In this section, the structures subsystem is analysed. First, a force analysis is carried out, with which a material choice is made. Continuing on, structural analysis on a few key components is performed, from which minimal structural dimensions follow. Afterwards, these results are verified using FEM software. Finally, the production method for the structures subsystem will be discussed.

4.1.1. Force analysis

For the determination of the overall design, it is important to define the maximum forces acting on the drone. These forces are calculated using the required collision speeds, thrust-to-weight ratio and weight of the drone. All the maximum values of the requirements are chosen in order to have a margin of error. A Free Body Diagram (FBD) is shown in Figure 4.1, and all the forces are summarised in Table 4.3. The forces are divided into three categories: flying forces (f_f), driving forces (f_d) and collision forces (f_c). For the collision forces not all arrows are present, this is for the sake of simplicity since the collisions are possible on all track wheels and all ducts in every direction.

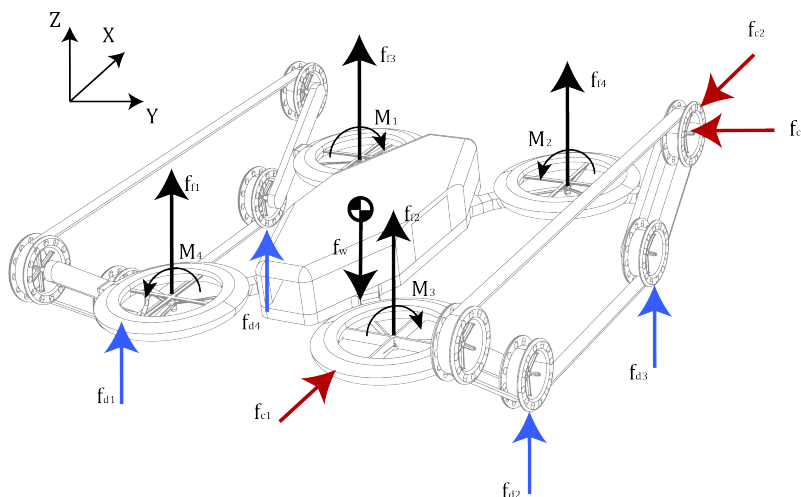


Figure 4.1: Free Body Diagram of the Drone

For the impact collision, the calculation is a bit more complex as it is dependent on time. Equation 4.1 is used for the impact calculation, with an impact time of 0.1 seconds [17, 18]. In this equation, \vec{V}_f is the final velocity and \vec{v}_i is the initial velocity, the difference between these, times the mass, is the total change in momentum $\delta\vec{p}$. This yields a force of 46.8 N as stated in Table 4.3. The maximum force on one track arm is the total weight of the drone since it can be assumed that in some situations the total weight of the drone falls on one corner of the drone. However, it should be noted that the collision force is significantly higher than the weight. Therefore, most of the structure sizing will be performed using the collision force.

$$\sum \vec{F} = m\vec{a} = m \left(\frac{\vec{V}_f - \vec{v}_i}{\Delta t} \right) \Rightarrow \sum \vec{F} = \frac{\Delta\vec{p}}{\Delta t} \quad (4.1)$$

4.1.2. Material choice

To perform an analysis of the induced stresses in the drone and determine the minimum dimensions required to carry the specified loads, it is crucial to determine the material used. A trade-off was performed between different materials for both the main structure of the drone and the ducts.

For the main structure of the drone, the specific strength and stiffness are the two most important criteria. This is because the drone needs to be as light as possible while still maintaining its strength and stiffness. Moreover, the manufacturing cost is weighed fairly high as it is important that the drone does not become too expensive. The full trade-off table can be seen in Table 4.1.

Table 4.1: Material Trade-Off [19, 20]

Criteria	Manufacturing Cost 20.0%	Material Availability 5.0%	Sustainability 5.0%	Specific Strength 30.0%	Specific Stiffness 25.0%	Fatigue Resistance 15.0%	Aggregate $\sigma_w = 0.09$
Options	$\sigma = 1.72$	$\sigma = 2.04$	$\sigma = 1.2$	$\sigma = 2.0$	$\sigma = 2.58$	$\sigma = 2.48$	
Titanium	4.0 $\omega = 0.0$	4.0 $\omega = 0.0$	4.0 $\omega = 0.01$	8.0 $\omega = 0.2$	7.0 $\omega = 0.13$	9.0 $\omega = 0.49$	6.7 $\omega = 0.0$
Aluminium	8.0 $\omega = 0.27$	9.0 $\omega = 0.26$	7.0 $\omega = 0.58$	6.0 $\omega = 0.04$	7.0 $\omega = 0.13$	5.0 $\omega = 0.04$	6.7 $\omega = 0.01$
Steel	7.0 $\omega = 0.12$	8.0 $\omega = 0.13$	6.0 $\omega = 0.2$	7.0 $\omega = 0.09$	7.0 $\omega = 0.13$	7.0 $\omega = 0.16$	7.0 $\omega = 0.0$
Plastic	9.0 $\omega = 0.56$	10.0 $\omega = 0.48$	6.0 $\omega = 0.2$	4.0 $\omega = 0.0$	2.0 $\omega = 0.0$	2.0 $\omega = 0.0$	4.6 $\omega = 0.0$
Composites	6.0 $\omega = 0.04$	8.0 $\omega = 0.13$	4.0 $\omega = 0.01$	10.0 $\omega = 0.67$	10.0 $\omega = 0.6$	8.0 $\omega = 0.31$	8.5 $\omega = 0.99$

As can be seen from the trade-off composites yields the best score. When looking at composites, Continuous Fibre Reinforced Composite (CFRC) is the best option as it has good structural properties while still being extremely light. The material properties used are summarised in Table 4.2. This composite utilises both a thermoset and a thermoplastic polymer (polyamide). The thermoset polymer is used to reinforce the continuous fibres while the thermoplastic is used to consolidate the fibres into a single structure.

4.1.3. Structural Analysis for Flying, Driving and Collision

In the design of the structure, three areas are analysed: the load carried due to the electric motor generating thrust, the loads on the tracks due to driving, and the load due to collisions. When looking at the thrust loads, the number of arms connecting the electric motor with the duct is one of the most important variables. This depends on the load-carrying capability of the carbon fibre. The optimal design will be the one that has the lowest weight and lowest

Table 4.2: CFRC Properties [20]

Property	Value	Unit
Density	1.35	[g/cm ³]
Tensile strength	511	[MPa]
Elongation at break	3	[%]
Shear strength	22.4	[MPa]
E-Modulus	43.7	[GPa]
Shear Modulus	0.42	[GPa]

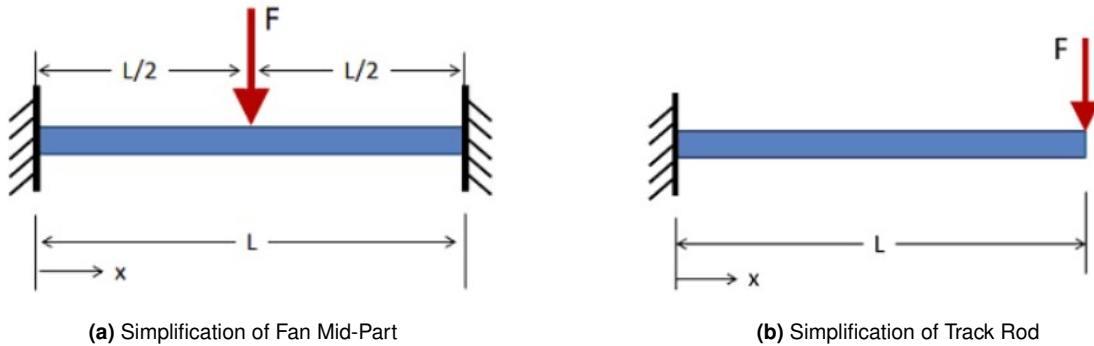
Table 4.3: Forces acting on Drone

Force type	Value	Unit
Total thrust	61.21	[N]
$f_{f1} - f_{f4}$	15.29	[N]
f_w	15.29	[N]
$f_{d1} - f_{d4}$	3.83	[N]
$f_{c1} - f_{c3}$	46.80	[N]
$M_1 - M_4$	0.382	[Nm]

obstruction of the airflow. Additionally, the structure connecting the tracks must ensure that the loads induced by the weight or collisions do not cause failure.

Motor Supports Analysis

The connections between the motor and the duct can be assumed to be a fixed beam with a load at the motor, as visualised in Figure 4.2a. There are two failure modes that could occur, either the beam fails by shear or by the normal force induced by the bending moment. The minimum width for which both these failure modes do not occur will be calculated.

**Figure 4.2:** Simplification of Drone Structures

$$\delta_{\max} = \frac{FL^3}{192EI} \quad @x = L \quad (4.2)$$

$$\tau = \frac{VQ}{I_c b} \quad \sigma = \frac{M * y}{I} \quad I = \frac{b \cdot h^3}{12} \quad (4.3)$$

The variables used in the calculation are summarised in Table 4.4 and the equations used in these calculations are equations 4.3 and 4.2. The weight of the propulsion system is not taken into account as this is an insignificant load compared to the forces described in Table 4.3. Also, it acts opposite of the thrust force and, thus, provides bending relief.

Table 4.5: Calculation Results and Values used for the Minimum Width of Motor Supports**Table 4.4:** Initial Variables used for the Calculation

Variable	Value	Unit
Total thrust	61.193	[N]
Thrust per motor	15.3	[N]
Height	3	[mm]
Length	60	[mm]
Width	1	[mm]

Variable	1 Beam	2 Beams	Unit
Minimum necessary width	0.6	0.3	[mm]
Deflection with minimum width	0.146	0.146	[mm]
Shear stress	12.78	12.78	[MPa]
Bending stress	511.0	511	[MPa]
Strain	1.17	1.17	[%]
Deflection 1mm width	0.0875	0.04375	[mm]
Shear stress	7.65	3.82	[MPa]
Bending stress	306	152.98	[MPa]
Strain	0.7	0.35	[%]

From Table 4.5, it is clear that carbon fibre allows for an extremely small width, which minimises the aerodynamic impact. The deflection and strain are also within acceptable limits. However, the minimum thickness is not viable in production and this analysis does not cover the loads induced by the tracks. In the code generated in the analysis, the height of the beam can be edited and it returns the minimum width necessary, the exact values will be generated in section 4.3.

Centre Plate Design

The centre plate is of vital importance because it provides the most structural rigidity for the drone. If the drone is not rigid enough, flying may become unstable or really hard to control. The thickness of this centre plate is therefore the most important variable to determine in terms of structures. Following similar coding and analysis as performed for the motor supports, a minimal centre plate thickness of **1.672 mm** is needed. This causes a maximum deflection of **0.509 mm**. The assumed loads are 4 upward forces with the same magnitude as the thrust, one on each corner of the centre plate. Additionally, there is a downward weight component of the sensors in the middle of the plate.

Tracks Rod Analysis

When looking at the loads sustained by the tracks, it is important to note that the drone traverses complex terrains. Therefore, to have sufficient structural integrity during operations it can be assumed that the entire weight of the structure could be loaded onto one of the arms at any time. The track rods are the rods connecting two track wheels on each corner of the drone.

The first failure mode is the connection arm itself, due to the simplicity of the design it can be modelled as a simply supported beam (Figure 4.2b). However, it should be noted that the forces can be from any direction depending on the orientation of the drone. The arm, therefore, can experience both a bending moment and a compression force. This also means that the beam should be of similar properties in all directions, which implies that a circular cross-section is the most optimal. Similar code as in the motor support analysis is used, the results are summarised in Table 4.6. Equation 4.4 and 4.5 are the formulas used for the calculation of the stress, strain and displacement. The force that was chosen for the analysis is the collision force as it is higher than the force due to the weight.

$$\delta_{\max} = \frac{FL^3}{3EI} \quad @x = L \quad (4.4)$$

$$I = \frac{\pi \cdot r^4}{4} \quad (4.5)$$

Table 4.6: Calculation Results and Values used for the Minimum Width of Motor Supports

Variable	Value	Unit	Result	Value	Unit
Length rod	70	[mm]	Minimum radius	1.6	[mm]
Compression force	46.8	[N]	Maximum deflection	2.99	[mm]
Bending force	46.8	[N]	Strain	0.585	[%]
			Bending stress	511	[MPa]
			Shear stress	8.75	[MPa]

Track Rod Connection and Duct Analysis

The ducts are the physical connection between the track's support and the main body. It carries all loads experienced by the tracks and motors to the body. Therefore, it is an integral part of the propulsion subsystem. The connection between the track rod and the duct is the most likely to be the failure point, therefore, it is crucial to determine the minimum dimensions to

be able to carry all loads. At a minimum it needs to have the dimensions of the track rod, however, the most important part is that no stress concentrations occur at the edges of the connection. Therefore, a smooth curving connection is proposed between the duct and the track rod. This will be visualised in the 3DEXperience model and verified with FEM. All forces and moments experienced by the arm connecting the track support structure and the duct are shown in Figure 4.3.

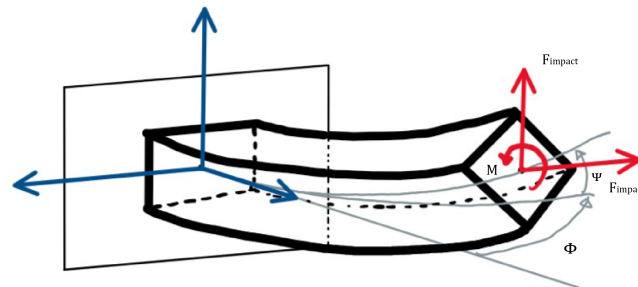


Figure 4.3: Forces acting on the Connection between the Track Rod and Duct

Since in the preliminary design, the ducts are significantly larger than the minimum values proposed in the previous analysis, it can be assumed that the duct can easily carry the loads proposed. Therefore, no further analysis of these forces on the duct is necessary. This assumption and the track rod connection will be verified using FEM.

4.1.4. Model Verification

Since the constructed models are based on certain assumptions, it is important to verify the validity of these models. The verification will be performed using FEM, as discussed previously. Figure 4.4 and Figure 4.5 show the fan mid-part and the track rod analysed by the FEM software. A numerical comparison of the results is given in Table 4.7

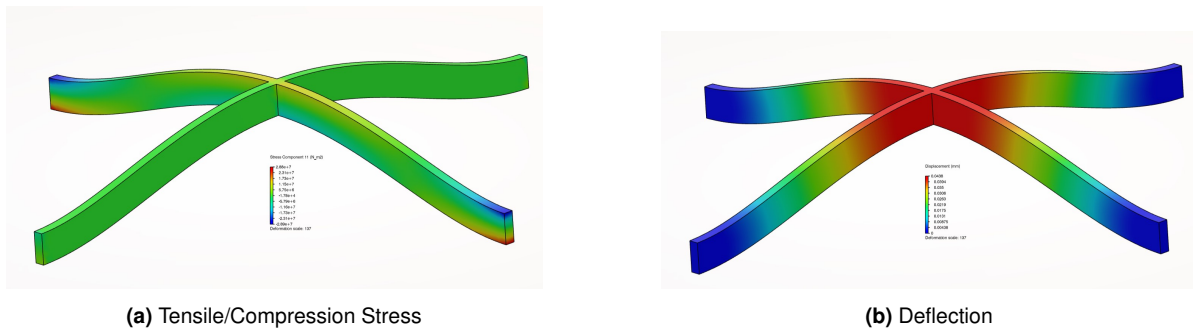


Figure 4.4: Fan Mid-Part FEM

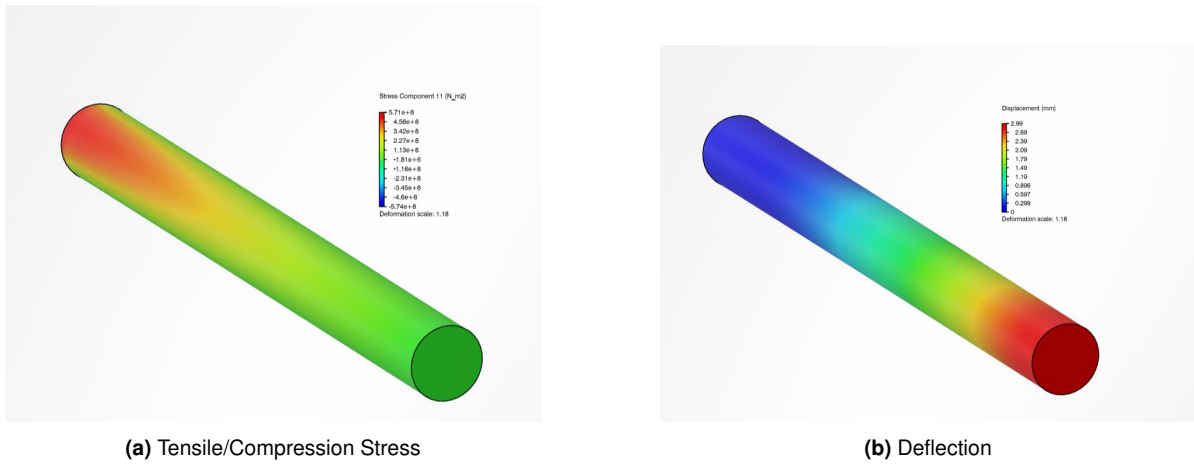


Figure 4.5: Track Rod FEM

Table 4.7: Comparison FEM and Model Results

	FEM Result	Unit	Model result	Unit	Error [%]
Deflection mid-part	0.04380	[mm]	0.04375	[mm]	0.114
Compression stress	28.8	[MPa]	25.5	[MPa]	11.46
Deflection track rod	2.990	[mm]	2.988	[mm]	0.067
Compression stress rod	57.1	[MPa]	51.1	[MPa]	10.50

As can be seen, the analytical model is accurate for both the track rod and the fan mid-part. It is clear that there are some errors in the forces displayed by the FEM software. These errors could be due to discretisation errors or numerical errors in the program. However, for the displacements, the software is accurate. This verifies that the 3DExperience program can be used for further confirmation of the drone’s structure. The results of this analysis will be discussed in section 4.3.

4.1.5. Production Method & Costs

As mentioned, the structure of the drone will be 3D printed using a continuous fibre-reinforced polymer. The production process uses two spools, one with a thermoplastic polymer (polyamide) while the other spool contains a pre-impregnated continuous carbon fibre. This can be seen in Figure 4.6.

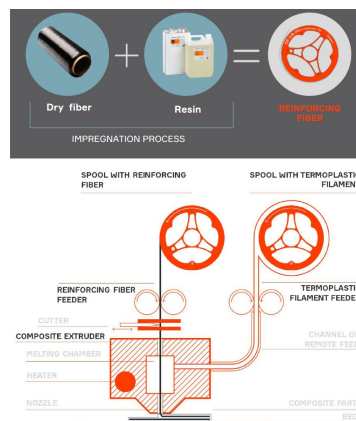


Figure 4.6: 3D Printing Production Method [21]

As for the production costs, since 3D printing is utilised the cost per product is constant. This

means that there is no cost decrease by increasing volume. The only costs that decrease while volume increases are the initial costs per unit produced. These initial investment costs, however, are not taken into account in the 5,000 euro requirement. The costs of CFRC printing are around 380 euros for the continuous carbon fibre spool of 750 *m* and an additional 130 euros for the polyamide plastic roll of 750 *g* [22]. In section 4.3 the final costs of the structures subsystem will be discussed.

4.2. Tracks Subsystem

During the design process of the tracks subsystem, various important design variables were identified. These are the track route, the material of the tracks, the track profile, the track tension, the track width, and the propulsion method of the tracks. These variables will be worked out in this section, followed by a short summary of the limitations of the proposed tracks.

4.2.1. Traction, Maximum Slope and Track Width

For the track wheels and width, it is important to determine the amount of traction the drone needs to have in order to propel itself. The amount of tractive force can be modelled by a normal distribution of the pressure around the wheels as shown in Figure 4.7.b. Afterwards, the total tractive force can be calculated using the pressure distribution (Equation 4.6) and the shear forces acting on the track (Equation 4.7) [23].

In the formulas, i is the slip rate, n is the number of wheels, b is the track width, W is the drone weight, l is the track length, K is the shear displacement and ϕ is the angle of internal shearing resistance. Values used for the calculation are listed in Table 4.8.

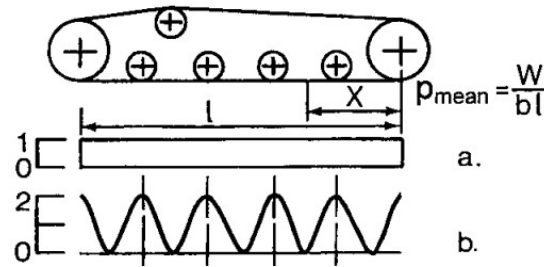


Figure 4.7: Approximation of Pressure Distribution of tracked Vehicle. [23]

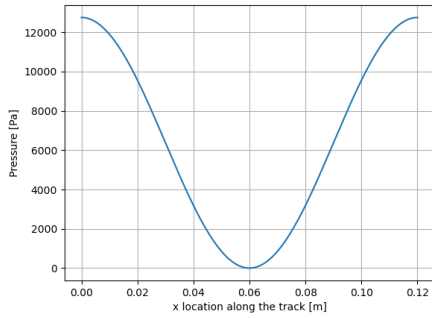
Table 4.8: Values used for Traction Calculations

Variable	Value	Unit
K [23].	2.5	[<i>cm</i>]
i	0.95	-
n	2	-
b	20	[<i>mm</i>]
l	120	[<i>mm</i>]
W	10	[<i>mm</i>]
ϕ	38	[<i>deg</i>]

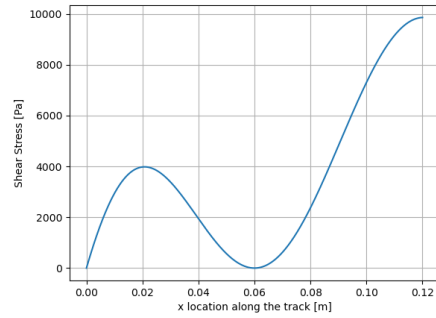
$$p = \frac{W}{bl} \left(1 + \cos \frac{2n\pi x}{l} \right) \quad (4.6)$$

$$\tau = \frac{W}{bl} \tan \phi \left(1 + \cos \frac{2n\pi x}{l} \right) \left(1 - e^{-ix/K} \right) \quad (4.7)$$

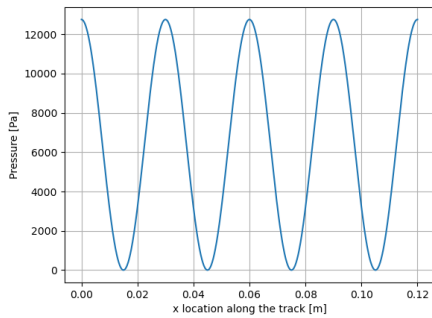
$$\begin{aligned}
 F_{traction} &= b \cdot \int_0^l \frac{W}{bl} \tan \phi \left(1 + \cos \frac{2n\pi x}{l} \right) \left(1 - e^{-ix/K} \right) dx \\
 &= W \tan \phi \left[1 + \frac{K}{il} \left(e^{-il/K} - 1 \right) + \frac{K \left(e^{-il/K} - 1 \right)}{il \left(1 + 4n^2 K^2 \pi^2 / i^2 l^2 \right)} \right] \tag{4.8}
 \end{aligned}$$



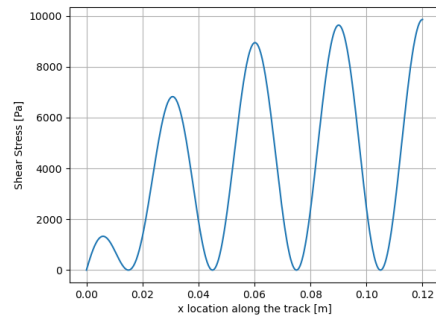
(a) Pressure Distribution Track with 2 Wheels



(b) Shear Forces on the Ground with 2 Wheels



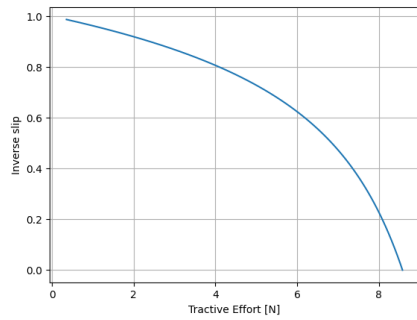
(c) Pressure Distribution Track with 5 Wheels



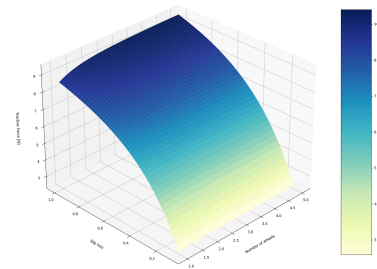
(d) Shear Forces on the Ground with 5 Wheels

Figure 4.8: Shear and Pressure Plots

Figure 4.8a and Figure 4.8c show the pressure distributions when using 2 and 5 wheels respectively. It can be seen by their shear stress plots (figures 4.8b and 4.8d) that the pressure mainly lies on the back wheels. This is logical as the moment the drone accelerates the weight shifts to the back wheels of the drone.

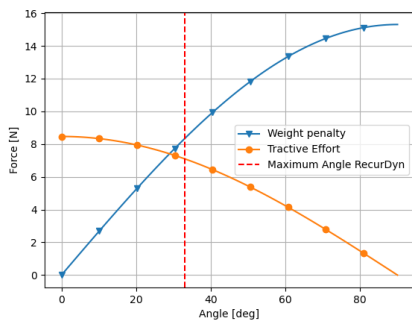


(a) Tractive Effort created against Slip Fraction

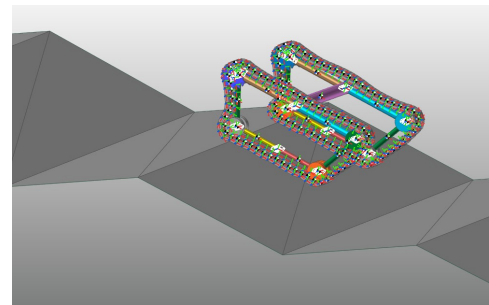


(b) Relation of Number of Wheels, Slip Loss and Traction Force

Figure 4.9: 3D Plot and Slip Plot



(a) The traction Force plotted against Weight Force Component in the Same Direction



(b) RecurDyn Setup

Figure 4.10: Numerical Results of Angle Analysis and Verification Setup

It can be concluded from the integral in equation Equation 4.8, that the width of the track does not play a role in the traction generated by the tracks. As seen in Figure 4.9b, the traction partially depends on the number of wheels used in the track configuration, however, as visible by the values it does not differ significantly due to the small size of the drone. The slip loss does have a big influence on the traction, as can be seen in the figure, this is mainly influenced by the track profile and not the width.

The traction force by the drone is **8.467 N** per track with a slip of 5% [23]. This allows the drone to traverse angles at a maximum of **29.32** degrees, as visible in Figure 4.10a. From the RecurDyn software, a maximum angle of 33 degrees was found. This small discrepancy can be due to various reasons such as different ground properties and track slips.

The chosen width of the track is **1 cm**, the main motivation for this is the production capabilities and weight. It should be noted that due to irregular terrain, the pressure distribution may be more uniform, as the track becomes more under tension, resulting in higher traction and better manoeuvrability.

4.2.2. Material and Profile Selection

Two options are considered when choosing a material for the drone tracks: plastics and rubber. Other materials are immediately ruled out due to weight and maintainability. Metals are too heavy and will wear quickly, whereas ceramics will fracture under the loads. Using plastic

tracks can be weight beneficial over using rubber tracks as it has a lower density, and does not have to be a solid track [24]. However, plastics will not dampen vibrational loads induced by driving and are also prone to fracturing. This will increase the maintenance costs, not only for the tracks but also for the drone. Therefore, rubber is chosen as the material for the tracks.

The drone needs to be able to drive on rough terrain. It will be uneven with surfaces like sand, gravel and dirt. This calls for a durable track profile that is able to drive on these materials. Also, it must dampen the vibrations induced by driving over these materials to protect the functionality of the drone. The rubber that is selected for the tracks is Hydrogenated Nitrile Rubber (HNR) which has great durability and tear resistance while being comparatively cheap and lightweight. It also has a high elongation before failure [25]. In Table 4.9, the mechanical properties of this rubber are listed.

Table 4.9: HNR Properties [26]

Property	Value	Unit
Density	1.3	$[g/cm^3]$
Tensile strength	23.2	$[MPa]$
Elongation at break	260.5	$[%]$
Tear strength	5.1	$[MPa]$
Modulus 100%	8.3	$[MPa]$

When using low-mobility applications, it was found through the simulation software RecurDyn that a relatively flat profile presents certain issues. When traversing small vertical steps, as visible in Figure 4.11, the track can not create enough grip and fails to overcome the step. The addition of ribs to the track could help with this (Figure 4.12b, however, this greatly reduces the ability to traverse steep angles. Due to the ribs, the maximum angle is reduced to 25 degrees. This is quite significant, therefore, a hybrid design was chosen. While this design compromises the gripping ability of the ribs, it maintains the same maximum angle as a flat track. This hybrid design is shown in Figure 4.12a, in which the profile is on the top. The protrusions are 5 mm long, the same width of the track and spaced every 10 mm with a profile depth of 1 mm.

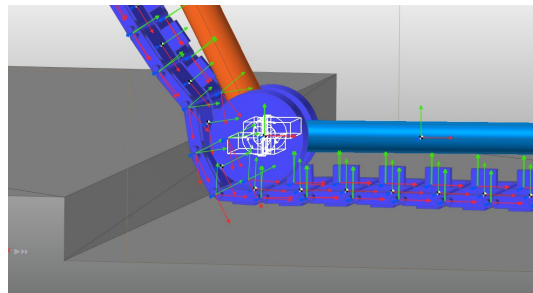
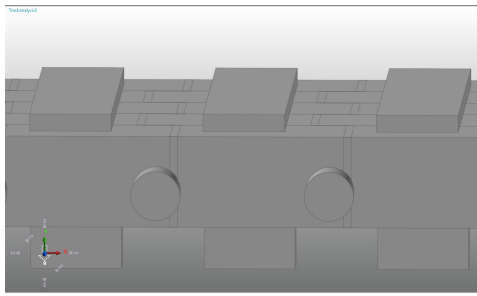
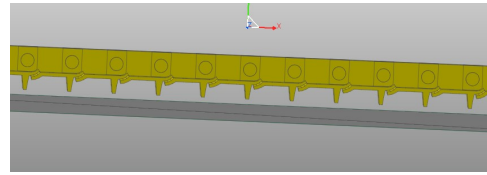


Figure 4.11: Flat Profile traversing Small Step



(a) Chosen Hybrid Design, Track Profile on Top



(b) Example of ribbed Track, Ground on the Bottom

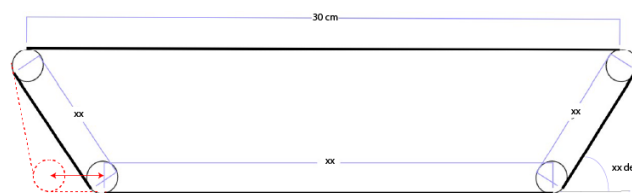
Figure 4.12: Considered Track Profiles

4.2.3. Track Route

The route the track takes is of great importance to the aerodynamics, size, and stability of the drone. Having the tracks run over and under the rotors causes the propulsion system to be less efficient. However, it allows for a smaller total size of the drone. Having the tracks closer together will reduce the stability, as it is more likely to tip over when going over the rubble. Therefore, it is decided that the best option is to have the tracks next to the propellers. This design allows for a maximum bank angle of 68° (Equation 4.9), assuming the centre of gravity is exactly half the total height. This means the tracks will slip way before any tipping occurs, this is therefore not a failure point.

$$\tan(\theta) = \frac{0.5 \cdot \text{width}}{0.5 \cdot \text{height}} \quad (4.9)$$

In the design of the track route, there are two constraints. The first reason is due to the size of the drone, which is a key variable in the success of the drone. Therefore, it is important that the tracks keep the dimensions at a minimum while protecting the components. As a result, the track has a maximum length of 32 cm and a height of 10 cm . Lastly, since the drone's body is situated in the middle of the entire assembly and has a maximum length of 23 cm , the track must ensure the body does not protrude past the tracks. Figure 4.13 shows a rough sketch of the drone's track route and also showcases a possible change in layout such that the slope and length of ground contact of the track increases.

**Figure 4.13:** Sketch of Track Lay-Out

Using the simulation software RecurDyn 2023 an analysis can be performed of the performance of the track in relation to the slope of the track and therefore the amount of ground contact. It was concluded that the increase in the amount of ground contact by moving the wheel forward did not have any advantage, both in maximum angle and traversing small obstacles. For large obstacles, a smaller angle is more optimal as it allows the track to grip the obstacle better. To conclude, the maximum angle has the most advantages, this angle is 63° .

Note: It is impossible to quantify these results as they rely on the visual observations of the model. The only observed difference between the different track slopes is the smoothness when traversing obstacles, they do not differ in maximum obstacle height.

4.2.4. Track Tension

Having enough tension in the tracks is of great importance as it prevents the tracks from coming loose from the wheels and increases the grip. The tensioning is possible due to an adjustable track wheel and can be adjusted during the operation. With the cross-sectional area and the Elastic Modulus (E), an estimation of the force due to the tension can be made. It is assumed the track is kept at a maximum of 10% deformation.

$$E = \frac{\sigma}{\epsilon} \quad (4.10)$$

$$\sigma = \frac{F}{A} \quad (4.11)$$

Following from Equation 4.10 and 4.11 a tensile force of 12.45 N is calculated. For the final dimensional calculations performed for section 4.3 this force will be added to the collision forces on the track rod as they can occur simultaneously.

4.2.5. Track Motor and Track Wheel

The tracks will be driven by two small electric motors, this is the most weight-optimal solution. The motors will be similar to the propeller motors but smaller in size. Using the maximum tractive force and the diameter of the track wheel, the maximum torque required by the electric motor can be calculated. The speed of the motor is not a constraining factor as the drone will not move very fast.

In the sizing of the electric motor, the torque, power usage and constant velocity of a motor (k_v) are the most critical variables. Having a higher k_v value implies that the motor can create a higher torque, but this comes at a weight, size and power penalty. To decide on a specific motor, the power required can be plotted as a function of k_v and the track wheel size. The relation of these three values can be seen in Figure 4.14. It is based on Equation 4.12, in which k_t is the inverse of k_v .

$$\text{Torque} = k_t \cdot \text{Current} \quad (4.12)$$

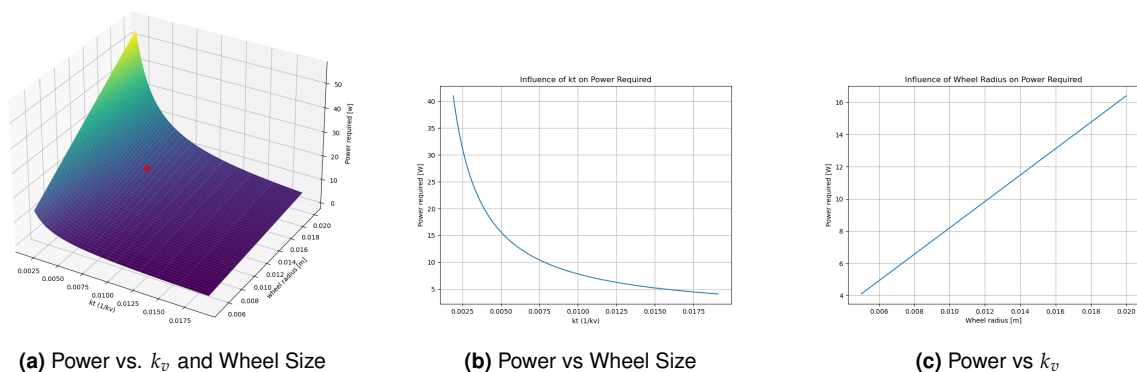
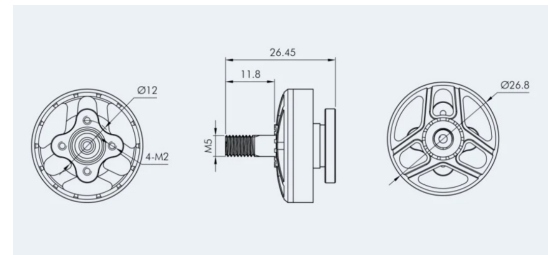


Figure 4.14: Relation between Variables and required Power

Using the maximum power requirement a motor can be selected. This is the red star in Figure 4.14a. The specifications for the "TMotor F2203.5 Motor 1500kv" are listed in Table 4.10

Table 4.10: Track Motor Specifications [27]

Specification	Value	Unit
Weight	17.8	[g]
K_v	1500	-
Max power usage	12.3 (with reduction)	[W]
Max current	19.5	[A]
Max torque	0.124 (no gear reduction)	[Nm]
Voltage	14.8	[V]

**Figure 4.15:** Technical Drawing Track Motor [27]

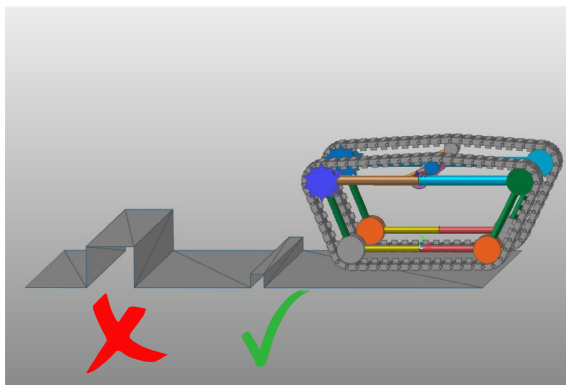
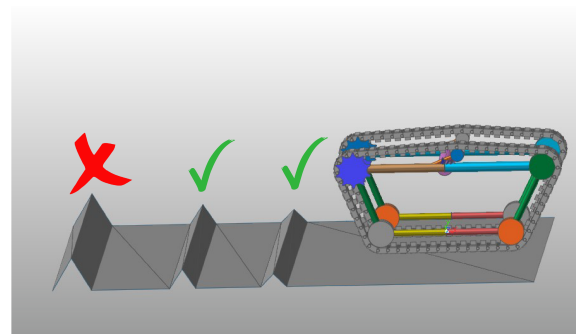
and its dimensions in Table 4.15 [27]. It can be observed that this motor is significantly larger than the motor for the propulsion subsystem. This is due to the significantly higher torque requirement at low RPM.

4.2.6. Track Limitations

Taking into account the above design decisions and dimensional values, the limitations of the track can be determined. They are summarised in Table 4.11. Some are already mentioned in the previous subsections, however, this section functions as a summary and gives some additional limitations. Figure 4.16a gives examples of vertical obstacles, while Figure 4.16b is an example of a sloped obstacle it can and can not traverse. However, it should be noted there is some inaccuracy in the software as it does not allow extra tensioning of the tracks. This causes some issues when traversing obstacles with sharp edges and, therefore, real-world performance is expected to be better.

Table 4.11: Limitation of the Tracks

Limitation	Value	Unit
Max. bank angle	63	[deg]
Max. slope before slipping	29.3	[deg]
Max. slope before tipping	71.57	[deg]
Max. sloped obstacle height	50	[mm]
Max. vertical obstacle height	30	[mm]

**(a)** Example of Vertical Obstacles (2 & 6 cm)**(b)** Example of Sloped Obstacles (2, 4 and 6 cm)**Figure 4.16:** Examples of Obstacles

4.3. Final Structure

In this section, the final structural parameters will be defined. Additionally, the total structure validation will be performed for collisions and normal operations. Finally, using 3DEXperience, a frequency response analysis will be performed.

4.3.1. Final Parameters chosen

Following the analysis in the previous sections, a final choice of the structure dimensions can be made. This is based on the minimum values obtained by the models, production capabilities and a safety factor. Because weight is of vital importance to the success of the mission it was decided that a marginal safety factor of 1.3 is used for the structural characteristics [28]. They are summarised in Table 4.12. Some values are increased more than the safety factor due to a minimum production thickness of 2 mm. These are indicated with a star [20].

Table 4.12: Final Dimensions of Load bearing Structure

Variable	Value	Unit
Center plate		
Thickness	2.2	[mm]
Width	50	[mm]
Length	120	[mm]
Motor supports		
Nr. of supports	2	-
Length	60	[mm]
Width*	2	[mm]
Thickness*	2	[mm]
Track Rod		
Length	70	[mm]
Angle	63	[deg]
Radius	2	[mm]
Tracks		
Track ground contact	200	[mm]
Track height	100	[mm]
Track max length	320	[mm]
Track Thickness (excl profile)	5	[mm]
Track angle	63.43	[deg]
Spacing track profile	10	[mm]
Track profile length	5	[mm]
Track profile depth	3	[mm]
Track wheel radius	15	[mm]

4.3.2. Weight of Structure & Costs

With the final dimensions the total structure weight, and therefore, the costs can be determined. The costs of the structure are calculated using the defined material costs in subsection 4.1.5, and the costs of the track are calculated using current market prices [29]. These are listed in Table 4.13.

Table 4.13: Tracks and Structure Weight

Part	Weight [g]	Costs [€]
Structure		
Main body	280	190
Track Rod	8	5.44
Ducts	72	48.96
Total	360	244.4
Tracks		
Tracks	23	0.10
Track wheels	8	5.44
Track motors	35.6	35
Total	66.6	40.54

4.3.3. FEM Analysis

Now that the entire structure is defined, the entire model can be verified using FEM simulations. Four situations will be analysed: normal flying operations, normal driving operations, frontal collision and frontal duct collision. In all simulations, the body of the drone will be clamped because at least one boundary condition is required. Additionally, a simplified version of the structure will be used due to computational limits.

The forces setup is shown in Figure 4.17, with the forces as described in subsection 4.1.3. In the analysis of the stresses, the shear stresses were deemed to be insignificant. Therefore, these will not be discussed any further.

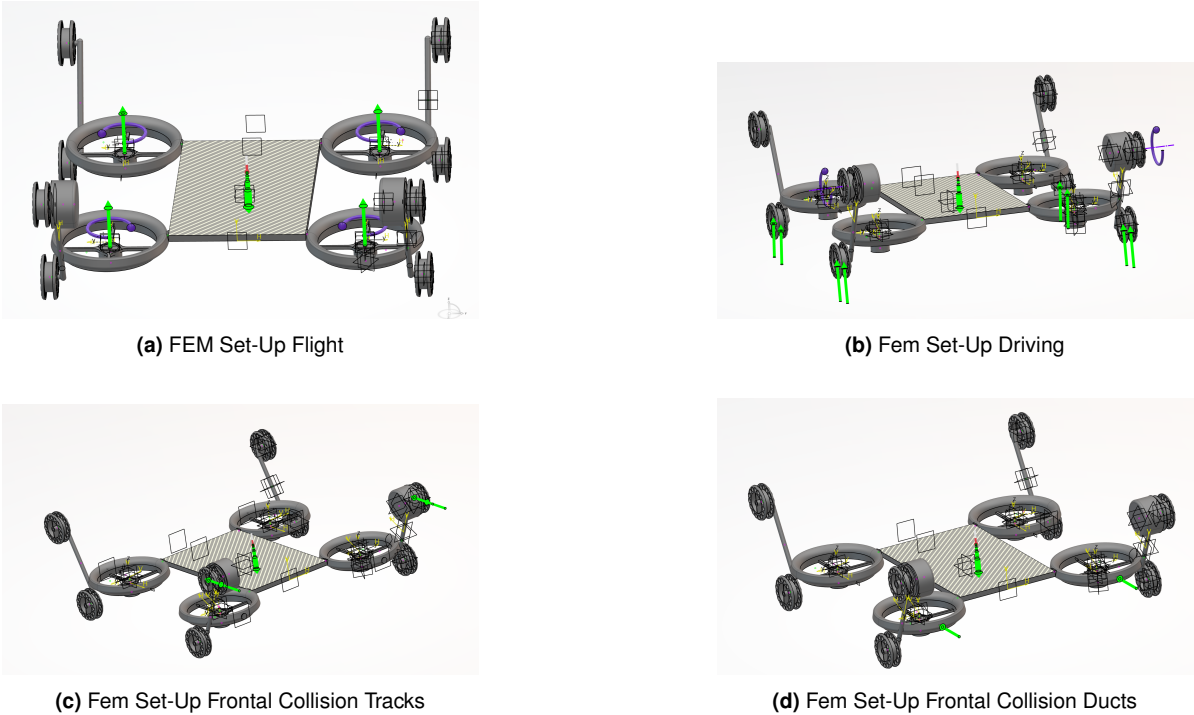


Figure 4.17: Forces and Clamping Set-Up of FEM

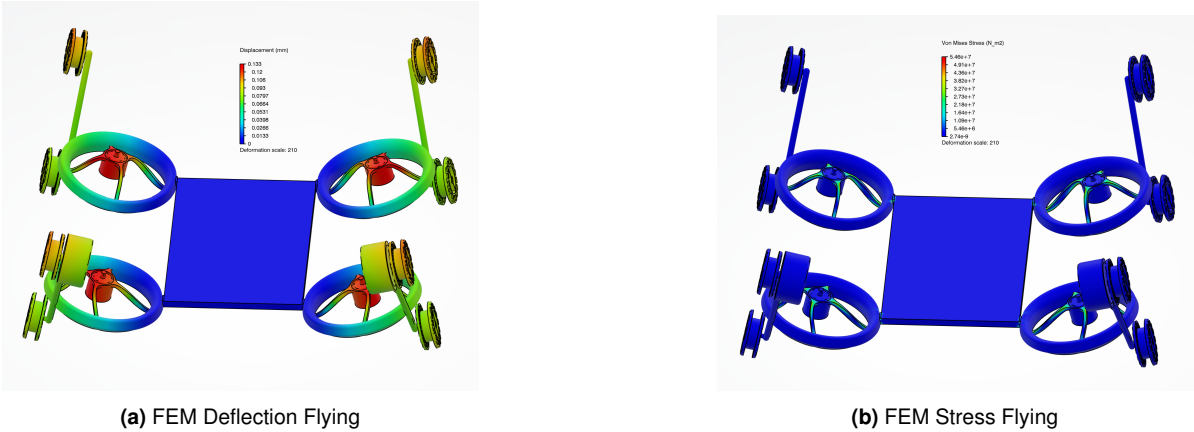


Figure 4.18: FEM Results Flying

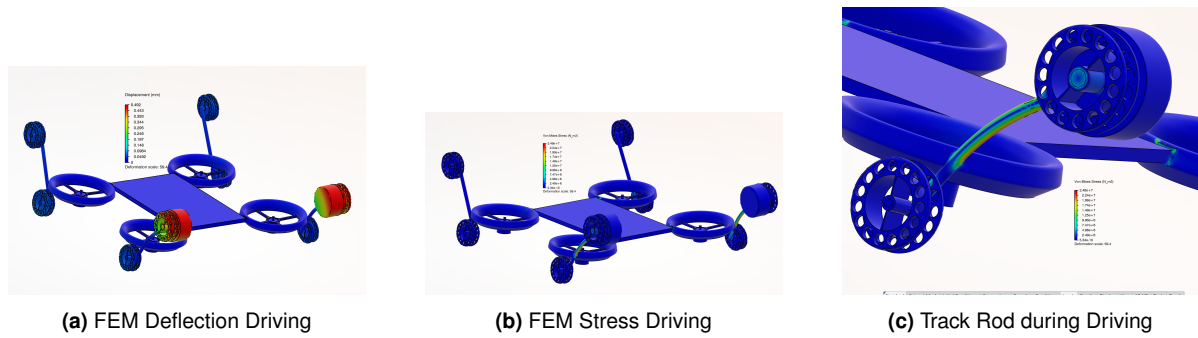


Figure 4.19: FEM Results Driving

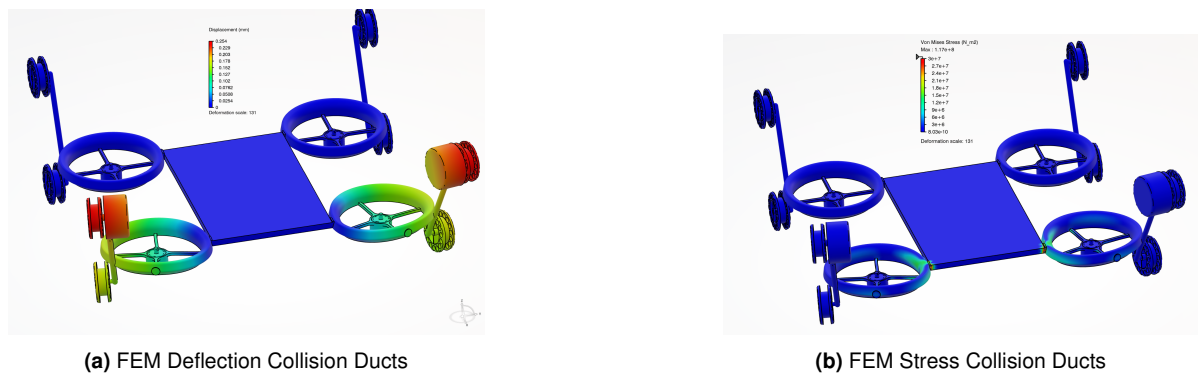


Figure 4.20: FEM Results Collision Ducts

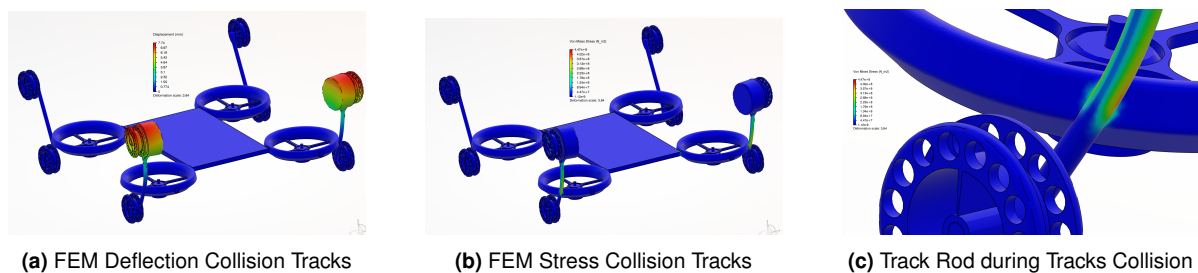


Figure 4.21: FEM Results Collision Tracks

As can be seen from all FEM results, the structure holds all loads as in no loading case in which the bending or compression force exceeds 511 MPa . Figure 4.18 shows that during normal flying conditions stresses are approximately ten times below failure and deflection is negligible. This ensures a rigid body which aids in controllability. During driving the main force is due to the torque generated by the electric motor, as can be seen in Figure 4.19c.

From the frontal collision with the ducts and all other analyses, it can be seen that the ducts are over-engineered for the forces they need to carry. This confirms the assumption made in subsection 4.1.3. As can be seen in Figure 4.21, the maximum deflection of the ducts is around 0.2 mm which falls way within the 1 mm clearance to the blades. Therefore, this collision case does not have any other negative effects.

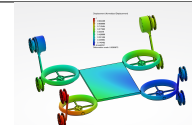
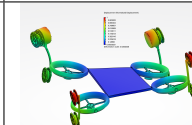
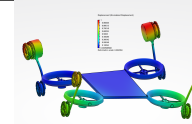
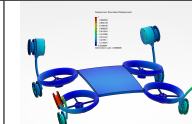
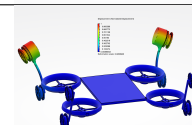
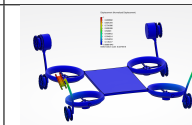
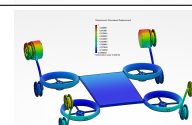
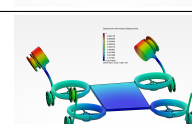
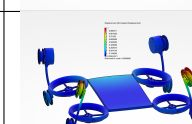
The most critical loading is the frontal collision on the tracks, as can be seen in Figure 4.21a, 4.21b and 4.21c. It causes a deflection of 7.74 mm with a maximum stress of 447 MPa . This is quite significant but not over the limits. For further development, an increase in structural

dimensions could be considered, however, for the sake of weight saving, this is not done in the current design. To conclude, the FEM software verifies the structural integrity of the drone in all operations, additionally, areas of structural strengthening can be identified in order to ensure more rigidity.

4.3.4. Eigenfrequency Frequency Analysis

Natural frequency analysis is an important step in the design of a drone. This is because if any components induce vibrations in one of the natural frequencies of the drone, the drone may become uncontrollable as it enters an uncontrollable oscillation. Table 4.14 lists the 6th until the 15th mode of the drone. All modes up to and including mode 6 are essentially zero and result from rigid body motion, making them negligible.

Table 4.14: Modes 6 to 15 with their Respective Frequency and Plot

Mode [Hz]	Figure	Mode [Hz]	Figure
0.004		136.5	
89.1		202.5	
91.8		233.5	
108.4		248.8	
120.6		285.0	

These modes can be taken into consideration when selecting electric motors and other components that may induce vibrations. For example, an electric motor was used with a nominal RPM of 4200, which could result in vibrations of 70 Hz. This is below the first critical vibration mode, thus, does not cause any unwanted resonance. There are situations in which the motor spins up to a higher RPM which could cause resonance with the natural frequencies. However, this is only for short times and, therefore, it is unlikely that this resonance occurs. It should be noted that this simplification of the structure does not include the entire main body, therefore, the actual modes may differ slightly.

Sensors and Data Handling

In this chapter the sensors subsystem, the data handling processes connected to it and the process of identifying victims are detailed. Section 5.1 deals with the sensors subsystem specifically. This includes identifying which sensors are crucial for the operation, choosing the specifications of the sensors and providing an overview of their location on the drone. The data handling for each sensor is described in section 5.2. The focus will be on how data is received and processed by the system. This section also includes a visual representation of how the data will flow. The chapter concludes with a discussion of the methods used for identifying a victim in section 5.3.

5.1. Sensors Subsystem

In this section, the selection procedure of the drone's sensors will be discussed and evaluated in subsection 5.1.1. After the description of the main sensors, other additional features and sensors of the drone will be discussed in subsection 5.1.2. For example, the lighting system, in principle, lacks the ability to 'sense' anything and therefore cannot be classified as a sensor. However, it is considered to be a crucial aspect of the drone as it plays a vital role in enhancing visibility for the optical camera. An overview of the chosen sensors and their allocation on the drone will be given in subsection 5.1.3. The section will conclude by assessing the impact of a sensor malfunctioning on the operation and how other sensors can provide redundancy in case another sensor fails in subsection 5.1.4.

5.1.1. Sensor Choice

This subsection will provide an overview of the main sensors that are considered for the drone. Furthermore, reasoning will be given for the chosen sensors. The main sensors are an optical camera, Light Detection And Ranging (LiDAR), and a thermal camera. The sensors described in this subsection are considered to be crucial as they contribute to fulfilling the requirements listed in section 2.1.

Optical Camera

To provide visual feedback to the operator, an optical camera is of paramount importance. A live video feed allows the operator to navigate through complex environments in case there is a stable connection between the drone and the operator. The visual feedback ensures a better situational awareness making it possible to avoid obstacles and manoeuvre through confined spaces.

Additionally, the camera will provide image data essential for creating accurate maps of the environment. The visual data can be processed together with point clouds from LiDAR scanners to make an accurate model. This also verifies the data from a LiDAR scanner.

Lastly, a camera is crucial for victim identification. Operators can identify a victim based on visuals. Artificial intelligence can also be used to identify or assist in identifying a victim [30]. This can be improved with the use of a thermal camera. An overview of considered cameras and their specifications can be seen in Table 5.1.

Table 5.1: An Overview of Considered Cameras

Camera	Weight [g]	Cost [€]	Size (LxWxH) [mm]	Additional Features
RunCam 5 [31]	56	125	38x38x36	Self-stabilising
RunCam Split 4 [31]	10.2	75	14x14x25	Switchable aspect ratio
Foxeer 4k Ambarella [32]	28	250	33x36x30	Low light conditions
RunCam Hybrid 2 [31]	18	178	19x25x25	Wide angle
RunCam Thumb Pro W [31]	16	99	54x26x21	Self-stabilising
ArduCam IMX477 [33]	10	95	25x24x23	Replaceable lens

From the considered options listed in Table 5.1, the RunCam Thumb Pro W was chosen. The ability to self-stabilise was considered crucial for our drone. Self-stabilisation is advantageous during flight, but it is considered to be essential during drive mode. The drone will vibrate because of the irregular terrain it has to drive on and a self-stabilising camera would still provide the operator with a steady video feed to navigate and search for victims. In addition, it offers a weight and cost advantage compared to the RunCam 5.

LiDAR

LiDAR enables accurate mapping and localisation inside a (collapsed) building. The LiDAR facilitates Simultaneous Localization And Mapping (SLAM) required for the navigation of the drone, explained in chapter 6. LiDAR emits a laser beam and measures the time it takes to bounce back. This way, a LiDAR scanner can make an accurate 3D map of its surroundings.

Because LiDAR can measure the distance to an object, it provides the ability to avoid obstacle collisions. Again, ensuring safe navigation during autonomous flight and assists the operator during manual flight.

Overall, one of the main purposes of the drone is to map the environment. A LiDAR scanner is crucial to generate an accurate 3D map of the environment. It can be combined with an optical camera to get an interpretable 3D map and will therefore be one of the crucial sensors on this drone. An overview of the considered LiDAR scanners is shown in Table 5.2. Only Two-Dimensional (2D) LiDAR scanners are considered in this table as two 2D LiDAR scanners are a cheaper way of computing a 3D map compared to a 3D LiDAR scanner [34]. 2D LiDAR scanners have also a significant size and weight advantage over 3D LiDAR scanners.

Table 5.2: An Overview of Considered LiDAR Scanners

Camera	Weight [g]	Cost [€]	Size (LxWxH) [mm]	Accuracy [mm]	View Angle [°]
SF45/B [35]	59	420	51x48x44	± 10	320
SF40/C [36]	261	745	56x56x70	± 30	360
YDLIDAR T-mini Pro [37]	45	83	39x39x33	± 20	360
LDROBOT D300 LiDAR [38]	50	90	39x39x35	± 45	360

From the considered option listed in Table 5.2, the YDLIDAR T-mini Pro was chosen as the LiDAR scanner on the drone. Compared to the other options this LiDAR has a high accuracy as well as a cost and weight advantage. Additionally, it is able to scan the surroundings a 360° [37].

Thermal Camera

An infrared (IR) camera, also called a thermal camera, detects thermal (heat) signatures. These can reveal a living victim in low light conditions or when partly obstructed. An optical camera may have difficulty identifying a living victim in these circumstances. Thermal cameras also simplify the process of distinguishing between heat-emitting objects and a person. The thermal camera can be combined with the LiDAR scanners and optical camera to create an as accurate as possible 3D map of the environment while also assisting in the identification

of victims. This makes an IR camera an invaluable addition to the drone. An overview of the considered thermal cameras can be seen in Table 5.3.

Table 5.3: An Overview of Considered Thermal Cameras

Camera	Weight [g]	Cost [€]	Size (LxWxH) [mm]	Resolution [pixels]
Lepton 160, 57° (HFOV), 3.5 mm [39]	0.9	479	11x13x8	160x120
Flir AX8, 48° (HFOV), 1.54 mm [40]	125.0	967	55x80x25	640x480
Flir Boson 320, 16° (HFOV), 13.8 mm [41]	7.5	1800	21x21x11	320x256
Flir Boson 320, 50° (HFOV), 4,3 mm [41]	7.5	1600	21x21x11	320x256
Flir Boson 640, 95° (HFOV), 4.9 mm [41]	7.5	3785	21x21x11	640x512

The thermal camera chosen for the drone is the Flir Boson 320 50° (HFOV) 4.3 mm. It provides the perfect combination of not exceeding the maximum cost of the sensors subsystem indicated by SYS-CO-1-1-4, being lightweight, and small in size. Furthermore, as the thermal camera will be used for identifying victims, 320x256 pixels is preferred over the 160x120 pixels alternative Lepton 160, 57° (HFOV), 3.5 mm camera. A larger horizontal field of view of 50° is preferred over only 16° as it allows for capturing a wider area in the thermal images. This provides more comprehensive coverage during the drone's operation.

5.1.2. Additional Drone Features and Sensors

This subsection elaborates on important features of the drone that support or add redundancy to one or multiple main sensors described in subsection 5.1.1, such as the lighting system and the proximity sensors. Furthermore, this subsection gives a brief overview of sensors that are not explicitly selected in this chapter but are already integrated into other components of the drone, such as the data processor.

Lighting System

The drone has to be operable in environments with a minimum light intensity of 0 *lm*, according to SYS-TC-OP-2 in Table 2.3. An adequate lighting system would not only be crucial to provide the operator with visual feedback to navigate the drone but it also allows the operator to search for victims in these dark environments. Therefore, the drone will be equipped with twelve 500 *lm* CH-COB-5W-CW Light Emitting Diodes (LEDs) [42]. The number of lights is based on SYS-TC-OP-2-1, which states that the drone shall have a light system of at least 6,000 *lm*.

Multiple smaller LEDs that generate less light intensity are preferred over one large LED that alone is able to provide 6,000 *lm*, as it allows for improved object definition, reduced glare, and better surface detail due to the oblique lighting angles created by the distributed light sources [43]. Furthermore, multiple LEDs close to each other increase the total lighting angle. This wider lighting angle enhances the coverage area and helps to illuminate a larger field of view, providing improved visibility for the operator and video feed shot with the optical camera. Further specifications on the light system will be provided in subsection 5.1.3.

Proximity Sensors

Even though the drone will have a LiDAR sensor, additional proximity sensors would benefit the drone. Having multiple sensors to measure distance adds redundancy to the drone. Additionally, a LiDAR sensor is not accurate up close. Dedicated distance sensors can accurately measure distances of a few centimetres. Distance sensors usually respond faster than optical cameras and LiDAR scanners [37, 44]. They can quickly react to nearby obstacles and prevent a collision. Therefore, proximity sensors are incorporated into the design.

The drone will operate in narrow environments. The proximity sensors need to be accurate at short distances and have a fast response time to be a valuable addition to the design. The GP2Y0A41SK0F IR proximity sensor by Sharp will be used as they can fulfil both prerequisites

[45]. Further specifications on this distance sensor will be provided in subsection 5.1.3 and subsection 5.2.2.

Gyroscope and Accelerometer

A 3-axis gyroscope and a 3-axis accelerometer are embedded in the drone's data processor described in subsection 5.2.1. Furthermore, the data processor includes a thermal sensor that is able to monitor the temperature of the data processor. The gyroscope is used for measuring (change in) the angular rate of the drone about its three axes: pitch, roll and yaw. It provides information about the determination and changes in the drone's orientation which is crucial for stabilising and controlling the drone's movement. More information on this topic is provided in chapter 6. The accelerometer, on the other hand, measures the (change in) acceleration. By analysing the acceleration data, the drone's subsystems can determine its position, velocity and acceleration.

5.1.3. Sensor Allocation

The drone will be equipped with one RunCam Thumb Pro W camera. This camera will be placed at the front of the drone on a tilting mechanism that can rotate the camera and increase the vertical field of view to 210 degrees. The tilting mechanism is necessary to provide the operator with optical vision in the forward as well as down- and upward directions. The Flir Boson 320, 50° (HFOV), 4,3 mm thermal camera will be placed next to the optical camera to have the same viewing direction. This makes an easy switch between the optical camera and thermal camera possible for the operator without having to reorient the drone. It also takes advantage of the already proposed tilting mechanism for the optical camera. The specifications of the tilting mechanism are left for further research.

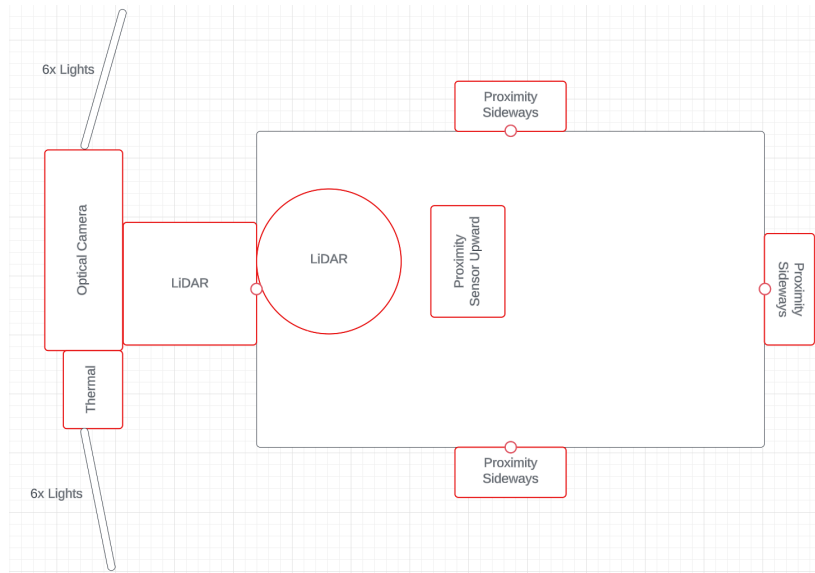
The lighting system will be located in front of the ducts of the propulsion subsystem to provide lighting in the direction the camera is pointing. Twelve CH-COB-5W-CW LEDs will be used, on each side of the camera six in two rows of three. This allows for 6,000 *lm* light intensity, while also providing oblique lighting and therefore increasing the visibility in dusty environments [46].

The drone will have two YDLIDAR T-mini Pro sensors. One in a vertical position so that walls, ceiling and floor can be scanned and one in a horizontal position in order to scan in the direction of flight and behind the drone. Because the LiDAR scanner does not have a tilt angle and a full-height view of the environment is desired, a tilting mechanism for the horizontal LiDAR scanner is proposed. This would increase the field of view of the scanner to 50 degrees. Specifications on this tilting mechanism are left to further research.

Five GP2Y0A41SK0F IR proximity sensors will be placed on each side of the drone, to be able to measure distances to, for example, obstacles in all directions. An exception is a proximity sensor on the bottom of the drone as there are no sensors that can break on this side so a proximity sensor is deemed unnecessary. The proximity sensor on the front side of the drone is placed on top of the vertical LiDAR. This is done in such a way that it will not restrict the functionality of the LiDAR or one of the cameras. An overview of the type, amount and some important characteristics is shown in Table 5.4. An overview of the locations of the sensors is shown in Figure 5.1.

Table 5.4: Overview of Sensors and their Characteristics

Sensor	Amount	Weight [g]	Cost [€]	Power Usage [W]	Size [mm]
RunCam Thumb Pro W [31]	1	16.0	99	2.5	54x26x21
CH-COB-5W-CW LED [42]	12	1.0	1.59	5	13x13x2
YDLIDAR T-mini Pro [37]	2	45.0	83	1.7	39x39x33
Boson 320, 50° (HFOV) 4,3 mm [41]	1	7.5	1600	0.6	21x21x11
GP2Y0A41SK0F IR [44]	5	3.6	5.76	0.06	29.5x20x13.5

**Figure 5.1:** Sensor Configuration of the Drone

5.1.4. Malfunctioning of Sensors

During operation, there is the possibility of one or multiple sensors malfunctioning. Malfunctioning can occur due to technical difficulties, environmental influences or damage to the drone. Assessing the impact of a sensor malfunctioning on the mission and mitigating the risk if possible is important for the success of the operation. The importance of each sensor has to be determined. The data the sensor provides, their criticality to the operation and the ability to continue the mission without the data can be estimated.

In case the optical camera breaks, no visual data can be measured anymore using this optical camera. The operator will only have visual feedback from the thermal camera during the remaining of, and after, the drone's mission. It will no longer be possible to create an easy-to-interpret map as the point clouds from the LiDAR scanner cannot be combined with visual data obtained from the optical camera anymore. Lastly, the visual data cannot be used for victim identification. This does not have a large impact on the success of the mission since victim identification can also be done with the thermal camera.

In case one of the lights breaks, the impact will be minimal. If, however, multiple lights break on the same side or all lights break, the optical camera would be useless. It would have the same effects as when the optical camera itself breaks. The risk of multiple lights failing at the same time will be mitigated by installing the lights in parallel.

If one of the two LiDAR scanners breaks, distance information in its direction will not be produced anymore. The distance can also be estimated based on visual data from the optical camera, but that is less reliable and less precise than a LiDAR scanner. In case both LiDAR scanners break, the drone will have no reliable way of mapping the environment. Collision

avoidance can still be done with proximity sensors, but they cannot be used to create a reliable 3D map. Losing the LiDAR scanner(s) would endanger the safe return of the drone to the base and would eliminate the possibility of having a reliable 3D map of the environment.

Should the thermal camera break, heat information on the environment will not be produced anymore. Differences in heat cannot be distinguished which makes it harder to interpret details of the environment. Additionally, heat signatures are crucial for victim identification. Identification can also be done with visual data, but it will be harder and less reliable.

The proximity sensors provide close-distance measurements. The drone will be equipped with multiple proximity sensors that produce distance measurements if the drone is close to an object. If one of the distance sensors breaks, the drone will lose fast feedback on proximity in that direction. This does not have a substantial effect on the performance of the drone because the LiDAR scanner provides distance measurements as well. The drone will lose the added accuracy, fast feedback on close objects and validation of the LiDAR data if the proximity sensors fail.

5.2. Data Handling

This section explores the drone's data handling and data processing. A data processor of the drone will be explained in subsection 5.2.1. A visual representation and explanation for each sensor of how data is handled and processed by the data processor are provided in subsection 5.2.2. The section concludes with a representation of the Kalman filter in subsection 5.2.3.

5.2.1. Data Processor and Flight Controller

A data processor is an essential part of the drone when it comes to data handling. It serves as the brains of the drone and is the central hub for real-time data handling in the *Needle's Eye* drone. The sensor data is all processed by this component and it integrates various systems within the drone. The ModalAI VOXL Flight has been chosen as it can not only be used to perform these tasks but also contains a flight controller [47]. A flight controller interprets inputs from various sensors such as LiDAR, proximity sensors and the optical camera. It translates these inputs into commands for the drone's motors and actuators. It, therefore, supports the possibility of autonomous flight, indoor navigation and obstacle avoidance [47]. The only 26 g heavy flight computer and controller, offers an open-source platform, allowing for sensor customization and expansion of the drone's capabilities [47]. The ModalAI VOXL Flight supports up to two microSD cards. A 256 Gb MicroSD card will be included in the drone [48].

The ModalAI VOXL Flight, shown in Figure 5.2, is equipped with five Inertial Measurement Units (IMU) of which three are located on the flight controller. The other two are placed on the VOXL part of the data processor. Unlike the flight controller part, which focuses on interpreting sensor data and generating control commands, the VOXL handles a wide range of tasks beyond flight control, such as sensor data fusion, data storage, and sensor monitoring. This makes it the primary computing unit of the drone. Both the Central Processing Unit (CPU) and the Graphical Processing Unit (GPU) are on the VOXL. The ModalAI VOXL Flight IMUs include an embedded thermal sensor, a 3-axis gyroscope and a 3-axis accelerometer. The thermal sensor monitors the temperature of the data processor and prevents overheating of the system.

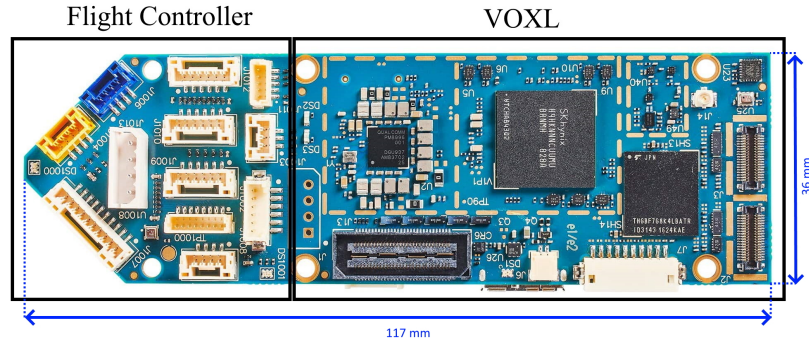


Figure 5.2: ModalAI VOXL Flight [47]

5.2.2. Sensor Data Processing

The data handling and processing diagram is shown in this subsection in Diagram 3. The data handling and processing diagram provides a clear visual representation of how the data is handled and processed for each below-described sensor and the integrated IMU, explained in subsection 5.2.1.

Optical Camera Processing

The RunCam Thumb Pro W complies with the Camera Serial Interface-2 (CSI-2) protocol [31]. The CSI-2 protocol is a widely adopted standard for handling data between image sensors such as the optical camera and the VOXL Flight data processor. Once the data reaches the VOXL Flight, it can be processed and transformed to use for further analysis. From the frames, either individual images are computed or all frames together are analysed. The individual images are used to identify possible victims and make a distinction between victims and objects. All the frames together can be used for tracking the movement of the identified victims and objects and generating a map of the surroundings. More about the process of victim identification is explained in section 5.3. A more elaborate overview of the steps involved in the data processing of the optical camera and their relations can be found in Diagram 3.

LiDAR Processing

The YDLIDAR T-mini Pro has an off-the-shelf format for commands to the scanner and data responses from the scanner [37]. The scanning response is shown in Figure 5.3. The fourth byte (LS) represents the number of data points in the response (S_i). The FSA and LSA nodes indicate the starting and stop angles of the data pack. Finally, the S_i nodes encode the intensity and distance of a measured point. Additionally, a flag for interference is encoded in the second byte of the node. This is a recommendation of the scanner if the point should be filtered out during the processing of the data. The rest of the response header encodes information about the package type and functional checks. Calculations on how the data can be transformed are included in the developer manual of the LiDAR [37]. After transformation to distances, data can be filtered out based on the interference flags that are encoded in the response.

PH		CT	LS	FSA		LSA		CS		S1			S2			..
LSB	MSB	1 st LSB	2 nd	3 rd MSB	1 st LSB	2 nd	3 rd MSB	..								

Figure 5.3: The Response of the YDLIDAR [37]

From all the individual distance measurements, a point cloud can be formed. By combining the trajectory data of the VOXL Flight’s integrated IMU with the point cloud generated by the LiDAR

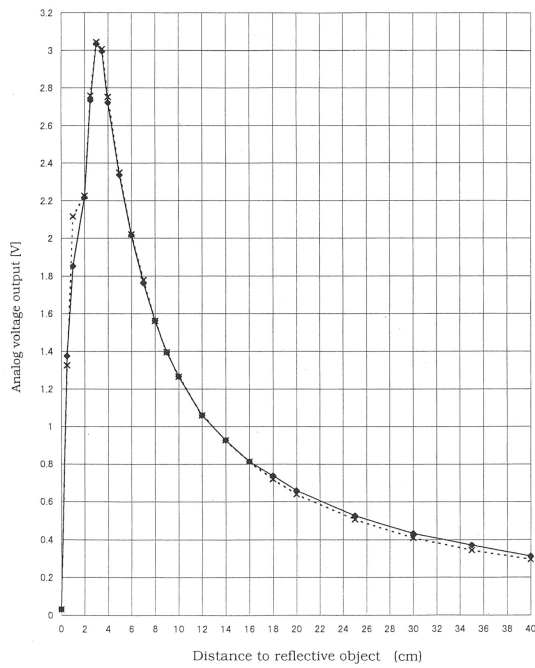
scanners, it becomes possible to perform georeferencing. Georeferencing is the process of assigning geographic coordinates to each point in the point cloud. After colourising and classifying each point of the point cloud and fusing the data with the optical camera, a map of the surroundings can be constructed.

Thermal Camera Processing

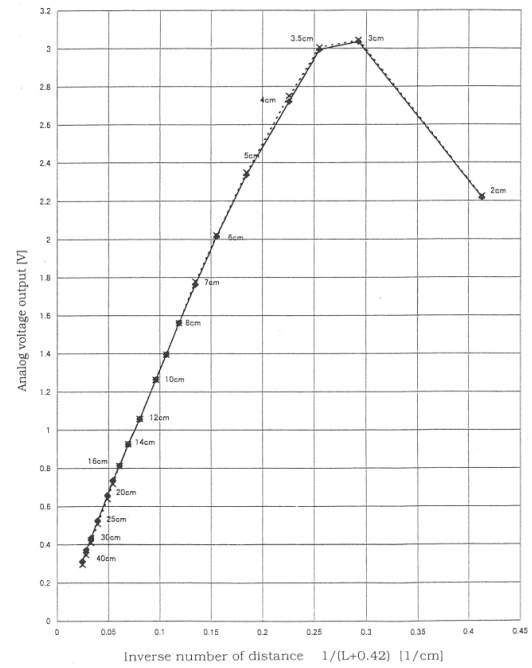
The Boson 320, 50° (HFOV) 4,3 mm thermal camera complies with the same protocol as the optical camera, the CSI-2 protocol [41]. First, the frames are divided into smaller elements. For each element, the emitted IR energy of that specific element is measured by the thermal camera. Thereafter, each element is given a colour based on the emitted IR energy. The elements are all analysed and processed individually. Elements that are considered to be outliers, and do not fall within the predefined temperature range are filtered out. This improves the quality, clarity, and interpretability of the thermal frames constructed from the individual elements. For further improvements, contextual image processing and histogram modification are applied to all frames. Contextual image is the process of comparing each element with its neighbourhood, the nearby elements. This allows for better identification and distinguishing of areas of interest, such as a possible victim, within the image. The contrast of the image will then be improved by applying a histogram modification. This modification adjusts the colouring range of all the elements based on the minimum and maximum temperature values. By mapping the temperature values to this new colour scale, it is easier to distinguish subtle temperature variations and details. With these processed thermal images, prediction on victim identification can be made either by the operator or autonomously. More about the process of victim identification is explained in section 5.3.

Proximity Sensor Processing

The GP2Y0A41SK0F IR proximity sensors have an output format in the form of a voltage drop [44]. This voltage drop can directly be read out and has an inverse relationship with the distance to an object. This relationship is shown in Figure 5.4a. By taking the inverse of the distance to the reflective object and plotting this against the analogue voltage output, Figure 5.4b can be constructed. From this figure, it can be seen that there is no clear distinction in voltage output if the distance to the reflective object is smaller than 3.5 *cm*. Additionally, the larger the distance to the reflective object is, the smaller the difference in voltage output becomes. If the distance to the reflective object becomes larger than 30 *cm*, the proximity sensor can be considered to be not accurate any more as the points lie too close to each other[44]. This range of accuracy fits with its purpose of providing distance information in the narrow operating environment of the drone.



(a) Output Distance Characteristics



(b) Output Inverse Distance Characteristics

Figure 5.4: Relationship between Output Voltage and Distance to Object [44]

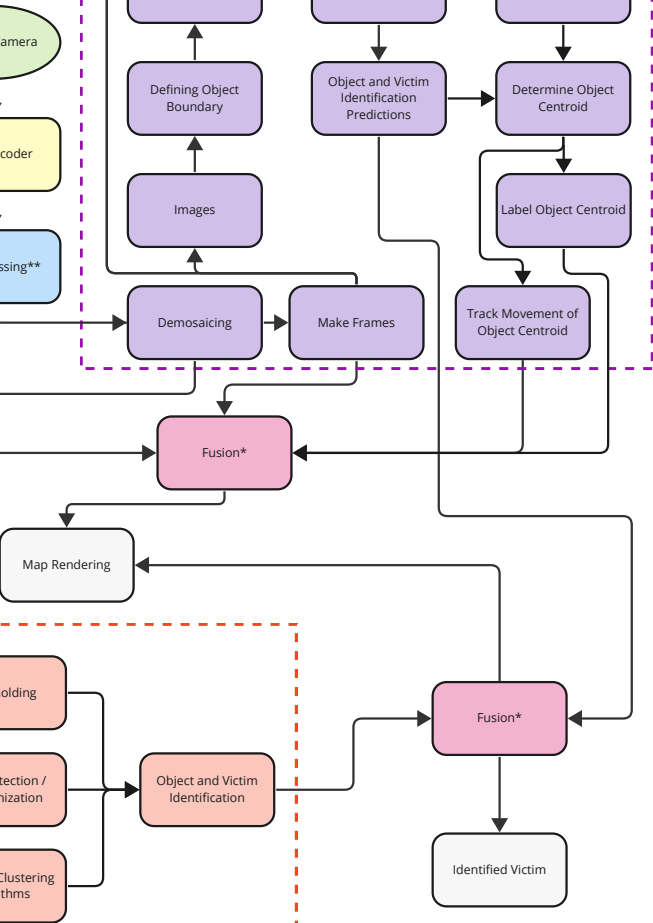
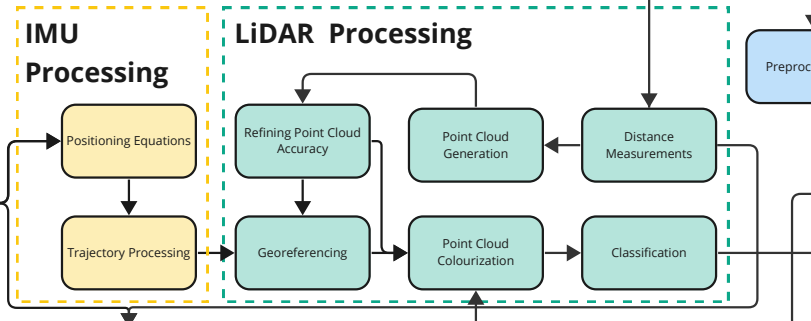
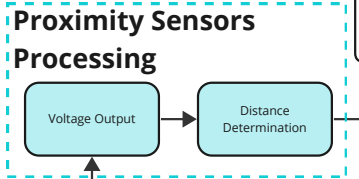
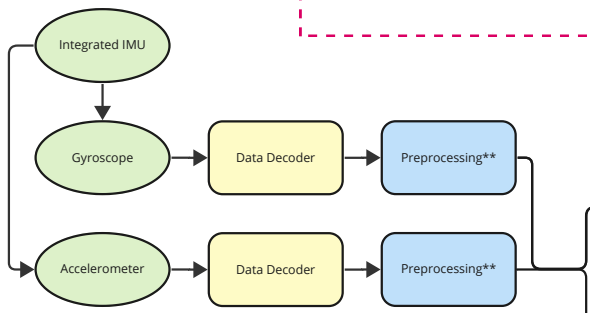
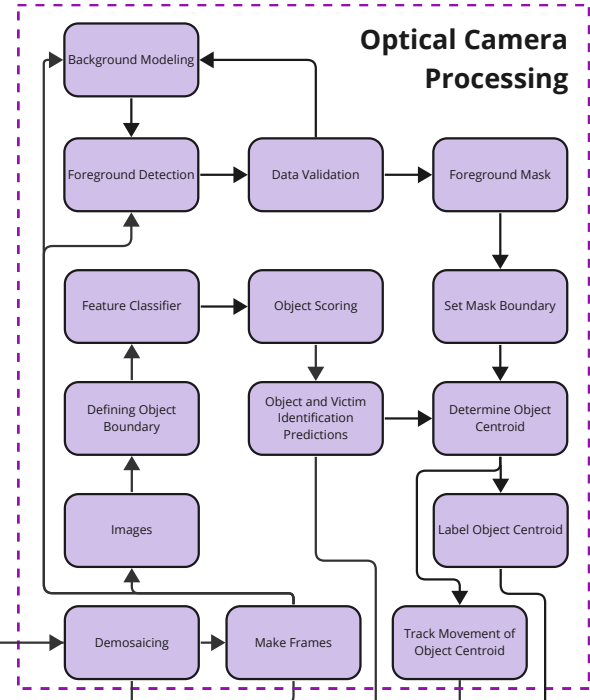
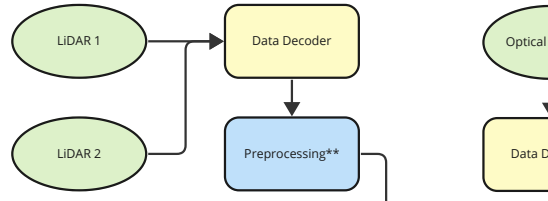
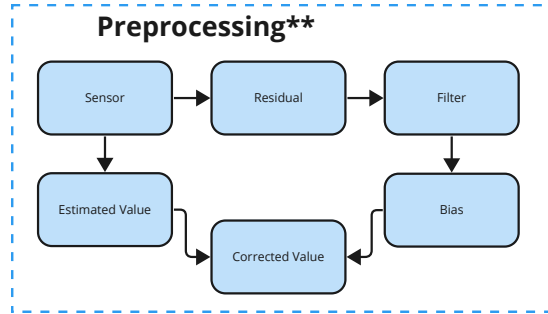
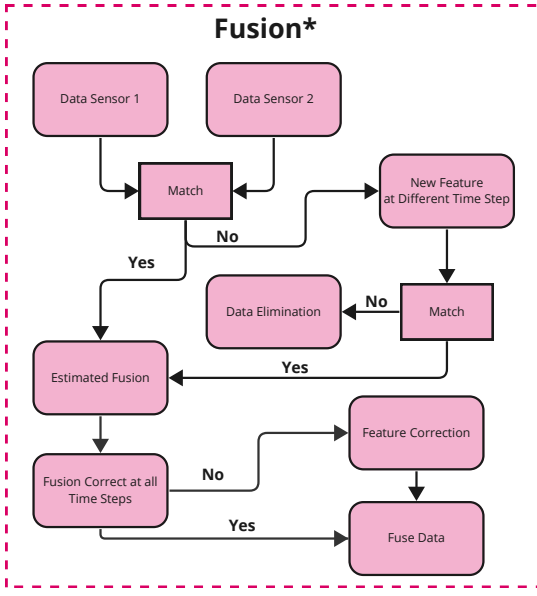
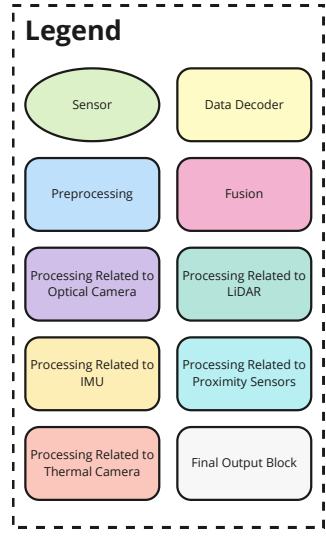
Fusion of Data and Calibration

An important step in data handling and processing, which is also included in Diagram 3, is the fusion of data. This step includes comparing data from several sensors with each other. This can either be done to complement the already existing data from one sensor with another sensor's data or to verify the data from one sensor with the data of another sensor. The data fusion process makes identifying the malfunctioning of certain sensors possible if the provided data by the malfunctioning sensor does not match with data from other sensors.

The sensors on a drone should be calibrated to work together and achieve optimal performance. Calibration includes, for example, the focusing of the (thermal) camera, but also determining the relative distance between the data points obtained from the LiDAR scanners [49]. Without proper calibration fusion of the data is not possible as it may result in inconsistencies, errors, and inaccurate interpretations.

Data Handling and Processing Block Diagram

Diagram 3



5.2.3. Kalman Filter

The Kalman filter is an algorithm used for estimation and prediction that excels in fields such as navigation and feature tracking [50]. Therefore, it will be used for data filtering on the drone before the data will be processed. It predicts the next state of a system based on the previous measurements and corrects its prediction method based on the current measurement. By iteratively updating the state estimate of the prediction, the filter provides a balanced trade-off between the accuracy of the measurements and the accuracy of the estimation model [51]. The effect of the Kalman filter in a one-dimensional case can be seen in Figure 5.5a. The blue line corresponds with the optimal solution and the green line is the computed solution. The red dots are the sample points that are the input of the filter. The error of the Kalman filter depends on the measuring frequency as can be seen in Figure 5.5b. The measuring frequency needs to be above a threshold for the filter to be useful. The Kalman filter can be extended in 2D or 3D to be of use for the drone.

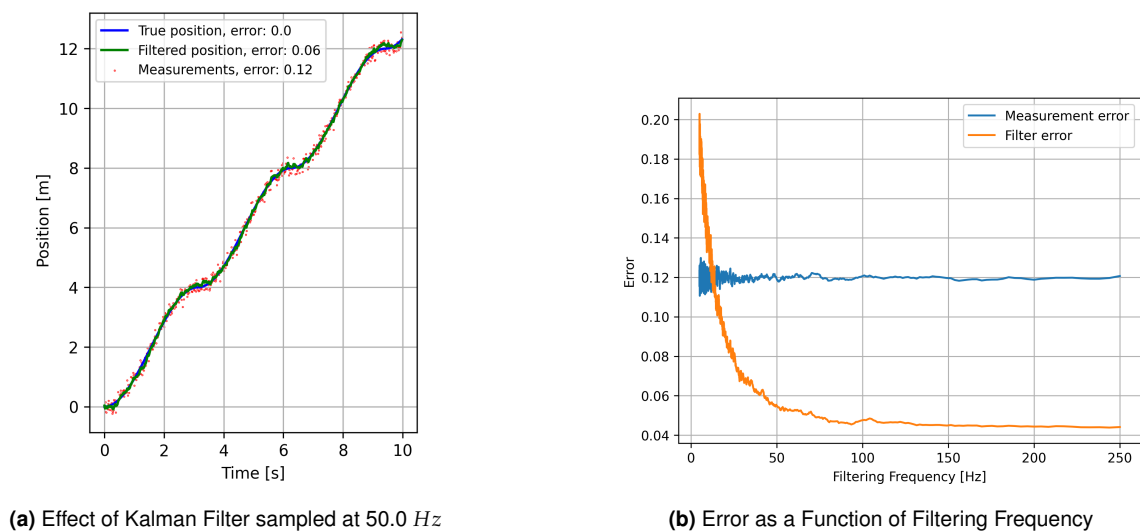


Figure 5.5: One-Dimensional Kalman Filter

5.3. Victim Identification

This subsection focuses on three important aspects to address the possibility of identifying victims during the search and rescue mission using a thermal camera. The Minimum Resolvable Temperature difference (MRT), the required visible area of a victim and, finally, the Depth of Field (DoF) of the thermal camera will be discussed in subsection 5.3.1, subsection 5.3.2 and subsection 5.3.3, respectively. It should be noted that not only the thermal camera will be used to identify victims during the mission. The optical camera also plays a vital role in this process. A brief discussion on the application of using algorithms to identify victims in combination with an optical and a thermal camera is provided in subsection 5.3.4.

5.3.1. Minimum Resolvable Temperature Difference

The MRT is a common measure to assess the performance of a thermal camera. The MRT is measured by placing four bars parallel to each other on top of a surface with a slightly different temperature. This is visualised by a difference in colour on the operator's screen. An operator is asked to try to identify the four bars. The lowest temperature difference at which the operator succeeds is the MRT [52].

The MRT is dependent on the distance between the bars, also known as the spatial period. Therefore, the MRT is often presented in a graph with, on the vertical axis the MRT, and on the

horizontal axis either the (angular) spatial period or its inverse, the (angular) spatial frequency. In Figure 5.6, the MRT is plotted against the angular frequency. To obtain an indication of how the quality of an image influences the required angular period for a range of MRT, multiple resolutions are plotted. This graph was computed based on the work by Chrzanowski [52]. In this paper, a method to determine the MRT using the specifications of thermal cameras was developed.

In Figure 5.6, it can be seen that, for a low resolution, the required MRT increases rapidly at a relatively high angular period compared to other resolutions. By increasing the resolution, a lower angular period is required for the same MRT value. This means that the bars can be distinguished at the same temperature difference even if they are closer together. This translates to the operator or an algorithm being able to distinguish a victim even if that victim is closer to other objects that emit heat. The benefits of increasing the resolution diminish as the resolutions become in the higher range. This supports the 320x256 pixels resolution of the thermal camera that is chosen in subsection 5.1.1. Upgrading from 320x256 pixels to 640x512 pixels is considered to not be worth the possible extra required (computational) power, mass and additional cost.

Small angle approximation together with the distance to the bars can be used to transform the angular period into the spatial period. To obtain the spatial period, the angular period is multiplied by the distance to the bars. This transformation is visualised in Figure 5.7. This figure also visualises the spatial period and the angular period.

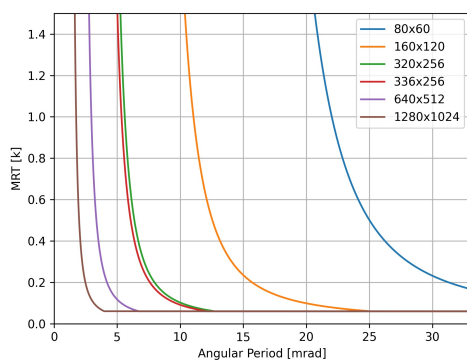


Figure 5.6: MRT based on the Angular Period of the Object for Different Resolutions

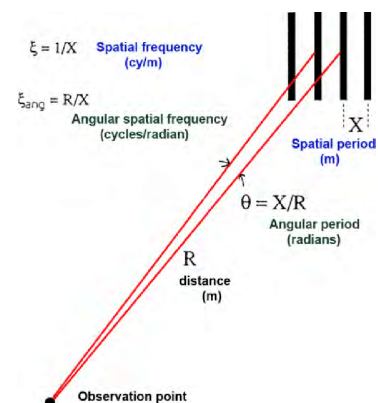


Figure 5.7: Relation between Angular and Spatial Frequency [53]

By combining Figure 5.6 and the transformation shown in Figure 5.7, the minimum required spatial period, when observing at a specific distance to two objects, to still distinguish two objects from each other, can be plotted for various MRTs. The change in the minimal spatial period for multiple temperature differences for the chosen 320x256 pixels thermal camera is shown in Figure 5.8. In Figure 5.8, it can be seen that the spatial period using the Boson 320, 50° (HFOV) 4,3 mm thermal camera is fifteen centimetres at twelve meters distance when the MRT is 0.4 K. As the distance to the object decreases, which is more likely to occur during the mission, the spatial period decreases even more.

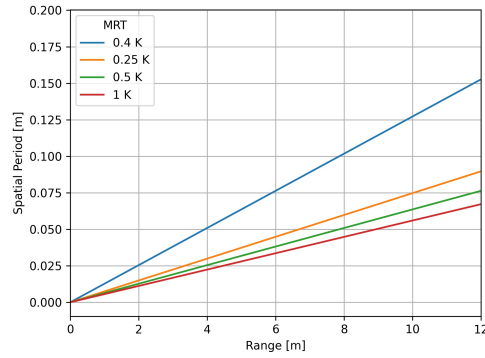


Figure 5.8: The Required Spatial Period at a Range of Distances for Multiple MRTs using the Boson 320, 50° (HFOV) 4,3 mm

5.3.2. Required Visible Area

In order for an operator to identify a victim, this person should be visible on at least 138, for example, 7x20 pixels, of the image according to Infinite Electro-Optics [54]. How much area of a person is captured on 138 pixels depends on the distance between the person and the camera. When an image is taken at a close distance, each pixel captures only a small fraction of the 'real world', resulting in a smaller portion of the victim's body being represented by those 138 pixels. On the other hand, when the picture is taken at a larger distance, more area of the 'real world' is captured in each pixel and vice versa. This means that a larger portion of the person's body is represented and that from closer distances, victims can already be identified from smaller body parts compared to when they are observed from larger distances. Figure 5.9. In the figure, it can be seen that with the Boson 320, 50° (HFOV) 4,3 mm thermal camera an average adult man can still be identified at approximately 60 meters. Also, a hand can be recognised from a distance of eight meters. These distances are significantly higher than what would be required for the use case of identifying victims in small and convened spaces.

Using the thermal camera chosen in subsection 5.1.1 a human can be identified based on only a hand from eight meters. This indicates that there is a high probability that the thermal camera is able to identify victims. However, due to obstructions caused by debris, the thermal camera might struggle. The complete effects will have to be studied further, but for now, the high amount of visibility for unobstructed views seems to indicate that even with obstructed views the camera will be able to identify victims.

5.3.3. Depth of Field

The DoF is the distance between the closest and farthest points at which a picture is considered to be sharp. The DoF depends on the specifications of the used camera, the distance to the object that the camera is focused on and the circle of Confusion (CoC). The CoC is a measure of the acceptable blur of an image. The CoC can be expressed as the number of pixels over which a single point in the real world is blurred out in an image. The far limit and the near limit of the DoF can be calculated with Equation 5.1 and Equation 5.2, respectively [55, 56]. Here, 'H' is the Hyperfocal distance, the focusing distance in which the maximum depth of field is obtained. This value is calculated using Equation 5.3.

$$DoF_{\text{far limit}} = \frac{H \cdot u}{H - (u - f)} \quad (5.1)$$

$$DoF_{\text{near limit}} = \frac{H \cdot u}{H + (u - f)} \quad (5.2)$$

$$H = f + \frac{f^2}{N \cdot C} \tag{5.3}$$

In these formulae, 'u' is the distance to the object that the camera is focused on in meters, 'f' indicates the focal length of the camera in meters, 'N' is the camera's f-number and 'C' is the CoC in meters.

Based on the pixel size of the camera, the CoC can be expressed in pixels. Figure 5.10 shows the relation between the CoC and the near and far limit of the depth of field. Figure 5.11 shows a thermal image with a 320x256 pixels resolution of a victim for various CoCs. From the images, it can be seen that with a CoC of five pixels, all possibly necessary details of the victim are still visible. Five pixels CoC is therefore considered to be sharp enough to identify victims. How the image would look with a fifteen pixels CoC is also provided in Figure 5.10. This image serves as a comparison for different CoCs. For fifteen pixels CoC some details in the face are clearly not visible anymore. The distance to the object that the camera is focused on is tweaked to obtain a far limit for DoF that goes to infinity and a near limit that goes to 15 cm for a CoC of five pixels. The near limit is based on the minimum distance to objects of ten centimetres and the design where the camera is located at least five centimetres away from the edges of the drone. This can be achieved by pre-focusing the infrared camera at a subject distance of 0.3 m.

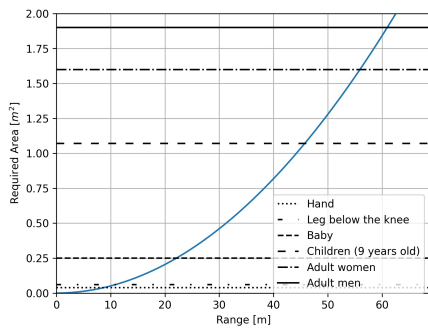


Figure 5.9: The Required Visible Area at Various Distances to identify a Victim with Reference Sizes of Average Human Body Parts

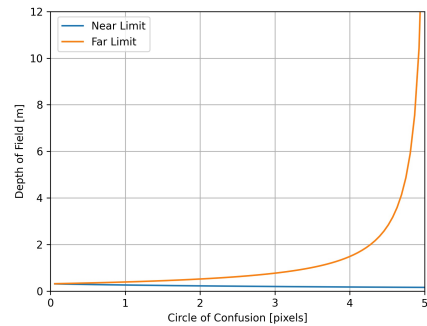


Figure 5.10: The Depth of Field Limits for a Range of Circles of Confusions

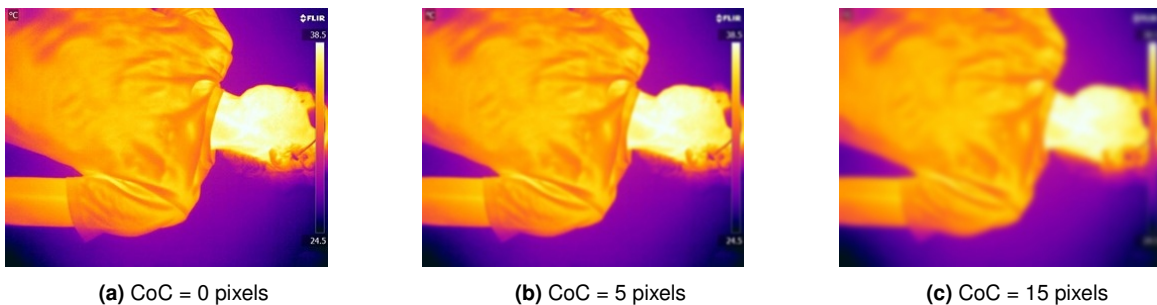


Figure 5.11: Example 320x256 Pixels IR Images with their corresponding CoC

5.3.4. Victim Identification Algorithms

There are currently several algorithm methods that can identify victims using optical and thermal cameras, such as the adaptive Gaussian mixture model and temporal differencing as discussed by Paul [30]. The Gaussian mixture model groups objects together by assuming it is

made up of multiple Gaussian distributions. This helps to capture the patterns and differences in the data more accurately [30]. Temporal differencing applies the concept of assigning each pixel a value based on its colour. By comparing the pixel values of multiple frames it can detect moving objects [30]. These algorithm methods have varying success rates according to the paper by Paul [30]. The drone will operate in environments where victims may be partially occluded. This makes predicting the success rate of identifying victims with the drone challenging. It has been shown by Paul [30] that algorithms struggle with identifying humans that are partially occluded. However, recent methods of identifying humans based only on detecting certain body parts have shown significant improvement and are likely to improve even more over time as shown by WU [57, 58].

Another challenge is the possible immobility of victims. Many algorithms use the distinct movements of humans to identify them as shown by Paul [30]. However, inside of a collapsed building victims might not be able to move as they are trapped or pinned down. Therefore, an algorithm that does not require movement has to be selected.

As the drone is able to manoeuvre through the building it will be able to better analyse a victim. Usually, research on human detection algorithms is done on either a picture or video from a mounted camera. This means that if the angle is sub-optimal or a possible human is too far it is difficult for the algorithm to determine if an object is a human. However, whenever a possible victim is identified but the algorithm is not certain, it is possible for the drone to fly towards it to get an improved picture of the object.

Navigation, Stability and Control

In this chapter, the navigation of the drone is discussed together with its stability and control (SC). For navigation, a method combining the 2D LiDAR data with path-finding algorithms is proposed in order to cover all grounds, fly autonomously, return to base and map its surroundings simultaneously. For stability and control, a method combining two controller types is discussed and the stability of the drone is assessed by simulating various scenarios.

6.1. Navigation Subsystem

For the USAR use case that this drone's design is focused on, it is not expected that the drone is able to have a continuous connection with the operator due to the debris of the collapsed buildings chapter 7. Therefore, autonomous flight needs to be implemented in order for the drone to function during the mission (SYS-TC-NAV-1). In outdoor environments, Global Positioning System (GPS) is readily available and by combining this with the drone's IMU, autonomous flight is feasible [59, 60]. However, indoor autonomous flight is far more challenging for small lightweight drones as GPS is not available and sensors are often too heavy or large in size [61, 62]. Therefore, indoors, another way of localising the drone is necessary [63]. In general, to have autonomous flight, the drone has to be able to generate a map, detect obstacles, avoid obstacles and localise itself within the space.

For navigating, drones can operate using sensors to identify their position with respect to their surroundings called visual-based navigation. Next to this, drones can also operate by non-visual-based navigation using GPS sensors or IMUs to detect their position and manoeuvre [64]. For indoor navigation, GPS is not an option neither is the Global Navigation Satellite System (GNSS) or WiFi [64]. As a solution, the drone can operate using IMU sensors in combination with visual sensors such as an optical camera or a LiDAR scanner [64].

The navigation is further complicated since the drone has to manoeuvre within collapsed and thus often unpredictable structures [65, 66]. For autonomous flight, the drone needs to find a path. It does this using path-finding algorithms. For these algorithms, various options are possible [67–69]. In known terrain or easily predictable terrain, a drone can operate by using Universal Path Planning [70]. However, the terrain in the use case is not standard which complicates the predictability and feasibility of path-finding. Overall, it is crucial that the computed path is safe and that the path is continuous and collision-free [70].

In order to achieve this a mapping strategy needs to be set up after which a path-finding algorithm can be used. Then, an obstacle detection approach needs to be proposed so that while the drone manoeuvres it ensures collision-free operations. To prove the concepts, the performance of the different algorithms is demonstrated using a simulation.

6.1.1. Mapping and Obstacle Detection

Mapping the environment is crucial for executing the drone's mission as it enables the creation of a virtual representation of the environment. By having a virtual map of the environment, the drone can navigate safely and efficiently through the environment to find its target.

In order to investigate different mapping algorithms, an environment and drone are simulated.

A random environment can be created through the use of cellular automata [71]. These maps can be modified after they have been generated to remove unreachable cells. The generated map is a grid in which zeros represent free cells and ones represent obstructed cells. An example of generated maps can be seen in Figure 6.4.

The drone is a simulated LiDAR scanner that keeps track of the environment it has scanned. The scanned map is initialised as a map of empty cells. Based on an angle, range and starting point, the drone determines the furthest scannable point. It draws a line between the points and uses the Bresenham algorithm to rasterise the line [72]. For each point, the drone checks, from the closest to the furthest, if that point corresponds to a wall. If this is the case, a value is added to this cell and the drone stops looking in this direction. If not, the drone subtracts a value from this cell and checks the next cell with the same procedure. To interpret these cell values, they are mapped to probabilities using Equation 6.1, where x is the value of the cell. The Bresenham method is shown in Figure 6.1a and the effect of it in the simulation in Figure 6.1b.

$$P = 1 - \frac{1}{1 + e^x} \quad (6.1)$$

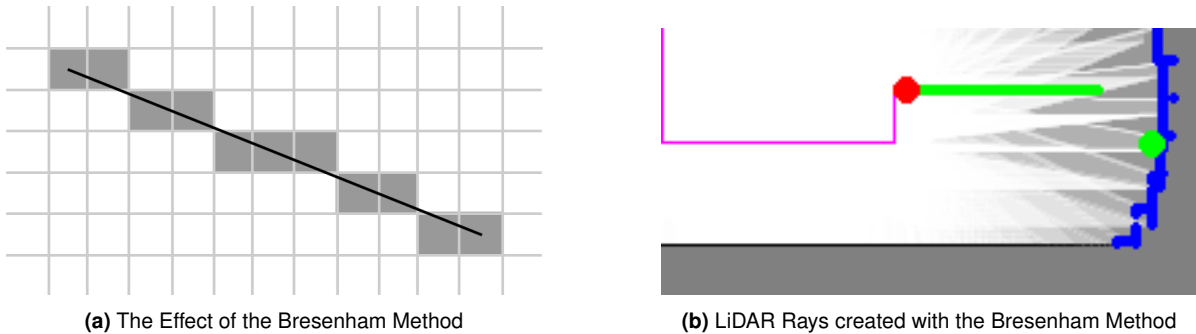


Figure 6.1: The Effect of the Bresenham Method in the Simulation

Using this method, a probability map of the scanned environment can be made by the drone. Free cells appear white on the map, occupied cells appear black and unknown cells are grey. This can be seen in Figure 6.2. This map can be used by mapping algorithms to determine the next step the drone will make.

However, there are limitations to what is possible in the current simulation. The simulation method can be applied to a 3D case which is subject to further research. Cells are interpreted in a discrete way, meaning it is either a wall or a free cell. This means that implemented algorithms do not take distance to a wall into account. This results in the drone not keeping a margin to a wall in the simulation. Additionally, the size of the drone is not accounted for. The focus of the simulation was to have it navigate by itself, only restricted by obstacles. Further development is needed to account for the drone's size. Lastly, it was aimed to make the resolution of the map made by the drone scalable. At the moment, this resolution is directly defined by the accuracy of the scanner and is not adjustable. This is done for the sake of simplifying the implementation of different path-finding algorithms.

In summary, an environment and a movable scanner are simulated to allow for investigating different mapping and path-finding algorithms. The current simulation has limitations, but with further development, it can be improved to more accurately represent real-world scenarios. The algorithms that have been investigated will be described in subsection 6.1.3.

6.1.2. Full Coverage Algorithms

When the drone starts its operation, it enters a fully unknown environment knowing that a victim is present within the collapsed building. Therefore, it is crucial that the drone ensures that it maps the collapsed environment. This is done by following a full coverage algorithm ensuring that it leaves no places unseen.

Three full-coverage path-finding algorithms with unknown destinations are considered. The algorithm spiral Spanning Tree Covering (STC) explores unknown environments while tracking the visited locations and ensures that all reachable areas are covered without revisiting previously explored locations [73]. Complete coverage D* explores and covers an area while adapting the path based on the available information [74]. Finally, Smooth Complete Coverage Path Planning (SCCPP) utilises clothoids to generate a computationally efficient, collision-free trajectory that ensures comprehensive coverage [75].

The paper by Thiayagarajan and Balaji [76] compares Complete Coverage D* and Spiral STC. Together with the paper by Gabriely and Rimon [73] and the paper by Dakulović et al. [74] it is clear that both algorithms do not perform ideally with respect to the quickest path-finding. Spiral STC and Complete Coverage D* cover grounds multiple times increasing operational time. SCCPP discussed by Šelek et al. [75], minimises overlapping areas, but does not ensure all the unknown places are mapped.

6.1.3. JuLiam Algorithm

The drone should find its way through multiple tunnels inside a map. In order to achieve this task successfully, two different routes need to be determined. First, the drone needs to fully explore the map, after which it needs to return home. The former is known as 'full coverage' and the latter as 'shortest path'. Determining these routes requires two very different path-finding philosophies. A navigation algorithm, incorporating both types, called the 'JuLiam' algorithm, is developed for a virtual drone to move around in the environment discussed in subsection 6.1.1.

The main challenge in 'full coverage' mode is for the drone to decide where to go next. In JuLiam this is achieved through 'point-of-interest (PoI) detection'. Points of interest are defined as spots where the drone still 'wants to go'. It identifies these points by checking if the last cell that the LiDAR ray touches is known (or seen) or not. If not, then the point is marked as a PoI.

The clustering algorithm 'DBSCAN' identifies the different groupings of PoI-points. DBSCAN only identifies a group of Pols as clusters if they lie within a certain distance from each other and are more than a certain amount. This distance and amount can be given as input parameters. The centre of mass of each cluster is then calculated and saved as a 'goal'. The drone decides, based on the shortest Euclidian distance, what goal it should navigate towards. Once the drone's LiDAR scanner 'sees' or 'detects' a PoI, the coordinate is 'known' and it is therefore no longer classified as unknown. If no more goals exist, but there are still Pols, the drone will plot a route towards these remaining Pols first before returning home. Home, in this case, is the starting point of the simulation. A snapshot from one of the simulation runs is shown in Figure 6.2. Here the Pols can be seen as blue dots and the goals as green dots. The drone is represented by the red dot.

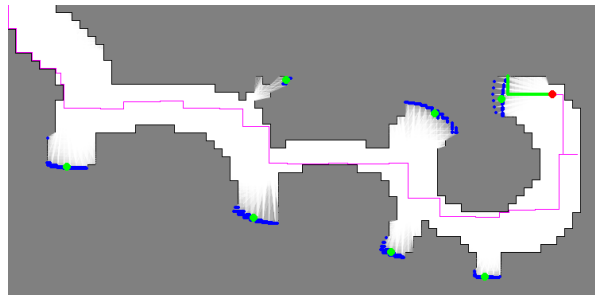
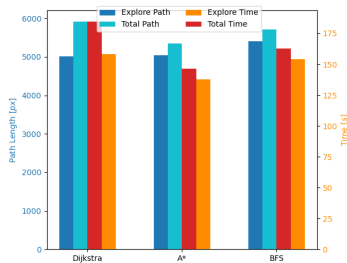


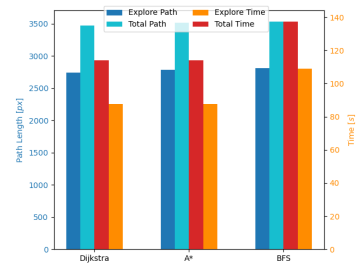
Figure 6.2: Snapshot of the Simulation Showing the Pol's (blue dots) and Goals (green dots)

Finding the best route to a destination (this being either a goal, a Pol or the starting point) is done using any one of the following three path-finding algorithms. These are A* [68], Dijkstra's Algorithm [67] and Breadth-First Search (BFS) [67]. All three aim to find the shortest path between two coordinates in a grid. The A* algorithm considers both distance travelled and remaining distance estimates, Dijkstra gradually explores grid cells based on connectivity. Finally, BFS starts from the starting point and finds the shortest route by exploring all neighbouring cells first.

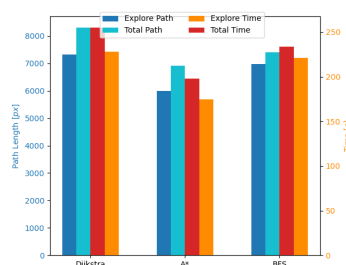
Within the JuLiam navigation program, these three algorithms can be used interchangeably. This way they may be benchmarked against each other in order to find the algorithm most suited to the project's needs. This is done by creating a map with tunnels of varying sizes. The drone must then first explore the entire tunnel system before returning to its start position. This process will be timed and the length of the path taken is measured. This simulation is run for all three algorithms, on three different maps, shown in Figure 6.4. The results of the tests are presented in Figure 6.3. An overview of the workings of the JuLiam algorithm is presented in the form of a decision block diagram in Figure 6.6.



(a) Results for Map 1



(b) Results for Map 2



(c) Results for Map 3

Figure 6.3: Benchmark Test Results

In Figure 6.3 four measurements are shown for each algorithm in each map. The explore path refers to the path length (in cells) of the 'full-coverage' mode. At the end of this path, the drone has no more Pols left. It will then return home, leading to the total path length. In Figure 6.5

the full paths of the three algorithms in map 1 are shown. It is clear from the figures, that all three calculate very different routes. Then the explore time and total time (this works the same as for the path lengths) are shown. For more representative results, all benchmark tests have been performed three times, and the average times are taken. Based on the results from the benchmark tests, the A* algorithm is chosen as the preferred method of calculating the route to the next location for the drone. It consistently scores better on explore and total time, and its path lengths are never the longest.

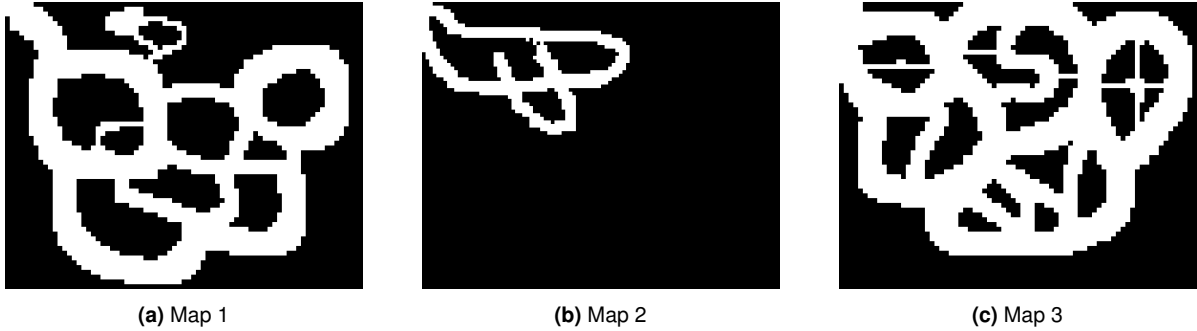


Figure 6.4: The Three Maps used for Benchmarking

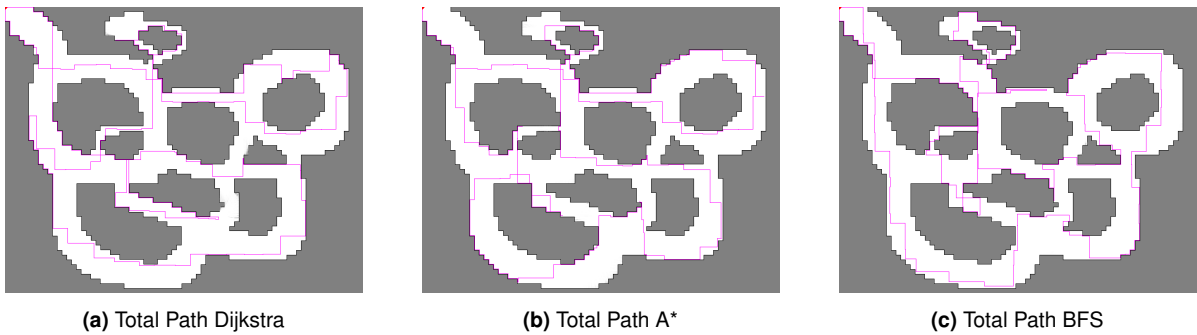


Figure 6.5: Visualisations of the Traversed Paths at Simulation End for Map 1

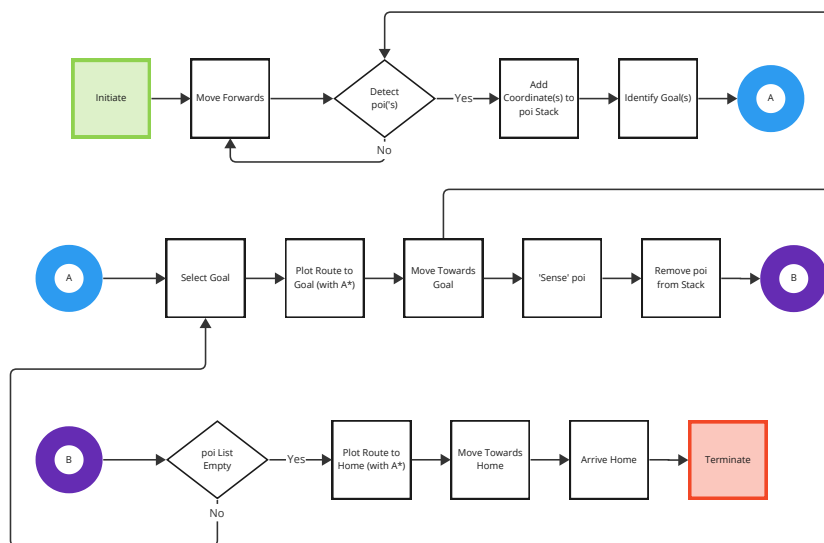


Figure 6.6: Decision Block Diagram for the JuLiam Algorithm

For the use case, the JuLiam algorithm is the best fit as it places points of interest at places it has not been. The points of interest ensure that the drone will visit all unknown spaces. Combined with the A* algorithm, JuLiam also makes sure that it will visit the unknown places in the quickest way by calculating the fastest and most efficient trajectory with the map it knows up until then. Because the drone maps while moving within the debris, it ensures a collision-free path as it takes into account the walls and obstructions on its way. This means that no place is left unseen and the operation time is maintained low making JuLiam the best-fit algorithm for the purpose of the drone. However, the proposed algorithm is solely for a 2D space. Expanding this into a 3D environment, different paths for either driving or flying can be realised. This means that based on the energy consumption of the two, the most efficient path can be determined.

6.1.4. Positioning/Localisation

Position determination for the drone is important for the accuracy of the movement of the drone within the debris so that it ensures a safe, collision-free path. Within the simulation, using this positioning system is unnecessary as it has its own within. However, to understand how the positioning of the drone works, it is explained in this subsection.

Non-visual position determination uses external signal generators such as WiFi or GPS [64]. However, in the use case, these signal generators are not usable. Therefore, non-visual in combination with visual position determination is utilised. With IMU and LiDAR an estimate of the position of the drone is generated while the drone simultaneously generates a map [77]. Also, having the LiDAR and IMU combination, the accuracy of position determination of the drone is increased in the absence of GPS [78].

A method proposed by Kaltenthaler et al. [78] can be used for 3D position estimation of the drone by combining the drone's sensor suite. The paper describes how using the linear acceleration and angular velocity measured by the IMU can be combined with the distance measurements of the LiDAR to obtain a pose, attitude and position, estimation. A similar method was proposed by Hussein et al. [79]. Then, a LiDAR/Inertial-Odometry algorithm was proposed by Fasano et al. [62] as a localisation technique in combination with an Iterative Closest Point (ICP) algorithm to constantly update the position to give an accurate pose estimation. Lastly, Petrlík et al. [77] show that pose estimation with a 2D LiDAR is possible. From these methods and algorithms proposed, it can be concluded that within a 3D space, the drone is able to determine its position using the sensors selected in section 5.1. So, these methods ensure that the JuLiam algorithm can function within the collapsed building.

6.1.5. Collision Handling

In case the navigation system malfunctions and the drone does collide with an obstacle, a recovery strategy should be in place. Assuming either the LiDAR or the proximity sensors still function as expected, it is known which side of the drone has collided with an obstacle. The first reaction should be that the drone moves away from the obstacle if possible. The aim is to move away from the wall according to the requirements (SYS-TC-OP-3-3 and SYS-TC-OP-3-4). If this is not possible, it should position itself the furthest away possible from any obstacle. After it has safely positioned itself, the drone will perform a systems check to ensure all systems are working as they should. If this is the case, the drone should continue its mission and otherwise return to base. Because the drone keeps updating the obstacle map during flight, it is able to handle dynamic environments. This means that it would recognise a moving obstacle and will update the map according to the current position of the obstacle.

6.2. Stability and Control Subsystem

Navigating through confined places requires high manoeuvrability. The stability and control subsystem deals with designing a control algorithm that meets these requirements. It ensures that the drone can reach a desired attitude and position by commanding the rotors according to sensor data. The continuous feedback from the sensors is used to accomplish autonomous flight. The subsystem design process starts with constructing a model for simulating the dynamics of the drone. Then, the control algorithm is designed in subsection 6.2.2, in which previously investigated controllers are combined. The stability is assessed in subsection 6.2.3 by simulating possible scenarios based on the use case. Lastly, implications and remarks are presented in subsection 6.2.4.

6.2.1. Quadcopter Model

A dynamic model that represents drone's open loop response is required to generate rotor inputs for the desired position and attitude. The model aims to simulate the dynamics of the drone in such a way that the outputs of the model can be used in a feedback loop for the controller.

Equations of Motion

A widely used body coordinate system for quadcopters has its x and y -axes oriented along the arms, as shown in Figure 6.7. It should be noted that the z -axis is downwards and the pitch-down motion is taken as positive. The thrust and torque of the rotors are depicted with τ_i, v_i . Rolling $\dot{\phi}$ is achieved by changing the relative speed of the rotors 4-3, similarly pitching $\dot{\theta}$ is achieved by the rotors 2-1 and yaw motion $\dot{\psi}$ is achieved by varying the speeds of the clockwise and counter-clockwise rotor pairs. Parameters u_1, u_2, u_3 and u_4 represent the rotor inputs for the total thrust, rolling, pitching and yawing moments respectively, where l is the distance between the rotors and the centre of mass. They are defined to simplify the notation of the equations of motion and can be shown below in accordance with the body axes system.

$$\begin{aligned} u_1 &= \tau_1 + \tau_2 + \tau_3 + \tau_4 \\ u_2 &= l(\tau_4 - \tau_3) \\ u_3 &= l(\tau_2 - \tau_1) \\ u_4 &= -v_1 - v_2 + v_3 + v_4 \end{aligned} \quad (6.2)$$

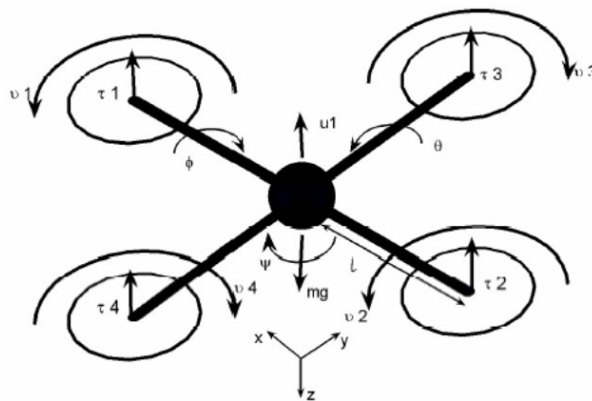


Figure 6.7: Body Axes of an X-Configuration Quadcopter (Cowling et al. [80])

By using a body-to-earth transformation matrix, as described in [80], equations of motion for the translational movement in x , y and z can be derived. These are shown in Equation 6.3,

where $s_\theta = \sin(\theta)$, $c_\theta = \cos(\theta)$, $t_\theta = \tan(\theta)$ with m being the mass and g the gravitational acceleration.

$$\ddot{x} = -\frac{s_\theta c_\phi}{m} u_1, \ddot{y} = \frac{s_\phi}{m} u_1, \ddot{z} = -\frac{c_\theta c_\phi}{m} u_1 + g \quad (6.3)$$

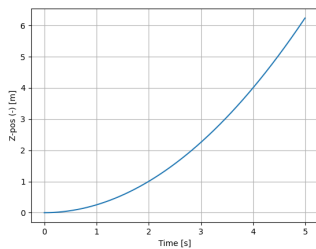
The rotational equations of motion can be derived in a similar way with the same notation by using Euler angles. The moments of inertia are represented with I_{xx} , I_{yy} and I_{zz} .

$$\begin{aligned} \ddot{\phi} &= -\dot{\psi}\dot{\theta} \cdot c_\phi + \frac{c_\psi}{I_{xx}} u_2 - \frac{s_\psi}{I_{yy}} u_3 + \frac{I_{yy} - I_{zz}}{I_{xx}} (\dot{\psi} - \dot{\theta} \cdot s_\phi) \dot{\theta} \cdot c_\phi \\ \ddot{\theta} &= \frac{\dot{\psi}\dot{\phi}}{c_\phi} + \dot{\phi}\dot{\theta} \cdot t_\phi + \frac{s_\psi}{c_\phi I_{xx}} u_2 + \frac{c_\psi}{c_\phi I_{yy}} u_3 - \frac{I_{yy} - I_{zz}}{I_{xx}} (\dot{\psi} - \dot{\theta} \cdot s_\phi) \frac{\dot{\phi}}{c_\phi} \\ \ddot{\psi} &= \dot{\phi}\dot{\psi} \cdot t_\phi + \frac{\dot{\phi}\dot{\theta}}{c_\phi} + \frac{s_\psi t_\phi}{I_{xx}} u_2 + \frac{c_\psi t_\phi}{I_{yy}} u_3 + \frac{1}{I_{zz}} u_4 - \frac{I_{yy} - I_{zz}}{I_{xx}} (\dot{\psi} - \dot{\theta} \cdot s_\phi) \dot{\phi} \cdot t_\phi \end{aligned} \quad (6.4)$$

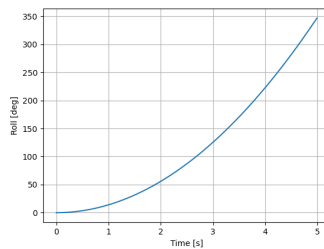
Dynamic Model

The dynamic model represents a system of second-order non-linear differential equations with coupled states. It uses the inputs u_1, u_2, u_3, u_4 and returns the states $x, y, z, \phi, \theta, \psi$ along with their respective rates. As the states are coupled with inputs, using a state space representation is not possible. A considerable amount of work in the literature uses small angle approximations to simplify the equations of motion. However, the drone often flies at angles where this approximation is not realistic any more. Therefore, a non-linear dynamic model is made by discretising the equations of motion in time. It uses the hover condition as the initial condition, in which all states are zero and where $u_1 = mg$. The responses for the vertical ascent, rolling/pitching and yawing motions can be seen in Figure 6.8 with their indicated step rotor inputs. The remaining states for each motion are not shown for conciseness and pitching is not depicted as it is analogous to rolling. The values for the moments of inertia are computed in 3D Experience by using the conceptual Computer-Aided Design (CAD) model by Bergmans et al. [4] with the incorporated changes after the detailed subsystem design.

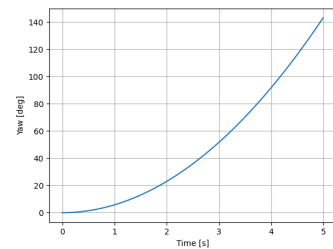
To introduce the first step for the model verification, it is verified that the responses obey Newton's second law in translational and rotational form. A complete verification and validation plan for the relation between the states is detailed in section 12.5. Lastly, it can be seen that the drone has a sensitive response to rotation, this is due to the relatively low inertia values it has.



(a) Ascent Motion with a Step Input of 1 N in Total Thrust Change



(b) Roll Motion with a Step Input of 0.01 N in Differential Thrust



(c) Yaw Motion with a Step Input of 0.001 Nm in Total Torque Change

Figure 6.8: Different Motions simulated by the Model with $m = 2\text{kg}$, $I_{xx} = 0.002\text{kgm}^2$, $I_{yy} = 0.003\text{kgm}^2$, $I_{zz} = 0.005\text{kgm}^2$ and $l = 0.097\text{m}$ (z-axis is inverted to comply with the body coordinate system)

6.2.2. Controller Design

A quadcopter is an inherently unstable system and thus requires a control system to stabilise it. A lot of methods have been investigated to achieve autonomous control and the H_{inf} controller was proposed for the conceptual design, mainly due to its robustness. In a meeting with Dr. IR. Smeur from the Control & Simulation department within the Aerospace Engineering Faculty at TU Delft, additional alternatives were also discussed. A method that is more applicable to the use case has been studied by Mellinger et al. [81], in which a Proportional Integral Derivative (PID) controller enables flying through narrow gaps and performing perching on inverted surfaces. The investigated controller design has been implemented on the manoeuvres shown in Figure 6.9.

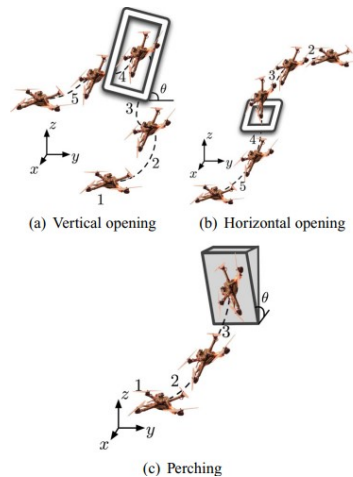


Figure 6.9: The Four Scenarios considered in the Work by Mellinger et al. [81] where θ denotes the Window/Perching Orientation

The controller types investigated by Mellinger et al. can be combined to achieve high manoeuvrability in different conditions. The robustness that was compromised by discarding the H_{inf} controller can be increased by using the Kalman filtering method described in subsection 5.2.3, allowing the controller to still tolerate uncertainties within the sensor data. In order to combine the controllers, it is important to realise that the attitude of the drone does not depend on translational states whereas the translational states depend on the attitude. Thus, the two components can be separated as visualised in Figure 6.10 in accordance with the notation used in equations of motion.

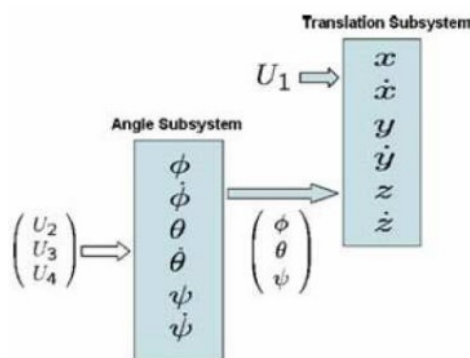


Figure 6.10: Decomposition of the Dynamic Model (Boubdallah [80])

By considering this relation between the states, the outer control loop can be constructed as

shown in Figure 6.11b, where the subscript 'des' depicts the desired parameter, \vec{r} the position vector and w_f the change angular velocity of the rotors to achieve the desired translation in z . This parameter is used to convert the required angular velocity w to the model input u_1 . The working principle of the outer loop can be better understood by detailing each sub-controller, namely the attitude and hover control.

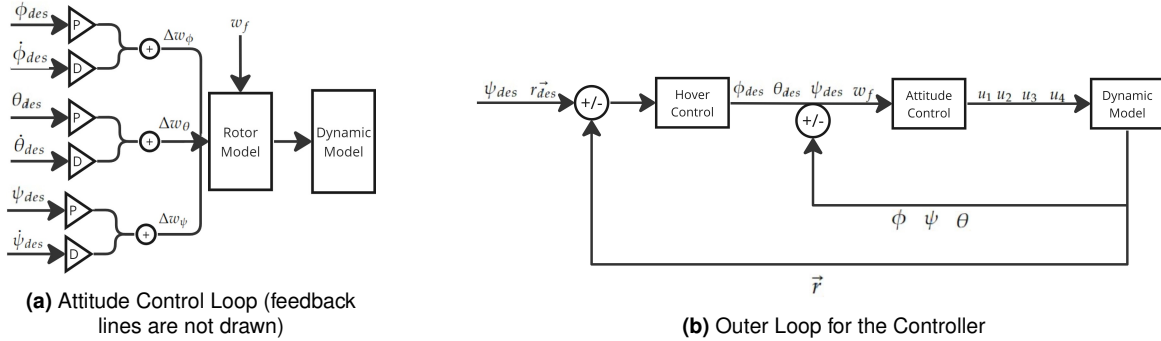


Figure 6.11: Controller Loops of the Outer and Inner Attitude Control Loop

Attitude Control

The purpose of the attitude control, shown in Figure 6.11a, is to reach a desired attitude with a specified angular velocity. For each desired rotational parameter, the P-D control branch takes the form of Equation 6.5 with the gains k_p and k_d . The rotor speeds required to produce rolling, pitching and yawing and the rotor speed w_f to produce a net force along the z axis are linearly combined to get the required angular speed for each rotor. These are fed into the rotor model to convert the angular speeds to the model inputs that were specified in Equation 6.2. The attitude response of the dynamic model is used in a feedback loop to compute the attitude error for each branch.

$$\Delta\omega_\phi = k_{p,\phi} (\phi^{\text{des}} - \phi) + k_{d,\phi} (\dot{p}^{\text{des}} - \dot{p}) \quad (6.5)$$

The most aggressive manoeuvres that the attitude controller can achieve for each angular state without overshooting the 90 degrees in pitch and roll and with enough rise time in a stable way are shown in Figure 6.12. The rotor thrust inputs that were fed into the model for roll and pitch are also shown along with the rotor torque inputs for yaw. The rotors provide the required thrust for roll/pitch and the torque for yaw as expected. The thrust and torque values they converge comply with the hover conditions in which there is no position change in the z -axis as w_f is set to zero. The steady-state value for roll and pitch is 83 degrees and converges approximately at 2.5 seconds. With a slightly higher rise time, the drone can achieve 85 degrees of yaw angle in 3 seconds.

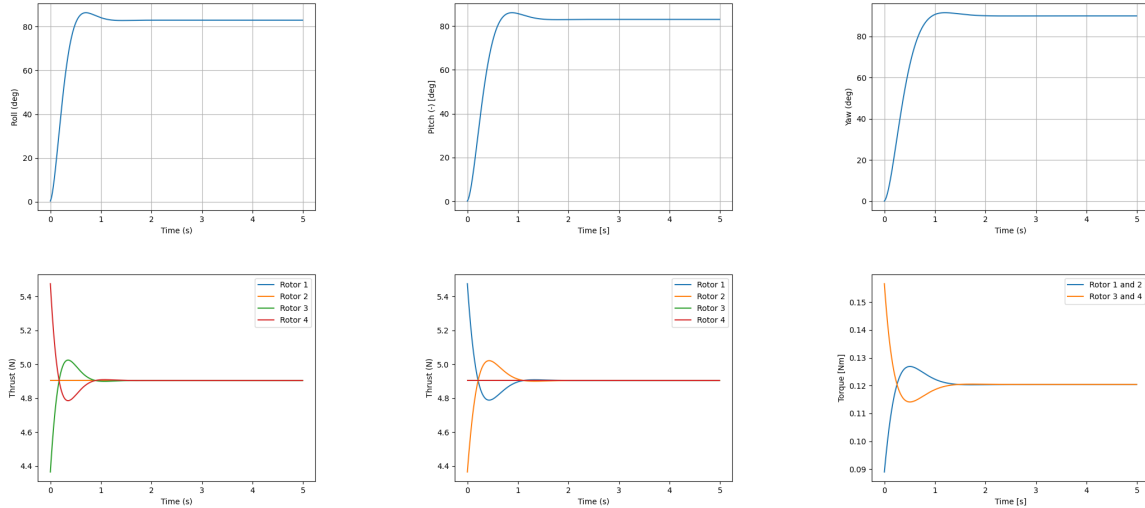


Figure 6.12: The Most Aggressive Attitude Change for Each Angular State (Roll, Pitch and Yaw) with Their Respective Rotor Inputs shown Below (pitch axis is inverted to comply with the body coordinate system) Gains: $k_{p,\phi} = k_{p,\theta} = 350, k_{d,\phi} = 80, k_{d,\theta} = 100, k_{p,\psi} = 800, k_{d,\psi} = 300$

Hover Control

The purpose of the hover control is to reach a desired position and yaw angle with zero and angular linear velocities. It first calculates the commanded acceleration \vec{r}_{des}'' from the position error in PID feedback. This process is done for each translational state i as shown in Equation 6.6 with the gains k_i .

$$\ddot{\mathbf{r}}_i^{des} = k_{p,i} (\mathbf{r}_{i,T} - \mathbf{r}_i) + k_{i,i} \int (\mathbf{r}_{i,T} - \mathbf{r}_i) dt + k_{d,i} (-\dot{\mathbf{r}}_i) \tag{6.6}$$

Translational accelerations are then converted to the required change in angles and the rotor angular velocity w_f to ascent or descent. These are used as input for the attitude control in which the model outputs can also be used to compute the position error in PID feedback control. An overview of this process is depicted in Figure 6.13.

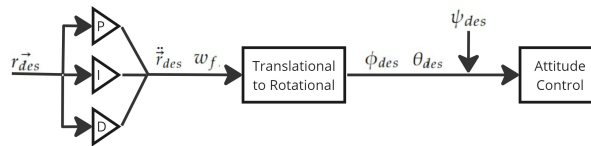


Figure 6.13: Hover Control Loop (feedback lines are depicted in the outer loop)

As investigated in section 6.1, indoor and outdoor navigation require different types of control abilities. The mapping method that was proposed introduces demanding requirements on controllability as the drone frequently navigates its way along the walls and obstacles. Therefore, two sets of gain will be used for the hover control. These are called 'soft' hover control with high proportional gains to achieve low rise time with high steady-state errors, and 'stiff' hover control with high integral/derivative gains to achieve low steady-state errors with high rise time. In accordance with the use case, the drone can use the soft hover control when it finds an opening to manoeuvre towards it in a short time whereas the stiff hover control can be used inside the building to achieve more accurate manoeuvring with longer convergence time. To simulate certain manoeuvres for the use case in chapter 9, limitations of the hover control should be assessed. For the soft control, how fast the drone can fly towards the highest possible range

based on the requirement U-REQ-14 is investigated. For stiff control, transient error around the desired position is investigated to confirm that it is able to move along obstructions with enough clearance from the requirement SYS-TC-OP-3-3. The response for achieving a position of 150 m in each direction with the soft control gains is shown in Figure 6.14. The relative steady-state error is approximately 5 % and the drone achieves this position in 150 seconds. Hence, the average speed is 1.7 m/s when the total displacement vector is considered.

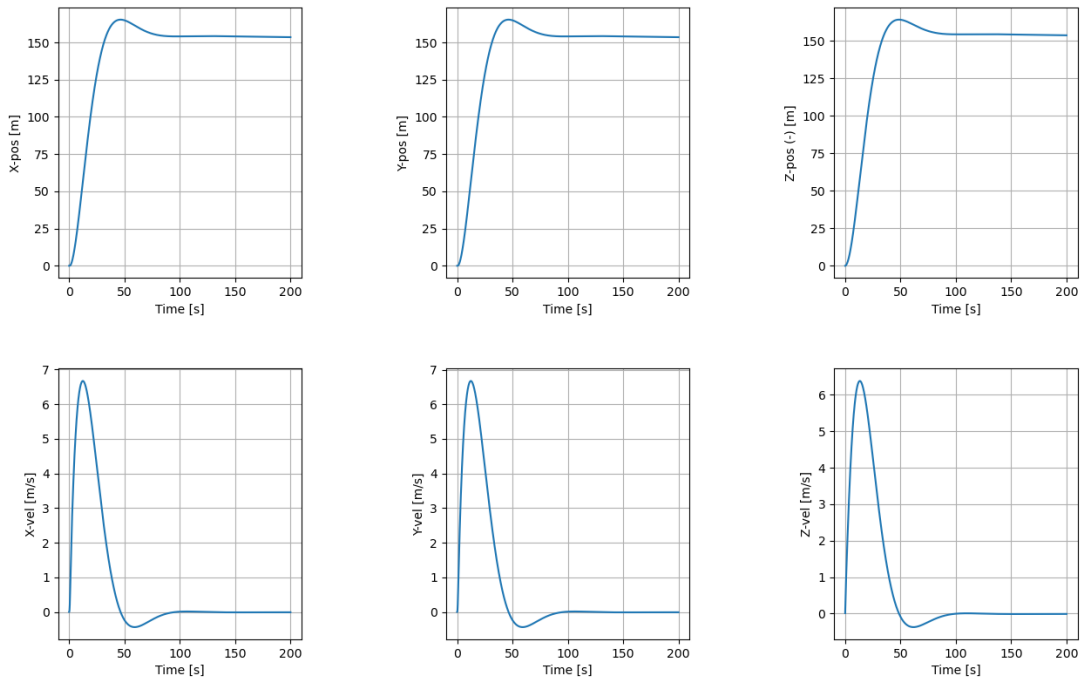


Figure 6.14: Drone moving to a Position of (150,150,150) m in an Unobstructed Area, using the Soft Hover Control (top: position plots, bottom: velocity plots)

The narrowest opening that the drone should pass through is a 40 by 40 cm hole with a clearance of 5 to 10 centimetres. A similar manoeuvre is depicted in the horizontal opening sketch that was shown in Figure 6.9. To simulate the most aggressive manoeuvre in such an opening with a length of 2 m , plots shown in Figure 6.15 are constructed. Also for visualisation, the manoeuvre is depicted in Figure 6.16. The drone can move along the walls with 10 cm clearance in both x and y directions. The gains for the x position state can be made softer without overshooting much, as it is the limiting motion that determines the convergence time for this case. The response is slow but meets the clearance requirement for the narrowest gap.

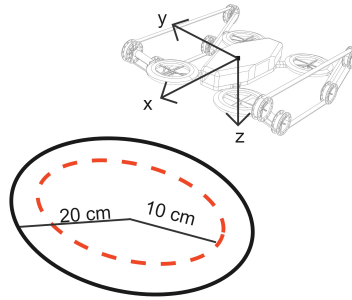


Figure 6.15: Sketch of the *Needle's Eye* Drone moving through a Gap with 2 m Length and 0.2 m Diameter using the Stiff Hover Control with 10 cm Clearance

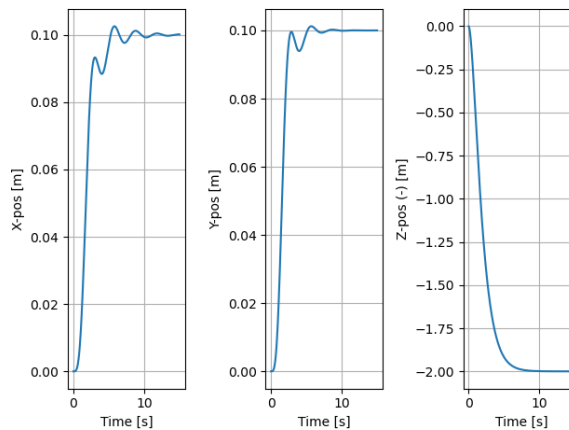


Figure 6.16: Response of a Drone moving through a Gap with 2 m Length and 0.2 m Diameter using the Stiff Hover Control

6.2.3. Stability

The controller types investigated so far don't have permanent oscillations when they are used within their limits. Thus, stability will be assessed based on the drone's reaction when a disturbance occurs. Disturbance rejection of the drone is investigated in three different scenarios: collision, wind gust and rotor failure.

Collision

As the lowest moment of inertia is around the x-axis, the worst-case collision would be an external force applied to rotor 3 or 4. The likeliness of this event is higher when the drone is inside, thus the stiff hover control would be in use. Based on the force analysis that was done in section 4.1, a force of 46.8 N is simulated as an impulse disturbance to rotor 3 in the negative z-direction. However, the drone could not stabilise itself and exceeded the 90 degrees in roll direction within 0.68 seconds. As the rotational deviation is found to be the limiting factor, the highest force that can be applied in such a way was computed by identifying the highest value for the external moment. This force is found to be 22.85 N and the drone's response at this value is shown in Figure 6.17. Due to the low proportional gains of the stiff controller, the response is slow with a convergence time of 15 seconds. However, transient errors are also high as the drone falls 4.5 meters and deviates 6 meters in a negative y-direction before converging to the hover condition.

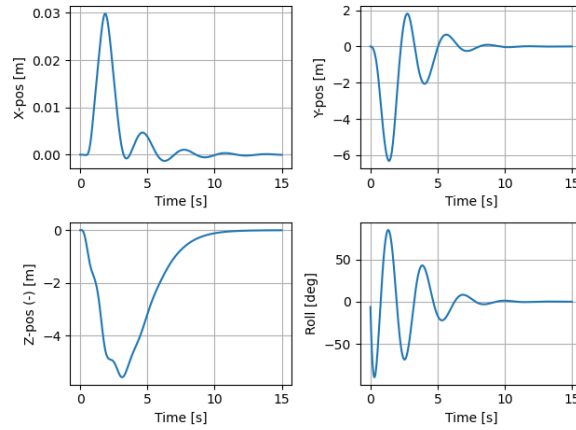


Figure 6.17: Change in Position and Roll after an Impulse Force of 22.85 N is applied to the Rotor 3 in Negative Z-Axis using the Stiff Hover Control

Wind Gust

The effects of wind gusts are prevalent when the drone gets close to the opening or is outside. Thus, the soft hover control would be in use for most of the time. The effects on the thrust of the rotors are more dominant than the drag force considering the small frontal area of the drone. Equation 6.7 is used for assessing the effect of the change in inlet velocity V_0 due to wind gusts. CFD analysis is done in chapter 3 has shown that the exhaust velocity V_e at the design inlet velocity of 1 m/s is 27 m/s. Assuming the exhaust velocity and density of air ρ stays constant, the new thrust due to wind gust can be computed as a ratio when considering the inlet area A is the same. This effect is implemented in the rotor model to simulate a cross-wind of 2 m/s along the positive x and y-axis. Thus, rotors 2 and 4 experience a change of 2 m/s in their inlet velocity.

$$F_T = 0.5\rho A(V_e^2 - V_0^2) \quad (6.7)$$

The positional change manoeuvre in subsection 6.2.2 was repeated with the implemented wind gust. However, the simulation results have resulted in a deflection of 300 meters from the desired 150 meters in each direction. Both the high convergence time and the overshoot have shown that the soft hover control is not able to handle a wind gust of 2 m/s. The same manoeuvre is simulated for the stiff hover control, which has resulted in a response shown in Figure 6.18. The drone is able to move 150 meters in each direction, but the convergence time is near twice the nominal value due to stiff control being in use. It deflects 20 meters in the x-direction and 5 meters in the y-direction from the desired position. Thus, steady-state errors should be considered carefully even when the stiff control is in use during cross-wind.

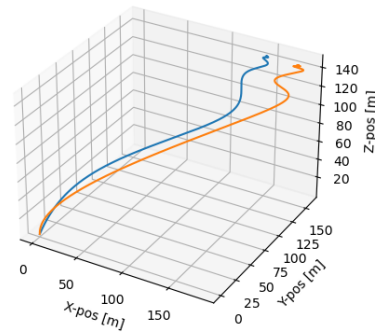


Figure 6.18: Drone moving to a Position of $150 \times 150 \times 150$ m using the Stiff Hover Control with a Cross-Wind of 2 m/s towards the Positive X and Y-Axes Blue: Nominal, Orange: with Crosswind

Rotor Failure

To achieve full control authority, having four rotors is a minimum requirement for drones without any tilting mechanisms. Therefore, the current design of the drone does not introduce any redundancies for rotor failure as it is a quadcopter. A decrease in efficiency is implemented in the rotor model for rotor 1 to simulate a partial rotor failure. This has shown that the soft hover control is not able to tolerate a partial rotor failure, whereas the stiff control has shown the response shown in Figure 6.19. The drone moves 15 meters in the x-axis direction as the opposite rotor (which is rotor 2) provides excessive thrust due to the failure and thus creates a pitch forward motion. With high oscillation around the y-axis, the drone lands from 20 meters altitude after the failure with an impact of 2.5 m/s as it overshoots the 20 meters. A full fault-tolerant control method is investigated by a PhD candidate Sihao Sun from TU Delft in [82], by implementing nonlinear control methods.

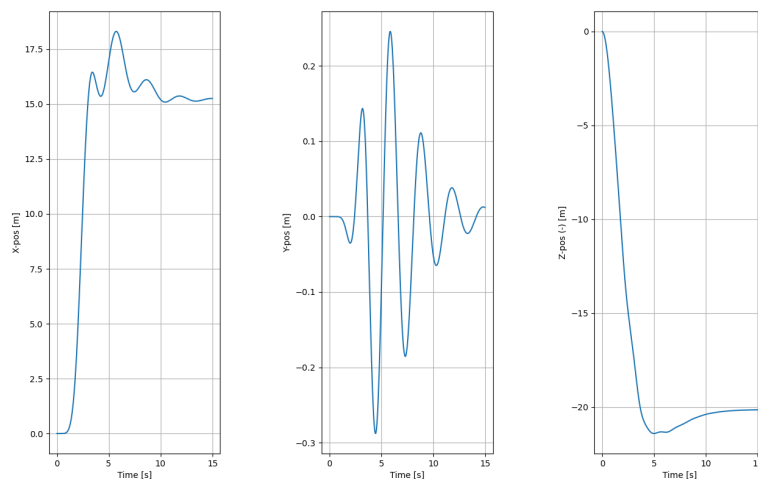


Figure 6.19: Position Change when hovering at 20 m after a Decrease of 0.5 in Percentage Efficiency for Rotor 1 (using the Stiff Control)

6.2.4. Implications and Remarks

The primary purpose of the proposed control subsystem was to generate the required rotor inputs based on a specified position and attitude. This trajectory-tracking method is designed

by combining different controllers in literature and by constructing a non-linear model for the drone. The proposed method allows one to fly autonomously and react to disturbances. Final remarks should be given for the first iteration of the stability and control subsystem as it's a crucial aspect for a drone with such mass and size. Firstly, compliance with the requirements will be addressed along with any additional requirements introduced by the stability and control subsystem. Then, the implications of the results for each control block and manoeuvre will be described. Lastly, final remarks will be presented for the complete stability and control subsystem.

The stability and control subsystem design has accomplished most of the manoeuvrability and operational requirements, as well as introduced additional requirements. Table 6.1 is constructed to confirm that the propulsion subsystem parameters are sufficient for the required rotor inputs. Required rotor performance in stable flight is presented for the limiting case for each manoeuvre. It was confirmed that the drone can have a stable flight with the required average speed, as investigated in the soft hover control. The required roll and pitch rates were accomplished in the attitude change manoeuvre. The yaw rate requirement could not be met due to the higher value for the moment of inertia in the z-direction. It is worth noting that the simulation takes the position as its input rather than the speed or rotation rate of the drone. Thus, the highest instantaneous speed for each manoeuvre is also presented in both translational and angular direction. These are deduced from the velocity plots as shown in Figure 6.14 and can be used to create new requirements on flight loads. The highest required value for the thrust is 13 N in case a collision occurs. Therefore, the current rotor performance parameters from chapter 3 only meet the required thrust/torque values for the nominal manoeuvres and the wind gust disturbance. A rotor with higher performance is needed to handle the collision and rotor failure disturbances. The highest possibility of the drone tumbling is when a rotor failure occurs as it acquires a roll/pitch rate of 100 deg/s from the hover condition. The drone can meet the positional change requirement with an instantaneous speed of 11 m/s and the inside manoeuvring requirement for the narrowest gap.

Table 6.1: Results of the Limiting Case for Each Manoeuvre Type showing the Maximum required Rotor Inputs along with Drone's Maximum Instantaneous Translational/Angular Speed

Manoeuvre	Max. Rotor Thrust [N]	Max. Rotor Torque [Nm]	Max. Speed
Attitude Change	5.5	0.16	120 [deg/s] in ϕ and θ
Positional Change	5.9	0.15	11 [m/s]
Narrowest Gap	4.9	0.13	0.7 [m/s], 0.6 [deg/s] in ϕ and θ
Collision	13	0.33	4.0 [m/s], 50 [deg/s] in ϕ and θ
Positional Change with Wind Gust	5.7	0.14	2 [m/s], 11 [deg/s] in ϕ and θ
Rotor Failure	9.0	0.23	7.2 [m/s], 100 [deg/s] in ϕ and θ

The attitude controller has shown that the drone is able to turn 83 degrees in each direction at once within 3 seconds. The soft hover control was able to command the rotors such that it reaches 150 meters in each direction within 150 seconds. The stiff hover control was able to simulate manoeuvring through a gap of 40 by 40 centimetres with a clearance of 10 centimetres within 12 seconds. However, it is important to realise that the simulation demonstrates the movement of the centre. Thus, the complete architecture should be implemented especially for simulations in obstructed areas.

Scenarios for assessing the stability have shown that the highest collision force that can be applied along the worst-case direction is 22 N . This implies that the drone can fail in stability before failing structurally if the impact force is applied vertically on one of the rotors. However, the collision force would not be higher than 10 N when considering the maximum speed value for the inside manoeuvres. The wind gust simulation has shown that the drone fails to stabilise

when using the soft hover control but achieves the positional change manoeuvre with half of the required average velocity. Finally, in the rotor failure simulation, it is found that even a partial rotor failure would be catastrophic for the inside manoeuvres as the drone moves 18 meters in the direction of the failed rotor. If it's in an unobstructed area, however, it is able to land from 20 meters with an impact force that can be tolerated structurally (considering an impact time of 0.1 seconds and a mass of 2 kg for the landing velocity found). If the proposed non-linear control methods designed by Sihao Sun [82] is implemented, the delay of the data handling subsystem to switch to the relevant controller should be considered. The reaction time to counteract a disturbance is critical, especially for a complete rotor failure. These results of each motion are summarised in Table 6.2.

Table 6.2: Achieved Motion for Every Manoeuvre Simulated

Manoeuvre	Achieved Motion
Positional Change (Soft)	Average speed 1.7 m/s
Attitude Change	Average roll/pitch rate 33 deg/s and average yaw rate 28 deg/s
Narrowest Gap (Stiff)	Average speed 0.2m/s with a clearance of 0.1 m
Collision (Stiff)	Stabilised to hover condition deflecting 6 m laterally, 5 m in altitude, 50 deg in roll
Wind Gust (Stiff)	Positional change manoeuvre with average speed 0.85 m/s, deflecting 20 m from the desired position
Partial Rotor Failure (Stiff)	Land with 2.5 m/s deflecting 15 m in the direction of the failed rotor

In a real flight, sensor outputs for the angular rates will also be used in a feedback loop along with the dynamic model. These not only help reduce the input errors but also the model errors by constantly comparing the model to the real response from the sensors. Incorporated sensors, namely gyroscope and accelerometer, 'feed-back' the angular rates to the inputs of attitude control and the translational accelerations to the inputs of hover control. Moreover, the actual rotor outputs can also be used in a feedback loop to assess the discrepancy between the generated and the actual response of the rotors. As a final remark, it should be realised that the data handling subsystem should be able to switch to the stiff hover control gains when needed. If the soft hover control would be in use when the drone is traversing with the tracks, flying through a narrow gap or is subjected to a cross-wind of 2 m/s catastrophic failures would occur.

Communication

In this chapter, the communications subsystem is looked at in detail. Section 7.1 will outline the general concept and approach of the system, for which the components are selected in section 7.2. Then, in section 7.3 the process of data transmission is outlined and the link budgets are presented. The limitations of the communications subsystem are examined in section 7.4 and in section 7.5 the communication flow diagram is shown.

7.1. Concept

The communications subsystem forms the link between the operator and the drone. Not only does it relay the control inputs of the operator, but it also returns telemetry, visual and LiDAR mapping data. It is imperative that this link is stable for data to be sent. However, as the *Needle's Eye* drone does not operate in line of sight of the operator, complications arise.

A meeting was set up with Erik van der Horst, from the Control & Simulation department within the Aerospace Engineering faculty at Delft University of Technology. He explained that, once a drone enters a collapsed building, there is a high chance that the building will start acting like a Faraday cage. In other terms, it will become difficult for signals to enter or exit the building once the drone is operating outside of the operator's line of sight. This is especially true for higher frequencies.

To combat this significant challenge, lower frequencies will be used, as they penetrate walls better. However, there is a limitation to this as higher bitrate transfers are only possible on higher frequencies [4]. Combining all of this, a frequency of 2.4 GHz is chosen for the visual data. It has a significant range advantage over 5.8 GHz, the standard video frequency, whilst it is still able to transfer video data.

For telemetry, mapping data and Remote Control (R/C), the 868 MHz frequency is selected. It penetrates walls much more effectively than 2.4 GHz (the standard telemetry and R/C frequency). Comparing it to 433 MHz it is found that it is a lot less crowded and thus less prone to interference from other transmitters. 433 MHz also features a bandwidth too small for mapping data transmissions. A visual overview of the drone's wireless communication links is provided in Figure 7.1.

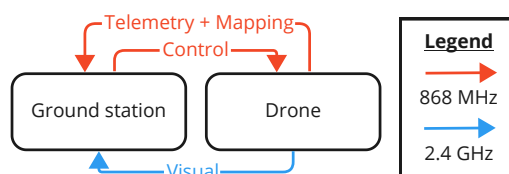


Figure 7.1: Data Transmission over Two Separate Frequency Links

7.2. Component Selection

In the previous section, the frequencies that the communication system will be operating at have been established. For telemetry, mapping data and R/C, the first antenna (band A) will be

using 868 MHz. The second antenna (band B), used for the transmission of visual data, uses 2.4 GHz. For this to work the drone will need to have a transceiver (band A), a transmitter (band B) and two antennas. The components for the lower frequency band will be selected in subsection 7.2.1 and in subsection 7.2.2 the higher frequency parts are chosen. Finally, in subsection 7.2.3 an overview of all chosen components is provided.

7.2.1. 868 MHz

As has been stated previously, the 868 MHz frequency is used for both telemetry and mapping data, drone to the base station, and R/C, base station to the drone. For this to be possible, the drone must have a transceiver. Three such transceivers, operating at 868 MHz, are considered. Relevant data about these transceivers is shown in Table 7.1.

Table 7.1: 868 MHz Transceiver Data

Transceiver	Cost [€]	Size [mm]	Protocol	Sensitivity [dBm]	IIP3 [dBm]
Semtech SX1276 [83]	13.39	28x20	LoRa	-148	-11
HopeRF RFM95M [84]	9.00	16x16	LoRa	-148	-12.5
HC-12 [85]	8.00	27.4x13.2	JY-MCU	-117	?

Comparing these three transceivers, the HopeRF RFM95M is the best-fit option. It is the smallest of the three and has the best IIP3¹ rating. Furthermore, it uses the highly compatible LoRa protocol. Next, an antenna that is compatible with this transceiver needs to be selected. Four such antennas are considered, their data is shown in Table 7.2.

Table 7.2: 868 MHz Antenna Data

Antenna	Type	Size [mm]	Weight [g]	Cost [€]	Polarisation	Gain [dBi]
SMP.868.35.6.A.02 [86]	Patch	35x35x6	34.3	25.13	RHCP	2
TL.08.C.0112 [87]	Whip	7x7x35	7	10.35	Linear	0.1
IS.04.B.301111 [88]	Puk	49x49x29	125	82.79	Linear	2
APAE868R2540JBDB2-T [89]	Patch	25x25x4	9	5.02	RHCP	-1.37

One of the most important factors for the decision to be made is the polarization. Two linear and two circular antennas are shown. As discussed in the *Midterm Report* [4] a circularly polarised antenna is preferred for the *Needle's Eye* use case. As such the two linear antennas are disregarded. The two remaining antennas are patch antennas, these are very space efficient. One is significantly smaller and cheaper, however, as its gain is negative, the decision is made to go with the SMP.868.35.6.A.02 antenna.

7.2.2. 2.4 GHz

Visual data is transmitted using the 2.4 GHz band. As no data will be sent to the drone on this frequency only a transmitter is needed on the drone. Three relevant transmitters are considered and their information is presented in Table 7.3.

Table 7.3: 2.4 GHz Transmitter Data

Transmitter	Cost [€]	Weight [g]	Size [mm]	Power [mW]
FuriousFPV VTX Stealth Long Range [90]	56.12	8.5	38.2x24.8x9	10 or 25 or 200 or 500 or 800
ImmersionRC 2.4GHz 700mW [91]	71.82	22	57x23x12	700
TBS Unify 2G4 800mW 16ch 2.4GHz A/V Transmitter [92]	96.68	14.4	37x26x8	500 or 800

¹IIP3 refers to the third order intercept point. It is a value that describes the dynamic range of the receiver and transmitter.

The most important parameters for the transmitter selection are the output power and size of the part. The ImmersionRC transmitter is rather large and as such, will not be chosen. The fact that the FuriousFPV transmitter can switch between so many different power levels is seen as an essential feature. Different countries come with different regulations as to what power may be outputted by a transmitting antenna. This ability to switch power output can greatly increase the useability of the drone. Therefore, the FuriousFPV VTx Stealth Long Range is selected for the drone. For the base station, the receiver chosen is the companion of the selected transmitter from FuriousFPV, the True-D 2.4 GHz Rx. Now, the corresponding antenna will be chosen. Three 2.4 GHz antennas are looked at. Their information is found in Table 7.4.

Table 7.4: 2.4 GHz Antenna Data

Antenna	Type	Size [mm]	Weight [g]	Cost [€]	Polarisation	Gain [dBi]
FuriousFPV Two Slice Patch Antenna 2.4 GHz [93]	Patch	70x70x6.5	21.5	19.90	RHCP	8.6
Flytron 2.4 GHz 11dB LHCP Patch Antenna [94]	Patch	80x80x20	35	11.90	LHCP	11
Menace RC Numskull 2.4 GHz Patch Antenna [95]	Patch	80x73x20	32	36	RHCP	8

All three antennas considered are patch antennas, due to their space efficiency. However, from the table, it is clear that the first option, the FuriousFPV Two Slice Patch is a bit smaller than the other two. It also features decent gain and is not the most expensive option. Therefore, it is chosen as the antenna to be fitted on the drone and the base station.

7.2.3. Component Overview

A table with the final components, their weight, maximum power draw and cost is given in Table 7.5. Here, the components are given for both the drone and the base station. For the base station, however, both the weight and maximum power draw are not provided as these are beyond the scope of this project. They will be determined in further development.

The total cost of the communications system is estimated to come down to 277.55 euros. Next to that, the total weight of the communication subsystem on the side of the drone is 67.40 g. Lastly, the max power draw on the drone's side of the subsystem is 1.196 W. This means that SYS-CO-1-1-3, SYS-TC-COM-5 and SYS-TC-COM-6 are all passed.

Table 7.5: Overview of Communication Subsystem Components & Properties

Component	Type	Channel	Weight [g]	Max. Power Draw [W]	Cost [€]
Drone					
HopeRF RFM95M	Transceiver	A	3.1	0.396	9
SMP.868.35.6.A.02	Antenna	A	34.3	-	25.13
FuriousFPV VTX Stealth Long Range	Transmitter	B	8.5	0.8	56.5
FuriousFPV Two Slice Patch Antenna 2.4 GHz	Antenna	B	21.5	-	19.90
Drone Total			67.40	1.196	110.53
Base Station					
HopeRF RFM95M	Transceiver	A	-	-	9
SMP.868.35.6.A.02	Antenna	A	-	-	25.13
FuriousFPV True-D 2.4 GHz Rx	Receiver	B	-	-	112.99
FuriousFPV Two Slice Patch Antenna 2.4 GHz	Antenna	B	-	-	19.90
Base Station Total			-	-	167.02
Grand Total			-	-	277.55

7.3. Data Transmission and Link Budget

All data gathered by the sensors of the drone will have to be processed and transmitted. Due to the possible weak wireless connection between the drone and the ground station, once the drone has entered the building, only relevant data will be transmitted wirelessly. Three cases can be distinguished within communication between the drone and the ground station. What data will be transmitted, is explained in Table 7.6.

Table 7.6: Data Transmission in Different Cases of Connection between the Drone and Ground Station

Case number	Case	Data transmitted			
		Visual	Mapping	Telemetry	Control
1	A 2.4 GHz connection can be established	X	X	X	X
2	The drone loses the 2.4 GHz connection, but maintains the 868 GHz connection		X	X	
3	The drone loses all connection to the ground station				

Creating a link budget helps in analysing the feasibility of data transmission via the established connections. For both frequencies, the link budget is given in Table 7.7. It provides an overview of the available power to transmit data over a given distance. Tx and Rx refer to the transmitter and receiver, respectively. The transmitted equivalent isotropic radiated power $EIRP$, the free space loss L_F , the Rx power P_R and excess margin P_m are calculated using Equation 7.1, Equation 7.2, Equation 7.3 and Equation 7.4 respectively, which were found in literature [96]. Receiver sensitivity P_s represents the minimum power level at which a receiver can detect and correctly demodulate a signal. This is measured in decibel milliwatts, dBm which is a logarithmic scale. This means the more negative the value, the less power it needs to receive to correctly process the signal. The excess margin P_m is the power available to transmit extra data. It should be noted that all types of losses besides L_F and signal noise are not considered in the link budget, as estimating those would require extensive system testing and in-depth analysis, which is beyond the scope of this project.

Table 7.7: Linkbudget for both Frequencies

Parameter	868 MHz	2.4 GHz	Unit
Bandwidth (B)	3	83.5	MHz
Distance (d)	150	150	m
Tx power (P_T)	25	100	mW
	13.98	20	dBm
Tx antenna gain (G_T)	2.17	6.2	dBi
Tx EIRP ($EIRP$)	16.15	28.6	dBm
Free space loss (L_F)	74.74	83.58	dB
Rx antenna gain (G_R)	2.17	8.6	dBi
Rx power (P_R)	-56.42	-46.38	dBm
Receiver sensitivity (P_S)	-148	-106	dBm
Excess margin (P_m)	91.58	59.62	dB

$$EIRP = G_T + P_T \quad (7.1)$$

$$L_F = 92.45 + 20 \log f + 20 \log d \quad (7.2)$$

$$P_R = EIRP - L_F + G_R \quad (7.3)$$

$$P_m = P_R - P_S \quad (7.4)$$

The value of B in Table 7.7 is based on the difference between the minimum and maximum used frequency around an 868 MHz and 2.4 GHz signal. Then d is the estimated range that the signal will have to travel during a mission. All P_T , G_T , G_R and P_S are characteristics of the selected transceiver and antennas. The unit DBi indicates the forward gain of an antenna, compared to an antenna transmitting an omnidirectional signal. A positive value indicates this antenna is able to focus its power if directed correctly, increasing the effective transmitted power. The remaining values are calculated according to the formulas provided. The excess margin in the link budget indicates that the transmitted signal will be received correctly over the chosen distance of 150 m. However, as stated previously, other types of losses, such as obstacles in the signal propagation path have not been taken into account. This means that

this budget provides a first estimate of the feasibility of signal transmission during the mission, but this will need to be revised in a later design stage.

The transceiver for the 868 MHz band does not compress data. However, it may be provided with compressed data by the VOXL Flight. This way, data is transmitted more efficiently. A so-called Deflate algorithm will be used for compressing the telemetry and map data. This lossless compression algorithm yields a compression ratio of 4.666 according to Alakuijala et al. [97]. It is therefore highly suitable for the *Needle's Eye* use case. The data will be decompressed on the receiver side in order to process the data.

7.4. Limitations of the Communication System

As previously mentioned, maintaining a stable connection whilst inside the collapsed structure is one of the main challenges for the design of the communications subsystem of the SAR drone. A number of factors play an important role here. The most important factor is the signal degradation through walls. Multi-path interference could be another serious concern, however, as stated in the *Midterm Report* [4], circularly polarised antennas were selected to minimise these effects.

In a SAR mission, the range of the drone's communication systems is heavily dependent on the amount of debris the signals need to go through. Multiple walls may be stacked on top of each other due to the collapse. Investigating the effects of this phenomenon is crucial to understanding the limits of the communication subsystem.

The paper by Carlofelice et al. [98] provides insights into the path losses inside collapsed buildings. The paper describes placing 868 MHz transmitters at different distances inside collapsed buildings and then measuring the average path losses. Path losses are heavily dependent on the exact environment and layout of the test sight. This study, however, can serve as a starting point for predicting the behaviour of the *Needle's Eye* communications system. An overview of the results from the paper is plotted in Figure 7.2a.

Looking at the figure it is clear that the deeper inside the structure, the higher the (average) path loss. The paper by Carlofelice et al. [98] uses linearly polarised antennas instead of the circular ones used by the *Needle's Eye* drone. These antenna types behave differently when interacting with collapsed structures. Linear antennas have the benefit that they penetrate better through walls, however, they do not have the resistance to multi-path interference that circular antennas have. Therefore, the *Needle's Eye* antennas will, when considering wall penetration, perform slightly worse than is shown in the graphs.

Another way of analysing signal behaviour through walls is presented in the papers by Bobkov et al. [99] and Ali-Rantala et al. [100]. In these works, data is provided on how the received signal strength is impacted by passing through a variable amount of walls or floors². The relevant datasets have been combined into Figure 7.2b. From the figure, it is clear that every wall that the signal has to pass through causes the signal strength to decrease.

It may be noted that the 2.4 GHz signal behaves rather differently from the 868 MHz signal. Whilst the exact reason is not verified, it is assumed to be caused by the difference in the conducted experiments. The 868 MHz data is generated with equal wall spacing in the Bobkov et al. paper, whereas the 2.4 GHz data is found from a variable wall spacing, provided by the Ali-Rantala et al. paper. Another interesting observation is the behaviour of the 868 MHz signal. From the data, it seems that from four walls onwards, the signal strength does not decrease any more. This is not realistic and likely there is an unknown factor at play here.

²For simplicity's sake in this analysis a floor and wall are seen as comparable obstructions

Finally, a study performed by Stone [101] shows how different frequencies propagate through different kinds of walls. For this analysis, concrete walls are taken as a reference point. Two figures, taken from the report³, are shown in Figure 7.3. Figure 7.3a shows the signal attenuation for different wall thicknesses (C14 is 10.2 cm, C18 is 20.3 cm and C112 is 30.5 cm) for the frequencies between 0.5 and 2 GHz. Figure 7.3b shows this for the frequencies between 3 and 8 GHz. From these figures, it can be seen that, for a signal at 868 MHz, such as band A for the *Needle's Eye* communications subsystem, the signal would lose about 35 dB in signal strength when passing through a 30.5 cm thick wall. It is important to note that the way the signal propagates through walls is extremely dependent on the wall type and material. As stated in section 7.1 there is a high probability of a collapsed building acting as a Faraday cage. This would inhibit signals from entering or exiting the building altogether.

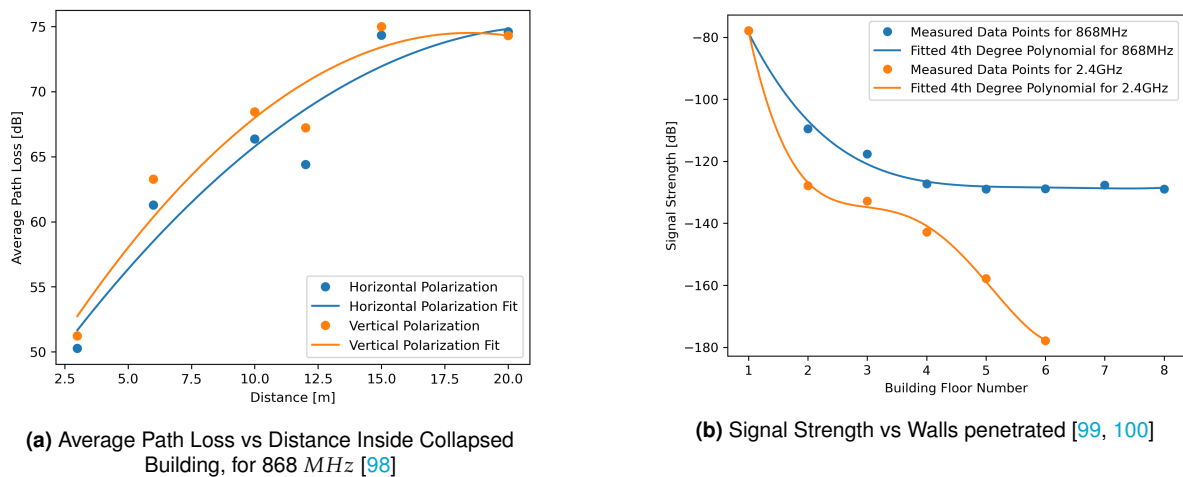


Figure 7.2: Signal Behaviour Data from Literature

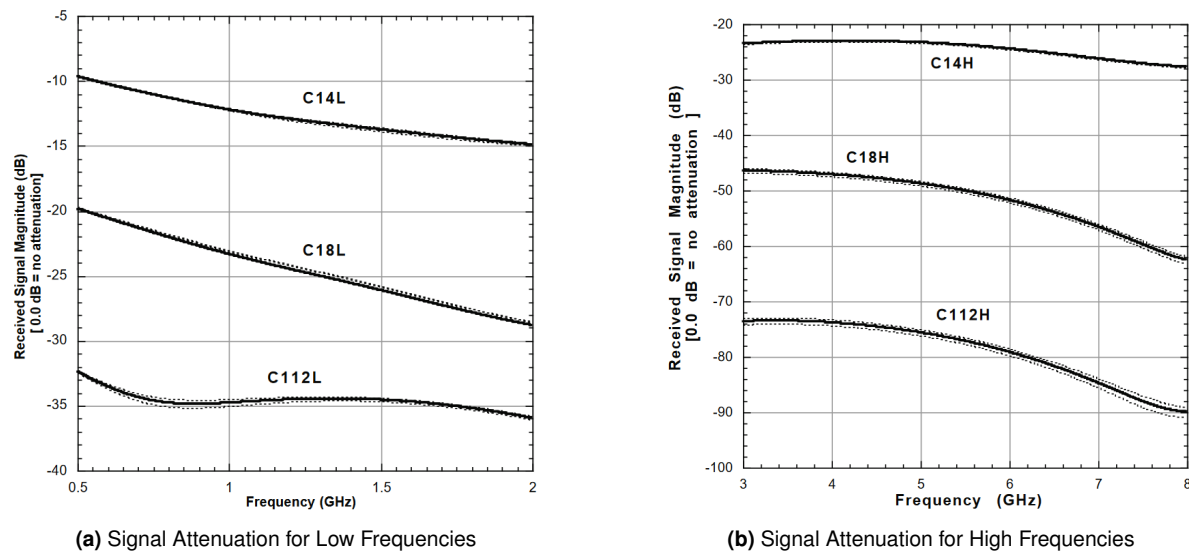


Figure 7.3: Signal Attenuation of Different Frequencies when Propagating Through a Single Plain Concrete Wall with Different Thicknesses [101]

From Figure 7.2b it can be concluded that signal attenuation is not linear and thus adding multiple walls in succession will not lead to a linear decrease in signal strength. This conclusion

³The wall type from the figures is 'plain concrete: batch 1 mix'

station does not receive a stable video feed from the drone over the 2.4 GHz frequency, it will send a message over the 868 MHz band. This message will contain the order to switch to autonomous mode. The drone will explore the structure on its own. The video feed will still be sent, as occasionally some footage may come through. Once the base station detects that it has received a stable video feed for at least ten seconds, the operator can choose whether to take back control or not. This is, again, achieved through sending a message over the 868 MHz band. The threshold for the stable video feed has been established as follows:

Parameter	Value	Unit
Frame rate f	10	fps
Resolution R (width R_w x height R_h)	480 x 360	p
Bit-depth D_b	4	-

Table 7.8: Minimum Signal Quality Threshold

$$b = f * R_w * R_h * D_b \quad (7.5)$$

The minimum bitrate can be calculated according to Equation 7.5. Where b denotes the required minimum bitrate. This results in a minimum required bitrate of 6,912 kbps for the video feed signal to aid the operator in navigation and victim identification. In Table 7.8 the minimum value for f is based on research by Stone [102], which showed that 10 fps is the minimum frame rate to prevent additional stress for the operator. The values for R and D_b are based on a subjective assessment of visual quality to identify obstructions and victims.

The final topic to be discussed in this chapter is transferring the drone's sensor data to the base station. This is done via an external SD card in the drone, where all data will be saved. It can be inserted into a computer and then the data can be analysed by the operator.

Drone Design

This chapter provides insights into the final configuration of the drone design, assesses its feasibility based on requirements, and addresses potential risks associated with its operation. section 8.1 describes the final configuration of the drone design, including the placement of components and the rationale behind the design choices. In section 8.2, an overview of the hardware and software itself and how they interface is given. An outline of the mass and cost budgets of the drone is presented in section 8.3. In section 8.4 highlights the requirements that are met as well as the requirements that still need verification or are not met, providing explanations for discrepancies. Lastly, in section 8.5 risks related to drone operation are described and a risk map is presented. Mitigation strategies are proposed to address critical risks, and an updated risk map is provided.

8.1. Configuration

Based on all design choices explained in the previous sections, a render has been created to visualise the final configuration of the drone design. As can be seen in Figure 8.1a. The drone consists of a rectangular body with rounded sides, fitted around the battery and part of the sensors. The bottom layer of the body houses the battery and a set of components, as indicated in Figure 8.1b. The battery is separated from the thermal layer by an aluminium plate. The thermal layer is included between the battery and the VOXL Flight, to dissipate the heat generated by those components, as can be seen in Figure 8.1c. Both the 868 MHz and the 2.4GHz antenna, as well as all cameras, are positioned on the outside of the body to optimise performance. Each track is connected to one motor, at the upper backside, to provide the torque needed for propulsion while driving. It was chosen to mount the motors on the backside to partly counteract the weight of the sensors on the front side of the drone. The optical camera, thermal camera and lights are located on a connective arc between the two rods at the front side to prevent obstructing the view of the LiDAR located on top of the body. They have been positioned in a way that they are still protected by the tracks. The distance sensors are located on each side of the drone to assist the LiDAR sensors with collision avoidance, except for the bottom of the drone, as the tracks will ensure a minimum distance from the drone to the ground.

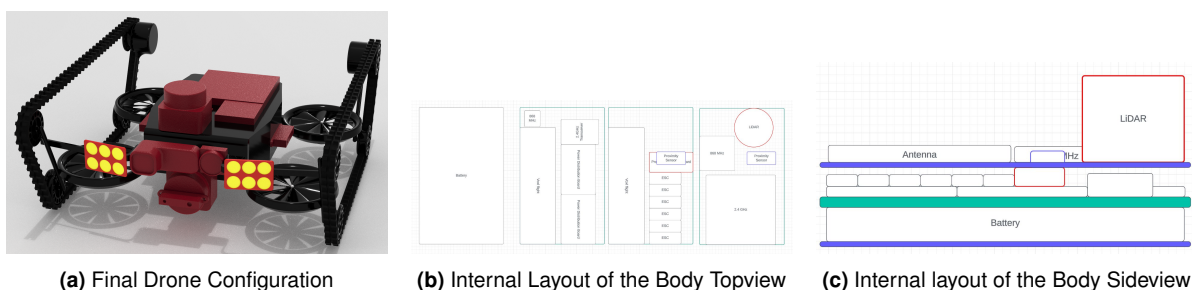


Figure 8.1: External and Internal Layout of the Drone

Each ducted fan is fitted directly to the body, to minimise the width of the drone. There is a

possibility of integrating them more closely together, mounting the body on top of the outside of the fans, but as this would decrease aerodynamic performance by blocking the incoming airflow, this option was disregarded. However, the rods supporting the tracks are integrated into the duct of the motor. The reason for this is the improvement of structural integrity, as the rods are only 4 *mm* in diameter, meaning a connection of that size between the duct and the rod would be more fragile as well as it would increase the width of the drone. Each ducted fan consists of a duct with a 60 *mm* diameter fan with nine GOE 450 airfoil blades and a motor.

The stability and controllability of the drone, as elaborated upon in chapter 6, are based on a spacing of 100 *mm* between the centre of gravity of the drone and the middle part of the fans. To comply with the results of this analysis, the fans have been positioned outside a radius of 100 *mm* from the centre of gravity. The final dimensions of the drone are 28.2 *cm* x 25.7 *cm* x 10.9 *cm* (l x w x h). This means that the drone fits within requirement SYS-TC-STRC-3 dictating its maximum size.

8.2. Hardware and Software Overview

The software that the drone uses during operations can be divided into three categories: handling sensor input, communication and flight control. Handling sensor input starts by processing the raw data from the sensors using a Kalman filter. This processed data can then be used to create a 3D map of the environment, detect obstacles and victims. Additionally from the sensor data and checks performed by the flight control system, the drone is able to ensure all systems work nominally.

The telemetry and map sent to the operator are first compressed and then encoded. The visual data sent to the operator and the commands originating from the operator are not compressed, however, they are encoded.

Using the positional data and 3D map obtained from the sensors, the navigation algorithm produces a path the drone can use to drive or fly to the next PoI, see section 6.1. It then chooses the most energy-efficient path and chooses whether to drive or fly and selects the respective controller. An overview of these software categories and the relations between them can be seen in Figure 8.2.

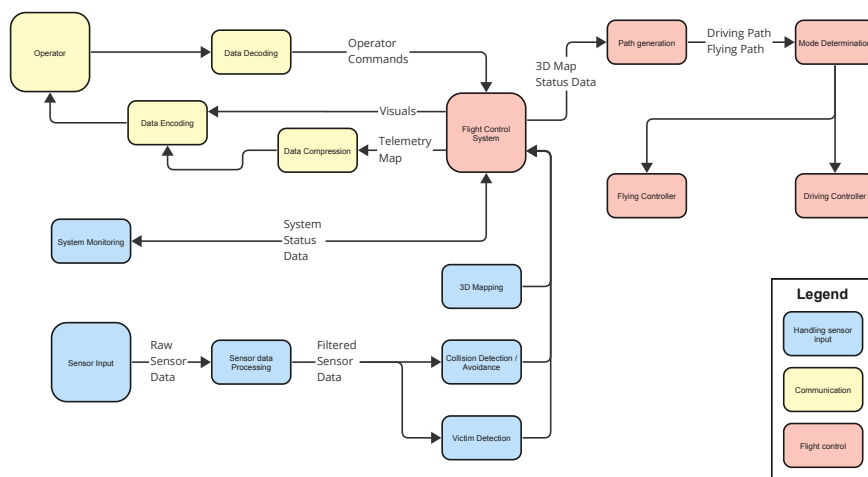


Figure 8.2: Software Block Diagram

The relations between the different hardware components are shown in Figure 8.3. The com-

ponents considered can be divided into five categories: Structural, Sensors, Communication, Movement and Electrical & Data Handling. The main hardware components are the frame and the track rod connectors, additionally the ducts and thermal control surface double as structural elements. The electrical components are all connected to the thermal control surface. This allows for the components to dissipate their heat via this surface. Note that the battery is connected via quick disconnects to all the components to allow the operator to swap it quickly. The tracks and propellers are both connected via the duct to the main frame of the drone, this does leave a single point of failure for both methods of movement, however, the structural efficiency gained by having this configuration outweighs this consideration.

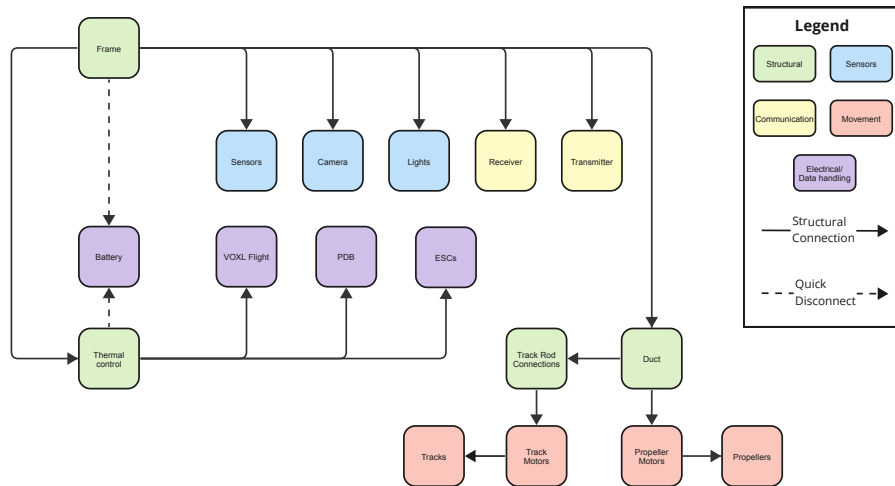


Figure 8.3: Hardware Block Diagram

8.3. Resource Allocation

In this section, all the resource budgets are presented. The budgets are split up into the subsystems and these are divided into the different components. These budgets are given in a range to account for future developments. It should be noted, however, that no power and link budget are presented since they already have been discussed in section 8.3 and section 7.3 respectively.

Mass Budget

Keeping the mass within budget is important as the propulsion subsystem is designed to fly the drone based on a certain mass. If the drone is heavier than expected the drone will not be able to perform the same manoeuvres as it was designed for. This would limit its practicality as it can not move through more complex environments.

In Table 8.1 the mass budget of the final design is presented. In this budget, the mass of each component is listed. All these components are part of a bigger subsystem. For these subsystems, all the components are added up to get the final mass of the subsystem. To account for the post-Design Synthesis Exercise (DSE) developments a ten per cent margin is given on top of the current mass budget.

The current maximum in the mass budget is well below the total allowable mass. Therefore, in a future iteration, it is, for example, possible to decrease the size of the propellers, as less thrust is required. This can result in a decrease in the required amount of power stored, which leads to a smaller mass of the battery. This snowball effect can lead to an improved design.

Component Cost Budget

Keeping the components cost within budget is important because a more expensive drone will decrease the possible customer base. Having a cheaper drone makes it easier for smaller SAR teams to buy and use the drone, and thus, ensures the technology is more widely used in the industry. This increases the market size and as a result, increases sales. Additionally, as more drones are distributed more data can be gathered on the performance of the drone and future improvement points can be found.

In Table 8.2 the cost budget of the final design is given. In this budget the cost of each of the subsystems is given with a range of ten per cent above the current price estimates, to allow for the costs of post-DSE developments. For all subsystems, the current price of each of its components is given as well.

In the final budget, the cost is more than €1000 below the maximum allowable cost. This means that the drone can be equipped with more advanced components and it can be made out of more advanced materials. This allows the drone's performance to increase significantly. On the other hand, the budget surplus can also be used to increase profit. This way the break-even point can be reached faster.

Table 8.1: Mass Budget

Component	Estimated Mass Range [g]
Propulsion	27.04 - 28.39
4 Propulsion motors	3.7
4 Propellers	3.06
Power	371.4 - 389.97
Battery	328
PDB	11
6 ESC	5.4
Communication	67.4 - 70.77
Drone Transceiver A	3.1
Drone Antenna A	34.1
Drone Transmitter B	8.5
Drone Antenna B	21.5
Sensors	145.1 - 152.36
Optical Camera	16
Thermal Camera	7.5
2 Lidar	90
6 Proximity Sensors	21.6
10 Lighting Systems	10
Structures	360 - 378
Main Body	280
Track Rod	8
Ducts	72
Data Processing	25.75 - 27.04
SD Card 256 GB	1.75
VOXL Flight	24
Tracks	66.6 - 69.93
Tracks	23
Track Wheels	8
Track Motors	35.6
Total Maximum Mass	1063-1116
Total Allowable Mass [g]	1560

Table 8.2: Component Cost Budget

Component	Estimated Cost Range [€]
Propulsion	39.44 - 41.41
4 Propulsion motors	9.8
4 Propellers	0.06
Power	138.65 - 145.58
Battery	54.87
PDB	6.92
6 ESC	12.81
Communication	277.55 - 291.43
Drone Transceiver A	9
Drone Antenna A	25.13
Drone Transmitter B	56.5
Drone Antenna B	19.9
Base Station Transceiver A	9
Base Station Antenna A	25.13
Base Station Receiver B	112.99
Base Station Antenna B	19.9
Sensors	1918.64 - 2014.57
Optical Camera	99
Thermal Camera	1600
2 LiDAR	166
5 Proximity Sensors	34.56
12 Lighting Systems	19.7
Structures	244.4 - 256.62
Main Body	190
Track Rod	5.44
Ducts	48.96
Data Processing	691.2 - 725.76
SD Card 256 GB	17.95
VOXL Flight	673.25
Tracks	40.54 - 42.57
Tracks	0.1
Track Wheels	5.44
Track Motors	35
Other	440 - 462
Case	240
Controller	200
Total Cost Range	3790.42 - 3979.94
Total Allowable Cost [€]	5,000

8.4. Feasibility Analysis

This section focuses on the process of conducting a feasibility analysis on the requirements described in chapter 2. A compliance matrix provides a clear overview of which requirements are met, which requirements still need to be verified and which requirements cannot be met with the drone design proposed in this report. Then, the requirements that still need to be verified and the requirements that are not met are analysed.

The first column of the compliance matrix shown in Table 8.3 represents the ID corresponding to the listed requirements in chapter 2. The second column indicates if the design of the drone complies with the requirement. The method (M), that is used to verify the requirement is specified in the third column of the compliance matrix. These three headers are repeated three times resulting in nine columns.

The requirements can be verified by analysis (A), inspection (I), demonstration (D) or test (T). However, often a combination of verification methods is used to verify a requirement. Performing analyses includes more in-depth calculations, whereas inspection involves examining the drone by, for example, placing components on a scale or measuring the dimensions. Demonstration is the process of simply showing that it works. On the other hand, testing is a more formal form of demonstration, where certain parts of the drone are tested within an experimental setup.

After the compliance matrix is set up, the requirements that are red, not complied, or orange, to-be-determined complied, are discussed in Table 8.4. For each, the required value together with the actual value is given if there is a value to verify. Next to this, it is explained why the compliance cannot be determined yet or why the difference in values is permitted. It can be noted that for the to-be-determined complied requirements within Table 8.3, an 'unknown' value is linked to this requirement in the 'Actual Value' column in Table 8.4.

Table 8.3: Compliance Matrix

ID	C	M	ID	C	M	ID	C	M
User Requirements (U-REQ)								
U-REQ-1	No	D	U-REQ-2	Yes	D	U-REQ-3	Yes	D
U-REQ-4	Yes	A&I	U-REQ-6	Yes	A	U-REQ-7	Yes	A
U-REQ-8	<tbd>	D	U-REQ-9	Yes	A&D	U-REQ-10	Yes	D
U-REQ-11	Yes	A	U-REQ-12	Yes	A&D	U-REQ-13	Yes	I
U-REQ-14	Yes	A&D	U-REQ-15	Yes	D	U-REQ-16	Yes	D
U-REQ-17	Yes	A&D	U-REQ-18	Yes	A&D	U-REQ-19	Yes	A&D
U-REQ-20	Yes	A&D						
Propulsion (SYS-TC-PROP)								
SYS-TC-PROP-1	Yes	T	SYS-TC-PROP-2	Yes	A&T	SYS-TC-PROP-3	Yes	A&T
SYS-TC-PROP-4	Yes	A&I						
Power (SYS-TC-PWR)								
SYS-TC-PWR-1	Yes	A&D	SYS-TC-PWR-1-1	No	A	SYS-TC-PWR-1-2	No	A&T
SYS-TC-PWR-2	Yes	D	SYS-TC-PWR-2-1	Yes	A&D	SYS-TC-PWR-2-2	Yes	D
SYS-TC-PWR-3	Yes	A&I						
Communication (SYS-TC-COM)								
SYS-TC-COM-1	No	D	SYS-TC-COM-1-1	Yes	I	SYS-TC-COM-1-1-2	Yes	I
SYS-TC-COM-1-1-3	Yes	I	SYS-TC-COM-1-2	Yes	I	SYS-TC-COM-1-2-1	Yes	I
SYS-TC-COM-2	No	I	SYS-TC-COM-2-2	No	I	SYS-TC-COM-3	Yes	A&D
SYS-TC-COM-3-4	Yes	I	SYS-TC-COM-3-5	Yes	A&I	SYS-TC-COM-5	Yes	A&I
SYS-TC-COM-6	Yes	A&T						
Deployment (SYS-TC-DEP)								
SYS-TC-DEP-1	Yes	D	SYS-TC-DEP-1-1	Yes	A&D	SYS-TC-DEP-1-2	Yes	A&D
SYS-TC-DEP-1-3	Yes	I&D	SYS-TC-DEP-2	<tbd>	D	SYS-TC-DEP-2-1	No	D
SYS-TC-DEP-2-2	No	A						
Navigation (SYS-TC-NAV)								
SYS-TC-NAV-1	Yes	A&D	SYS-TC-NAV-1-1	Yes	A&D	SYS-TC-NAV-1-2	No	A

SYS-TC-NAV-1-3	Yes	A	SYS-TC-NAV-1-4	Yes	A&D	SYS-TC-NAV-2	Yes	D
SYS-TC-NAV-2-1	Yes	T	SYS-TC-NAV-2-2	Yes	T			
Operation (SYS-TC-OP)								
SYS-TC-OP-2	Yes	D	SYS-TC-OP-2-1	Yes	A&I	SYS-TC-OP-3	Yes	I
SYS-TC-OP-3-2	Yes	A&D	SYS-TC-OP-3-3	No	A&D	SYS-TC-OP-3-4	No	A&D
SYS-TC-OP-4	Yes	A&D	SYS-TC-OP-4-1	Yes	A&D	SYS-TC-OP-4-2	Yes	A&D
SYS-TC-OP-5	<td>	T						
Safety (SYS-TC-SFTY)								
SYS-TC-SFTY-1	Yes	I	SYS-TC-SFTY-2	No	A&D			
Sensors (SYS-TC-SNSR)								
SYS-TC-SNSR-1	Yes	A&I	SYS-TC-SNSR-1-1	Yes	A&D	SYS-TC-SNSR-1-2	Yes	A&D
SYS-TC-SNSR-1-3	Yes	A&D	SYS-TC-SNSR-4	Yes	A&I	SYS-TC-SNSR-5	Yes	A&T
Maneuverability (SYS-TC-MNVR)								
SYS-TC-MNVR-1	Yes	A&D	SYS-TC-MNVR-1-1	Yes	D	SYS-TC-MNVR-1-2	Yes	D
SYS-TC-MNVR-2	Yes	A&I	SYS-TC-MNVR-2-1	Yes	D	SYS-TC-MNVR-2-2	Yes	D
SYS-TC-MNVR-3	Yes	A&D	SYS-TC-MNVR-3-1	Yes	T	SYS-TC-MNVR-3-2	Yes	T
SYS-TC-MNVR-3-3	No	T	SYS-TC-MNVR-4	Yes	A&D	SYS-TC-MNVR-4-1	Yes	A&T
SYS-TC-MNVR-4-2	Yes	T	SYS-TC-MNVR-4-3	Yes	T			
Structures (SYS-TC-STRC)								
SYS-TC-STRC-1	Yes	A&I	SYS-TC-STRC-2-2	<td>	T	SYS-TC-STRC-3	Yes	I
SYS-TC-STRC-4	Yes	A&D	SYS-TC-STRC-5	<td>	T	SYS-TC-STRC-6	No	A&I
Data Processing (SYS-TC-DAT)								
SYS-TC-DAT-1	Yes	A	SYS-TC-DAT-2	Yes	A	SYS-TC-DAT-3	Yes	A&D
SYS-TC-DAT-4	Yes	A&T	SYS-TC-DAT-5	Yes	I	SYS-TC-DAT-5-1	No	A&I
SYS-TC-DAT-5-2	Yes	A&I	SYS-TC-DAT-5-3	Yes	A&I			
Tracks (SYS-TC-TRA)								
SYS-TC-TRA-1	Yes	D	SYS-TC-TRA-1-1	Yes	D	SYS-TC-TRA-1-2	Yes	A&T
SYS-TC-TRA-1-3	No	A&T	SYS-TC-TRA-2	Yes	A&T	SYS-TC-TRA-3	Yes	A&I
Thermal Management (SYS-TC-TM)								
SYS-TC-TM-1	Yes	A&I	SYS-TC-TM-1-1	<td>	T			
Keep within budget (SYS-CO-1)								
SYS-CO-1-1	Yes	A&I	SYS-CO-1-1-1	Yes	A&I	SYS-CO-1-1-2	Yes	A&I
SYS-CO-1-1-3	Yes	A&I	SYS-CO-1-1-4	Yes	A&I	SYS-CO-1-1-5	Yes	A&I
SYS-CO-1-1-6	Yes	A&I	SYS-CO-1-2	Yes	A&I			
Keep within schedule (SYS-CO-2)								
SYS-CO-2-1	<td>	D	SYS-CO-2-2-1	No	I	SYS-CO-2-2-2	No	I
Adhere to legal constraints and regulations (SYS-CO-3)								
SYS-CO-3-2	Yes	D	SYS-CO-3-3	<td>	T			
Make efficient use of resources (SYS-CO-4)								
SYS-CO-4-4-1	Yes	A	SYS-CO-4-4-2	Yes	A	SYS-CO-4-4-3	Yes	A
SYS-CO-4-4-4	Yes	A						

Table 8.4: Feasibility Analysis

ID	Required Value	Actual Value	Explanation
U-REQ-1	20 cm	0 cm	Easily implemented within the code, not possible within the time constraint.
U-REQ-8	1 week	Unknown	This value can only be determined once the drone is manufactured.
SYS-TC-PWR-1-1	4,500 mAh	3,300 mAh	From the power budget in subsection 3.2.2 it followed that the required battery energy (mAh) to sustain the operational requirements no longer equal 4500 mAh, but only 3300 mAh.
SYS-TC-PWR-1-2	190 W	146 W	The battery can provide a maximum power discharge of 1,500 W, meeting the requirement. However, the average power provided by the battery based on subsection 3.2.2 is 146 W. This is enough to sustain a SAR operation of 20 minutes.

SYS-TC-COM-1	5.8 GHz	2.4 GHz	This frequency is proven to function significantly better in range as shown in chapter 7. Therefore, it was chosen for the drone's design based on the use case.
SYS-TC-COM-2	5.8 GHz	-	Audio is discarded because the thermal camera (IR) and the optical camera are sufficient for victim identification, this is further elaborated on subsection 5.1.1.
SYS-TC-COM-2-2	128 kbits/s	-	No audio will be transmitted.
SYS-TC-DEP-2	-	-	Because the drone is not produced, this requirement cannot be tested. Therefore, it is uncertain whether it can take off from the operator's hand.
SYS-TC-DEP-2-1	-	-	No supports are added underneath the structure because the drone has tracks and is able to land by itself.
SYS-TC-DEP-2-2	-	-	No supports are added underneath the structure because the drone has tracks and is able to land by itself.
SYS-TC-NAV-1-2	10 %	Unknown	The battery level is not yet enforced within the navigation algorithm, however, it can be implemented. Due to time constraints, this requirement was not met.
SYS-TC-OP-3-3	10 cm	0 cm	No obstacle clearance has been incorporated. This can be implemented, however, due to time constraints, this requirement was not complied with.
SYS-TC-OP-3-4	20 cm	0 cm	No obstacle clearance has been incorporated. This can be implemented, however, due to time constraints, this requirement was not met.
SYS-TC-OP-5	273.15 - 323.15 K	Unknown	Due to passive cooling, components in the drone will not be cooler than the environment. All components in the drone can handle the temperature required, but the performance of the components is significantly reduced at extreme temperatures. Further analysis should be performed to verify this requirement.
SYS-TC-SFTY-2	-	-	The drone will not attempt to land on the ground but will try to proceed with operations after a systems check. Otherwise, the drone will return to base, this was discussed in subsection 6.1.5.
SYS-TC-MNVR-3-3	0.75 rad/s	0.3 rad/s	The drone is not able to meet this requirement, however, it was determined in section 6.2 that for the use case, this value does not have to be as high as the first estimate.
SYS-TC-STRC-2-2	1000 loading cycles	Unknown	The drone is not produced, therefore, it cannot be known how many loading cycles it can sustain. This number will be verified once produced.
SYS-TC-STRC-5	IP34	Unknown	The drone is not manufactured yet, therefore, it cannot be tested whether it can achieve this rating.
SYS-TC-STRC-6	220 g	360 g	The weight of the ducts are included in the structural weight and not the propulsion system weight which was assumed when the requirements were established. Therefore, this requirement is not met and SYS-TC-PROP-4 is easily met.
SYS-TC-DAT-5-1	-	-	No audio is stored as the thermal camera (IR) and the optical camera are sufficient for victim identification
SYS-TC-TRA-1-3	10 cm	0 cm	No obstacle clearance has been incorporated. This can be implemented, however, due to time constraints it is not.
SYS-TC-TM-1-1	288.15 - 308.15 K	Unknown	No operating temperature can be determined, this can be tested when the drone is produced.
SYS-CO-2-1	1 week	Unknown	The drone is not manufactured, therefore, the training time necessary cannot be determined yet.
SYS-CO-2-2-1	44 days	> 44 days	The drone is not fully developed yet within the 44 days as still, some recommendations remain on how to improve the design that can be implemented.
SYS-CO-2-2-2	10 members	10 members	The drone is not completed as it is not manufactured.
SYS-CO-3-3	EASA	Unknown	The drone is not manufactured and tested and therefore not certified yet.

8.5. Technical Risk Assessment

In this section, the most significant risks for the drone during its operation are described. These risks are also visualised in a risk map based on performance consequences and probability. From the risk map, the most critical risks are identified. These risks are mitigated by reducing, removing or accepting them. After the mitigation strategies have been applied an updated risk map is created.

The identified risks consist of risks of individual subsystems as well as risks of multiple overlapping subsystems and the complete drone. All the risks that were found are presented in Table 8.5. In the first column, the risk is given a number, which is also used in the risk map. In the second column, the risk is described. In the third column, the risks are divided into one of the two different risk types: 'Design risks' are risks that come from a possible mistake in the design, which can be solved by changing the design and 'Operational risks' are risks that occur during operation. This can be either mitigated by changing the design or changing the operational parameters of the drone. In the final column of Table 8.5 an analysis of the risks is given, providing the reasoning behind the locations of the risks in the risk map.

Table 8.5: Technical Risks

Id	Risk	Risk Type	Risk Analysis
1	The drone requires parts that are too small to 3D print	Design	As explained in subsection 4.1.3 the material chosen is strong enough that the required thickness is lower than the smallest thickness that can be 3D printed. As the minimum thickness has been increased to account for this, it is improbable that some parts are too small to be 3D printed.
2	The structure is not able to carry the applied loads	Design	As discussed in subsection 4.1.4, the model is accurate but has a small error in the stress. However, the structure has already been over-designed and FEM analysis shows that in no circumstance failure occurs, therefore, the probability of this risk is low.
3	The tracks do not have enough traction to drive on all use case-specific terrains	Operational	As discussed in subsection 4.2.1 it is difficult to estimate and model the terrain the drone will face. However, in case the drone is unable to drive over certain terrain it will usually be able to fly over it reducing the performance consequence.
4	The motor can not provide enough torque to drive over the terrain	Design	A motor that complies with the required torque has been chosen in subsection 4.2.5. If the motor can not provide enough torque, the drone can usually fly over the debris.
5	The tracks break	Design/ Operational	As explained in subsection 4.2.1 the tracks experience loads up to 8.5 N. Due to uneven terrain and repeated loading the tracks have a substantial chance of failure.
6	The drone does not have sufficient battery level to return to the base station	Operational	As explained in section 8.4 the drone will return to the base station whenever it has enough power left to return to the base station with an extra 10% battery level. However, the drone could require more power than anticipated if, for example, the debris has moved blocking the planned route.
7	Too much data is gathered to be transmitted by the communication subsystem	Operational	In section 7.3 the challenges of the data transfer are discussed. Even though there is the possibility of transmitting issues, the SD card allows the data to be temporarily stored until the drone returns to the base station resulting in the impact of this risk being marginal.
8	The propeller power efficiency is lower than expected	Design	In subsection 3.1.3 the efficiency of the propeller is analysed and computed. If these results turn out to be not valid, more power is required by the propulsion subsystem.
9	(Part of) the drone short-circuits due to water	Operational	If water gets into the coils of the motors that part of the drone short circuits resulting in a mission failure.

10	The propeller duct breaks	Operational	The propeller duct is on the edge of the design. Therefore, it is possible that due to repeated collisions the propeller duct fails. If this happens the thrust provided by the propellers decreases.
11	The propellers can not provide sufficient thrust	Design	The drone will not be able to fly without sufficient thrust making the risk catastrophic. However, in subsection 3.1.3 the propeller thrust is analysed, so the probability is minimal.
12	The battery overheats	Operational	The battery already has a thermal management system preventing overheating as described in subsection 3.2.1, reducing the probability of this risk occurring.
13	LiDAR scanners malfunction/break	Operational	The probability of malfunctions of the LiDAR is minimal [37]. However, LiDAR scanners are crucial for the navigation of the drone, a failure would be catastrophic for the mission.
14	The drone collides with an object or wall	Operational	Due to an environment with debris sticking out, the chances of colliding with an object are plausible. However, as the drone will be flying at a low speed the effects of these collisions will be limited.
15	The drone is not able to stabilise after a collision	Design	The drone would not be able to continue its mission and crash, resulting in a mission failure. The environments that the drone needs to operate in are continuously changing making them hard to predict. The probability of the risk occurring is therefore plausible.
16	The drone is not able to detect a malfunction of one of the components	Operational	If one of the components malfunctions it is important to know this so other components can adapt. Otherwise, the drone could, for example, become unstable.
17	The drone controller gains are not switched when the drone is inside a building	Operational	The controller gain is changed depending on the environment, not switching between controller gains would be critical as the drone would possibly crash.
18	Insufficient area is visible for the algorithm or operator to identify a victim	Operational	In subsection 5.3.2 and subsection 5.3.4 the limitations of identifying a victim are discussed, showing the probability of having too little area visible for a victim to be identified to be very high.
19	The algorithm or operator is unable to distinguish a victim from a surrounding object	Operational	In subsection 5.3.1 the probability of victims being indistinguishable from surrounding objects is discussed.
20	The drone is too big to reach victims in real-world situations.	Design	Inside a collapsed building there is a lot of debris of different sizes. Therefore, this debris will have openings of different sizes. At this moment in time, it is unknown how large the openings are. This means it is unknown at what size the drone is small enough to explore a large percentage of the building without being constrained by the size of the openings.
21	The navigation subsystem fails to function properly due to its long computational time	Operational	During the mission, the drone needs to recalculate its path which might take up more computational time than expected. This could lead to the drone colliding with obstructions and/or increasing operational time. This is likely to happen, however, not catastrophic.
22	The navigation subsystem fails to position itself	Operational	If the drone fails to position itself within the debris, collisions are very likely to happen. These are catastrophic, however, are not highly probable as the proposed positioning system is proven.

A risk map is shown in Figure 8.4a indicating the severity of the risk and the probability of the risk occurring. For all the risks in red, the risks with the highest probability and the most significant consequence, a mitigation strategy is selected. These mitigation strategies lead to a decrease in either the severity or the probability of the risks. However, the mitigations may not only affect the targeted risk but also have effects on other risks. The complete overview of all mitigation strategies and the affected risks is shown in Table 8.6.

After the mitigation strategies have been taken into account, a new risk map is constructed

and shown in Figure 8.4b. It can be seen that due to the risk mitigation, all the risks have been moved out of the red zone except risks 15 and 20. These are: the drone is not stable after a collision and the drone is not able to fly through all openings. A lot of uncertainties remain about the environment the drone will be flying in. Therefore, risks 15 and 20 will always be present until more testing has taken place. Also, it can be seen that due to some residual effects, some risks are increased, such as risk four: the motor can not provide enough torque to drive over the terrain. This is acceptable as the risk remains outside the critical red zone.

Feasible in theory	14	3, 7	18	20	← Probability
Working laboratory model			5	15	
Based on non-flight existing engineering		4	10, 21	6, 9	
Extrapolated from existing design		8	1, 12, 16	11, 13, 17, 22	
Proven design				2, 19	
	Negligible	Marginal	Critical	Catastrophic	
	Performance Consequence →				

(a) Risk Map before Mitigation

Feasible in theory					← Probability
Working laboratory model	14	4	20		
Based on non-flight existing engineering	7	3	1, 10	15	
Extrapolated from existing design		8	5, 16, 18, 21	2, 6, 11, 13, 17, 19	
Proven design			12	9, 22	
	Negligible	Marginal	Critical	Catastrophic	
	Performance Consequence →				

(b) Risk Map after Mitigation

Figure 8.4: Risk Map

Table 8.6: Risk Mitigation Strategies

Risk	Mitigation Strategy	Mitigation Type	Affected Risks	Increase/ Decrease
3	Propose improved track profiles	Remove/Reduce	4 5	Increase/Decrease Increase/Decrease
5	Increase the width/thickness of the tracks	Remove/Reduce	3 4 10 11 12 20	Decrease Increase Increase Increase Increase Increase
6	Turn off the LEDs and optical camera	Remove/Reduce	7 12 14 18 19	Decrease Decrease Increase Increase Increase
7	Compress and prioritise the data	Reduce	6 18 19	Increase Increase Increase
9	Apply a layer of waterproof coating	Remove	12	Increase
15	Decrease the drone's velocity	Reduce	5 6 10 12 14 21 22	Decrease Decrease Decrease Decrease Decrease Decrease Decrease
18	Decrease the distance to the detected area of interest	Reduce	6 14 19	Increase Increase Decrease
20	Decrease the size of the drone	Reduce	1 2 3 14 15	Increase Increase Increase Decrease Increase

Performance Analysis and Use Case Example

In this chapter, the performance of the drone during the mission is analysed. General performance analysis of the drone is shown in section 9.1, and the sensitivity of these characteristics and the impact a change in them has on the system is discussed in section 9.2. In section 9.3, an example of the drone's use case is presented to show that for nominal conditions the drone can perform the mission.

9.1. Performance Analysis

From the previous chapters, the most important performance characteristics related to the mission performance of the drone are gathered and displayed in Table 9.1. From the table, it can be seen that flying takes around three times as much power as driving. Thus, choosing when to fly and when to drive has a significant impact on the operational time of the drone.

Table 9.1: Performance Characteristics of the Drone

Flying			Driving		
P_{avg}	70	[W]	P_{avg}	24.8	[W]
T	31.2	[N]	Traction force	16.9	[N]
Turn t_{90°	1.8	[s]			
v_f	0.35	[m/s]	v_d	1	[m/s]

To easily see how long the drone is able to drive or fly, a figure is constructed that shows how long the drone can drive for a certain flying time, see Figure 9.1. In the plot, above the shaded area is everything that falls within the required ten minutes of flying time. This is calculated using Equation 9.1.

Additionally, it is interesting to note that the lights on the drone account for a significant part of the overall power budget. While these lights are essential for direct operator control and victim identification, they do not necessarily need to be on for the whole duration of the mission. As a large part of the mission is performed autonomously using the LiDAR and IMU sensors, the lights could be turned off (partially) during this part. When the thermal camera detects a possible victim, the lights can be turned on again, temporarily. They can also be turned off and on at given intervals to take a snapshot of the surroundings or when the LiDAR or IMU sensors fail. This gives a significant increase in operational time as can be seen from the graph. Determining when the lights can be turned off or have to be turned on is something the operator or the control algorithm needs to decide on.

$$t_d = \frac{E_{bat} - (P_0 + P_f) \cdot t_f}{P_0 + P_d} \quad (9.1)$$

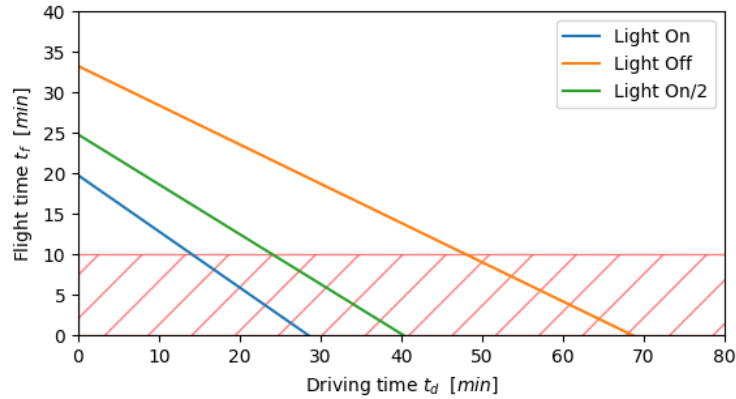


Figure 9.1: The Flight Time t_f versus Driving Time t_d for a Battery of 3300 mAh

9.2. Sensitivity Analysis

The performance analysis is done for the nominal operation of the drone. However, the nominal operation cannot always be guaranteed due to a multitude of different factors: manufacturing tolerances, incorrect assembly, environmental conditions and use case scenarios. The non-nominal performance of the most important parameters of the drone is considered. An overview of the impact of this performance decrease is shown in Table 9.2. Note that the change in some of the parameters affects the performance of other parameters in the table.

Table 9.2: Affects of Non-Nominal Performance on Subsystems and the Mission

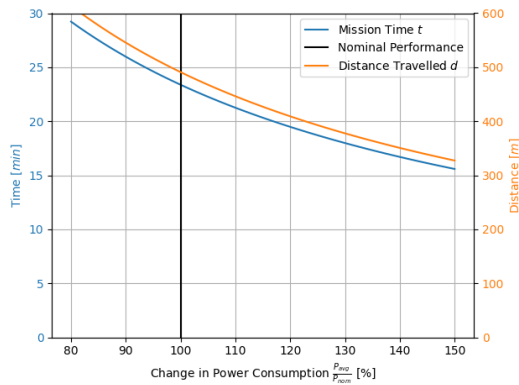
Non-Nominal Parameter	Subsystem Affected	Mission Influence	Mitigation
Thrust T Power P	S&C, Navigation Power, Propulsion, Sensors, Data Handling	Flight Speed v_f Mission time, Sensor capabilities, Redundancy	Increase driving time t_d Selectively turn off electrical components
Temperature \mathcal{T}	Sensors, Power, Data- Handling	Power, Sensor Capabilities, Data Processing	Return to base, avoid hot areas.
Operational Velocity v	Navigation, S&C	Mission Distance	Accept

Thrust Sensitivity

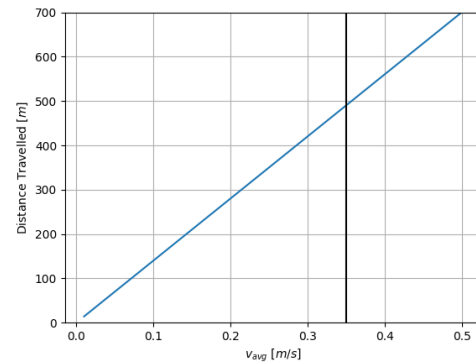
Next to possible manufacturing errors, the obtained thrust could decrease due to a decrease in air density. This can be caused by a higher temperature at the operational site or by being at a higher altitude. Additionally, air currents or wind inside the building might cause the *effective excess* thrust to be lower. This decreased effective excess thrust makes it harder for the drone to manoeuvre and stay stable, affecting the navigation and S&C subsystems. The drone will have to fly at a lower speed due to this decrease in thrust. This will have a large influence on the distance the drone can cover. The influence of travelling at a decreased speed is further discussed in the Operational Speed Sensitivity section. It is possible to mitigate this reduction in performance by driving more, which might increase the speed the drone can travel, depending on the terrain it encounters.

Power Consumption Sensitivity

The power consumption of the drone can be higher than expected due to a larger amount of manoeuvres than expected or a significant headwind. Additionally, an electrical failure or short-circuit could induce a leak current adding to the power consumption of the drone. However, the power consumption of the drone can also be less than expected due to sensors that are not used or the drone moving slower than expected. An overview of the influence of a change in nominal power consumption on the mission time and the distance the drone is able to travel is shown in Figure 9.2a. For simplification, this analysis assumes that the drone drives half of the time and flies the other half.



(a) The Impact on the Distance Travelled and Mission Time Due to a Change in Power Consumption, at $v_{avg} = 0.35m/s$ and $P_{nom} = 125.356W$



(b) The Impact of a Change in Operational Velocity on the Distance Travelled Within the Mission Time of 20 minutes, at $P_{nom} = 125.356W$

Figure 9.2: The Sensitivity of Different Parameters

Temperature Sensitivity

The temperature of the environment has an impact on the performance of the drone. As the drone uses a passive cooling system, the components of the drone cannot be cooled to a lower temperature than the environment. The impact of non-nominal temperatures is twofold. First of all, the temperature range in which the electrical components can operate is limited, as they start to deteriorate at extreme temperatures. Additionally, for some components, the individual performance is significantly influenced by the ambient temperature of the drone.

For example, the performance of batteries varies with the temperature of the battery. Low-temperature environments result in reduced battery capacity and output performance [6, 103], see Figure 9.3. Higher temperatures are also not ideal for batteries as they can be prone to overheating reducing performance and causing long-term damage to the battery. The nominal operating temperature range for lithium batteries is between 25°C and 45°C.

The performance of the thermal camera (IR camera) is also influenced by the ambient temperature. To identify a victim, a certain temperature difference from the environment is needed. If the environment becomes around the same temperature as the victim it will be more difficult to distinguish them, see subsection 5.3.1.

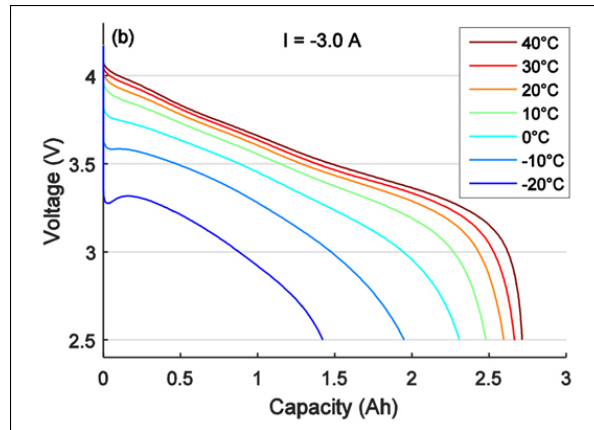


Figure 9.3: Temperature Sensitivity of LiPo Batteries [103]

Operational Speed Sensitivity

The operational speed of the drone might decrease due to a lower thrust performance, large headwinds, and difficult-to-navigate terrain. A reduction in the operational speed of the drone lowers the distance the drone can travel before it has to return to the operator. An overview of the distance the drone can travel for the nominal power consumption case using a 50-50 driving and flight time is shown in Figure 9.2b.

9.3. Use Case Example

Using the algorithm benchmarking program from section 6.1, a simulation is run in order to predict the behaviour of the drone in a real-world environment. There are limitations to this. No terrain effects are taken into account and the map consists only of walls and free spaces, so no other obstructions are present. Navigating through the building is done exclusively in autonomous mode. There are no elevation changes and no atmospheric effects or hazardous situations. Lastly, the drone is assumed to only be flying.

Two runs are done, one with and one without optimisation of the JuLiam algorithm. The routes taken by the drone are shown in Figure 9.4. The map created is 500 by 500 *px*. This equates to 25 by 25 *m* or a pixel size of 5 *cm*. Turning on optimisation causes the drone to first move towards the selected goal before re-calculating its path. Considering a 90-degree turn time of 1.8 seconds, the average speed of the drone is assumed to be 0.35 *m/s*. The results of the simulations can be seen below in Table 9.3.

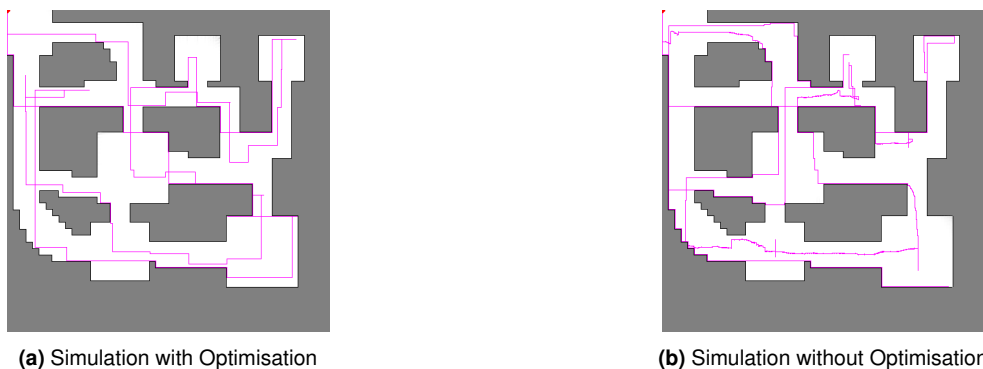


Figure 9.4: The Routes Taken by the Drone in the Simulations

Table 9.3: Results from Simulations

	Optimisation On	Optimisation Off
Path Length	4500 [px] 225 [m]	5200 [px] 260 [m]
Operational Time	10 [min] 43 [s]	12 [min] 23 [s]

From these simulations, it is clear that the following requirements are met for the *Needle's Eye* drone: SYS-TC-OP-3, SYS-TC-NAV-1, SYS-TC-NAV-1-1, SYS-TC-NAV-1-2. Therefore, it can be concluded that the navigation subsystem proposed for the drone is sufficient for this stage of the design.

Next to the navigation requirements being met, also the operational requirements are satisfied. With a flight time of a least 10 minutes, SYS-TC-OP-4-1 is met. In the power budget provided in Table 3.11 all the systems that use up power are taken into account. Within the calculation, it is considered that the operational time is a total of 20 minutes and the flight/driving time is 10 minutes. Relating it to this use case example, where the drone flies solely, the battery is able to deliver enough power to sustain the operation for 20 minutes. This means that SYS-TC-OP-4-2 is met. Next to this, knowing that driving takes up less energy, the drone is also able to provide enough power if the mission would be driving and flying together.

In conclusion, the presented use case example demonstrates the capabilities and effectiveness of the SAR drone. Through simulation, the drone successfully navigates the map, considering optimisations. The requirements for both the navigation and operations are met, ensuring efficient and reliable performance of the drone in real-world scenarios. The results validate the conceptual design and show the value of the use case of the SAR operation by the drone being able to manoeuvre as quickly while mapping and localising victims.

Reliability, Availability, Maintainability and Safety

This chapter will cover the Reliability, Availability, Maintainability, and Safety (RAMS) characteristics of the drone. In section 10.1, an approximation of the subsystem failure likelihood will be discussed. Then, the ability of the drone to remain operational and accessible during the required time frame is discussed in section 10.2. Using the reliability characteristics, a maintenance plan will be proposed in section 10.3. This includes scheduled and unscheduled maintenance operations, their time duration and expected costs per operation. Finally in section 10.4, the safety characteristics of the drone will be presented.

10.1. Reliability Characteristics

The reliability of parts can be expressed in various ways. Often, reliability is defined by Mean Time Between Failure (MTBF) and Mean Time To Failure (MTTF). Multiple failure types that influence these indicators can be identified: early, random and wear-out failures. Together, they form the bathtub curve of failure probability as visualised in Figure 10.1.

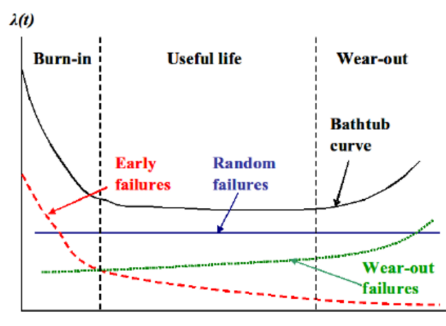


Figure 10.1: Illustration of the Failure Rate over Lifetime [104]

Now, the focus is laid on preventing random and wear-out failures as early failures should already be detected during manufacturing testing. All failure cases that relate to these failure types are listed in Table 10.1 along with their approximated failure likelihood. This likelihood is based on indicators, such as MTBF and MTTF and is categorised into three groups: Low, Medium, and High risk.

Parts with a low likelihood have no moving parts and generally have high reliability in similar equipment. Medium failure likelihood has some moving parts like the tilting mechanisms or is prone to damage during operations. High likelihood means that the component is really complex, easy to damage or has inherent reliability issues.

The drone is designed to meet the reliability requirements. In order to guarantee this, extensive maintenance and inspection will be performed during the operation of the drone. This will be further discussed in the maintenance characteristics.

Table 10.1: Components prone to Failure

Category	Failure type	Failure likelihood
Sensor reliability	LiDAR failure Optical Camera failure Proximity sensors failure Infrared Camera failure	Low Low Low Low
Flight system reliability	Motor failure Propeller failure ESC failure VOXL Flight Failure	Medium Medium Low Low
Power reliability	Battery failure Battery degradation Cabling failure	High High Low
Track reliability	Track motor failure Track grip failure Complete track failure (breaks)	Medium Medium Low
Structure reliability	Structural failure Tilting Mechanism failure	Low Medium
Communication reliability	Antenna failure Transceiver/receiver failure	Medium Low

10.2. Availability Characteristics

The drone is designed to be quickly deployable without much effort. The only actions the operator has to perform are: take the drone out of the box (2 min), set it on the ground (1 min), perform initial drive and flight checks (4 min), put down the antenna (2 min) and take off. The drive checks consist of checking if the drone can move forward, backwards, left and right. Then, the flight checks are similar as they consist of checking whether the drone is able to move up, down, left and right. Next to this, the sensors are checked to make sure they all functioning as required. This means that the total set-up time of the drone will be below 10 minutes.

It is an out-of-the-box solution, so no additional construction or assembly has to be performed. Additionally, the drone does not use any one-time use products. This reduces set-up time, decreases operational costs and decreases operational complexity. .

10.3. Maintainability Characteristics

To make sure the drone operates correctly, the drone will need to undergo maintenance operations. This section will cover which subsystems are maintainable. Next to this, the scheduled and unscheduled maintenance operations are discussed.

As the design proposed is modular it is by definition maintainable. Each subsystem can be removed, repaired and/or replaced. There is, however, a difference in repair time, location and costs. Table 10.2 lists all these characteristics.

Table 10.2: Repairability of Subsystems

Subsystem	Subsystem part	Repair location	Repair Time
Propulsion	Propellers Motors	During mission Base station	5 min 30 min
Power	Replace battery Any other issues	During mission Factory	1 min N.A.
Structure	Structure replacement	Factory	5 hours
Tracks	Belt Motor Track wheel	During mission Base station During mission	5 min 30 min 5 min
Data Handling	VOXL Flight core	Factory Factory	5 hours 5 hours
Sensors	Optical camera IR camera LiDAR Proximity sensors	Base station Base station Base station Base station	45 min
Communication	Antenna replacement Transceiver/Receiver	During mission Base station	5 min 30 min

10.3.1. Scheduled Maintenance

Scheduled maintenance will be performed at regular intervals. This maintenance schedule is important because it limits the downtime of the drone, ensures a longer lifetime of the product and aids predictive maintenance. During scheduled maintenance, more issues may come to light that would not have been detected otherwise. Therefore, due to all these reasons, scheduled maintenance reduces overall operational costs and increases safety. All scheduled maintenance operations and their explanation are listed in Table 10.3.

Table 10.3: Scheduled Maintenance Activities

Maintenance Activity	Sub-Activities	Interval	Time Required	Maintenance Costs (per operation)
(Damage) inspection	Chassis Propellers Electric motors Battery swelling Structure Wiring Track tension	1 flight	10 min	50 (expected damage)
Cleaning	-	1 day	30 min	0
Track maintenance	Track tensioning Track replacement	1 day When inspection fails	5 min 10 min	10
Electric motor maintenance	Motor cleaning Motor replacement when needed	1 week	5 min 15 min	0 30
Drone performance testing	Electric motor performance Thrust performance Sensor result testing Flight control testing	1 deployment	10 hours	0
Sensors	Sensor cleaning Sensor calibration Sensor replacement	1 flight 1 day	10 min 30 min 20 min	0 0 20
Battery replacement	-	300 cycles	1 hour	10
Firmware update	-	1 deployment	1 hour	0

The maintenance costs are calculated based on a single operation. The costs do not reflect the actual costs of replacement but the costs divided by the number of operations that it supports. These are rough estimates based on the probability of failure and replacement costs.

10.3.2. Unscheduled Maintenance

Unscheduled maintenance is hard to account for as it would otherwise be implemented in the scheduled maintenance. However, to ensure a low downtime, there should be a spare for every part of the drone. This may include parts that are not taken into the normal maintenance activities.

10.4. Safety Characteristics

In terms of safety, there is simply one situation that should be avoided: the drone harms people. This can be either by hitting a person during flight and driving operations or due to the batteries catching fire and causing harm to the environment or people.

Collision will be avoided using the static collision avoidance algorithm developed. Potential battery failure will be prevented by the maintenance and inspection program proposed. Also, a thermal management system is in place to make sure the battery or other components do not overheat. There is, of course, still a chance one of these two risks happen. It is, however, not possible to mitigate them completely and they are part of the SAR operations.

Sustainability

Ensuring sustainable development requires consideration of many factors. The materials used for the drone, the product manufacturing plan, the drone packaging materials and end-of-life plans should be specified. Additionally, the product has to keep contributing to sustainability after its development. This chapter describes what is being done to develop, produce, use and dispose of the drone sustainably.

In the production phase, packaging and the power source of the drone are important aspects. Making use of sustainable packaging materials and energy and minimising the amount of packaging contributes to the sustainability of the product. This also aligns with lean manufacturing methods [105]. The philosophy of lean manufacturing relies on eliminating waste and 'creating value'. Any action that does not add value to the product should be avoided as much as possible. Otherwise, material would be used or even produced that does not contribute to the value of the product making it a wasteful activity.

When choosing materials, it is important to take into account the toxicity levels of the materials. In the design phase, the use of toxic materials was minimised. Toxic components on the drone include the battery. However, no suitable alternative could be found so it was decided to keep the battery in spite of its toxicity. Additionally, production methods for in-house components were chosen in a way that minimal byproduct is produced. For example, the use of additive manufacturing is proposed which produces a negligible amount of byproduct. This makes the production method sustainable compared to other methods which do produce byproducts such as machining or casting. In case off-the-shelf components are used, the sustainability of the supplier is taken into account. Suppliers are compared based on different factors. These include transportation time and method, treatment and rights of employees and their method of acquiring raw materials. The optimal supplier is chosen if it fits within the budget. These measures all contribute to the ethical and sustainable production of the drone.

After the production of the drone, it has to be tested. The amount of test and testing material should be minimised as much as possible. Careful design and production are measures taken into account to minimise the need for testing. The tests that are done are mostly non-destructive tests. Tests that affect the performance of the drone should be done in the design phase of the drone with a prototype. This ensures that the maximum amount of produced products can be used by customers.

For the EOL phase, a recycling strategy needs to be developed. Different means of recycling can be relevant for different components of the drone. Selective disassembly is key to being able to apply different recycling strategies. Extensive research has been done in this area, in which optimised disassembly methods are discussed [106]. Customers will be informed about recycling partners that meet these requirements in order to limit the environmental impact of the EOL phase of the drone.

The frame of the drone is mainly made of carbon fibre composites, due to the weight properties. Carbon fibre can be recycled using mechanical, thermal or chemical methods [107]. This requires a lot of energy and resources [108]. However, it is 30-40% less than producing

a composite from scratch [107]. Different carbon fibre recycling methods are proposed by Baimova J et al. [109]. The recycling of the main frame will be outsourced to a company that specialises in carbon fibre recycling. This ensures that recycling is done as sustainably as possible.

In the frame, metal is also used. A layer of aluminium is present in the structure housing the components to provide a passive cooling system. Aluminium can easily be recycled in multiple ways. It can be reshaped or melted down, but also re-used.

Batteries are hard to recycle and it is not feasible to do this in-house. Therefore, at the end of life, batteries should be sent to specialised battery recyclers. Multiple governments have a centralised system for battery recycling [110]. Because companies are used that are specialised in recycling batteries, the way sustainability is taken into account cannot be influenced by the team.

Lastly, for motors and sensors, a similar approach to the batteries is taken. After they stop working, a centralised recycling company is sought out. Recycling companies are compared based on different criteria. The way they recycle and dispose of materials is looked at. Also, the distance that needs to be travelled by the component to arrive at the recycling company is taken into account in this choice.

For some components, no clear recycling strategy can be decided upon. Therefore, it is important to make components durable because if the components still work at the EOL of the drone, they can be reused or sold as separate products. Should components break and no recycling strategy is in place, components could be used as museum items or incorporated into an art piece. In case new recycling methods arise that are applicable to these components, they should be evaluated.

The sustainability plan is not a final plan and needs to be updated should new ways of promoting sustainability in the design arise. Moreover, it should be noted that the *Needle's Eye* mission promotes sustainability from a general perspective as well. Making use of drones could reduce the need for manpower, which means fewer people have to be transported to the disaster area. This reduces transportation emissions. Additionally, if the drone can pinpoint a victim accurately, the SAR team knows where to look. This reduces the use of tools to find the location of the victim, which in turn reduce the need for equipment and power. This reduction contributes to sustainability.

The contribution to the sustainability of the *Needle's Eye* mission is not of the highest priority. The drone is designed to save lives and thus needs to be able to do so without being constrained by requirements on sustainability. However, the team does aim to design and produce the drone as sustainably as possible using the strategies mentioned above.

Development, Production and Operations

This chapter outlines the steps that still need to be taken before the drone can enter the market. Additionally, it describes how the drone would arrive at the customer as well as the way a customer would use it in operation. In section 12.1 an overview is provided of the phases and their corresponding activities to be done before the drone enters the market. Then, in section 12.2 an in-depth description is given about the manufacturing process of the drone. Lastly, in section 12.4, the logistics around distribution and operations are discussed. Additionally, a flow diagram is provided which outlines the processes involved in utilising the drone.

12.1. Product Design and Development

In this section, a plan is presented for further production and development of the drone after the DSE is finished. The plan consists of a proposal of steps to finalise the design that is presented at the end of the DSE and bring it to the market. This Production Design & Development (PD&D) plan is presented as a flowchart in Diagram 4. As can be seen, several phases are included in the PD&D logic, which are all briefly elaborated on in the following subsections.

Development

The development phase is divided into two parts, "Development A" and "Development B". Within "Development A" subsystems that are designed on a high level will be designed in detail, such as the controller of the drone and its casing. Also, a proper material analysis will be done. Hereafter "Development B" starts, where the subsystems and the performance of the whole system are analysed in detail with the use of CFD and FEM. During these phases, the design is updated several times in order to end up with the optimal design. Finally, when the design is done, the verification and validation of the whole drone will be accomplished. These procedures are outlined in section 12.5.

Manufacturing and Promotion

After the development phase is completed the manufacturing and promotion phase can start. In this phase, the technical drawings of all the components and an assembly drawing are made. With the help of a manufacturing plan, a prototype of the drone is built. How the production takes place is further elaborated on in section 12.2. During the manufacturing process, the marketing of the drone is also done. This includes getting a patent confirmed, and a slogan is thought of together with looking for a product advocate. Thereafter, money is gathered by finding sponsors and partners. Also, a social media strategy is set up and a website is made. Events, such as a symposium, are used to show and advertise the drone. This promotes the drone and makes it easier for it to enter the market. If the market is not informed of the drone, sales will be too low to sustain production and that increases the chance of product failure. The marketing will continue until the drone is out of the market.

Testing

When the prototype of the drone is built it can be tested in the testing phases, "Testing A" and "Testing B". First, non-destructive and destructive tests are performed on a drone prototype, such as ultimate strength tests and limit tests. When these tests are performed and the

drone passes them, a case test and user test are performed. These tests may include flight performance tests or in-field training exercises with SAR personnel. Feedback is given after these tests and is incorporated when the design is updated. This is all performed in "Testing A". In "Testing B" operator tests are performed. This means training an operator and executing a mission after which feedback is given. This feedback can be used to update the design for the last time. This leads to the final design.

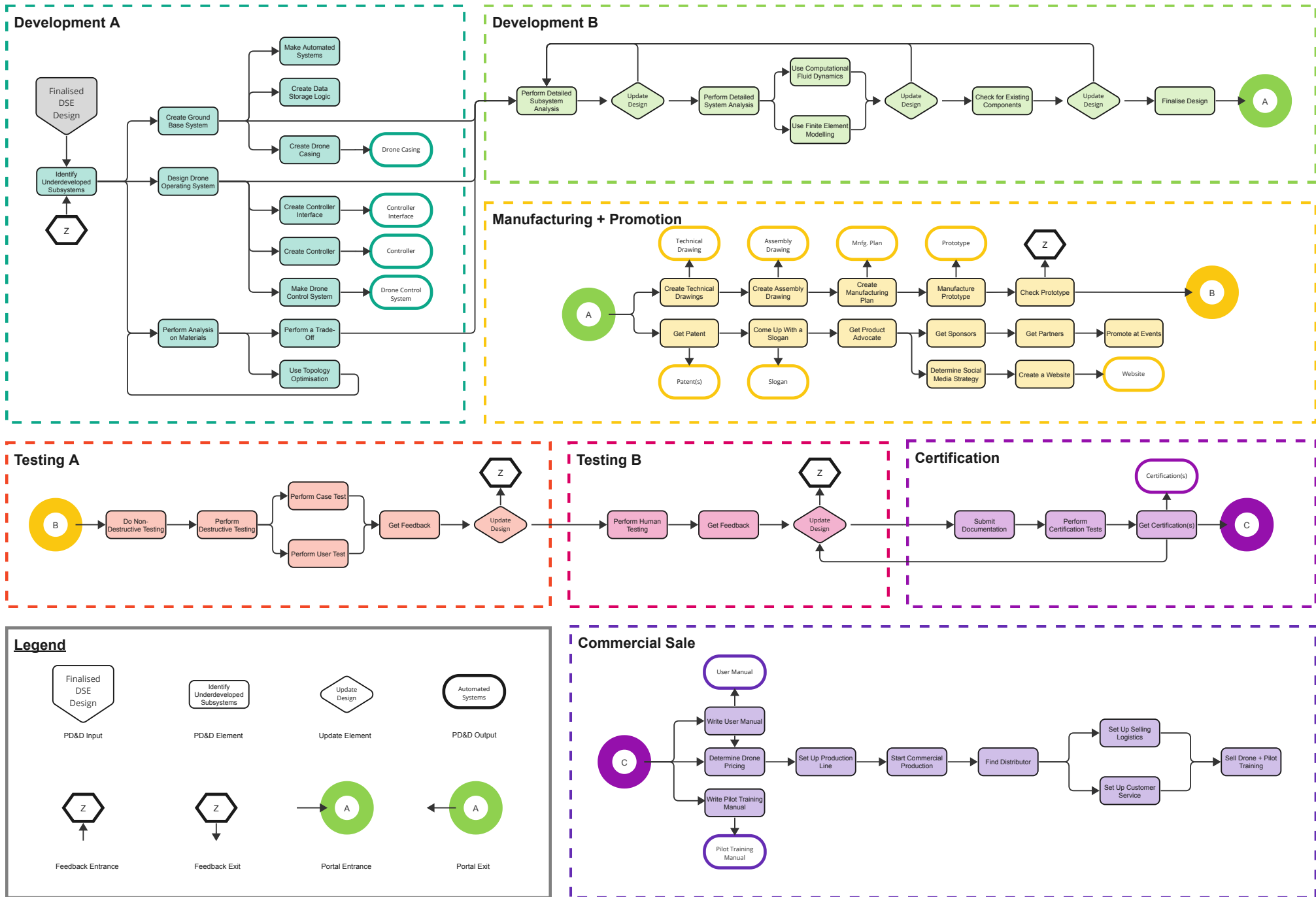
Certification

When the final design is completed, the drone needs to be certified. This is done in the certification phase. All documentation from previous phases, including the documents made during the DSE, have to be submitted to the certifying authorities. After passing the certification tests, the last phase is started.

Commercial Production and Sale

In this last phase, "Commercial Sale", the commercial production and sale of the drone start. First, a user manual and pilot training are written and the pricing of the drone is determined. Secondly, a production line is set up and commercial production starts. Thirdly, a distributor is needed to actually sell the drones to the customers and a selling logistics and customer service is set up. Finally, the drone can be sold together with operator training.

'Needle's Eye': Project Design & Development Logic Diagram 4



12.2. Manufacturing, Assembly and Integration

For the assembly and manufacturing of the drone, it is important to know how long each step in the manufacturing process takes and what the throughput is of the entire process. This, in turn, determines the amount of tooling and personnel needed to meet a certain production goal. In this section, a manufacturing goal of 140 units per year is assumed.

12.2.1. Manufacturing Timeline

The production timeline of the drone can be seen in Diagram 5, all arrows that flow into blocks but do not have an origin are inflows of materials. This means that these components are outsourced. The only in-house produced components are the structure, tracks and propeller blades.

For the production timeline, there are a few crucial steps. As can be seen in Diagram 5, the 3D printing of the structure takes the most time, taking an estimated 27 hours of time. However, since this is an automated process, personnel can simultaneously manufacture, assemble and test other critical subsystems. After the production of the structure has finished, it needs to be processed as the printing process is not perfect. Afterwards, the subsystems get mounted on the main body and wiring is installed. Then, the software is loaded and the system is tested as a whole. This includes software tests, subsystem integration and flight tests. Finally, the drone is packaged with all additional components such as spare parts, batteries and the base station.

12.2.2. Tools and Personnel Use

In the manufacturing process, there are multiple processes that happen simultaneously and others that can not. Following the manufacturing assembly and integration plan, an estimate can be made of the amount of personnel and manufacturing equipment that is needed.

When looking at the tooling and manufacturing equipment, the first major requirement is a 3D printer capable of continuous fibre-reinforced composite printing. AnisoPrint offers such a solution for 17800 euros, with a printing speed of $60 \text{ cm}^3/\text{h}$ [21]. If the 100 units per year (2080 working hours) need to be produced, with a time per unit of 87 hours, there need to be at least three 3 Aniso printers continuously running. Next to that, considering the amount of manual labour, an additional four production and assembly staff are needed to meet the production quota. This implies a manufacturing cost of 750 euros when taking into account average salary costs [111]. These costs are not taken into account into the 5,000 euros requirement. However, these costs should be recovered. Figure 12.1 shows the needed drone price to recover the initial investment and personnel costs, dependent on the number of drones produced.

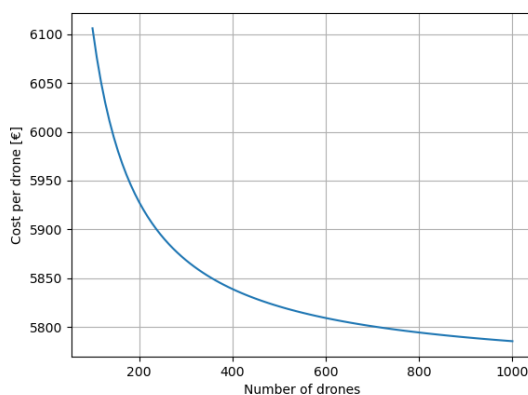
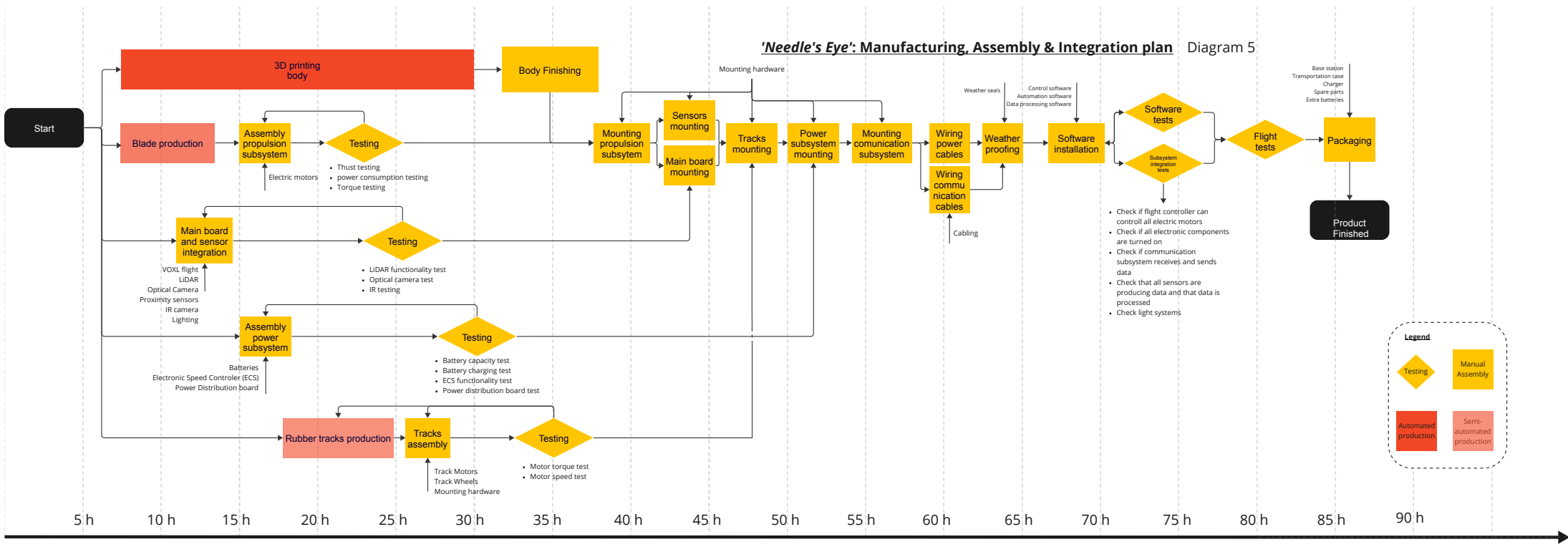


Figure 12.1: Production Costs per Drone with Varying Number of Drones

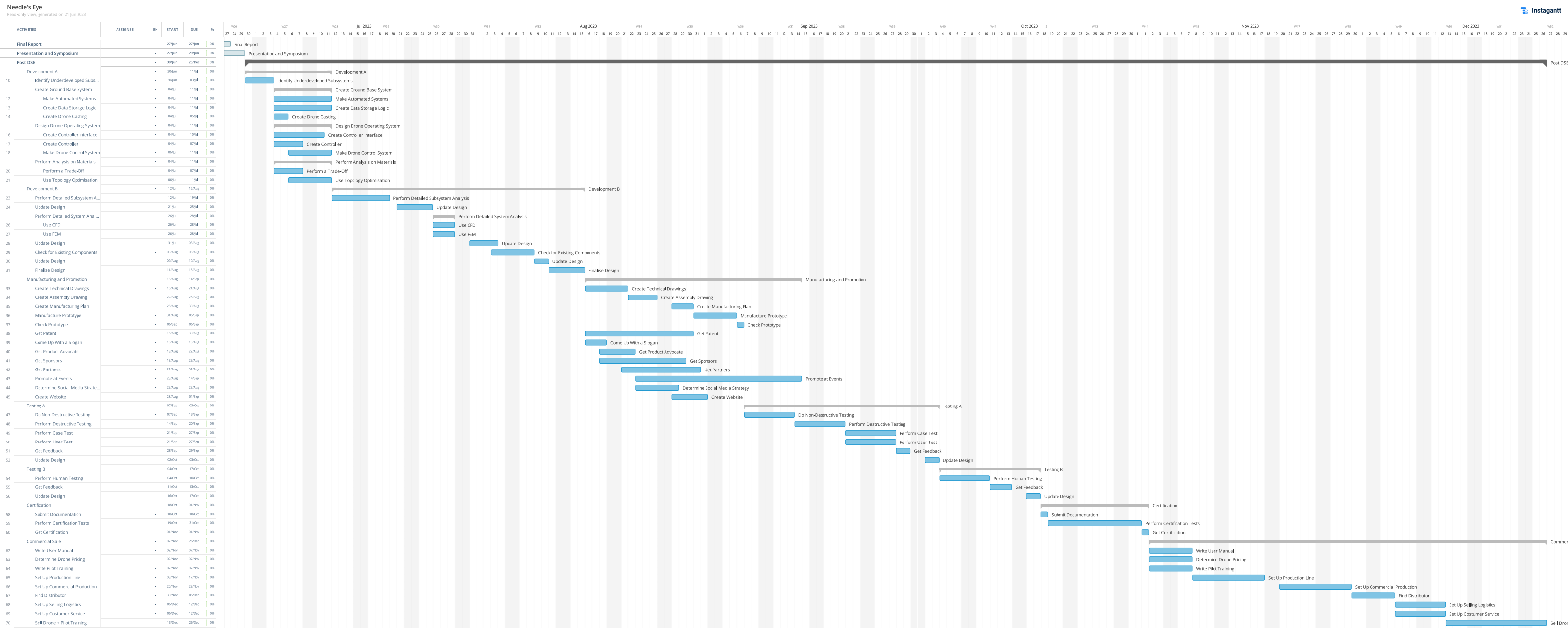
'Needle's Eye': Manufacturing, Assembly & Integration plan Diagram 5



Legend

- Testing (Yellow Diamond)
- Manual Assembly (Yellow Square)
- Automated production (Red Square)
- Semi-automated production (Light Red Square)

Gantt Chart Diagram 6



12.3. Project Gantt Chart

For the post-DSE timeline a Gantt Chart is made, shown in the Diagram 6. This Gantt Chart is a combination of the PD&D and the Manufacturing, Assembly and Integration (MAI) made previously. A rough time estimation is made for each process in the future design and manufacturing steps. It is estimated it will take half a year to bring the drone fully on the market.

12.4. Operations and Logistics

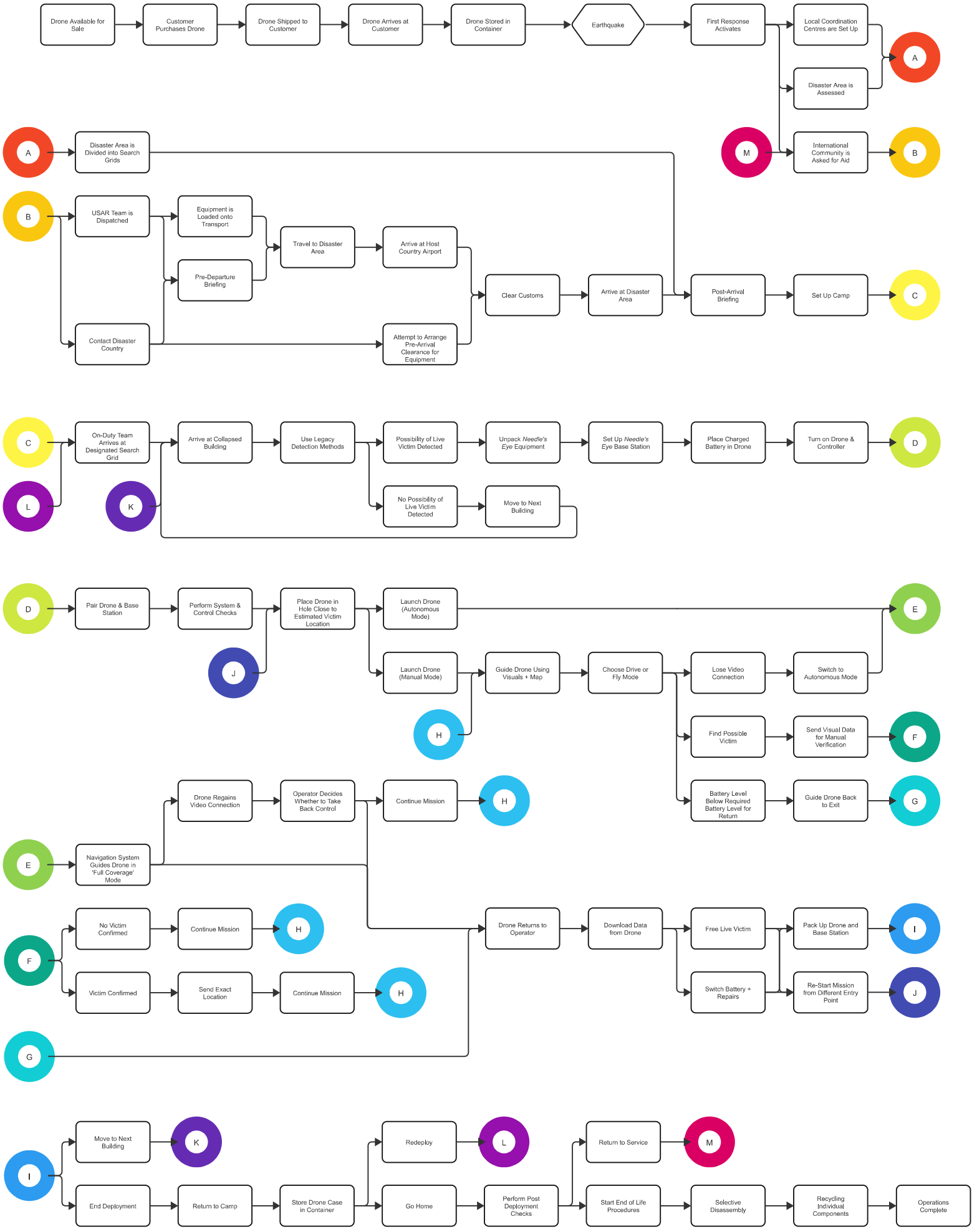
The PD&D plan was finalised with the commercial production and sale of the drone. The next phase is the logistics around distribution activities along with the operations that take place during the *Needle's Eye* mission. Maintainability characteristics were already addressed in section 10.3. Therefore, this section will specify the regulations and procedures undertaken during the operational phase along with an operational flow diagram that provides a complete overview.

- **Distribution Logistics:** The drone will be shipped with a case. In this case, the drone, batteries, charger, controller, base station and spare parts for the most critical components will be present. It will be a Samsonite S'Cure Spinner suitcase with paddings on the inside to prevent the drone from breaking. The final layout will look similar to the NANUK 970. The case and padding together cost between 210-260€. The specifications of the design are left to further research. The case, including the drone, will be shipped in a cardboard box. The padding used inside the box will also be made out of cardboard and not plastic. This is done to make the packaging as sustainable as possible.
- **Ground Operations:** SAR operations often provide an electrical power source for rescue teams. Charging procedures should allow for continuous operation. This is achieved by choosing a rechargeable and swappable battery. The charging cycles of such a battery, as the chosen one in chapter 3, are around 300 charges. To comply with the safe use philosophy, the current charging cycle should be documented. For the controller, it is aimed to make a deal with DJI. They have excellent drone controllers and there would not be a need to design one in-house. This design includes antennas and other technology which are not needed for our drone. The controller will be tailored to the needs of our drone in cooperation with DJI. The expected cost of the controller is 180-210 euros.
- **Operator Training:** For the drone to be operated safely, operators of the drone should be trained. As the operators of the drone will already have a drone pilot's license an online course will be developed. This course will instruct the operators on the exact functionalities of the drone in different situations and how the automated systems work. Once finished, the operator is an expert in piloting the drone and interpreting its sensor data. This course, whilst encouraged, will cost an optional €2000,- on top of the €5,000,- drone price. However, as an operator is likely to be able to use this drone for at least 30 missions the total operational costs for the *Needle's Eye* drone are €66.67 per mission.

To give a better overview of the exact way the operations of the *Needle's Eye* drone will unfold an operational flow diagram is presented on page 114. It outlines the key steps and processes involved in utilising the drone, from purchase to EOL.

Operational Flow Diagram

Diagram 7



12.5. Verification and Validation

In this report, numerous verification strategies have already been performed. However, there are still verification and validation procedures that have not yet been carried out. This section will propose all validation and verification procedures to be performed in the further development of the drone. The V&V procedures will be discussed per subsystem.

Power and Propulsion

For verification on the propulsion subsystem, other CFD programs will be used and compared to the Ansys program. Examples of other CFD programs that could be used for the verification are OpenFOAM and SimScale. Moreover, a comparison of thrust with existing propellers of the same size and shape could be made. The main validation activity for the propulsion system will be a static test of the whole propulsion system. Performing this static test will give the real thrust values the propulsion system is able to generate and its efficiency. The performance values calculated will be compared with the numerical values obtained from the static test.

The power subsystem will be validated by testing the run time of the battery. This is done by discharging the battery under realistic operation conditions. Also, a thermal analysis will be done to ensure enough heat dissipation is possible with passive airflow cooling.

Structures and Tracks

For structures, the main verification activities have already been performed. As explained in chapter 4, models were verified using FEM for the structure and RecurDyn for the tracks. As for the validation, it is important to test the performance of the track in real-world conditions with different kinds of soils and obstacles. Table 12.1 lists all validation procedures proposed for the tracks and structure

Table 12.1: Validation for Structures Subsystem

Validation method	Explanation
Tracks	
Obstacle size testing	Testing multiple sizes of obstacles in order to validate the RecurDYn model results
Maximum slope testing Tip over angle	Test at what angle the drone tips over to the side
Slip test	More accurate testing on which soils the track slips and how much. Validate the 5 % slip percentage used in the design.
Ground material test	Test the performance of the tracks on multiple terrain types.
Structures	
Collision test	Testing collisions of the required speeds and compare to the FEM results.
Structure failure tests	Validate the structural strength of the drone by applying loads proposed in the structures. Additionally, test the material until failure to validate the structural properties of the CFRC.
Structure weighing	Weighing the 3D printed structure and validating the calculated results.

Sensors and Data Handling

The verification process for the sensors and data handling subsystems involves testing the sensors and the VOXL Flight against their predefined specifications to confirm their functioning. This includes sensor calibration, performing sensor accuracy tests and assessing the integration with other sensors and subsystems of the drone that the sensors and data handling subsystems interact with. This ensures that the sensors can exchange data with all the necessary subsystems, such as navigation and stability and control.

The validation phase focuses on evaluating the overall performance and functionality of the sensors. This will be assessed with field tests. In these field tests, the sensors are appraised in simulated operational conditions. Various tests will be performed where the ability of the optical camera and thermal camera to identify victims is evaluated under different conditions. For example, assessing their performance in dark and dusty environments. Additionally, the results from subsection 5.3.1, subsection 5.3.2 and subsection 5.3.3 will be verified and validated by analysing the ability of the sensor to detect victims at varying distances and by assessing their effectiveness in distinguishing between a victim and an object or background.

Navigation

For verifying the navigation subsystem, the code can be unit tested. This will ensure that the code, containing the algorithms, functions properly. Next to this, the algorithms can be run on a variety of maps. With this, the algorithms are tested more extensively, evaluated in variable environments and can be verified by the different scenarios. Combining these two verification methods, the navigation subsystem can be used with confidence. Validation of the navigation subsystem refers to checking if the expectations of the system comply with real-world scenarios. This can be done by testing the navigation system in predetermined scenarios. These can be simulated as well and the result can be compared. The navigation model is considered validated if the drone reacts similarly in both environments in different scenarios.

Stability and Control

The verification for the dynamic model was done by simulating a vertical thrust, pure rolling/pitching and yawing. These responses to respective step rotor thrust and torque inputs were compared with Newton's second law in both translational and rotational ($\tau = I\dot{\alpha}$) forms. A dynamic model is constructed as a non-linear system to represent the system more accurately. However, it should still be validated by comparing the model predictions with experimental data collected in a real system. This would help to assess the discrepancies, which would improve the controller's accuracy to generate the required rotor commands. For the verification of the controllers, system tests have been performed to ensure that the rotor commands comply with the model response. Each block of the control loop diagrams was checked by simulating typical manoeuvres to identify any unusual behaviour. Along with system tests, verification can be done for smaller blocks of code by implementing unit tests. However, the complete controller should still be validated by integrating them into the hardware/software system. It should be confirmed that the processed sensor data can be used in feedback for the controller before validating the controller in a flight test.

Communication

Validation of the communication subsystem is done by testing the hypotheses set up in section 7.4. The 2.4 GHz signal is expected to penetrate up to two concrete walls and the 868 MHz signal will go through a maximum of three. This can be tested in an experimental setup. The results will provide insights into the performance of the designed subsystem.

Financial Evaluation

In this chapter, the financial parts of the *Needle's Eye* project are examined. First, in section 13.1 the costs associated with post-DSE development and production of a single drone are outlined. Then, a market analysis is performed in section 13.2, after which, in section 13.3 the Return on Investment of the entire project is calculated.

13.1. Cost Breakdown

This section elaborates upon the development costs of the *Needle's Eye* drone after the DSE, as well as the costs associated with producing a single drone. The values are based on both literature and figures from previous sections of the report. This section is also closely related to the product design and development section, seen in section 12.1. At the end of the section the cost breakdown structure is presented in Figure 13.1. In this figure all the different cost components are categorised and visualised in an AND tree.

Once the Design Synthesis Exercise is finished the drone should be developed further in order for it to enter commercial production. It is estimated that, at the current rate of ten students working full-time, this shall take four months. For this, office space of 70 m^2 needs to be rented, according to Lansink [112]. In the province of Zuid-Holland, this will cost €73.40 per square meter (on average) according to NVM [113]. Furthermore, wages need to be paid. It is determined that, for students, a reasonable wage is €12 an hour. Certification, testing and prototype creation are also accounted for, combined these will amount to €27,000 for this project, based on work by Khair [114]. An overview of these costs is provided in Table 13.1.

Table 13.1: Post-DSE Development Costs

Post-DSE Development Costs			
Cost Element	Cost	Quantity	Total Cost [€]
Office Rent	5,138 [€/month]	4	20,552
Salary	19,200 [€/month]	4	76,800
Certification	5,000 [€]	1	5,000
Testing	10,000 [€]	1	10,000
Prototype Creation	6,000 [€/unit]	2	12,000
Total:			124,352

The production costs for one drone are outlined in Table 13.2. Based on the component costs found in the resource allocation section in section 8.3, and adding a 5% margin to account for inflation a total component cost of €3,979.94 per drone is found. Manufacturing costs will be €750 per drone. The drone will be sold to customers for €5,000, and thus the gross profit, not accounting for investments or development costs, is established to be €270.06 per drone.

Table 13.2: Production Costs per Drone

Production Costs	
Cost Element	Cost [€]
Components	3,979.94
Manufacturing	750
Total:	4,729.94
Gross Profit:	270.06

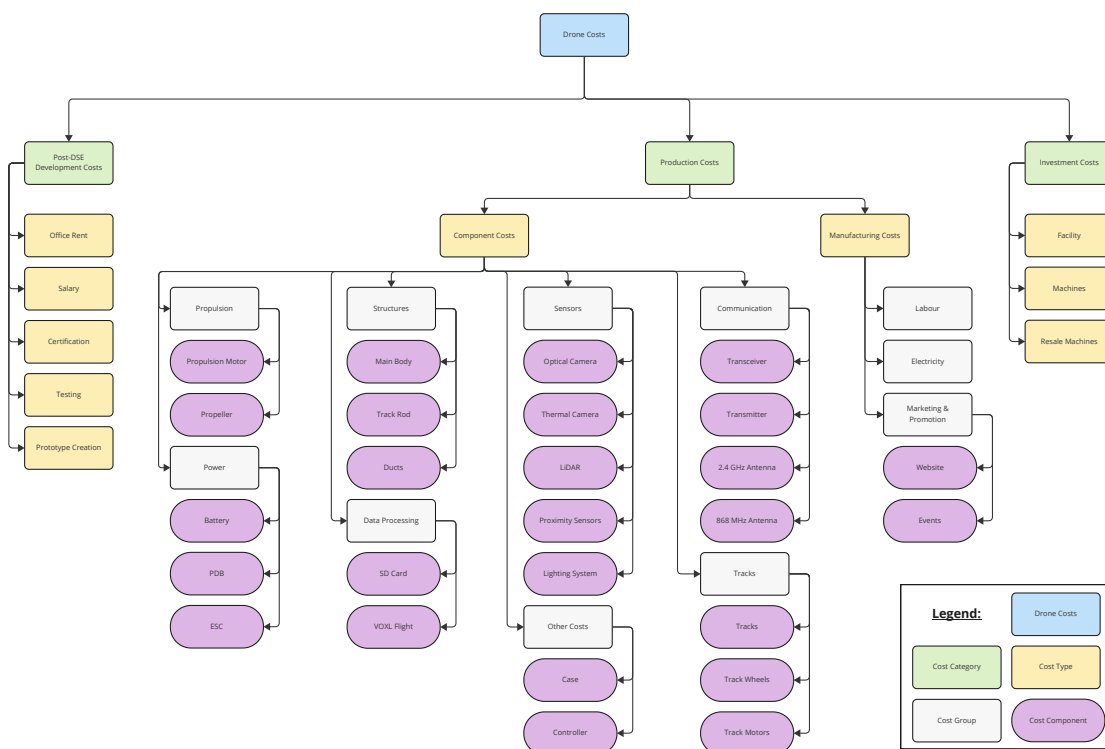


Figure 13.1: Cost Breakdown Structure

13.2. Market Analysis

The following section provides an analysis of the current market, a competitor analysis, an assessment of additional value, a prediction of future markets, an establishment of new markets, and a Strengths, Weaknesses, Opportunities and Threats (SWOT) analysis. These analyses are crucial for understanding the potential success and market position of the proposed *Needle’s Eye* drone for USAR missions. By evaluating the market landscape and considering various factors, the strengths, weaknesses, opportunities, and threats associated with the design can be identified and analysed.

Current Market

Three markets in which the drone will appear can be identified: the total Search and Rescue (SAR) equipment market, the SAR drone market and the indoor SAR drone market. Each market has its own worth of which the drone will be a part. Analysing the worth of each market indicates if there is a need for this SAR drone. For every market, the added value of the drone can be determined.

The total worth of the current SAR equipment market is 87.45 billion dollars and is expected to grow to 106.48 billion dollars in 2027 [115]. The current SAR drone market, which is a subset of this equipment market, is estimated to grow to 3.25 billion dollars this year, with a growth rate of 13.6 per cent [116]. Europe has the largest share in this market which is 31.4 per cent [117]. The indoor SAR market is not well established yet and only consists of a few products which are aimed at indoor inspection. Therefore, it is clear there is still a significant gap in the market for indoor SAR drones.

Competitor Analysis

Within the indoor SAR drone market, there are not many products available. However, some products are already on the market that satisfy some of the project objectives. These products are considered competitors to the proposed drone. In Table 13.4, possible competitive drones are listed together with their manufacturer. Next to that, some specifications are mentioned such as price, weight, size etc. For size, a specific scale is used which can be seen in Table 13.3.

Table 13.3: Drone Size Scale

Very Small	Small	Medium	Large
≤ 20x20 cm	≤ 40x40 cm	≤ 60x60 cm	> 60x60 cm

Table 13.4: Drones Currently on the Market and in Development

Drone	Manufacturer	Price [€]	Mass [g]	Size	Flight Time [min]	Autonomous Flight	Sensors
Scout 137 [118]	ScoutID	-	3,200	Medium	Unlimited	No	LiDAR, Camera, Lights and Proximity Sensors
Elios 3 [119]	Flyability	35,000	2,350	Medium	9.2	No	LiDAR, Camera, Thermal Camera, Lights and Proximity Sensors
DJI Avata [120]	DJI	579	410	Small	18	No	Camera and Proximity Sensors
Dronut [121]	Cleo	9,800	439.4	Small	12	No	LiDAR, Camera and Lights
V2 drone [122]	4DRC	50	300	Very Small	10	No	Camera
Stereo 2 [123]	Multinnov	900	1,400	Small	12	No	LiDAR, Camera, Lights and Proximity Sensors
Needle's Eye	TU Delft	5,000	1,300	Small	10-20	Yes	LiDAR, Camera, Thermal Camera, Lights and Proximity Sensors

At first glance, the design concept of the *Needle's Eye* drone outperforms its competitors based on the sensor capability. On top of that the *Needle's Eye* drone focuses on autonomous flight which is not common. This makes this drone stand out and it can be concluded that from first glance, the *Needle's Eye* drone will do well in the indoor SAR drone market.

Additional Value Assessment

The SAR drone market accounts for around 3.7% of the total SAR equipment market. The majority of this percentage is made up of large outdoor drones used for finding missing persons and mapping disaster zones. In contrast, urban rescue drones for indoor use are a relatively scarcely explored concept. These drones can provide critical benefits for rescue workers by mapping dangerous and confined spaces and finding victims before any rescue attempt is made. Additionally, the time to find a victim is the most important factor in the chance of survival. However, many currently available drones do not have the battery life to sustain a long flight duration [124].

The *Needle's Eye* drone provides a cost-efficient solution to these problems. It has a unique selling point, because of its size and the addition of tracks. It is a first of its kind which makes it appealing to the market. The tracks enhance the manoeuvrability of the drone which gives it an advantage over its competitors. The small size allows it to explore confined spaces where search dogs cannot enter. Lastly, the *Needle's Eye* drone has an autonomous navigation

system. Something that is not currently seen on the market. This extends the number of applications and possibilities of this drone beyond what its competitors can do. Because of these innovative features, the drone will add substantial value to the indoor SAR drone market.

Prediction of Future Markets

Indoor SAR drones are still a relatively new concept. The development of new systems and the improvement of already proven models can generate growth in this market significantly. In a recent study, the growth rate for the commercial drone market was estimated to be 38.6% from 2023 to 2030 in the US market, as visualised in figure 13.2 [125]. While this is not a one-on-one relation with the SAR drone global market, it is a clear indication that the overall drone market is growing significantly fast and thus the SAR drone market will likely follow.

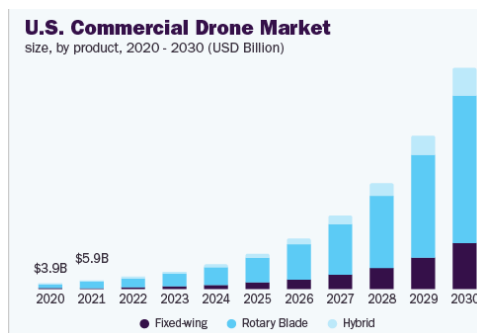


Figure 13.2: Drone Market Development US [125]

Establishment of New Markets

The main focus of this project was to develop a drone that can aid in SAR missions to locate people who are still alive. Moreover, the drone could easily be used for remote inspection activities. If the SAR drone market is not large enough to develop a profitable drone, it can be decided to enter the remote inspection market for industrial purposes, as this is a considerable additional customer base with similar requirements. Additionally, if breakthroughs lead to a significant increase in power budget, improvements in flight time and/or sensory capabilities are possible. These improvements will allow the drone to be more effective in its main purpose of finding victims.

SWOT Analysis

In this section, the operational SWOT analysis is performed and presented. This SWOT analysis is completed for the design process and decision-making. This can be done starting from the project objective "*In 10 weeks, a group of 10 students will create a design for a small drone that is energy-efficient and has the ability to fly and navigate through demolished and collapsed structures in order to search for survivors*" [2]. The result of the SWOT analysis is presented in table 13.5.

The strengths are helpful internal influences. These are the positive features of the design that are an advantage over the other products already in the market. The weaknesses are the internal factors that hinder the design from meeting the project objective. The opportunities are external factors that the product can benefit from. These could be possible tactics that will help elevate the design above others. Lastly, the threats are external factors that harm the product in the market. These are the aspects that cause the product to not reach the main objective [126, 127].

Table 13.5: SWOT Analysis

		Helpful	Harmful
Internal	Strengths		Weaknesses
		Product has autonomy	Autonomous flight operates worse than expected
		Product has low cost and is lightweight	Limited support during operations
		Product improves safety for SAR crew	Product requires additional training for SAR operators
		Product aids the usage of dogs	The project has limited resources
		Product allows access to environments not easily accessible for humans or dogs	Regulations in other countries may not allow the drone.
	Product is cheap with relation to products on the market.		
	Product reduces time to find victims		
External	Opportunities		Threats
		Government subsidies make operational and purchasing cost cheaper	Drone regulations could increase operational costs
		Technological advances in motors and efficiency increase flight time	Product is not competitive in the market with respect to new developed autonomous systems
		Component costs decrease due economics of scale	Material and component costs increase
		Increasing amount of natural disasters due to climate change	
		Drone could be used for other use-cases, increasing market size	

13.3. Return on Investment

Combining the information from the market analysis and the production capabilities found in the production plan in chapter 12, the project expects to be able to produce and sell 700 drones over a period of five years. Investments into the project need to be made. These can be seen in Table 13.6. Based on real estate research [128] the costs for the production facility are estimated to be €1,000 per month. The costs for the machines are taken from the production plan in section 12.2 and amount to €17,800 per unit. After the five-year production period, these are to be sold again. They are revalued based on a 5% linear depreciation.

Table 13.6: Investments

Investment Costs			
Cost Element	Cost	Quantity	Total Cost [€]
Facility	1,000 [€/month]	60	60,000
Machines	17,800 [€/unit]	3	53,400
Resale Machines	-13,773.30 [€/unit]	3	-41,319.90
		Total:	72,080.10
		Total (excl. machines):	60,000

The Return on Investment (RoI) is calculated with the help of Equation 13.1. Note that this calculates the gross RoI, as no taxation is taken into account. The calculation needed to arrive at the final gross RoI is shown in Table 13.7. The investment into machines is not taken into account for this calculation as it is expected that this project will be part of a larger conglomerate. These machines will likely be provided. In the case that they are not, the investment costs for these machines are shown in the table. It can be estimated that, of the €5,000 received for each drone produced, €6.70 are pure profit (without taking tax into account).

$$RoI = \frac{\text{Gross Return}}{\text{Cost of Investment}} \quad (13.1)$$

As is seen in the table, the *Needle's Eye* project, with an asking price of €5,000 only has a return on investment of 2.54%. This is very low and would not make it interesting for external parties to invest money in the project. However, Matthijs Schellaars explained that it will be possible to ask much more for a drone with functionalities like those of the *Needle's Eye* drone. If the asking price for the drone would be increased by only €200, up to €5,200, a RoI of 78.5% can be attained. This is much better and very interesting for investors. The way the

return on investment responds to differences in asking price is shown in Table 13.7. It is also concluded that the break-even point for the drone is €4,993.30.

Table 13.7: Return on Investment Calculation

Element	Amount	Unit
Profit per Drone	270.06	[€/drones]
No. of Drones	140	[drones/year]
No. of Years	5	[years]
Total Drones Produced:	700	[drones]
Gross Profit:	189,042	[€]
Development Costs	124,352	[€]
Investment (excl. machines)	60,000	[€]
Total Costs:	184,352	[€]
Gross Return:	4,690	[€]
Gross Rol:	2.54	[%]

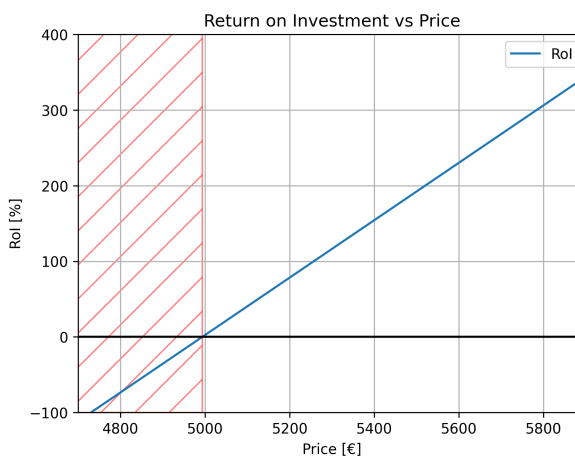


Figure 13.3: Rol Response to Price Changes

Conclusion

The purpose of this report was to finalise and present the design of a SAR drone that is able to localise victims while moving within confined environments underneath the debris. First, the project objectives and requirements were summarised. Based on these objectives and requirements, the drone functionality is presented in a functional flow diagram and functional breakdown structure. Hereafter, each subsystem was designed in detail using different types of analyses. These subsystems were combined, and a configuration and a hard- and software overview were made. Performance analysis on the design was performed and its capabilities and effectiveness were shown in a use case example. The reliability, availability, maintainability and safety characteristics were elaborated on, after which a product design and development plan was presented. This plan highlights the development, manufacturing, promotion, testing, certification, commercial production and sale of the drone. The operations and logistics of the drone were shown in an operational flow diagram. A verification and validation plan per subsystem was proposed for further development. Lastly, a financial evaluation was performed, analysing how financially viable the product is.

Table 14.1: Characteristics of the Drone

Characteristics		
Max. Thrust	31.2	[N]
Average Power	70	[W]
Weight Drone	1,116	[g]
Width Drone	257	[mm]
Length Drone	282	[mm]
Height Drone	109	[mm]
Number of Blades	9	
Propeller Diameter	60	[mm]
Propulsion Type	Quad Ducted Propeller	
Operating Time	10-20	[min]
Battery Type	Gens Ace Soaring	
Battery Capacity	3300	[mAh]
Battery Voltage	11.1	[V]
Number Propeller Motors	4	
Propeller Motor Type	Racerstar BR1103B	
Number Track Motors	2	
Track Motor Type	TMotor F2203.5 Motor 1500kV [27]	
Number ESCs	6	
ESC Type	Hobbywing Flyfun	
PDB Type	Matek PDB-XT60	
Thermal Management Type	Passive airflow cooling	
Transceiver	HopeRF RFM95M	
Antenna A	SMP.868.35.6.A.02	
Transmitter	FuriousFPV VTX Stealth Long	
Antenna B	FuriousFPV Two Slice Patch Antenna 2.4 GHz	
Flight Controller	VOXL Flight	
Main Sensors	LiDAR, Optical Camera & Thermal Camera	
Additional Features	Lighting system, Proximity Sensors, Gyroscope & Accelerometer	

An overview of the characteristics of the subsystems for the final design is listed in Table 14.1. Additionally, the material choices for different components of the drone are listed in Table 14.2.

Table 14.2: Material Selections

Materials	
Center Plate	CFRC
Tracks support	CFRC
Arms	CFRC
Propeller Blades	CFRP
Tracks	HNR

Structures and Tracks

For the structure, a continuous fibre-reinforced polymer will be used as a material. This will be produced using a 3D printing method. Following from analysis minimum dimensions were calculated for the base plate, track rod, and fan mid-part. These dimensions ensured that the stresses in the structure do not exceed 511 MPa . All load cases were verified using FEM software and this confirmed the analytical model. For the tracks, HNR was chosen as a material as it posed to have superior material characteristics. The tracks run over the drone and are situated next to the ducts. This ensures the protection of all drone components while not blocking the airflow of the propulsion subsystem.

Navigation, Stability and Control

The drone will use its LiDAR sensors to make a 3D map that can be used for navigation. It will use an algorithm which first determines points of interest, then, sets a goal and finally finds a path towards it. These points are placed at locations the drone has not been to yet. Based on the DBSCAN clustering algorithm, points that refer to the same passage are combined to create a goal. The drone then uses the A* algorithm to find the best path towards that goal and the best path back to base. This method has been simulated and proven in 2D. A control method combining a PD for the attitude manoeuvres and a PID controller for the positional manoeuvres is designed. Two sets of gains are implemented for the positional controller: stiff gains with more accuracy but slow response and soft gains with less accurate but fast response. With stiff control in use, it is found that the drone is able to move through the narrowest gap with a clearance of 10 cm . The stability analysis has shown that any worst-case disturbance occurring when the soft control is in use results in catastrophic failures.

Propulsion and Power

Using literature, a Blade Element Analysis (BEA) model and a Computational Fluid Dynamics (CFD) model a ducted fan propeller was designed. The designed propeller meets all the requirements stated. However, it was found that optimisation is still possible. Specifically, due to the short duct the direction of the flow at the duct outlet is directed outwards, reducing the useful thrust gained. A longer duct is thus likely preferable. For the power subsystem a trade-off has been performed on electrical components and a selection was made. The drone uses a Power Distribution Board (PDB), six Electronic Speed Controllers (ESCs) and a $3,300 \text{ mAh}$ battery. Additionally, these components are cooled using a passive thermal system based on a 3D printed aluminium alloy Tetrahedral Lattice Porous Plate (TLPP).

Sensors

The drone has been equipped with two LiDAR sensors, five proximity sensors, a lighting system and an optical and a thermal camera. The LiDAR system will be used for the construction of a 3D map and preventing collisions, with proximity sensors as a redundancy. The thermal camera will be the main sensor to detect victims. The optical camera is added as redundant, as it is not as good at identifying victims. The lighting system is installed as the optical camera requires lights to identify victims. Also, the optical camera can be used to allow a drone operator to fly the drone.

Communications

The main challenge of the communication system is to maximise the range of the signal through multiple layers of reinforced concrete, to allow the drone to operate optimally inside collapsed buildings. To minimise communication losses, telemetry and mapping will be sent from the drone to the operator, while it receives control input all via an 868 MHz signal, as signal attenuation is worse for higher frequencies. Only visual data will have to be transmitted from the drone to the ground station via a 2.4 GHz link to ensure sufficient quality for remote control of the drone, as well as to allow visual identification of victims. Suitable antennas, transmitters, receivers and a transceiver have been selected to comply with the communication requirements. The link budget indicated an excess margin in signal power, although this margin will reduce in a more detailed analysis of the signal quality, as at this moment only free space loss has been taken into account. It has been established that the 868 MHz signal can penetrate three walls of 30.5 cm thickness before a communication link can no longer be established between the drone and the ground station. For the 2.4 GHz signal, this already happens when the signal has to penetrate two walls. Once the video feed quality received by the ground station falls below an established threshold, the drone will continue autonomously until a stable connection has been re-established for more than ten seconds.

Sustainability

While designing the drone, it was aimed to implement sustainability as much as possible, as well as to produce the drone in the most sustainable way. Therefore, a sustainability plan was proposed. In this proposal, the lean manufacturing philosophy is aimed for and the amount of testing material and testing should be minimised. Selective disassembly is key in recycling the drone and the components for which no clear recycling strategy could be decided upon should be made as durable as possible. The contribution of sustainability is not of the highest priority as the drone needs to be able to save lives without being constrained by sustainability requirements. The system characteristics that are not specified in Table 14.2 can be detailed for each technical aspect.

Post-DSE Developments

Once DSE is finished, multiple steps need to be taken in order to bring the drone to the market. These steps were outlined in a Product Design and Development (PD&D) plan. Furthermore, a production plan was created, outlining the steps and machines to manufacture the drone and the production timeline. Plans for validation and verification of the drone were drawn up and the operations of drone usage were specified. The operational costs amount to €66.67 per mission, due to training. A financial evaluation, including a market and SWOT analysis outlined the costs associated with drone production and development. The return on investment is 2.54%.

To conclude, the *Needle's Eye* drone is considered a viable option for missions that require identifying a victim in confined places. However, the detailed design can still be optimised with further iterations and developments. Therefore, recommendations are provided in chapter 15.

Recommendations

In this chapter, suggestions are made to further optimise the design of the drone. First, recommendations for all the separate subsystems are provided. Then, recommendations for the drone as a whole as proposed.

Power and Propulsion

First of all, in the CFD analysis, the fan mid-part is not accounted for. The design was simplified to only the duct and the propeller, without its connections to the duct. This may result in differences in how the flow goes through the duct and may give different results. Hence, performing a CFD analysis including the fan mid-part is recommended. Next to this, it is encouraged to optimise the design of the fan mid-part. At the moment, it only functions as a load-carrying structure, however, giving it an aerodynamic shape, it can function as a stator blade ¹. Thereby, as already stated in subsection 3.1.3, it is advised to optimise the design of the duct in future designs. The full advantages of using a duct are not yet achieved, as the flow is not yet effectively directed downwards. By increasing the height of the duct, the downward direction of the flow will be improved.

Also, analyses of the structural design of the blades and on-the-ground and wall effects are suggested. It is interesting to look at forces acting on the blades and how they will handle these. Ground and wall effects are not negligible, as in the USAR-use case, the drone has to fly through small spaces. Thus, the drone will experience, for example, increased induced flow. This may result in a change in propeller thrust and efficiency.

Lastly, for the power subsystem, it is recommended to perform a quantitative analysis of the thermal management. The use of passive cooling is selected. However, it is needed to look at the heat-transferring capabilities of the materials and to do research on the common air temperatures emerging in the USAR-use case.

Structure and Track

In the analysis of the track and structure, a few recommendations arose. These analyses were not performed in this report due to time constraints. First, an operational combination of the track and propulsion subsystem could be made. When the track slips the propulsion subsystem could help create extra grip or provide additional thrust. An analysis could be performed in order to determine the maximum slope and bank angle with this addition. When looking at the structure, topology optimisation is an interesting area to look at. This could reduce the mass of the body by a significant amount and strengthen parts of the drone that are now under high stress. This is possible since the production method also allows for more complex shapes.

For the tracks, it is interesting to look at the detection of track slips. If the drone is able to detect when it slips it can determine earlier and easier if the terrain is not suitable for tracked operations. This could increase operational time efficiency.

Lastly, the analysis of different road materials. The software RecurDyn does not allow for

¹A stator blade is a stationary airfoil component in a turbine or compressor that directs the flow, increasing its efficiency.

different road materials and it is unclear what the properties are of the used road material. Therefore, it is recommended that different software can be used for the analysis of the tracks on different types of terrain. This would give more insight into the capabilities of the tracks.

Sensors and Data Handling

The main recommendation for the sensors subsystem is to perform further research into developing an algorithm that is able to identify victims in dark and dusty environments using an optical camera and a thermal camera. The existing algorithms mentioned in subsection 5.3.4 can be improved or adjusted making them more applicable to the operating environments of the drone. Most existing victim identification algorithms are focused on detecting movement or require the entire victim to be visible. Both might be unattainable in confined environments as victims are (partially) obstructed. These are the environments encountered by the drone in its specific use case.

Furthermore, for the data handling subsystem, the benefits of sensor data fusion can be explored in further research. Data fusion is combining data from multiple sensors, such as the optical camera and the thermal camera. Combining information from several sensors can improve the accuracy of identifying victims.

Navigation, Stability and Control

The proposed solution for navigating the drone is not complete. As discussed, the simulation proposition is for a 2D space. However, in real-life situations and the USAR use case, the drone should function within a 3D environment. Therefore, some recommendations are suggested.

As of now, the drone is able to map while moving in an unknown 2D environment. The 3D PAEDT algorithm by Li et al. [70] presents a solution for extending the shortest path algorithm used in the navigation of the drone into a 3D environment combining A* and distance transformations. Also, Andreas Nüchter, one of the authors of 'Pose estimation and mapping based on IMU and LiDAR' by Kaltenthaler et al. [78] suggested looking into Rapidly exploring Random Trees (RRT) as it performs better. Furthermore, Lee et al. [129] prove a concept for 3D exploration that can be used within our navigation subsystem. Lastly, The paper discussed by Famili et al. [63] proposes a method called ROLATIN using acoustics that can be utilised to extend to the 3D space. However, further research is necessary for this method, as it utilises different sensors in the proposed solution.

All the above-mentioned methods are recommended to look into as they pose solutions to the real-life situations that the drone may encounter in this use case. The main recommendation is to extend the 2D navigation subsystem to the 3D space. Next to this, obstacle clearance is suggested to be incorporated. This can extend to a clearance distance difference between walls and victims. Lastly, the battery-level return-to-base implementation is recommended to use as it is important for the drone to return to base when battery levels are low and the drone will not be operable for much longer.

The stability and control subsystem used the mass value from the conceptual design as the complete payload mass was not determined yet. Final inertia and rotor moment arm values were already incorporated in the simulations. The next iteration should investigate the trade-off between stability and controllability. The used mass of 2 kg is half a kilogram higher than the current mass, which could negatively affect stability but would result in easier control with less required propeller thrust. Moreover, the robustness of the controller can be assessed by performing a sensitivity analysis on the drone parameters. Another aspect that should be further investigated is the effect of the tracks, in terms of center of mass location. Its effect on the manoeuvrability in narrow gaps can be explored as the simulation represents the movement of the centre. Lastly, it is important to note that the designed controllers were tuned manually.

Methods such as root locus can be used to tune the gains more efficiently in terms of time and accuracy.

Communication

The communications subsystem has been designed with maximum wall penetration in mind. To that end, the frequencies used by the drone are 868 *MHz* and 2.4 *GHz* as these have a longer range. Also, the chosen antennas are circularly polarised in order to minimise the effects of multi-path interference. However, in future developments, it is recommended to perform extensive real-world testing on the communications subsystem. Not only outside and in obstructed indoor spaces, but also in collapsed buildings. This way, the true range of the system can be estimated more accurately. This does not take away from the fact that the communications range will always be heavily dependent on the specific building layout, collapse type and materials. Therefore, it is impossible to accurately describe the properties of the received signals for all situations. When performing physical testing, it is also important to compare linear and circular antennas against each other. Linear antennas have an advantage in that they, due to their polarization, tend to penetrate walls better than circular antennas. They are, however, very sensitive to multi-path interference. Finding out exactly what antenna type works best for collapsed buildings is an important aspect of further research. Additionally, different types of circular antennas may be tested. Lastly, the drone may be fitted with a WiFi (or Bluetooth) module. This would allow the drone to transmit all the data wirelessly to the operator upon return. In the current configuration, this has to be done by downloading the data from the external SD card inside the drone. Doing this with a wireless connection would be better for the overall effectiveness of the operation.

General Recommendations

Next to the recommendations made for each of the subsystems, recommendations are also suggested for the drone as a whole. This is mainly focusing on the complete concept and design. Additionally, some suggestions are made considering the drone's operational versatility, user interface, and maintenance requirements.

The final design is a ducted-fan quadcopter with tracks such that the drone can drive next to flying. Even though this is a solid design, another look could be taken at the tilting rotors concept. It is suggested to see whether tilting rotors can be implemented within the design as this would significantly increase the stability of the drone.

In addition, a comprehensive analysis can be conducted to explore possibilities for enhancing the design's modularity. The drone will greatly benefit from having such a design, as parts can easily be replaced and repair costs will decrease. Next to this, the possibility of having swappable sensors could be explored. This allows the operator to select the right combination of sensors based on the mission environment. With this, the functional value and the operational time will increase as not all sensors will be used at all times. Additionally, the concept of removable tracks could be explored. This will mean that the drone's body does not have protection from the tracks, however, it is smaller making it possible to fit through holes the drone with tracks might not be able to go through.

For the drone, it is suggested to look into the use of standardised interfaces. By implementing more common industry standards, easy integration of parts is enabled and the user can easily replace parts. Also, it is recommended to look into incorporating user-friendly features enhancing intuitive operations such as simplified controls and/or user assistance systems.

In conclusion, taking into account all the recommendations mentioned above, future developments should aim to optimise the drone's stability, modularity, and user-friendliness. This will ultimately improve the drone design, which ensures SAR operation is more effective.

Bibliography

- [1] Hotpot. AI Art Generator, 2023. URL <https://hotpot.ai/art-generator>.
- [2] Ryan Bergmans, Mischa De Gooijer, Julia Huigen, Rosa De Jong, Jonas Meij, Jelmer Ottens, Timo Van der Paardt, Liam Saanen, Alexandra Schelling, and Egement Süülker. Project Plan Needle ' s. Technical report, Technische Universiteit Delft, 2023.
- [3] Ryan Bergmans, Mischa de Gooijer, Julia Huigen, Rosa de Jong, Jonas Meij, Jelmer Ottens, Timo van der Paardt, Liam Saanen, Alexandra Schelling, and Egemen Süülker. Needle's Eye A Drone to Find the Last Ones Baseline Report. Technical report, Technische Universiteit Delft, Delft, 2023.
- [4] Ryan Bergmans, Mischa de Gooijer, Julia Huigen, Rosa de Jong, Jonas Meij, Jelmer Ottens, Timo van der Paardt, Liam Saanen, Alexandra Schelling, and Egemen Süülker. Needle's Eye A Drone to Find the Last Ones Midterm Report. Technical report, Technische Universiteit Delft, Delft, 2023.
- [5] Yu Hu, Ji xiang Qing, Zhong Huan Liu, Zachary J Conrad, Jia Ning Cao, and Xue Peng Zhang. Hovering efficiency optimization of the ducted propeller with weight penalty taken into account. *Aerospace Science and Technology*, 117:106937, 2021. ISSN 1270-9638. doi: <https://doi.org/10.1016/j.ast.2021.106937>. URL <https://www.sciencedirect.com/science/article/pii/S1270963821004478>.
- [6] Young Woo Son, Deokhun Kang, and Jonghoon Kim. Passive battery thermal management system for an unmanned aerial vehicle using a tetrahedral lattice porous plate. *Applied Thermal Engineering*, 225(August 2022):120186, 2023. ISSN 13594311. doi: 10.1016/j.applthermaleng.2023.120186. URL <https://doi.org/10.1016/j.applthermaleng.2023.120186>.
- [7] Rhea Mogul, Gul Tuysuz, Isil Sariyuce, Kareen El Damanhoury, and Rob Picheta. More than 4,300 dead in Turkey and Syria after powerful quake, 2 2023. URL <https://edition.cnn.com/2023/02/05/europe/earthquake-hits-turkey-intl-hnk/index.html>.
- [8] Joanna Pietrzak. Development of high-rise buildings in Europe in the 20 th and 21 st centuries Civil Engineering , Urban Planning and Architecture. *Challenges of Modern Technology*, 5(4):31–38, 2013.
- [9] Andrei Anisimov. Project Guide Design Synthesis Exercise. Technical report, 2023.
- [10] Knut Giljarhus. pyBEMT: An implementation of the Blade Element Momentum Theory in Python. *Journal of Open Source Software*, 5(53):2480, 2020. doi: 10.21105/joss.02480.
- [11] Airfoiltools. Airfoiltools, 2023. URL <http://airfoiltools.com/index>.
- [12] Inc. Ansys. ANSYS FLUENT 12.0 Theory Guide. Technical report, 1 2009.
- [13] FR Menter, R Sechner, Ansys A Germany GmbH Matyushenko, and St Petersburg. Best Practice: RANS Turbulence Modeling in Ansys CFD. Technical report, 2021.
- [14] Pasquale M. Sforza. *Propellers*. 2017. ISBN 9780128093269. doi: 10.1016/b978-0-12-809326-9.00010-5.
- [15] ASSUN MOTORS. Understanding DC Brushless Motor Efficiency & How to Test For It, 2022. URL <https://assunmotor.com/blog/dc-brushless-motor-efficiency/>.
- [16] Ali Akturk and Cengiz Camci. Tip clearance investigation of a ducted fan used in VTOL unmanned aerial vehicles- part I: Baseline experiments and computational validation. *Journal of Turbomachinery*, 136(2): 1–10, 2013. ISSN 0889504X. doi: 10.1115/1.4023468.
- [17] Roy Beardmore. Torsion Formula's, 2023. URL https://roymech.org/Useful_Tables/Torsion.html.
- [18] LibreTexts Physics. 9.3: Impulse And Collissions, 2023. URL [https://phys.libretexts.org/Courses/Joliet_Junior_College/Physics_201_-_Fall_2019v2/Book%3A_Custom_Physics_textbook_for_JJC/09%3A_Linear_Momentum_and_Collissions/9.03%3A_Impulse_and_Collissions_\(Part_1\)](https://phys.libretexts.org/Courses/Joliet_Junior_College/Physics_201_-_Fall_2019v2/Book%3A_Custom_Physics_textbook_for_JJC/09%3A_Linear_Momentum_and_Collissions/9.03%3A_Impulse_and_Collissions_(Part_1)).
- [19] M. Zaludek, S. Rusnakova, M. Kubisova, O. Bilek, and K. Karvanis. Fatigue life of thermoset composite materials. In *IOP Conference Series: Materials Science and Engineering*, volume 726. Institute of Physics Publishing, 1 2020. doi: 10.1088/1757-899X/726/1/012016.
- [20] Andrey V Azarov, Fedor K Antonov, Mikhail V Golubev, Aleksey R Khaziev, and Sergey A Ushanov. Composite 3D printing for the small size unmanned aerial vehicle structure. *Composites Part B: Engineering*, 169: 157–163, 2019. ISSN 1359-8368. doi: <https://doi.org/10.1016/j.compositesb.2019.03.073>. URL <https://www.sciencedirect.com/science/article/pii/S1359836818320031>.
- [21] Aniso Print. Aniso Print CFRP, 2023. URL <https://anisoprint.com>.
- [22] Imakr. ANISOPRINT, 2023. URL <https://www.imakr.com/eu/409-anisoprint>.
- [23] J. Y. Wong. *Theory Of Ground Vehicles*, volume 1. John Wiley Sons, New York, 1 edition, 2001.
- [24] The University of Akron: School of Polymer Science and Polymer Engineering. Plastics and Rubber: What's the Difference?, 2023. URL <https://www.uakron.edu/polymer/agpa-k12outreach/lesson-plans/plastics-and-rubber-whats-the-difference>.

- [25] Ronald J. Schaefer. *Shock and Vibration Handbook*, volume 1. McGraw Hill, 1 edition, 1995.
- [26] FCS FLUORO CARBON SEALS PVT LTD. HNBR, 2023. URL <https://www.fluorocarbonseals.com/hnbr.html>.
- [27] UnmannedXtech. TMotor F2203.5 Motor (1500kV), 2023. URL <https://www.unmannedtechshop.co.uk/product/tmotor-f2203-motor/>.
- [28] The Engineering Toolbox. Factors of Safety - FOS - are important in engineering designs., 2010. URL https://www.engineeringtoolbox.com/factors-safety-fos-d_1624.html.
- [29] Statista. Monthly price of rubber at the Singapore Commodity Exchange from January 2020 to April 2023 , 2023. URL <https://www.statista.com/statistics/727582/price-of-rubber-per-pound/>.
- [30] Manoranjan Paul, Shah M.E. Haque, and Subrata Chakraborty. Human detection in surveillance videos and its applications - a review. Technical Report 1, 2013.
- [31] RunCam. RunCam Cameras, 2023. URL <https://www.runcam.com/>.
- [32] Foxeer. Foxeer 4K Ambarella A12 Camera, 2023. URL <https://www.foxeer.com/foxeer-4k-ambarella-a12-camera-uav-pwm-remote-control-wifi-distortionless-lens-tv-out-micro-hdmi-new-version>.
- [33] ArduCam. ArduCam IMX477, 2023. URL <https://www.arducam.com/product/b0242-arducam-imx477-hq-camera/>.
- [34] A Llamazares, Ej Molinos, M Ocaña, LM Bergasa, N Hernández, and F Herranz. 3D Map Building Using a 2D Laser Scanner. Technical report, 2011.
- [35] LightWare LLC. SF45/B Product Guide. URL <https://support.lightware.co.za/sf45b/#/introduction>.
- [36] LightWare Optoelectronics. SF40/C Product Guide. Technical report, 2019. URL www.lightware.co.za.
- [37] YDLIDAR. YDLIDAR T-MINI PRO DEVELOPMENT MANUAL. Technical report, 2022. URL www.ydlidar.com.
- [38] LDROBOT. LDROBOT D300 LiDAR Kit – 360-degree Laser Range Scanner (12 m). URL <https://www.elektor.com/ldrobot-d300-lidar-kit-360-degree-laser-range-scanner-12-m>.
- [39] Teledyne FLIR. FLIR LEPTON Datasheet. Technical report.
- [40] Teledyne FLIR. FLIR AX8, 2023. URL <https://www.flir.eu/products/ax8-automation/?vertical=rd+science&segment=solutions>.
- [41] Teledyne FLIR. TELEDYNE FLIR BOSON AND BOSON+ THERMAL IMAGING CORE PRODUCT DATA SHEET. Technical report, 2022.
- [42] GreenICE. CH-COB-5W-CW, 2023. URL <https://greenice.com/nl/hoog-vermogen-cobs/4176-led-hoge-spanning-5w-500lm-6000ok-cob-40-000h-ch-cob-5w-cw-8435402541806.html>.
- [43] Carlos Sanchez, Gabriel Cristóbal, Gloria Bueno, Saul Blanco, Maria Borrego-Ramos, Adriana Olenici, Anibal Pedraza, and Jesus Ruiz-Santaquiteria. Oblique illumination in microscopy: a quantitative evaluation. Technical report.
- [44] Sharp. gp2y0a41sk_e. .
- [45] Sharp. GP2Y0A41SK0F_datasheet. .
- [46] How to Choose Lighting for Harsh Industrial Environments. URL <https://www.bannerengineering.com/sg/en/company/expert-insights/lighting-harsh-industrial-environments.html>.
- [47] ModalAI. VOXL Flight, 2022. URL <https://docs.modalai.com/voxl-flight/>.
- [48] Samsung. Samsung micro SD UHS-I Card: EVO Plus Lineup. Technical report, 2023.
- [49] Mengwen He, Huijing Zhao, Jinshi Cui, and Hongbin Zha. Calibration method for multiple 2D LIDARs system. In *Proceedings - IEEE International Conference on Robotics and Automation*, pages 3034–3041. Institute of Electrical and Electronics Engineers Inc., 9 2014. ISBN 9781479936854. doi: 10.1109/ICRA.2014.6907296.
- [50] Renu Khandelwal. An Easy Explanation of Kalman Filter, 3 2022.
- [51] Richard E. Thomson and William J. Emery. The Spatial Analyses of Data Fields. *Data Analysis Methods in Physical Oceanography*, pages 313–424, 1 2014. doi: 10.1016/B978-0-12-387782-6.00004-1.
- [52] K Chrzanowski. Simple minimum resolvable temperature difference model for thermal imaging systems. Technical Report 1, 1990.
- [53] M Gašparović and D Gajski. Testing of Image Quality Parameters of... Technical report, 2016. URL <https://www.researchgate.net/publication/311487225>.
- [54] Infinite Electro-Optics. Rating Camera Performance. Technical report, 2021.
- [55] Alambra K Mah J. Depth of Field Calculator, 2023. URL <https://www.omnicalculator.com/other/depth-of-field>.
- [56] Damien Fournier Photography. DoF – The simplified formula to understand DoF. URL <https://damienfournier.co/dof-the-simplified-formula-to-understand-dof/>.
- [57] Bo Wu and Ram Nevatia. Detection of Multiple, Partially Occluded Humans in a Single Image by Bayesian Combination of Edgelet Part Detectors. Technical report, 2005.

- [58] Bo Wu and Ram Nevatia. Detection and tracking of multiple, partially occluded humans by Bayesian combination of edgelet based part detectors. Technical Report 2, 11 2007.
- [59] Sander Krul, Christos Pantos, Mihai Frangulea, and João Valente. Visual slam for indoor livestock and farming using a small drone with a monocular camera: A feasibility study. *Drones*, 5(2), 6 2021. ISSN 2504446X. doi: 10.3390/drones5020041.
- [60] Institute of Electrical and Electronics Engineers. Enhanced UAV Indoor Navigation throughSLAM-Augmented UWB Localization. 2018.
- [61] Amin Basiri, Valerio Mariani, and Luigi Glielmo. Enhanced V-SLAM combining SVO and ORB-SLAM2, with reduced computational complexity, to improve autonomous indoor mini-drone navigation under varying conditions. In *IECON Proceedings (Industrial Electronics Conference)*, volume 2022-October. IEEE Computer Society, 2022. ISBN 9781665480253. doi: 10.1109/IECON49645.2022.9968605.
- [62] Giancarmine Fasano, Michele Grassi, Roberto Opromolla, and Giancarlo Rufino. LIDAR-Inertial Integration for UAV Localization and Mapping in Complex Environments. Arlington, 6 2016. 2016 International Conference on Unmanned Aircraft Systems (ICUAS). ISBN 9781467393331.
- [63] Alireza Famili and Jung-Min Park. ROLATIN: Robust Localization and Tracking for Indoor Navigation of Drones. Technical report.
- [64] Jonathan Putra and Dany Eka Saputra. Autonomous Drone Indoor Navigation Based on Virtual 3D Map Reference.
- [65] IEEE Singapore Section. Control Systems Chapter, Guo li zhong xing da xue, IEEE Control Systems Society, and Institute of Electrical and Electronics Engineers. An Efficient UAV Navigation Solution for Confined but Partially KnownIndoor Environments : Evergreen Laurel Hotel, Taichung, Taiwan, June 18-20, 2014. Eleventh IEEE International Conference on Control and Automation, 2014. ISBN 9781479928378.
- [66] D. Michael Sobers, Girish Chowdhary, and Eric N. Johnson. Indoor navigation for Unmanned Aerial Vehicles. In *AIAA Guidance, Navigation, and Control Conference and Exhibit*, 2009. ISBN 9781563479786. doi: 10.2514/6.2009-5658.
- [67] Hurna Hybasis. Pathfinding algorithms : the four Pillars., 2020. URL <https://medium.com/@urna.hybasis/pathfinding-algorithms-the-four-pillars-1ebad85d4c6b>.
- [68] Nicholas Swift. Easy A* (star) Pathfinding, 2017. URL <https://medium.com/@nicholas.w.swift/easy-a-star-pathfinding-7e6689c7f7b2>.
- [69] Ryan Leigh, Sushil J Louis, and Chris Miles. Using a Genetic Algorithm to Explore A*-like Pathfinding Algorithms. Technical report.
- [70] Fangyu Li, Sisi Zlatanova, Martijn Koopman, Xueying Bai, and Abdoulaye Diakit . Universal path planning for an indoor drone. *Automation in Construction*, 95:275–283, 11 2018. ISSN 09265805. doi: 10.1016/j.autcon.2018.07.025.
- [71] Rafael. Bidarra, ACM Digital Library., ACM Special Interest Group on Computer Graphics and Interactive Techniques., SIGART., Association for Computing Machinery. Special Interest Group on Management of Data., Hypermedia Association for Computing Machinery. Special Interest Group on Hypertext, Web., and Association for Computing Machinery. Special Interest Group on Computer Science Education. *Proceedings of the 2010 Workshop on Procedural Content Generation in Games*. ACM, 2010. ISBN 9781450300230.
- [72] Alois Zingl Wien, Rasterizing Algorithms, and Alois Zingl. A Rasterizing Algorithm for Drawing Curves Multimedia und Softwareentwicklung Technikum-Wien. Technical report.
- [73] Yoav Gabriely and Elon Rimon. Spiral-STC: An On-Line Coverage Algorithm of Grid Environments by a Mobile Robot. Technical report, 2002.
- [74] Marija Dakulovi , Sanja Horvati , and Ivan Petrovi . Complete coverage D*; Algorithm for path planning of a floor-cleaning mobile robot. In *IFAC Proceedings Volumes (IFAC-PapersOnline)*, volume 44, pages 5950–5955. IFAC Secretariat, 2011. ISBN 9783902661937. doi: 10.3182/20110828-6-IT-1002.03400.
- [75] Ana  elek, Marija Seder, Mi el Brezak, and Ivan Petrovi . Smooth Complete Coverage Trajectory Planning Algorithm for a Nonholonomic Robot. *Sensors*, 22(23), 12 2022. ISSN 14248220. doi: 10.3390/s22239269.
- [76] Kavitha Thiayagarajan and Coimbatore Ganeshsankar Balaji. Traversal algorithm for complete coverage. *Journal of Computer Science*, 8(12):2032–2041, 2012. ISSN 15493636. doi: 10.3844/jcssp.2012.2032.2041.
- [77] Mat j Petr k, Tom   Krajn k, and Martin Saska. LIDAR-based Stabilization, Navigation and Localization for UAVs Operating in Dark Indoor Environments. Technical report, 2021. URL <https://s3.amazonaws.com/>.
- [78] Janis Kaltenthaler, Helge A. Lauterbach, Dorit Borrmann, and Andreas N chter. Pose estimation and mapping based on IMU and LiDAR. In *IFAC-PapersOnLine*, volume 55, pages 71–76. Elsevier B.V., 6 2022. doi: 10.1016/j.ifacol.2022.08.012.
- [79] Ahmed Hussein, Abdulla Al-Kaff, Arturo de la Escalera, and Jos  Armingol. Autonomous Indoor Navigation of Low-Cost Quadcopters. 2015. ISBN 9781467384803.
- [80] Quadcopter_simulink_paper.

- [81] Daniel Mellinger, Nathan Michael, and Vijay Kumar. Trajectory generation and control for precise aggressive maneuvers with quadrotors. In *International Journal of Robotics Research*, volume 31, pages 664–674, 4 2012. doi: 10.1177/0278364911434236.
- [82] S Sun. Quadrotor Fault Tolerant Flight Control and Aerodynamic Model Identification. doi: 10.4233/uuid:f0bdac3d-376d-4b24-9241-3a1e35731373. URL <https://doi.org/10.4233/uuid:f0bdac3d-376d-4b24-9241-3a1e35731373>.
- [83] Semtech. DS_SX1276-7-8-9_W_APP_V7. URL <https://www.semtech.com/products/wireless-rf/lora-connect/sx1276>.
- [84] Low Power Long Range Transceiver Module. Technical report, . URL www.hoperf.com.
- [85] TinyTronics. HC-12 SI4463 Wireless Serial Port Module - 433Mhz. URL <https://www.tinytronics.nl/shop/en/hc-12-si4463-wireless-serial-port-module-433mhz>.
- [86] ISMP.868.35.6.A.02 Specifications, .
- [87] Taoglas. TI.08.C.0112, . URL <https://www.taoglas.com/product/ti-08-c-868mhz-terminal-antenna-smamra/>.
- [88] Taoglas. IS.04.B.301111, . URL <https://www.taoglas.com/datasheets/IS.04.B.301111.pdf>.
- [89] APAE868R2540JBDB2-T. Technical report, . URL www.abracon.com.
- [90] FuriousFPV. FuriousFPV VTX Stealth Long Range 2.4G 25/200/500/800 mW. URL https://furiousfpv.com/product_info.php?cPath=28&products_id=666.
- [91] NexWaveRF. ImmersionRC 2.4 GHz 700mW Audio/Video Transmitter Instruction Manual - International Edition. URL <https://www.immersionrc.com/manuals/ImmersionRC%202.4GHz%20700mW%20Tx.pdf>.
- [92] TBS UNIFY 2G4 500mW / 800mW 16ch Video Tx. Technical report, .
- [93] myFPVStore.com. FuriousFPV Two Slices 2.4G Patch Antenna RHCP. URL <https://www.myfpvstore.com/antennas/furiousfpv-two-slices-2-4g-patch-antenna-rhcp/>.
- [94] flytron.com. 2.4ghz 11dB LHCP Patch Antenna. URL <https://store.flytron.com/products/2-4ghz-11db-lhcp-patch-antenna>.
- [95] Menace RC Numskull 2.4Ghz Patch Antenna (RHCP) , . URL <https://www.getfpv.com/fpv/antennas/menace-numskull-2-4ghz-patch-antenna-rhcp.html>.
- [96] Chaoxing Yan, Lingang Fu, Jiankang Zhang, and Jingjing Wang. A Comprehensive Survey on UAV Communication Channel Modeling. *IEEE Access*, 7:107769–107792, 2019. ISSN 21693536. doi: 10.1109/ACCESS.2019.2933173.
- [97] Jyrki Alakuijala, Evgenii Kliuchnikov, Zoltan Szabadka, and Lode Vandevenne. Comparison of Brotli, Deflate, Zopfli, LZMA, LZHAM and Bzip2 Compression Algorithms. Technical report.
- [98] A. Di Carlofelice, E. Di Giampaolo, M. Elaiopoulos, M. Feliziani, M. Roselli, and P. Tognolatti. Localization of radio emitters into collapsed buildings after earthquake: Measurements of path loss and direction of arrival. In *IEEE International Symposium on Electromagnetic Compatibility*, 2012. ISBN 9781467307185. doi: 10.1109/EMCEurope.2012.6396813.
- [99] Ivan Bobkov, Alexey Rolich, Maria Denisova, and Leonid Voskov. Study of LoRa Performance at 433 MHz and 868 MHz Bands Inside a Multistory Building. In *Moscow Workshop on Electronic and Networking Technologies, MWENT 2020 - Proceedings*. Institute of Electrical and Electronics Engineers Inc., 3 2020. ISBN 9781728125718. doi: 10.1109/MWENT47943.2020.9067427.
- [100] Panu Ah-Rantala, Leena Ukkonen, Lauri Sydanheimo, Mikko Keskilammi, and Mark : Ku Kivikoski. DIFFERENT KINDS OF WALLS AND THEIR EFFECT ON THE ATTENUATION OF RADIO WAVES INDOORS. Technical report.
- [101] William C Stone. NIST construction automation program, report no. 3:. Technical report, National Institute of Standards and Technology, Gaithersburg, MD, 1997. URL <https://nvlpubs.nist.gov/nistpubs/Legacy/IR/nistir6055.pdf>.
- [102] Jessie Y.C. Chen and Jennifer E. Thropp. Review of low frame rate effects on human performance, 11 2007. ISSN 10834427.
- [103] Battery University. BU-502: Discharging at High and Low Temperatures. URL <https://batteryuniversity.com/article/bu-502-discharging-at-high-and-low-temperatures>.
- [104] Chung-Hao Chen, Yi Yao, Andreas Koschan, and Mongi Abidi. A novel performance evaluation paradigm for automated video surveillance systems. *Central Europ. J. Computer Science*, 1:430–441, 12 2011. doi: 10.2478/s13537-011-0030-0.
- [105] Sinke Jos. AE3211-II_CH10_Lean Manufacturing_2023.
- [106] M. M.L. Chang, S. K. Ong, and A. Y.C. Nee. Approaches and Challenges in Product Disassembly Planning for Sustainability. In *Procedia CIRP*, volume 60, pages 506–511. Elsevier B.V., 2017. doi: 10.1016/j.procir.2017.01.013.

- [107] Is Carbon Fibre Recyclable? URL <https://www.fairmat.tech/blog/is-carbon-fiber-recyclable/>.
- [108] Hongfang Sun, Guanping Guo, Shazim Ali Memon, Weiting Xu, Qiwu Zhang, Ji-Hua Zhu, and Feng Xing. Recycling of carbon fibers from carbon fiber reinforced polymer using electrochemical method. *Composites Part A: Applied Science and Manufacturing*, 78:10–17, 2015. ISSN 1359-835X. doi: <https://doi.org/10.1016/j.compositesa.2015.07.015>. URL <https://www.sciencedirect.com/science/article/pii/S1359835X1500247X>.
- [109] Academic Editor, Julia A Baimova, Amiruddin Isa, Norlin Nosbi, Mokhtar Che Ismail, Hazizan Md Akil, Wan Fahmin Faiz Wan Ali, and Mohd Firdaus Omar. materials A Review on Recycling of Carbon Fibres: Methods to Reinforce and Expected Fibre Composite Degradations. 2022. doi: 10.3390/ma15144991. URL <https://doi.org/10.3390/ma15144991>.
- [110] Recycling Lipo Batteries. URL <https://www.epa.gov/recycle/used-lithium-ion-batteries>.
- [111] PayScale. Average Production Worker Hourly Pay in Netherlands, 2023. URL https://www.payscale.com/research/NL/Job=Production_Worker/Hourly_Rate.
- [112] Joost Lansink. Zoveel vierkante meter kantooruimte heb je nodig per persoon. URL <https://skepp.nl/nl/blog/kantooruimtetips/zoveel-vierkante-meter-kantooruimte-heb-je-nodig-per-persoon>.
- [113] Stand van zaken: Bedrijfsruimte Markt 2022, . URL https://www.nvm.nl/media/d1mhteai/nvm_bedrijfsruimtemarkt_2022_enkel.pdf.
- [114] Riyaz Khair. The Costs of New Product Development. URL <https://ventrify.ca/news/costs-of-new-product-development/>.
- [115] The Business Company. Search And Rescue Equipment Global Market Report 2023 . *The Business Company*, 1 2023. URL <https://www.thebusinessresearchcompany.com/report/search-and-rescue-sar-equipment-global-market-report>.
- [116] S. N. Jha. Search and rescue Drone Market. Technical report, 10 2022. URL <https://www.factmr.com/report/search-and-rescue-drone-market>.
- [117] Fact MR. <https://www.factmr.com/report/search-and-rescue-drone-market>.
- [118] ScoutID. ScoutID Scout137 Specifications, 2022. URL <https://www.scoutdi.com/scout-137-drone-system/>.
- [119] Flyability. Flyability Elios 3 Specifications, 2023. URL <https://www.flyability.com/elios-3>.
- [120] DJI. DJI Avata Specifications, 2023. URL <https://www.dji.com/nl/avata/specs>.
- [121] Cleo. Cleo Dronut Specifications, 2023. URL <https://cleorobotics.com/product/>.
- [122] 4drc. 4drc 4D-V2 Specifications, 2023. URL <https://www.4drc.com/products/4dv2?variant=40169001386032>.
- [123] Multinnov. Multinnov Stereo 2 Specifications, 2023. URL <https://www.multinnov.com/products/stereo2>.
- [124] Ariel Braverman. Unmanned Aerial Systems (UAS) in Urban Search and Rescue – Methodology, Capacity Development and Integration. 2021.
- [125] Grand View Research. Commercial Drone Market Size, Share & Trends Analysis Report By Product (Fixed-wing, Rotary Blade, Hybrid), By Application, By End-use, By Region, And Segment Forecasts, 2023 - 2030. 1 2022. URL <https://www.grandviewresearch.com/industry-analysis/global-commercial-drones-market#:~:text=The%20global%20commercial%20drone%20market,including%20filming%20and%20emergency%20response>.
- [126] Nathan Ellering. Marketing SWOT Analysis: How To Do It (With Examples & Template), 11 2020. URL <https://coschedule.com/marketing-strategy/swot-analysis>.
- [127] Alex Lindley. How to Do a SWOT Analysis, 11 2022. URL <https://www.semrush.com/blog/swot-analysis-examples/>.
- [128] Industriële Gebouwen te Huur, . URL <https://www.immoweb.be/nl/zoekertje/industriële-gebouwen/te-huur/herent/3020/10516125>.
- [129] Eungchang Mason Lee, Junho Choi, Hyungtae Lim, and Hyun Myung. REAL: Rapid Exploration with Active Loop-Closing toward Large-Scale 3D Mapping using UAVs. 8 2021. URL <http://arxiv.org/abs/2108.02590>.

A

Task Distribution

Table A.1: Task Distribution of the Documentation

Section	Jonas	Julia	Jelmer	Timo	Ryan	Alexandra	Liam	Mischa	Egemen	Rosa
Preface							•			
Executive Overview					•			•		•
1		•								
2 Introduction		•								
2.1		•		•						
2.2		•	•	•						
2.3										
2.4			•	•			•	•		
3 Introduction					•					
3.1					•	•				
3.2					•	•				
4 introduction	•									
4.1	•									
4.2	•									
4.3	•									
5 introduction			•							
5.1			•	•			•			
5.2			•				•			
5.3			•	•						
6 introduction		•							•	
6.1		•					•	•		
6.2									•	
7 introduction								•		
7.1								•		
7.2								•		
7.3							•	•		•
7.4								•		•
7.5								•		•
8 introduction							•			
8.1										•
8.2					•					
8.3			•							
8.4		•	•	•						
8.5		•	•	•						
9 Introduction					•					
9.1					•					
9.2			•		•					
9.3		•						•		
10 Introduction	•									
10.1	•									
10.2	•									
10.3	•									
10.4	•									
11							•	•		
12 introduction							•			
12.1							•			
12.2	•									
12.3						•				
12.4							•	•	•	
12.5		•	•			•	•	•	•	
13 Introduction								•		
13.1			•				•	•	•	
13.2							•			
13.3								•		
14	•				•	•		•		•
15	•	•	•	•		•	•	•	•	
Document Managing	•		•							
CATIA										•